Multiscale, multiphysic modeling of the skeletal muscle during isometric contraction

Vincent Carriou

▶ **To cite this version:**

Vincent Carriou. Multiscale, multiphysic modeling of the skeletal muscle during isometric contraction. Biomechanics [physics.med-ph]. Université de Technologie de Compiègne, 2017. English. NNT : 2017COMP2376 . tel-02067013

HAL Id: tel-02067013
https://theses.hal.science/tel-02067013

Submitted on 13 Mar 2019

HAL is a multi-disciplinary open access archive for the deposit and dissemination of scientific research documents, whether they are published or not. The documents may come from teaching and research institutions in France or abroad, or from public or private research centers.

L'archive ouverte pluridisciplinaire **HAL**, est destinée au dépôt et à la diffusion de documents scientifiques de niveau recherche, publiés ou non, émanant des établissements d'enseignement et de recherche français ou étrangers, des laboratoires publics ou privés.

Par **Vincent CARRIOU**

Multiscale, multiphysic modeling of the skeletal muscle during isometric contraction

Thèse présentée pour l'obtention du grade de Docteur de l'UTC

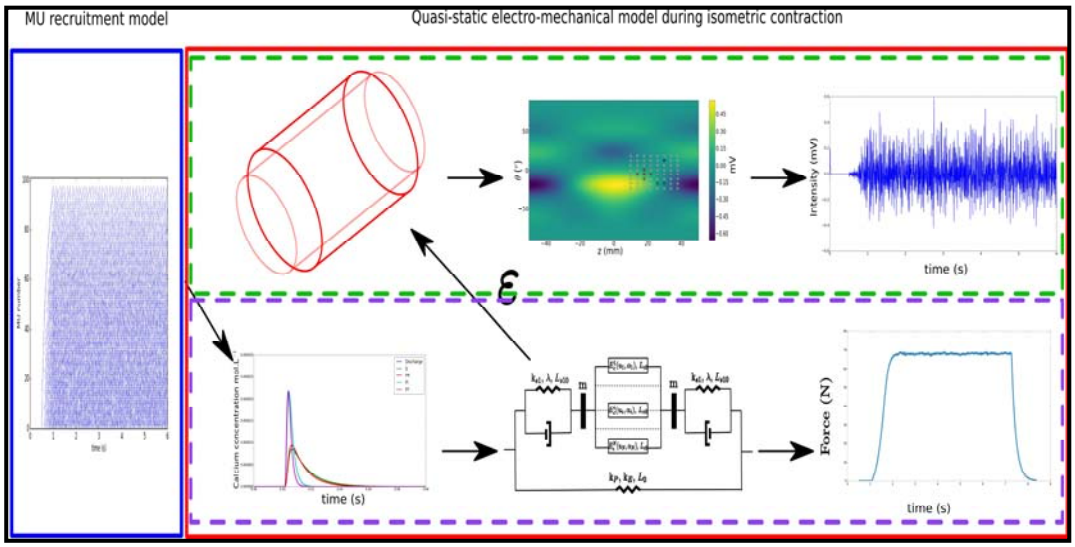

Soutenue le 4 octobre 2017
Spécialité : Biomécanique et Bio-ingénierie : Unité de Recherche Biomécanique et Bio-ingénierie (UMR-7338)
D2376

Université de Technologie de
Compiègne
Ecole Doctorale
15 Rue Roger Couttolenc
60200 Compiègne

Multiscale, multiphysic modeling of the skeletal muscle during isometric contraction

Thesis Presented to

Sorbonne University, Université de Technologie de Compiègne Doctoral school « Sciences pour l'ingénieur » for the Degree of

Doctor in Biomechanics and Bioengineering

Presented and publicly defended by:

4 october 2017

Spécialité : Biomécanique et Bio-ingénierie

CARRIOU Vincent

Jury members :

Reviewers:

Pr. Dario Farina, Professor, Imperial College London, Department of Bioengineering Dr. Alfredo I. Hernandez, Research Director INSERM, Université de Rennes 1, LTSI

Examiners:

Pr. Catherine Marque, Professor, Université de Technologie de Compiegne, BMBI Dr. David Guiraud, Research Director INRIA, University of Montpellier 2, LIRMM

Supervisors:

Dr. Sofiane Boudaoud, Associate Professor, Université de Technologie de Compiègne, BMBI

Dr. Jérémy Laforêt, Research Engineer CNRS, Université de Technologie de Compiègne, BMBI

Remerciements

Ce travail a été réalisé dans le cadre du Labex MS2T. Il a été supporté par le gouvernement français, à travers le "Programme Investissement pour l'Avenir" encadré par l'Agence Nationale pour la Recherche (Reference ANR-11-IDEX-0004-02).

Dans un premier temps, je tiens à remercier Prof. Marie-Christine Ho Ba Tho, directrice du laboratoire BMBI et Dr. Karim El Kirat, maître de conférence au laboratoire BMBI et responsable du Master MS2C, pour m'avoir donné l'opportunité de réaliser cette thèse dans le laboratoire BMBI. Je tiens aussi à remercier Prof. Catherine Marque, responsable de l'équipe NSE du laboratoire BMBI dans laquelle j'ai réalisé ma thèse, pour son soutien et ses encouragements indéfectibles tout au long de cette thèse ainsi que pour l'ensemble de ses conseils avisés qu'elle a su me donner au bon moment.

Merci aux membres du jury, Prof. Dario Farina, Prof. Alfredo I. Hernandez, Prof. Catherine Marque, Dr. Guiraud David qui ont trouvé du temps et ont fait le déplacement pour assister à la soutenance de thèse malgré leur emploi du temps chargé.

Un grand merci à mes directeurs de thèse, Dr. Sofiane Boudaoud et Dr. Jérémy Laforêt pour m'avoir fait confiance durant la thèse. J'aurai énormément appris professionellement et personnelement auprès d'eux. Merci pour leur investissement constant et sans faille durant ces 3 années. Ils ont su m'insuffler une excellente dynamique pour tirer le maximum de mon potentiel. Merci Dr. Sofiane Boudaoud pour ces réunions enflammées nourries par ton dynamisme, ta vision et tes idées avant gardistes du domaine, ta rigueur, ta motivation omniprésente et ta bienveillance. Merci pour toujours avoir cru en moi et en ce que l'on faisait, merci pour m'avoir constamment encouragé même dans les moments plus difficiles. Merci Dr. Jérémy Lafôret pour ces longues heures de discussion et de réflexion autour de ma thèse ou de sujets diverses. Merci pour m'avoir transmis tes connaissances, ta culture et ta curiosité qui sont sans limites. Merci d'avoir toujours pris le temps de m'écouter et d'avoir toujours eu les mots exacts aux bons moments. Je vous aurai bien embêté durant ces 3 années mais nous avons formé une excellente équipe et fourni du très bon travail. Ça aura été difficile mais en regardant en arrière, ça en valait le coup.

De plus, merci à l'ensemble des membres du laboratoire BMBI et de l'UTC plus globalement : Adrien Letocart, Dr. Firas Farhat, Dr. Noujoude Nader, Kevin Lepetit, Saeed Zahran, Dr. Malek Kammoun, Quentin Demigny, Dr. Redouane Ternifi, Dr. Francis Canon, Dr. Didier Gamet, Dr. Jean-François Grosset, Dr. Khalil Ben Mansour, Lilandra Boulais et Megane Beldjilali Labro. Merci pour ces moments dont je me souviendrai toute ma vie et merci pour ces discussions/collaborations scientifiques que nous avons pu avoir.

Un merci tout particulier à mes parents Nelly et Jean-René qui m'ont toujours soutenu depuis le début. Merci pour votre soutien sans faille et votre amour continue. Si j'en suis ici aujourd'hui, c'est en grande partie grâce à eux. Merci à Marine et Dominique, ma soeur et mon frère, pour vos encouragements et ces moments passés ensemble qui m'ont permis de me déconnecter et de décompresser. Merci à mes amis que je considère comme des membres de ma famille, Ludovic, Soraya, Nour, Côme, Laéticia et Véronique pour

toujours avoir su m'écouter et me soutenir dans les moments les plus difficiles. J'ai de la chance de vous avoir à mes côtés, merci pour tout encore.

Finalement, je tiens à remercier ma femme, Mariam Al Harrach, avec qui j'ai eu la chance de réaliser ma thèse. Merci pour tous les moments qu'on passe ensemble, la vie est beaucoup plus belle avec toi à mes côtés. Merci pour ton soutien sans faille et les discussions scientifiques que l'on peut avoir, celles-ci m'ont beaucoup aidé durant la thèse.

Avant propos: Les systèmes neuromusculaire et musculosquelettique sont des systèmes de systèmes complexes qui interagissent parfaitement entre eux afin de produire le mouvemement. En y regardant de plus près, ce mouvement est la résultante d'une force musculaire créée à partir d'une activation du muscle par le système nerveux centrale. En parallèle de cette activité mécanique, le muscle produit aussi une activité électrique elle aussi contrôlée par la même activation. Cette activité électrique peut être mesurée à la surface de la peau à l'aide d'électrode, ce signal enregistré par l'électrode se nomme le signal Electromyogramme de surface (sEMG). Comprendre comment ces résultats de l'activation du muscle sont générés est primordiale en biomécanique ou pour des applications cliniques. Evaluer and quantifier ces interactions intervenant durant la contraction musculaire est difficile et complexe à étudier dans des conditions expérimentales. Par conséquent, il est nécessaire de développer un moyen pour pouvoir décrire et estimater ces interactions. Dans la littérature de la bioingénierie, plusieurs modèles de génération de signaux sEMG et de force ont été publiés. Ces modèles sont principalment utilisés pour décrire une partie des résultats de la contraction musculaire. Ces modèles souffrent de plusieurs limites telles que le manque de réalisme physiologique, la personnalisation des paramètres, ou la représentativité lorsqu'un muscle complet est considéré. Dans ce travail de thèse, nous nous proposons de développer un modèle biofidèle, personnalisable et rapide décrivant l'activité électrique et mécanique du muscle en contraction isométrique. Pour se faire, nous proposons d'abord un modèle décrivant l'activité électrique du muscle à la surfac de la peau. Cette activité électrique sera commandé par une commande volontaire venant du système nerveux périphérique, qui va activer les fibres musculaires qui vont alors dépolariser leur membrane. Cette dépolarisation sera alors filtrée par le volume conducteur afin d'obtenir l'activité électrique à la surface de la peau. Une fois cette activité obtenue, le système d'enregistrement décrivant une grille d'électrode à haute densité (HD-sEMG) est modélisée à la surface de la peau afin d'obtenir les signaux sEMG à partir d'une intégration surfacique sous le domaine de l'électrode. Dans ce modèle de génération de l'activité électrique, le membre est considéré cylindrique et multi couches avec la considération des tissues musculaire, adipeux et la peau. Par la suite, nous proposons un modèle mécanique du muscle décrit à l'échelle de l'Unité Motrice (UM). L'ensemble des résultats mécanique de la contraction musculaire (force, raideur et déformation) sont déterminées à partir de la même commande excitatrice du système nerveux périphérique. Ce modèle est basé sur le modèle de coulissement des filaments d'actine-myosine proposé par Huxley que l'on modélise à l'échelle UM en utilisant la théorie des moments utilisée par Zahalak. Ce modèle mécanique est validé avec un profil de force enregistré sur un sujet paraplégique avec un implant de stimulation neurale. Finalement, nous proposons aussi trois applications des modèles proposés afin d'illustrer leurs fiabilité ainsi que leurs utilité. Tout d'abord une analyse de sensibilité globale des paramètres de la grille HD-sEMG est présentée. Puis, nous présenterons un travail fait en collaboration avec une autre doctorante une nouvelle étude plus précise sur la modélisation de la relation HD-sEMG/force en personnalisant les paramètres afin de mimer au mieux le comportement du Biceps Brachii. Pour conclure, nous proposons un dernier modèle quasi-dynamique décrivant l'activité électro-mécanique du muscle en contraction isométrique. Ce modèle déformable va actualiser l'anatomie cylindrique du membre sous une hypothèse isovolumique du muscle.

Mots-clés: Système de systèmes; modélisation; contraction du muscle squelettique; activité électrique; activité mécanique; optimisation; modèle couplé; analyse de sensibilité; relation sEMG/force

Abstract: The neuromuscular and musculoskeletal systems are complex System of Systems (SoS) that perfectly interact to provide motion. From this interaction, a muscular force is generated from the muscle activation commanded by the Central Nervous System (CNS) that pilots joint motion. In parallel an electrical activity of the muscle is generated driven by the same command of the CNS. This electrical activity can be measured at the skin surface using electrodes, namely the surface electromyogram (sEMG). The knowledge of how these muscle outcomes are generated is highly important in biomechanical and clinical applications. Evaluating and quantifying the interactions arising during the muscle activation are hard and complex to investigate in experimental conditions. Therefore, it is necessary to develop a way to describe and estimate it. In the bioengineering literature, several models of the sEMG and the force generation are provided. They are principally used to describe subparts of the muscular outcomes. These models suffer from several important limitations such lacks of physiological realism, personalization, and representability when a complete muscle is considered. In this work, we propose to construct bioreliable, personalized and fast models describing electrical and mechanical activities of the muscle during contraction. For this purpose, we first propose a model describing the electrical activity at the skin surface of the muscle where this electrical activity is determined from a voluntary command of the Peripheral Nervous System (PNS), activating the muscle fibers that generate a depolarization of their membrane that is filtered by the limb volume. Once this electrical activity is computed, the recording system, i.e. the High Density sEMG (HD-sEMG) grid is defined over the skin where the sEMG signals is determined as a numerical integration of the electrical activity under the electrode area. In this model, the limb is considered as a multilayered cylinder where muscle, adipose and skin tissues are described. Therefore, we propose a mechanical model described at the Motor Unit (MU) scale. The mechanical outcomes (muscle force, stiffness and deformation) are determined from the same voluntary command of the PNS, and is based on the Huxley sliding filaments model upscale at the MU scale using the distribution-moment theory proposed by Zahalak. This model is validated with force profile recorded from a subject implanted with an electrical stimulation device. Finally, we proposed three applications of the proposed models to illustrate their reliability and usefulness. A global sensitivity analysis of the statistics computed over the sEMG signals according to variation of the HD-sEMG electrode grid is performed. Then, we proposed in collaboration a new HD-sEMG/force relationship, using personalized simulated data of the Biceps Brachii from the electrical model and a Twitch based model to estimate a specific force profile corresponding to a specific sEMG sensor network and muscle configuration. To conclude, a deformable electro-mechanical model coupling the two proposed models is proposed. This deformable model updates the limb cylinder anatomy considering isovolumic assumption and respecting incompressible property of the muscle.

Keywords: System of systems; modeling; skeletal muscle contraction; electrical activity; mechanical activity; optimization; coupling model; sensitivity analysis; sEMG/force relationship

Publications

International journal papers:

- **V. Carriou**, S. Boudaoud, J. Laforet, and F. S. Ayachi. Fast generation model of high density surface EMG signals in a cylindrical conductor volume. *Computers in Biology and Medicine*, 74: 54–68. Esteemed paper 2016, 3^{rd}/300 [1]

- **V. Carriou**, J. Laforet, S. Boudaoud, and M. Al Harrach. Sensitivity analysis of HD-sEMG amplitude descriptors relative to grid parameter variations of a cylindrical multilayered muscle model. *Biomedical Physics & Engineering Express*, 2(6), 2016.

- M. Al Harrach, **V. Carriou**, S. Boudaoud, J. Laforet, F. Marin. Analysis of the sEMG/Force Relationship using HD-sEMG Technique and Data Fusion: A Simulation Study. *Computers in Biology and Medicine*, 83: 34-47.

- **V. Carriou**, S. Boudaoud, and J. Laforet. Speedup computation of HD-sEMG signals using a motor unit specific electrical source model. *Medical & Biological Engineering & Computing*. In review.

- M. Al Harrach, S. Boudaoud, **V. Carriou**, J. Laforet, A. J., Letocart, J-F. Grosset, and F. Marin. Investigation of the HD-sEMG Probability Density Function Shapes with Varying Muscle Force using Data Fusion and Shape Descriptors. *Computers in Biology and Medicine*. In review.

- **V. Carriou**, S. Boudaoud, J. Laforet, A. Mendes, F. Canon, and D. Guiraud. Multiscale modeling of skeletal muscle contractile properties in isometric conditions. *Journal of Neural Engineering*. Under preparation.

International conference papers:

- **V. Carriou**, M. Al Harrach, J. Laforet, and S. Boudaoud. Sensitivity Analysis of HD-sEMG Amplitude Descriptors Relative to Grid Parameter Variation. *In XIV Mediterranean Conference on Medical and Biological Engineering and Computing*, 57: 119–123. Springer International Publishing, 2016.

- **V. Carriou**, J. Laforet, S. Boudaoud, and M. Al Harrach. Realistic motor unit placement in a cylindrical HD-sEMG generation model. *In 2016 38th Annual International Conference of the IEEE Engineering in Medicine and Biology Society* (EMBS), 1704–1707, 2016.

- M. Al Harrach, B. Afsharipour, S. Boudaoud, **V. Carriou**, F. Marin and R. Merletti. Extraction of the Brachialis muscle activity using HD-sEMG technique and Canonical Correlation Analysis. *In 2016 38th Annual International Conference of the IEEE Engineering in Medicine and Biology Society* (EMBS), 2378-2381, 2016.

- R. El Koury, **V. Carriou**, S. Boudaoud, J. Laforet, and A. Diab. Precise Assessment of HD-sEMG Grid Misalignment Using Nonlinear Correlation. *In 4th International Conference on Advances in BioMedical Engineering* (ICABME). Accepted.

- **V. Carriou**, J. Laforet, and S. Boudaoud. Object-oriented programming of optimized analytic neuromuscular model. *In 7th International Conference on Computational Bioengineering* (ICCB). Accepted.

Glossary

Acetylcholine	**ACh**
Action Potential	**AP**
Adenosine DiphosPhate	**ADP**
Adenosine TriPhosphate	**ATP**
Averaged rectified value	**ARV**
Best Candidate	**BC**
Biceps Brachii	**BB**
Body Mass Indicator	**BMI**
Brachialis	**BR**
Central Nervous System	**CNS**
Coefficient of Variation	**CoV**
Design Of Experiment	**DOE**
Electrical Stimulation	**ES**
Electromyogram	**EMG**
Elementary Effect	**EE**
Elementary Effect Method	**EEM**
Electroencephalogram	**EEG**
Fast Fatigable	**FF**
Fast Fatigable MU	**FFMU**
Fast Intermediate	**FI**
Fast Intermediate MU	**FIMU**
Fast Resistant	**FR**
Fast Resistant MU	**FRMU**
Fiber Action Potential	**FAP**
Finite Element Method	**FEM**
Functional Electrical Stimulation	**FES**
Hermite Rodriguez	**HR**
High Density	**HD**
High Density sEMG	**HD-sEMG**
High Recruitment Strategy	**HRS**
High order Statistics	**HOS**
Human Machine Interface	**HMI**
Inter Spike Intervals	**ISI**
Intracellular Action Potential	**IAP**
IntraClass Correlation	**ICC**

Low Recruitment strategy	**LRS**
Magnetic Resonance Imaging	**MRI**
Maximal Voluntary Contraction	**MVC**
Motor Unit	**MU**
MU Action Potential	**MUAP**
MyoTendinous Zone	**MTZ**
Neural Electrical Stimulation	**NES**
Neuromuscular Junction	**NMJ**
Non Propagating Component	**NPC**
Normalized-Root-Mean-Square-Error	**NRMSE**
Ordinary Differential Equations	**ODEs**
Peak firing rate	**PFR**
Peripheral Nervous System	**PNS**
Power Spectral Density	**PSD**
Probability Density Function	**PDF**
Recruitment Threshold Excitation	**RTE**
Rectus Femoris	**RF**
Root Mean Square	**RMS**
Sarcosplasmic Reticulum	**SR**
Single Fiber action potential	**SFAP**
Slow	**S**
Sensitivity Index	**SI**
Slow MU	**SMU**
Standard Deviation	**std**
surface ElectroMyoGram	**sEMG**
System of Systems	**SoS**
Vastus intermedius	**VI**
Vastus lateralis	**VL**
Vastus medialis	**VM**

Contents

List of Tables

List of Figures

General introduction

The neuromuscular and musculoskeletal systems are complex System of Systems (SoS) that mutually interact during motion genesis. In fact, the human motion is managed by the Central Nervous System (CNS) through activation of skeletal muscle fibers. The muscle activation produces two types of responses; mechanical and electrical [2]. These two outcomes have different properties, nevertheless they are linked through multiple interactions during the contraction. The mechanical outcome of skeletal muscle contraction manifests by a force production and the deformation of the muscle [3]. This muscle deformation can induce the motion of a specific joint according to the type of contraction. Yet, movement is crucial for survival and human life, thus it is imperative to understand all its aspects that can determine the functions and detect anomalies of the musculoskeletal and neuromuscular systems [3]. Accordingly, the neuromuscular and musculoskeletal systems can be evaluated along with the diagnosis and management of both neurological and orthopedic diseases through estimation and qualification of this mechanical response which is the force [4]. However, as mentioned earlier, the muscle activation have another response that is correlated to the mechanical one; the electrical activity. This electrical response is called the Electromyogram (EMG) and can be measured in a non invasive manner at the skin surface using surface electrodes [2].

These two phenomena occuring during the contraction of the muscle are the outcomes of complex microscopic interactions. During muscular pathologies one or several of these interactions are disrupted inducing serious consequences on the contractile responses. Considering the complex underlying interactions arising during the muscle contraction these disruptions are hardly diagnosed. For these reasons, bioreliable modeling of the skeletal muscle during contraction is one of the leading challenges in biomechanics and motor control. Bioreliable models can accurately describe the mechanisms controling the muscle activation. Moreover, major interest in such models is the possibility to know all the variables involved during the phenomenon. During experimental protocols studying the muscle contraction, some properties of the muscle cannot be known and thus, may be different among the subjects. These different properties can lead to misinterpret the results of the study. In order to reduce this error due to inter-variability of the muscle composition the number of subjects for this study must be important leading to expensive and long study. Using such a model can reduce this inter-variability since all the parameters physiologically representing the skeletal muscle are controlled by the user.

Understanding the muscle contraction and how these phenomena are created, is fundamental in many areas such as the study of joints and body motion. Moreover this possible new knowledge can help practitioners with diagnosis or development of new treatments. In this thesis we will propose three models describing, the electrical activity of the muscle, the mechanical activity of the muscle and a deformable electro-mechanical activity of the muscle during isometric, isotonic and anisotonic non fatiguing contractions. Since the beginning of the 21^{st} century, computational power significantly increased leading to the

possibility to perform large and precise simulations or complex data processing using a classical workstation. Following this drift, use of high-level programming language by the scientific community emerges. Stimulating by the scientific community, a large ecosystem of generic methods in several research fields (image and signal processing, multi-domain dynamic systems dynamic, multi-channel processing, linear algebra computation, etc.) is developed and accessible. For this purpose, the proposed models are developed in Python programming language, providing access to several scientific libraries that allow an optimized programming that will minimize the computation time of the models. Based on all of the above, this manuscript is organized as follow:

- Chapter 1: in this chapter, we will introduce the main notions concerning the neuromuscular system and motion genesis, essentially the skeletal muscle properties and architecture, the Motor Unit (MU) and the fiber types. Wherein, we describe also the mechanisms of muscle contraction and sEMG signal generations by detailing the generation and propagation of Fiber Action Potential (FAP), the description of MU Action Potential (MUAP), the MU recruitment and firing and enumerating the different types of contractions and the relations between the discharge frequency and the generated force. Afterwards, in the next section, we introduce the HD-sEMG technique as a innovative recording procedure that have many applications and advantages and can improve sEMG based force estimation. In the second section, we propose a state of the art of the electrical, mechanical and neural models of the skeletal muscle that exist in the literature. Finally, we finish this chapter by positioning the proposed thesis work in the face of the current skeletal muscle modeling and indicating the objectives and innovation of the thesis;

- Chapter 2: in this chapter, we will propose a fast modeling of the electrical activity of the skeletal muscle. This model describes the electrical muscle activity from the firing moments of the motoneuron, to the generation, propagation and extinction of the induced intracellular potential along muscle fibers. The muscle is considered as a section inside a multilayered cylinder representing the limb. This electrical activity is described as a 3D spatio-temporal map over the skin surface. Recording of the electrode at the skin surface is defined with numerical integration under the area of the electrode. Representing the muscle electrical activity as a 3D map allows a decoupling between the physical phenomenon and the recording system. Thus, any type of electrode or electrode grid can be defined over the same simulation of the electrical activity. Concerning the model implementation, parallel computing was considered in this model in order to significantly speedup the computation. Yet, simulating realist muscle electrical activity during contraction implies to compute all the fiber electrical sources leading to the determination of hundreds of thousands sources. Even if parallel computing was used to reduce the model computation time, realist simulation lasts several hours. For this purpose, we propose to simulate the electrical sources at the MU scale. The proposed electrical source is MU specific based on the fiber composing it. Use of such a model significantly reduces the computation time of the model allowing to perform infeasible studies before such as inverse problems or global sensitivity analysis.

- Chapter 3: in this chapter, we will propose a mechanical model of the skeletal muscle. This model describes the generated force, the muscle stiffness as well as the muscle deformation. On the contrary of most of the mechanical models, the muscle

modeling is described at the MU scale allowing more details and knowledge on the muscle contraction. The proposed model is driven by the same input definition as the electrical model, i.e., a voluntary MU recruitment scheme for a desired contraction level. This model is validated using data recorded during electrical stimulation performed on paraplegic patients. Modeling the muscle at the MU scale and its contractile properties allows a direct access of the MU contribution in the corresponding muscle force and stiffness. Furthermore, this model solves one of the main issue in skeletal muscle mechanical modeling concerning a bioreliable definition of the muscle activation, which is directly related to the neural drive comparing to the widely used Hill model where the neural drive is simply represented by one scalar parameter.

- Chapter 4: in this chapter, we will present the different possible applications of the proposed models and exhibit preliminar study using the first deformable model that is able to compute both electrical and mechanical activity of the muscle accounting for the muscle deformation during isometric contractions. First a global sensitivity analysis is proposed where the sensitivity of the statistics computed over the HD-sEMG signals is assessed according to the variation of the recording system parameters. Second, in collaboration with another PhD work, we propose a simulation study of the sEMG/force relationship. The electrical model was used and personalized with experimental measurements and focused literature. This study was performed for the Biceps Brachii muscle. Finally, a deformable model during isometric contractions combining both electrical and mechanical models is presented. This model considered in a first place the muscle deformation during the contraction, then this deformation is used to update the cylindrical representation of the limb.

Chapter 1

State of the art and problematic

Contents

1.1 Introduction

Since the early human life, man has shown unceasing interest in the organs responsible for mobility in his own body first and those of animals after. This extreme curiosity is due to the fact that movement is considered as the capital sign of animal life; "Il moto è cause d'ogni vita" Leonardo Da Vinci, "the motion is the principle of all life". Actually, part of the first ever scientific experiments were conducted on muscles to study its functions. A lot of philosophers and scientists from Leonardo Da Vinci, Galvani to Etienne-Jules Marey, whose findings constructed the beginning of neurophysiology and muscle contraction dynamics studies, showed immense interest in the neuro-musculo-skeletal system. This complex system can be decomposed into two subsystems: the neuro-muscular system and the musculo-skeletal system. The neuro-muscular system interprets the neural coding from the Peripheral Nervous System (PNS) into contraction of the muscle fibers and thus, into muscle force. On the other hand, the musculo-skeletal system transforms this muscle force into motion through the multiple joints of the body.

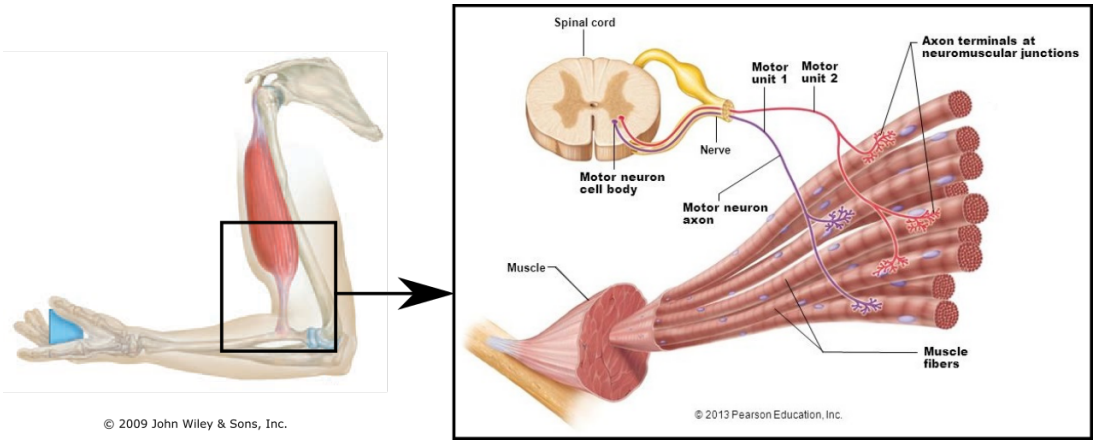

Figure 1.1: Illustration of the neuro-musculo-skeletal system of the Biceps Brachii. (L) The musculo-skeletal system with the muscle attached to the bones through the tendons. (R) The neuro-muscular system with the muscle connected to the CNS that innervates the motor unit motoneurons.

Actually, these complex systems perfectly interact in order to provide the specific muscle contraction needed for a specific motion. In the neuro-muscular system, the muscle contraction is driven by the PNS which is controlled by the Central Nervous System (CNS). The muscle contraction can be characterized from two phenomena, which arise only during the muscle contraction [2]. One perceptible phenomenon is the production of the muscle force and its deformation. Nonetheless, the other physical phenomenon invisible to the eyes occurs in parallel to the force production. This phenomenon corresponds to the depolarization of the muscle fibers when the PNS activates the muscle and thus is an electrical phenomenon. This electrical activity can be recorded through surface electrode placed over the skin [2]. This recorded signal is named the surface ElectroMyoGram (sEMG). Understanding the muscle contraction and how these phenomena are created, is fundamental in many areas such as the study of joints and body motion. Moreover this possible new knowledge can help practitioners with diagnosis or development of new treatments.

Modestly, this thesis will continue the investigation of the neuro-muscular system by focusing on the modeling of the interaction arising in order to provide a better understanding of the underlying mechanisms happening during the voluntary muscle isometric contraction .

This work is motivated by the fact that during muscle contraction we cannot, in a non-invasive way, experimentally quantify or analyze the underlying physiological mechanisms involved. In fact, too much variability such as the neural firings activating the muscle or the precise muscle properties aren't accessible nowadays without clinical invasive procedures [5]. Consequently, it is essential to model the muscle contraction with its electro-mechanical manifestation in agreement with the muscle physiology and variability for a deeper understanding of its functioning. Very accurate models can be developed to the cost of the computation time [6]. Thus, some simplifying assumptions have to be set in order to find a compromise without greatly altering the physiological processes meaning. At the current stage, we don't know any fast model simulating the mechanical and the electrical phenomena with their interactions. Accordingly, the majority of the proposed models [7, 8, 9, 10, 11, 12, 13, 14] are only modeling one phenomenon of the muscle contraction or aren't able to realistically represent a skeletal muscle with its physiological properties because of the complexity of such a model. Thus, in this work we propose to develop a new model describing the voluntary isometric muscle contraction as the mechanical outcomes and the electrical activity produced from the transcription of a specific neural coding provided by the PNS. Furthermore, this model should be able to compute a simulation in a reasonable computation time.

In this chapter, we propose to introduce the notions of the neuro-musculo-skeletal system (sections 1.2) and more particularly the neuro-muscular system (section 1.3) decomposed into the PNS (see section 1.3.1) and the muscular system (see section 1.3.2). Then, after introducing the recording technique of HD-sEMG (section 1.4), we will detail the existing models (section 1.5) of the neural coding provided by the PNS (see section 1.5.1), and the electrical and the mechanical activities induced (see sections 1.5.2 and 1.5.3) as well as models dealing with all this phenomena together and their interactions (see section 1.5.4). Finally, we will conclude this chapter by presenting the problem and the objectives of this thesis (section 1.6).

1.2 The neuro-musculo-skeletal system

This section aims at presenting the essential concepts of the neuro-musculo-skeletal system. Description of its anatomy, as well as its functions in the human body are presented. These notions are required in order to understand the intricate mechanisms involved in the contraction of the skeletal muscles [2, 15]. As introduced, the neuro-musculo-skeletal complex system can be divided into two complex sub-systems: the neuro-muscular system and the musculo-skeletal system. The neuro-muscular system is responsible for the translation of the neural command in order to contract the muscle and generate force as well as electrical activity. While the musculo-skeletal is in charge for transmitting this muscle force to the bones in order to generate a motion.

Commonly, all the voluntary movements involved in the human body are the result of a command or firing of the nervous system. The nervous system in humans and all vertebrates consist of the CNS that includes the brain and the spinal cord; And of the PNS composed of the sensory (afferent) and motor (efferent) nerves innervating the organs [15].

The neural command is generated at the level of the CNS and then transmitted to the motor actors of the human body through the PNS. In the case of movement generation, the targeted organs are the skeletal muscles that are commanded to generate specific motion of the body. The signal is sent to the muscle by activating several motor neurons each supplying a set of muscle fibers (see Fig. 1.2).

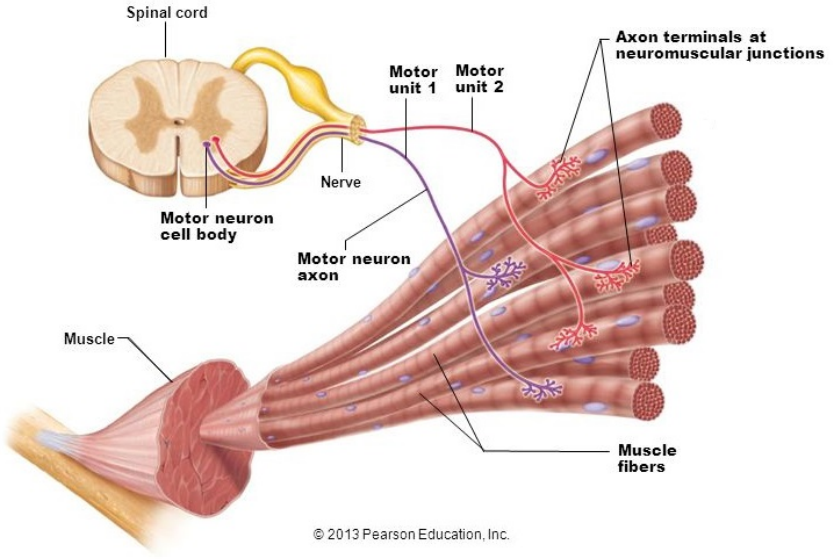

Figure 1.2: Two motoneurons from the spinal cord innervating different fibers within the muscle.

The muscle activation and its phenomena are therefore the results of this anatomical ensemble, commonly defined as the **neuro-muscular system**. When a skeletal muscle is activated, it will produce force as well as electrical activity proportional to the intensity of the neural firings. This force is the result of a chain of chemical reaction occurring at the level of each skeletal fiber after each nerve firing (see section 1.3.1). To generate the movement, the force produced by the muscle must be transmitted to its connected tendons. Then, these tendons are shortened or elongated in order to apply a stress to the connected bones, which then produce a movement of a particular joint. All these systems interacting together are defined by the scientific community as the **neuro-musculo-skeletal system** (see Fig. 1.1).

1.2.1 Motion genesis

The motion production is feasible because of the four essential characteristics of the skeletal muscles:

- **Excitability**: is the capability of the muscle tissue to contract when stimulated by a voluntary or involuntary neural command;
- **Contractility**: is the ability of the muscle tissue to respond to a stimulus by developing a tension;
- **Extensibility**: refers to the ability of the muscle tissue to be stretched or increased in length;

- **Elasticity**: refers to the ability of the muscle tissue to return to its resting state after being stretched.

By definition, all the muscles attached to two bones by tendon are defined as **striated skeletal muscles** or skeletal muscles. The tendons are tough band of fibrous connective tissues whose strong collagen fibers firmly attach muscles to bones. Tendons are able to withstand tension. During contraction, they are put under extreme stress by the muscle, so they are robust and are interlaced into the covering of both muscles and bones.

During the muscle contraction, the muscle may shorten, lengthen or remain the same depending of the nature of the contraction. It is this change in muscle length that will induce effort on the tendons and thus generate the movement of the corresponding bones. We categorize the muscle contraction into four classes:

- Isotonic contractions (see Fig. 1.3) corresponding to constant force generate by the muscle while the muscle length changes [16]. This type of contraction can be either concentric (shortening) or eccentric (lengthening);

- Anisotonic contractions corresponding to non constant force generation with possible change in muscle length. As isotonic contraction, it can be either concentric or eccentric;

- Isometric contractions (see Fig. 1.3) corresponding to constant muscle length with possible variation of the produced force [16]. This contraction doesn't imply the movement of the joint;

- Anisometric contractions (see Fig.1.3) corresponding to non constant muscle length during contraction with possible variation of the generated force [17]. Thus, the contraction can be concentric or eccentric.

Considering the complexity of the muscle contraction nature and with the specified underlying processes interacting for each kind of contraction, we decided to focus on the modeling of the skeletal muscle during voluntary, isometric and non fatiguing contractions.

1.3 The neuro-muscular system

The skeletal muscles are the effectors of the neural system and are muscles that are controlled voluntarily. Considering the complex structures, unknown properties and interactions occurring in the CNS, we only focused this work on the transmitting signals propagate by the PNS to the muscles.

1.3.1 The peripheral neural system

Anatomy

Transmission of the neural signal in the PNS is realized through a neural action potential produces by an α-motoneuron (or somatic motor neuron) placed in the spinal cord and propagates along its axon surrounded by a thick myelin sheath [15]. Each α-motoneuron innervates several fibers composing the targeting muscle. A muscle fiber can only be innervated by one α-motoneuron. This set of fibers innervated by the same α-motoneuron is called a **motor unit** (MU) (see Fig. 1.4). Thus, we consider that the MU is the smallest

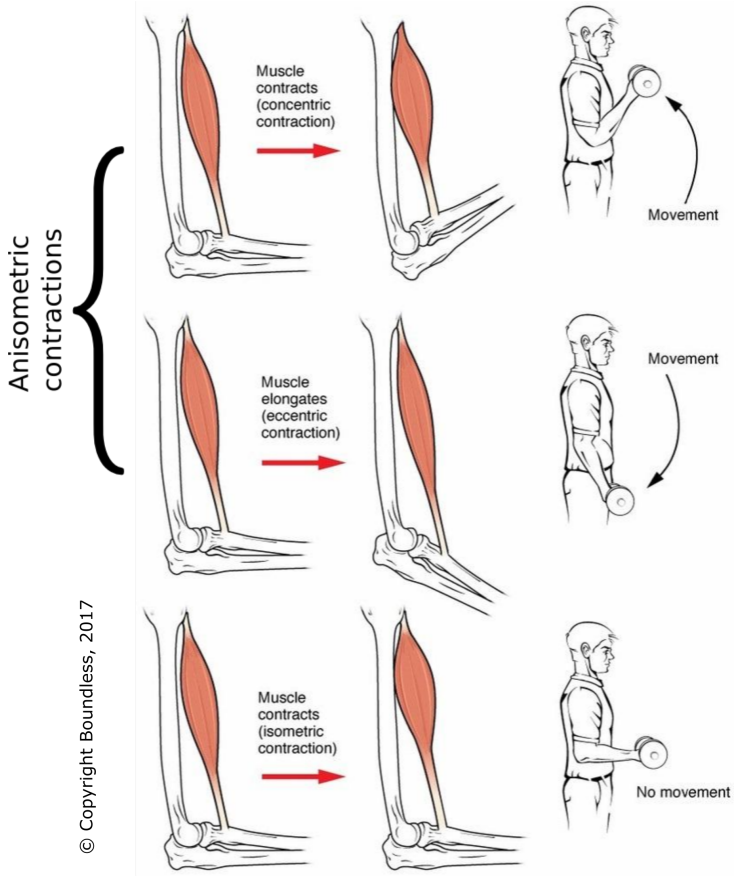

Figure 1.3: Different types of muscle contraction.

functional entity of the muscle contraction [2]. It generates force as well as electrical activity [2].

The axon of the α-motoneuron ends in a synapse, which is an area of communication between the fiber and the motoneuron called the **neuromuscular junction** (NMJ) (see Fig. 1.4). Usually, the NMJ is located around the middle of the muscle fibers. This position allows a quasi-simultaneous contraction of the whole muscular fiber. There is no direct contact between the synapse and the muscle fiber, the communication between these two cells is made through chemical processes. At the end of the axon, there are synaptic vesicles containing thousands of acetylcholine (ACh) molecules (see Fig. 1.4). These ACh molecules are neurotransmitters that communicate with the fiber. The region of the fiber facing the axonal termination is called the **motor end-plate**. Each motor end-plate consists of several millions of ACh receivers. When a nerve firing arrives at the axonal termination it causes a contraction of the fiber following several chemical phenomena. If a new nerve firing arrives at the NMJ, all this chemical processing chain is repeated.

Neural control of the muscular system

When a muscle is voluntary contracted, the chemical and physical phenomena are modulated by the CNS through the supra-spinal centers with two principal mechanisms: the spatial recruitment (number and localization of recruited MUs) and the MU rate coding (firing rate modulation). Thus, force and electrical activity intensity increase according

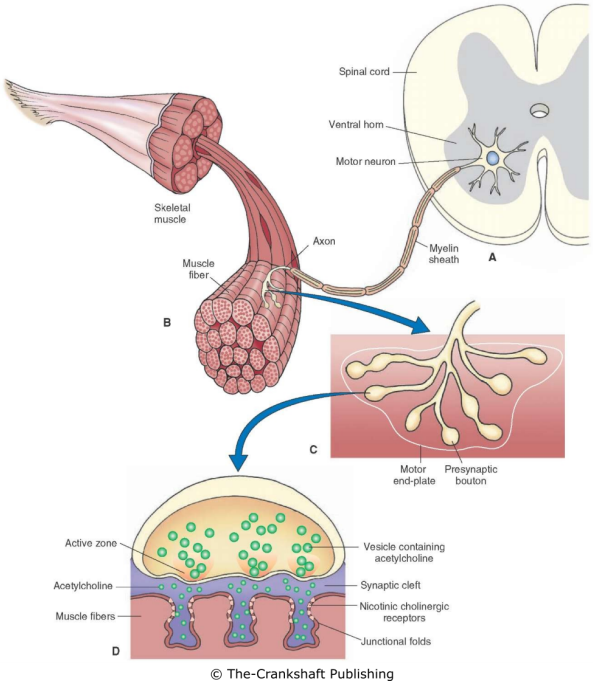

Figure 1.4: Description of the PNS and its communication with the muscular system. (A) Cell body of an α-motoneuron. (B) and (C) Myelinated axon innervating skeletal fibers. (D) The synaptic description with its vesicles and ACh.

to the rise of the number of recruited MUs and the increase of their corresponding firing rate.

The spatial recruitment of the MUs is modulated by the intensity of contraction and follow a rule called the "size principle" defined by Henneman and al. [18, 19]. The "size principle" assessed that during isometric contraction the recruitment of MUs is done through increasing the motoneuron size and thus, the MU size. Thus, MUs are recruited from the MU innervated by the smallest diameter motoneuron to the MU innervated by the highest diameter. Each MU is excited according to the goal of the contraction level, if the goal is below its intensity threshold, the MU is not recruited for this contraction. It has been assessed that the MU recruitment law describing the evolution of the MUs threshold according to contraction level is exponential [20]. Depending on the muscle characteristics, all the MUs are recruited for a contraction level varying between 60 and 90% of the Maximal Voluntary Contraction (MVC) [21]. Beyond this threshold, only increasing the MU firing rate can increase the generated force.

In complement to the MUs spatial recruitment, the CNS also controls the MU rate coding. When a MU is recruited, the motoneuron discharges follow random point processes at a minimal frequency that increases according to the increase of the contraction level following a specific rise [20]. In the literature, we found studies defining different type of rate coding strategies [20, 22, 23, 21]. These strategies can be linear or non linear with defined minimal and maximal discharge frequencies according to the muscle characteristics [23, 21]. The minimal frequency varies between 3 to 10 Hz and the maximal frequency can vary from 7 to 150 Hz [2]. The MU firing regularity can be assessed by computing the Coefficient of Variation (CoV) determined on the Inter Spike Intervals (ISI), corresponding to the elapsed time between two successive firings, which is supposed

to respect a Gaussian distribution [20].

Moreover, according to [5] during natural movements, the MU recruitment pattern varies and doesn't hold to the size principle. Size principle recruitment ensures that the slowest, most fatigue resistant MUs are recruited first for any given task. In contrary, the faster, very fatiguing MUs are therefore reserved for infrequent, high intensity tasks such as jumping. Studies on humans have shown that auditory and visual feedback can alter recruitment orders [24]. It has been suggested that MUs, within an individual muscle, may form groups that can be independently activated to fulfill specific functional roles [25]. These pools of MUs have been termed "task groups" and have showed to be selectively recruited for different kinematic conditions within a motor task such as a stride or a grasping movement [26]. It is, therefore, likely that recruitment strategies other than those predicted by the size principle may be used during gait.

Considering the specific focus upon the muscular contraction physical phenomena, we decided to use a MU recruitment pattern based on the size principle that correctly describe the MU recruitment pattern during isometric contractions [20].

1.3.2 Skeletal muscle

Macroscopic anatomy

The skeletal muscles are attached to bones by the tendons, they are in charge to produce the body motion, to maintain the posture, to produce heat and to protect the inner organs and the body. In the human body, the skeletal muscles have a variety of shapes depending on its fiber orientations and on whether the tendon junction is aligned with the tendon (fusiform muscle) or is at an angle (pennated muscle). In the case of pennated muscles, the muscle fibers are connected to the **aponeurosis** of the muscle [27]. Thus, we can classify the skeletal muscles according to their forms as illustrated in Fig 1.5.

Considering the complex shapes describing the skeletal muscles and thus, specific interactions acting, we had to orientate the model to only one shape description as a first modeling effort. We decided to start to describe the fusiform muscles, such as the Biceps Brachii.

The skeletal muscles of the human body are surrounded by connective tissue, which protects the muscles. The outermost of these connective tissues is called the **hypodermis**, located just below the skin. In addition to protecting the muscles, its role is also to regulate the heat loss generated by the muscles as well as to store the triglyceride surplus of the human body. Below this layer is a set of connective tissues, called **fascia** or **aponeurosis** (see Figure 1.6), continuously surrounding the muscle and some sub-parts.

These fascia are present in all the muscle up to the tendon to form what is defined as the **myotendinous junction**. The tendon then extends to the bone to form what is called the osteo-tendinous junction.

Microscopic anatomy

The most important component in the skeletal muscle is the muscle fiber which includes several hundred nuclei. The muscle fiber diameter varies from 10 μm to 100 μm according to the considered muscle. Similarly, its length differs depending on the muscle and varies between 10 and 30 cm in a healthy adult human body. Like all cells in the human body, the muscle fibers are surrounded by a plasma membrane called the **sarcolemma**. Combined with the sarcolemma, thousands of tunnel-shaped **transverses tubules** connect

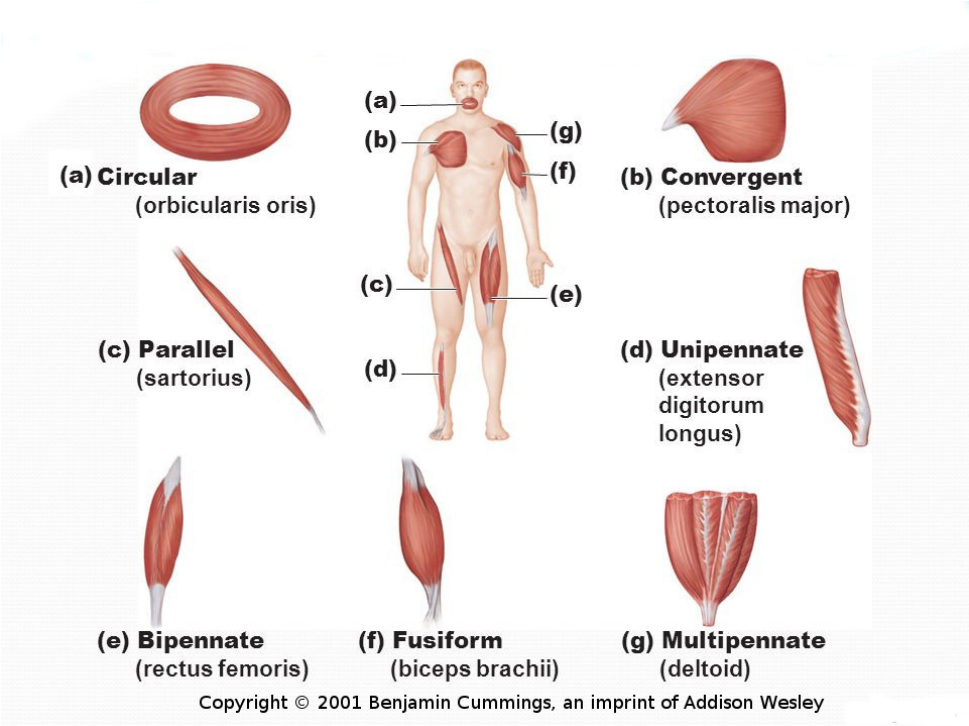

Figure 1.5: Variety of muscle architecture in the human body.

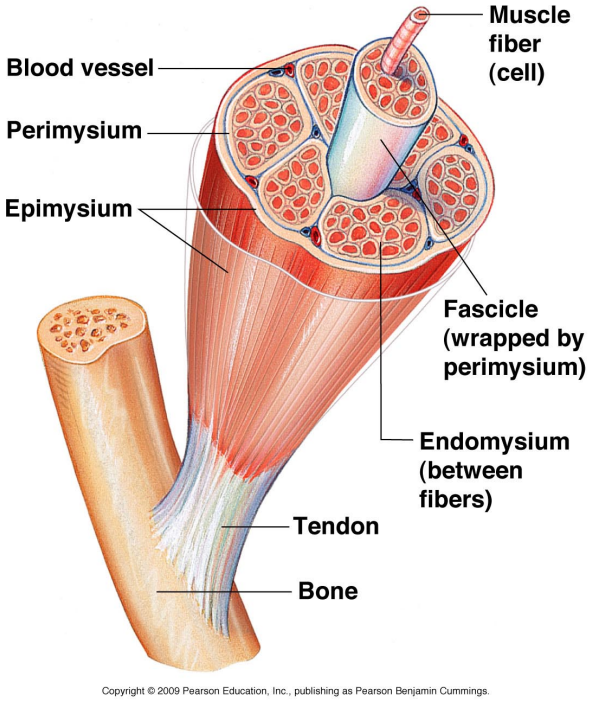

Figure 1.6: Macroscopic structure of skeletal muscle.

the center of the muscle fiber with the outside. Inside the sarcolemma is the **sarcoplasm**, corresponding to the cytoplasm of the fiber. Similar to the cytoplasm, the sarcoplasm mainly holds glycogen, used for the synthesis of adenosine triphosphate (ATP) which acts

as energitical supply for the fiber [15]. In addition, myoglobin protein is also found in sarcoplasm. This protein only exists in the muscles of vertebrates. It stores oxygen molecules for the formation of ATP by the mitochondria when needed. Inside the sarcoplasm there are also numerous cylindrical subunits extending all along the muscle. These subunits are called **myofibrils** (muscle fibrils) (see Figure 1.7). These myofibrils are the smallest contractile units in the muscle, with a diameter of about 2μm. Around each fiber, myofibrils are fluid-filled membrane bags called the **sarcosplasmic reticulum** (SR). When the muscle is at rest, the SR stores a certain amount of calcium ions (Ca^{2+}). Then, during muscle contraction following a neural command from the CNS, the SR will release the Ca^{2+} stored in the fiber in order to realize the muscle contraction (see section 1.3.3).

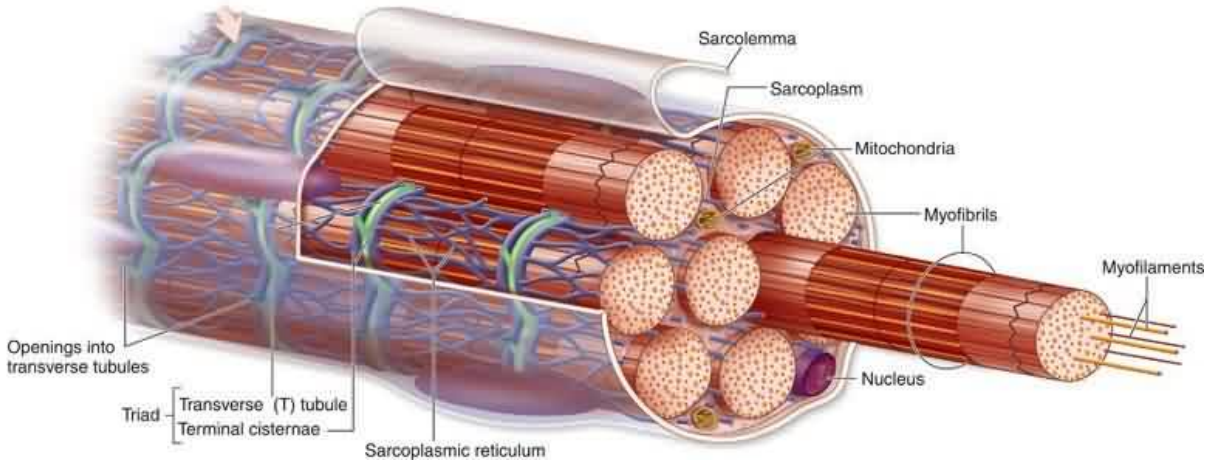

Figure 1.7: Microscopic structure of a skeletal muscle fiber.

Each myofibril consists of several small structures placed in series called **sarcomeres**. The sarcomere is an arrangement of several proteins defining three different filaments (see Figure 1.8):

- The **thick filaments** composed of **myosin** with a diameter of 16 nm and a length of 1-2 μm;
- The **thin filament** consisting of **actin** with a diameter of 8 nm and a length of 1-2 μm;
- The **elastic filaments** composed of **titine**.

To each thick filament is associated two thin filaments. Moreover, at the end of each thick filament is embedded an elastic filament going up to the **Z disk**. The Z disk is the zone that separates the sarcomeres within the myofibril. The thin and thick filaments overlap over a certain length depending on whether the muscle is relaxed, stretched or contracted. Thus each sarcomere can be decomposed into several visible bands using an electronic microscope. There is the **A Band** extending along the thick filament. In this band, there are two zones of superposition with the thin filaments placed at the ends. The area where there is no superposition of thin filaments is called the **H band**. In the middle of this H band, there is a line formed of proteins supporting the thick filaments, this support is called the **M line**. Finally, we define the **I bands** which contain the parts of the thin filaments that does not overlap and the thin filament up to the thick filament of the neighboring sarcomere (see Figure 1.7).

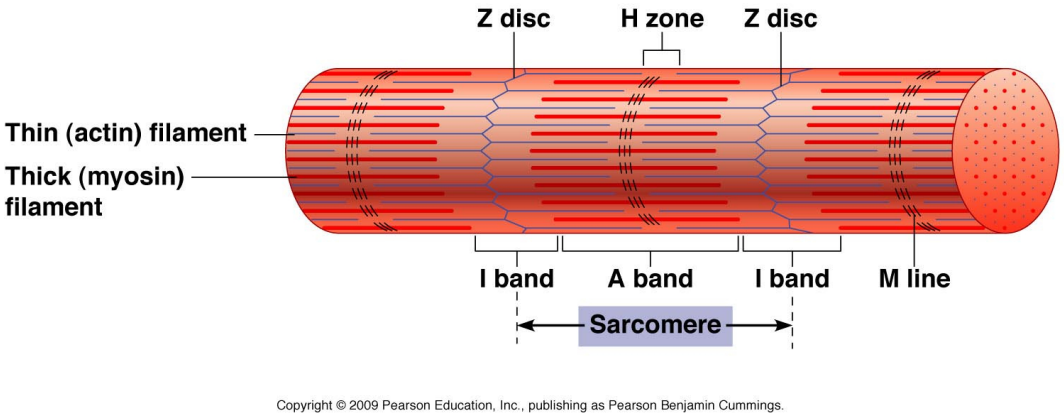

Figure 1.8: Anatomic structure of a muscle myofibril.

Fiber types

As stated in section 1.3.1, a MU is the set of fibers innervated by the same α-motoneuron. Thus, all of the fibers composing a MU possess the same biochemical, histochemical and contractile properties. The identification of the type of MU through its physiological properties is still a challenge today. Most studies attempt to quantify the amount of fibers according to their type by a histochemical study from a cross section of the muscle [28, 29, 30] (see Figure 1.9).

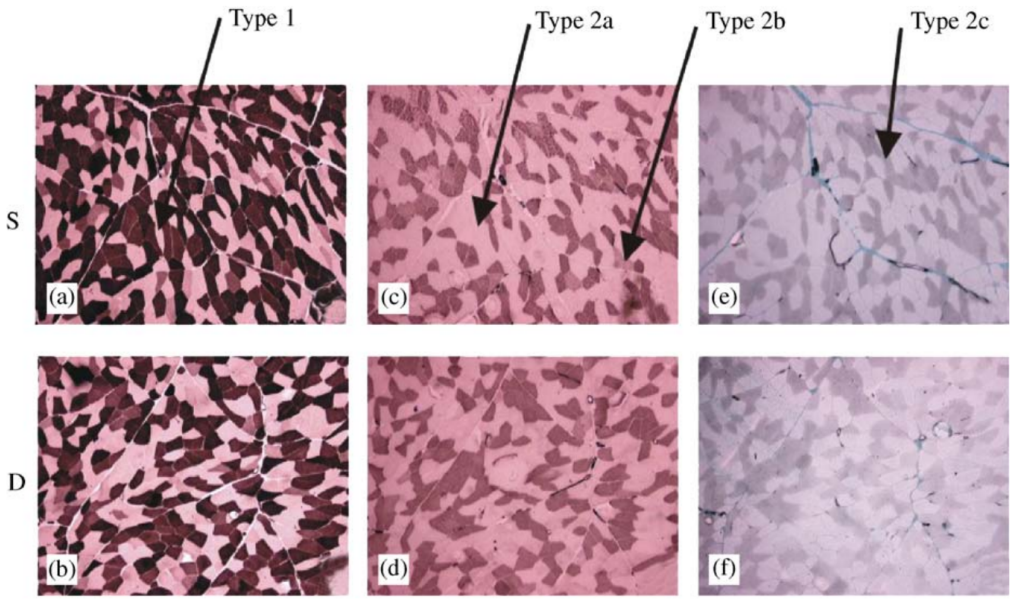

Figure 1.9: Histochemical appearance of different types of fiber in the Brachialis muscle [28].

Despite the difficulty of classification, the type of the MU is determined according to the properties of its fibers. According to published studies, fibers can be categorized into two main groups, type I fibers and type II fibers.

- Type I fibers (or slow fibers) are the fibers with the smallest diameter and thus,

the fibers generating the least force. They appear dark red in the histochemical study (see Fig. 1.9) because they contain a large amount of myoglobin and blood capillaries. These fibers synthesize Adenosine TriPhosphate (ATP) mainly by the aerobic respiration of cells because they are also composed of large mitochondria. These fibers are considered to be slow because hydrolysis by the ATPase enzymes is slower than in type II fibers. Type I fibers slowly produce low force but are highly resistant to muscle fatigue and are therefore capable of providing prolonged activity and maintain it for several hours. These fibers are mainly present in the muscles responsible for maintaining the posture;

- Type II fibers (or fast fibers) have a larger diameter than type I but have less myoglobin. Therefore, they have a clearer appearance in the histochemical study (see Fig. 1.9). In addition, the release of calcium by the SR takes place more rapidly as well as the hydrolysis of the ATPase enzymes. Within fast fibers, we can also differentiate three types:

  1. Type IIA fibers (or fast resistant fiber). They are similar in their composition to slow fibers and are more resistant to fatigue than other fast fibers;
  2. Type IIB fibers (or fatigable fast fibers). These fibers are the closest to the definition of fast fiber, they produce a lot of force very quickly but are very sensitive to muscle fatigue;
  3. The fibers of type IIC (or IIX, or intermediate fiber). These fibers are called intermediate fibers because they are in their composition and characteristics in between the fibers of type IIA and IIB.

The set of fiber types and their characteristics are summarized in Table 1.2.

Table 1.1: Summary of the different types of fibers and their characteristics.

	Type I	Type IIA	Type IIC	Type IIB
Diameter	Small	Medium	Medium	Large
Myoglobin	A lot	A lot	Moderate	Little
Mitochondria	A lot	A lot	Moderate	Little
Histochemistry	Dark red	Red rose	Light red	White
Contraction vilocity	Slow	Fast	Fast	Very fast
Fatigue resistance	High	Medium	Medium	Low
Generated force	Low	Medium	Medium	High
Recrutment order	1st	2nd	3rd	4th

1.3.3 Muscle contraction

Electrical phenomenon

When a neural Action Potential (AP) arrives to the NMJ, a depolarization of the fiber membrane arises. Then, an AP, called the Fiber AP (FAP), generated by this depolarization varies rapidly between -70 mV and 30 mV approximately as depicted in Fig.1.10 [31]. This FAP propagates along the fiber length in the two directions with a velocity that lies between 2 and 6 m.s^{-1} and an intensity of $\sim$ 100 mV.

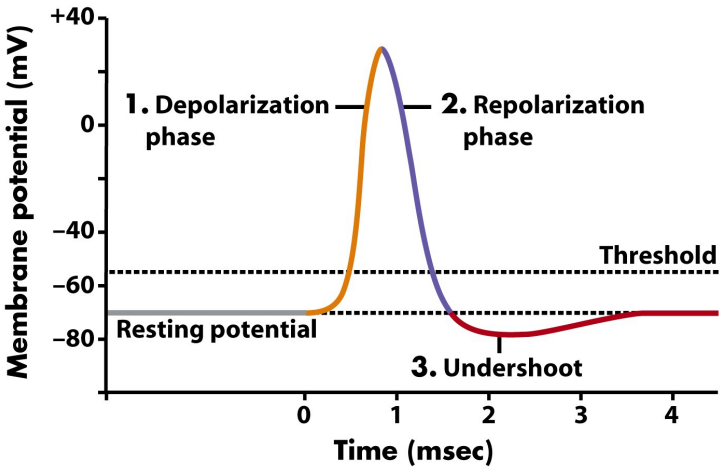

Figure 1.10: The AP of a fiber membrane when a nerve firing arrives. At rest, the tension is at -70 mV. When the pulse arrives, a depolarization occurs rapidly followed by a repolarization of the membrane. This repolarization falls below the voltage at rest, at this time a phenomenon of hyperpolarization intervenes to return potential to the rest tension. (image de ©Pearson Prentice Hall, Inc 2005)

As said above, an α-motoneuron innervates several fibers forming a MU. When a neural firing reaches the NMJ of the fibers, they all generate at the same time a FAP. Thus, we can define a Motor Unit Action Potential (MUAP) corresponding to the sum of the FAP generated by its corresponding fibers. During the muscle contraction, the depolarization of the fibers can be recorded at the skin surface using **surface EMG** (sEMG) electrodes (see section 1.4) or directly in the muscle using the needle EMG. Considering the invasive recording of the needle EMG, we decided to focus on the modeling of sEMG, which seems to have promising abilities. The muscle electrical activity corresponds to the sum of the generated MUAPs.

With this definition, it is clear that the electrical activity generated by the muscle during contraction is dependent of the fiber type composition as well as the number of fiber within the muscle and many other muscle fiber properties. Nevertheless, the wide variability in electrical activity description is also due to the limb anatomy. In fact, the generated FAPs have to progress through different media (muscle, blood vessel, adipose and skin tissues) with different electrical properties. Propagation across these media has a filtering effect on the FAP according to the conductivity and the thickness of the materials [2]. Summation of all these filtering effect on the generated FAP is defined as the effect of the conductor volume leading to the conductor volume theory.

Mechanical phenomenon

As indicated above (see section 1.3.1), the contraction of the muscle fiber is realized after the arrival of a nervous firing to the NMJ. Physiologically, it is only when the SR releases Ca^{2+} that the fiber contraction starts. Once the Ca^{2+} is released in the **cytosol**, which is the liquid interface in which the fibers are bathed, these ions will bind to the **troponin**. The troponin then removes the **tropomyosin** present at the actin binding sites. Once these sites are free, the cycle of contraction begins and is repeated until

tropomyosin returns to attach to these sites. The contractile cycle consists of four steps in the following order:

1. **The ATP hydrolysis**. At the top of myosin are ATP attachment sites and ATPase enzymes that will perform the hydrolysis reaction that transforms the ATP into Adenosine DiphosPhate (ADP). This reaction will then produce energy for the myosin heads;

2. **Creation of actin-myosine bridges**. Due to the energy produced by the hydrolysis of ATP, myosin heads will be able to attach to actin at the myosin attachment site. When a myosin is attached to an actin during contraction, an actin-myosin bridge is created;

3. **Force generation**. Once the actin-myosin bridges are formed, the myosin heads will pull the actin filaments to the M-line of the muscle fibril, creating a superposition of thin and thick filaments. This phenomenon will produce force and the ADP at the head of the myosin is released.

4. **Detachment of myosin from actin**. After the force generation the myosin heads remain attached to actin as long as a new ATP molecule does not attach to the myosin site.

All these steps are repeated as long as the ATPase can hydrolyze the ATP molecules and the Ca^{2+} concentration is sufficiently high in the cytosol. In order to constantly generate force, some myosin heads are attached to actin to form bridges and generate strength while others are detached and ready to attach to continue to generate force. The set of stages of muscle contraction is summarized in Fig. 1.11.

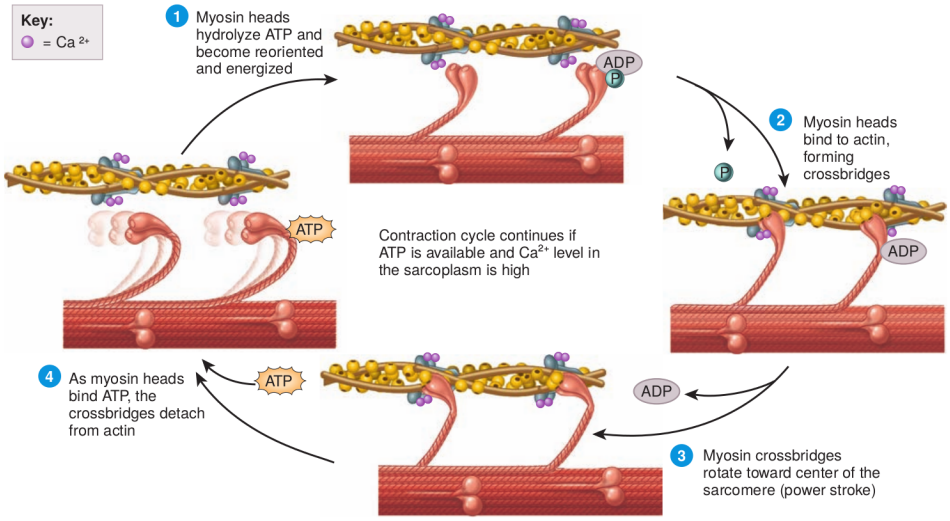

Figure 1.11: The different stages of muscle fiber contraction cycle [15].

As introduced in the previous section, the generation of muscle force is done by the creation of actin-myosin bridges with the myosin heads that will pull on the actin filaments thus generating force and shortening the muscle.

This generation of force in response to a nerve firing is called a **muscle twitch**. The general shape of a fiber muscle twitch is detailed in Fig. 1.12.

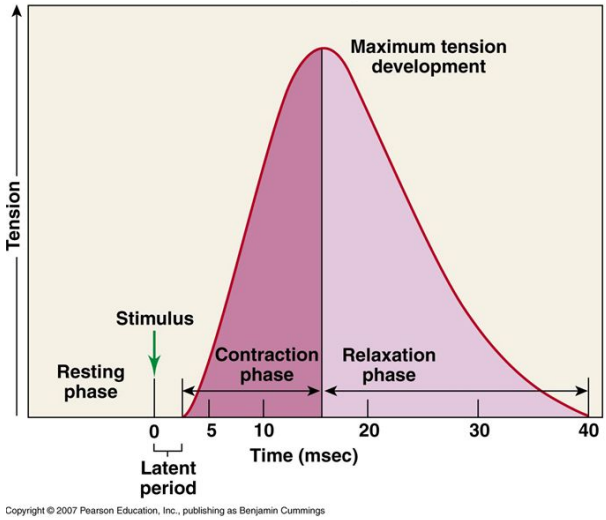

Figure 1.12: General shape of a fiber twitch.

As we can see in Fig. 1.12, there is a delay of response between the beginning of the arrival of the nerve firing and the generation of the force. This delay is called the electromechanical delay and corresponds to the response time of the chemical phenomena (membrane depolarization with Na^+, and Ca^{2+} release by the SR in the cytosol) to the propagation of AP along the sarcomere. Note that the three variables corresponding to the contraction time, the relaxation time as well as the maximum force developed during a twitch is dependent on the type of fiber (see section 1.3.2). The contraction and relaxation times are important because they will tune the summation of the twitches. This is also dependent on wether a nerve firing arrives before or after the mechanical activity of the fiber returns to rest. This twitch summation phenomenon is called partial tetanus (voir Fig. 1.13).

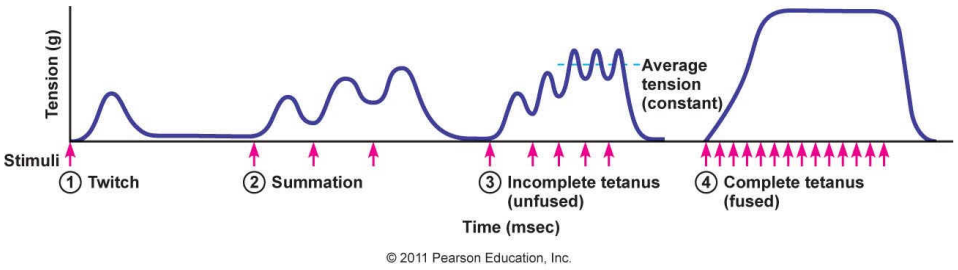

Figure 1.13: Different response of the twitch according to the stimulation time.

Finally, as we can see on Fig. 1.13, when new neural firings reach the NMJ before the twitch relaxation phase occurs, a force plateau is formed. This phenomenon that creates the plateau is called a fused or complete tetanus. Arising of a new neural firing at the MU and thus at its fibers is controlled by the CNS. Creation of the force plateau for a specific intent is a complex task ordered by the CNS.

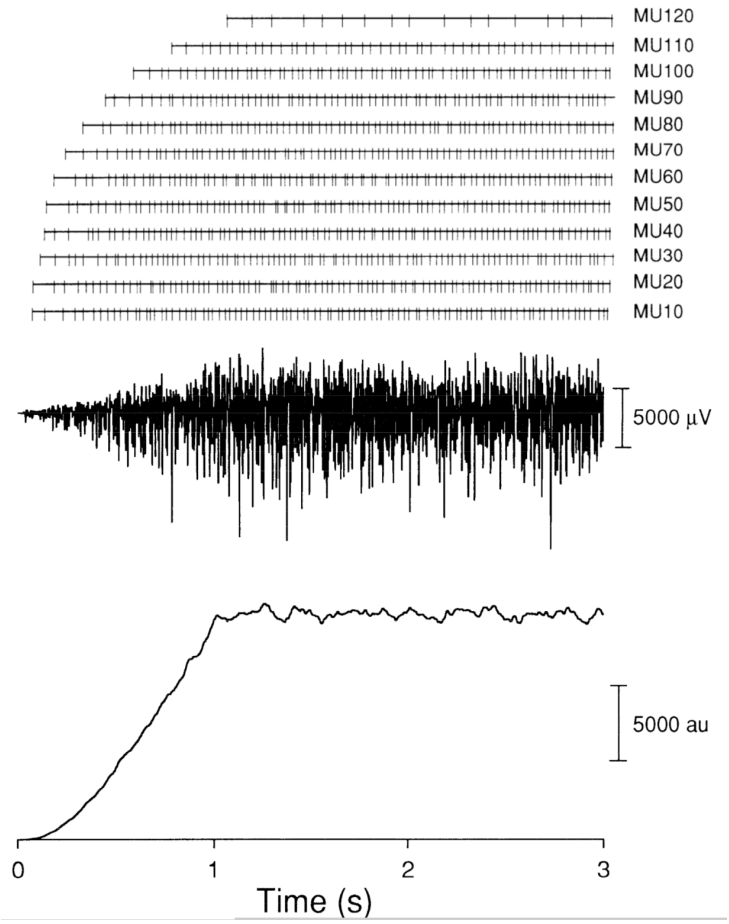

Figure 1.14: Example of MU recruitment pattern exhibiting the firing discharge of every 10^{th} MU (Top). The corresponding simulated sEMG signal detected by bipolar surface electrode according to the recruitment pattern (Middle). The corresponding simulated force according to the same recruitment pattern (Bottom) [20].

1.4 Surface electromyography

The first referenced experimentation studying EMG was in 1666 with the work of Francesco Redi. He discovered that highly specialized muscle of the electric ray fish generates electricity. However, the first actual recording of this electric activity was made by Etienne-Jules Marey in 1890, who also introduced the term EMG. Then, Gasser and Erlanger used an oscilloscope to display the EMG signal from muscles. Afterwards, during this time, similar studies appeared by different researchers among which the concentric electrode technique was introduced [32]. Then, through the 50's and 70's major contributions were achieved [33, 34, 35] including the quantitative analysis of the MUAP, EMG decomposition techniques and EMG amplitude analysis. Clinical use of sEMG for the treatment of more specific disorders began in the 60's [36, 37, 38]. It was introduced as a non invasive technique that can detect the MUs activity in a large volume as opposed to the needle EMG technique that detects the MUs activity in a small volume near the needle tip. Hardyck and his researchers are known as the first practitioners to use sEMG technique [39]. Then, the use of sEMG technique was spread across the scientific community in the following years. In spite of that the sEMG signals are stochastic and non stationary sig-

nal, it appears that this technique can assess the functional behaviors of skeletal muscles [40, 41, 42].

1.4.1 Electrode configurations and spatial filtering

The electrodes usually used in sEMG technique are simple silver chloride discs of different sizes. Compare to the needle electrode, their main advantages are being noninvasive and suitable for use without causing discomfort to the subjects. Yet, the electrical conduction between the skin and the electrodes has to be verified before recording the signals. This can be prepared by removing first the dead cells layer and the oils of the skin in order to reduce the skin-electrode interface impedance to ~ 3 kΩ [43]. Using sufficient quantity of conductive gel between the electrode and the skin should be then enough to have a suitable conduction.

Classically, three electrodes arrangements can be used for sEMG signal recording with each one different interests and properties. First, there is the monopolar arrangement when the signal is recorded using differential amplifier by measuring the difference between two signals; a signal recovered by a surface electrode placed on the skin surface above a certain muscle (active electrode) and the signal recorded by an electrode placed in a neutral position (a reference electrode as you can see on Fig.1.15). This arrangement has the largest detection volume compared to the others [43]. Then, when two electrodes placed on the skin surface over the muscle are connected to the differential amplifier, the sEMG signal is called bipolar. The bipolar arrangement has a filtering effect on the obtained sEMG signals [44], it eliminates the common noise between the two electrodes and hence provide cleaner sEMG signal. This filtering effect causes a reduction of the detection volume by altering the spatial selectivity of the electrode system [45]. Another setup, the Laplacian configuration has the advantage to better filter the signal and the Non Propagating Component (NPC) of the MUAPs than the bipolar arrangement. This NPC arises from the extinction of the FAP at the myotendinous junction. It is important to remark that the detection volume of the electrode arrangement is dependent to the electrode setup. In fact, increasing the filtering order reduces the detection volume as well as the signal amplitude. Finally, in order to record an sEMG signal with the best quality and representativity, there are a number of factors to consider such as the electrode arragement, the electrode placement on the skin surface or the electrodes alignment in respect to the fibers orientation [46, 47].

It can be noticed, the conventional sEMG recording techniques suffer from many limitations. One of these is the deficient spatial resolution related to the use of only few electrodes [2]. In fact, the electrical activity of the muscle upon the skin surface is heterogeneous and thus, recording a signal from few electrodes will be representative about this particular area on the muscle [48]. Moreover, it can only give information about the activity of a group of MUs but not a single MU. Obtaining information about the activity of a single MU is substantially beneficial in many domains such as therapy monitoring and neuromuscular disorder diagnosis and evaluation [2]. Other limitation linked to the spatial resolution would be the electrode placement problem [48]. This variable has direct influence on the precision of the latter applications like muscle force estimation [49]. Thus, the placement of the electrodes with respect to the active MUs should be as constant and robust as possible between subjects and recordings [48, 47]. The recommendations for sensor placement for sEMG recordings are reported in [50]. Finally, there is also what is known as the auto-cancellation phenomenon [51, 52]. This major problem describes the

superposition of different MUAPs, due to their phasic nature, it can significantly alter the information provided from the signal by underestimating its amplitude and energy [51].

1.4.2 High Density sEMG (HD-sEMG) technique

After introducing the sEMG technique and its different setups, we will present a novel sEMG recording technique, the HD-sEMG technique which has many advantages comparing to the classical sEMG recording method previously described.

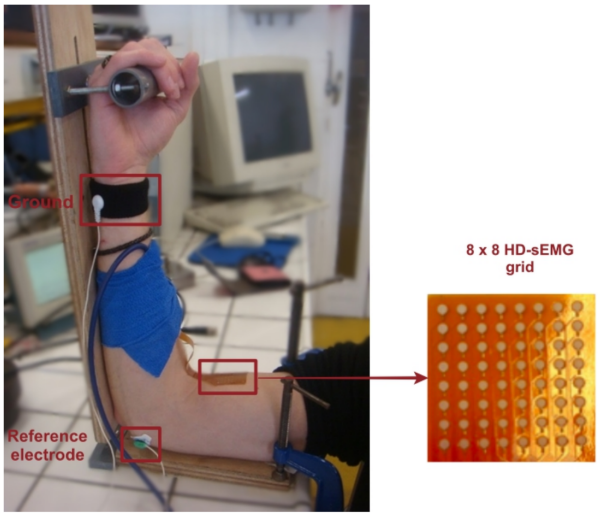

Figure 1.15: Example of an 8×8 HD surface electrode grid placed on the Biceps Brachii muscle (Refa 136, TMSI, Netherlands) [53].

The HD-sEMG technique is based on the multiplication of the recording electrodes to form a multi-channel electrode recording system. It is composed of a two dimensional array of electrodes called a HD-sEMG grid that forms a spatio-temporal variant of the usual single channel sEMG techniques [54, 55]. This novel technique surpasses the classical singular and bipolar recordings by taking into account aspects of spatial distribution of electrical potentials [56] and by overcoming their basic limitations describe above. Most of the limitations of the classical sEMG recordings can be overcome by using the HD-sEMG technique. For these reasons, the HD-sEMG recording technique has growing interest in the last few years due to multiple reasons. Yet, the HD-sEMG technique is a complex technique that needs a strong expertise in multichannel signal processing. This technique allows the multiplication of the collected data and thus provides wider information about the electrical activity of the muscle than one channel. Multiplication of the data also needs pre-processing processes since all the data aren't significant and may bias the analysis [57, 58]. The HD-sEMG can provide rich information about the muscle anatomy such as the MUs number [59], the muscle properties [60, 61] and the neural command by HD-sEMG decomposition [62, 54]. In addition, the HD-sEMG found its way into clinical applications such as fatigue studies, neurogenic changes, myopathies and positive muscle phenomena [63]. Thus, this recent technique has strong abilities to become a valuable clinical diagnostic tool in the near future.

1.5 Modeling of the neuromuscular system

In this section, we will present the state of the art concerning the modeling of the neuromuscular system. We divided this section into three parts corresponding to the studied phenomenon. Some models only describe the electrical behavior of the muscle contraction, others only the mechanical outcomes and few simulate both. Commonly, modeling of the neural drive is included in a more or less realism. Considering the important number of existing models, we decided to only present what we considered to be the pillars on which muscle modeling paradigm is constructed.

1.5.1 MU recruitment scheme models

As far as we know, recruitment of the MU during contraction has always been considered as a sum of Dirac impulses $\delta(t)$ describing a random point process. Where each Dirac impulse represents a firing discharge of the motoneuron, which will induce a contraction of the MU fibers. Several studies have attempted to describe this random point process with mathematical equations [64, 65, 20, 21, 66]. One of the first reported study [64] described the activation of the MUs at the muscle scale. Authors described the sum of all the firing moments of all MUs as a non-stationary Poisson distribution respecting some assessed relationships. Yet, with this model representation, some properties of the recruitment at the MU scale such as the inter-pulse (or inter-spike) interval, the frequency discharge or the orderly sequence recruitment of the MU are lost.

Then, in [65], authors also considered the firing train as a sum of Dirac impulse in time but at the MU scale. This random process is described considering some properties of the recruitment such as the inter-pulse interval described with a Weibull probability distribution. Thus, the probability of having a firing in the interval dt is:

$$P_{\delta_i}\left(\delta_i = 1\right) = \lambda_i(t, f)dt \tag{1.1}$$

where $\lambda_i(t, f)$ is the firing rate. f corresponds to the force level since the firing rate is correlated to the force level of the isometric contraction. This firing rate is computed by considering the inverse of the mean value of the Weibull probability distribution function. This modeling significantly improves the understanding of the MUs scheme recruitment at that time. However, some issues like the MU recruitment threshold remained unresolved.

The major increment in the modeling of the MU recruitment scheme was developed in the study of Fuglevand and al. [20]. In this model, authors represented the MUs in a motor neuron pool. MUs were recruited according to the size principle previsouly introduced [18]. Moreover, following former studies [65] the motoneuron firing rate had a linear dependence with the force level of the contraction. Thus, each motoneuron had a peak firing rate due this correlation, and also the inter-spike interval (ISI) properties were considered.

Considering the conditions of the MU recruitment, the authors proposed to describe a Recruitment Threshold Excitation (RTE) for each MU according to the force level developed. According to previous studies [67], many MUs are recruited at low force level and a few at high force level. Thus, the RTE was described as:

$$RTE_i = e^{i\frac{ln(RR)}{N}} \tag{1.2}$$

where RTE_i represents the RTE of the i^{th} MU, RR is the recruitment range corresponding to the force level where all the MUs are recruited and N is the number of motoneuron. It must be emphasized that all the parameters describing RTE are muscle specific parameters [68]. According to this modeling, a MU remains inactive as long as the force level is below its RTE value. It is supposed that the first discharge occurs when the MU starts to be recruited.

Then, concerning the progression of the motoneuron firing rate during voluntary muscle contraction. The authors supposed that the minimum firing rate (Fr_{min}) is similar for all the MUs within the muscle [69]. From this assumption, the author described a linear relationship between the firing rate and the force level (see Fig. 1.16).

$$Fr_i(t) = g_i(E(t) - RTE_i) + Fr_{min}, \ \texttt{if} \ \ E(t) \geq RTE_i \tag{1.3}$$

$$g_i = \frac{PFR_i - Fr_{min}}{100 - RTE_i} \tag{1.4}$$

$$PFR_i = Fr_{max_1} - PFRD\frac{RTE_i}{RTE_N} \tag{1.5}$$

With $PFRD$ is the peak firing rate difference corresponding to the difference of firing rate between the first and the last MU. The authors also proposed to consider the peak firing rate (PFR) since it was assessed that the motoneuron firing rate increases according to the force level to a certain frequency [69]. This PFR generally ranges from 20 to 45 impulsions/s in human muscles during voluntary isometric contractions. However, it is still unknown how the PFR is related to the recruitment threshold of the corresponding motoneuron. In this model [20] (see eq(1.5)), authors assumed that the PFR of the last recruited motoneuron is lower than the PFR of the first recruited motoneuron. One explanation can be, last recruited motoneuron are fatigued more quickly than the first recruited motoneuron and thereby won't be able to sustain the contraction. This neurological phenomenon is often referred as the "onion skin" phenomenon introduced by De Luca and al in [70]. Equation (1.3) was also considered as non linear increasing (see Fig. 1.16) as De Luca and al. assessed [71], giving:

$$Fr_i(t) = PFR_i\left(1 - e^{-\left(\frac{E(t)-RTE_i}{\tau_i}\right)}\right) + Fr_{min} \tag{1.6}$$

where, $\tau_i = \dfrac{-(100 - RTE_i)}{ln\left(\frac{Fr_{min}}{Fr_{max_i}}\right)}$.

Finally, analysis of MU discharges indicated that the ISI is like a random process described through a Gaussian probability density function [72]. The ISI corresponds to time interval between two successive firings of the motoneuron. The mean and standard deviation of the ISI distribution are related such that the coefficient of variation ($CoV = \frac{\sigma}{\mu}$) is assumed constant with mean ISI changes [73]. Usually, the CoV range in $[0.1, 0.3]$ according to the studied muscle and the subject [20, 74]. Yet, in [75, 76], the authors assessed that this CoV is modified according to the force level generated such as:

$$CoV_i = 200e^{-\frac{\Delta F_i}{2.5}} \tag{1.7}$$

where ΔF_i is the force difference between the actual generated force and RTE_i.

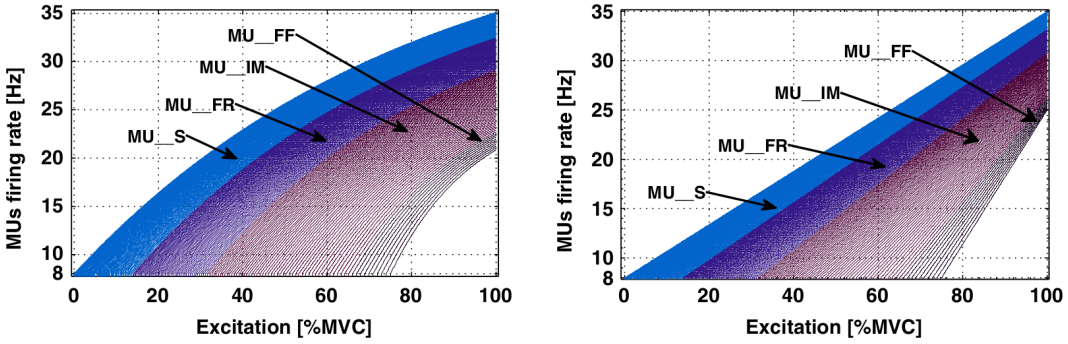

Figure 1.16: Different rate coding strategies. MU firing rate increases linearly (L) and non-linearly (R) according to the force level increase [23].

However, the authors described the probability to a firing in the interval dt such as [20]:

$$P_{\delta_i}\left(\delta_i = 1\right) = \mathcal{N}\left(Fr_i dt, \frac{1}{cv}\right) \tag{1.8}$$

where, $\mathcal{N}\left(\mu, \sigma\right)$ is a Gaussian distribution, F_i is the computed firing rate and dt the time interval.

Thanks to this important improvement in the motoneuron recruitment modeling, motoneuron discharges activating the MU during voluntary isometric contraction can be described in a more realistic manner according to the neurophysiology (see Fig. 1.17).

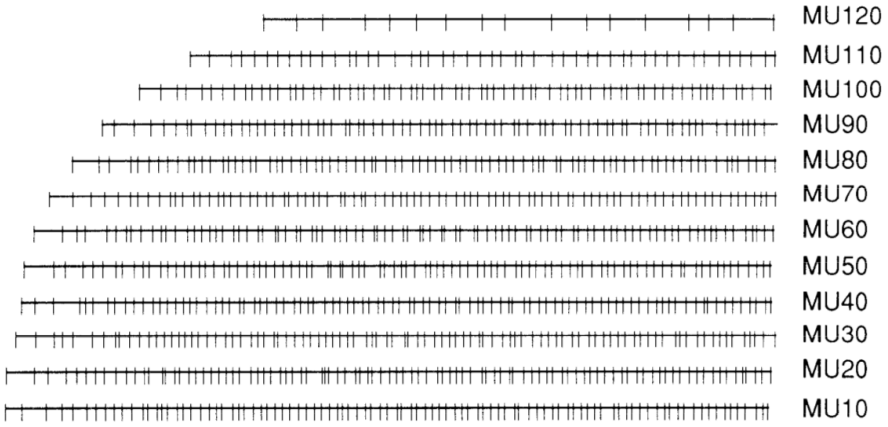

Figure 1.17: Example of the discharge instants (vertical strokes) of every 10^{th} MU in a pool of 120 MUs [20].

Then, few studies were performed to improve the above model based on experimental recordings [41, 71, 76, 75]. This model becomes more accurate when the muscle specific properties of the recruitment scheme of the motoneuron [41] is considered.

1.5.2 Electrical models

Models describing the electrophysiology of the muscle through sEMG signal representation really started with the work of Rosenfalck [31] where he defined the first equation

describing a skeletal muscle single fiber action potential (SFAP). He defined an analytical expression [31] for the longitudinal intracellular action potential as:

$$V_i(z) = Az^3e^{-\lambda z} - B \quad \texttt{for} \quad z \geq 0 \tag{1.9}$$

With, $A = 96$ mV.mm^{-3}, $B = -90$ mV and $\lambda = 1$ mm^{-1}. This equation can be transformed to the temporal domain using the relation $z = vt$, where v defines the conduction velocity of the muscle fiber. Then the transmembrane current source density I can be defined as proportional to the second derivative of equation (1.9) [31].

Then, SFAP was determined as an integration along this cylindrical source line [31]:

$$\phi(\rho, z) = \int_{-L}^{L} 2\pi a I(s) W(\rho, z, s) ds \tag{1.10}$$

Where, ρ and z represent the radial and axial coordinates, respectively. s the location of the source along the muscle fiber of length $2L$, a is the diameter of the fiber, I the defined transmembrane current source density and W the volume conductor transfer function. Finally, W was defined for infinite, homogeneous, anisotropic tissue as:

$$W(\rho, z, s) = \frac{1}{4\pi\sqrt{r^2\sigma_\rho\sigma_z + (z-s)^2\sigma_\rho^2}} \tag{1.11}$$

This computation formalism initiated the next two decaded of SFAP and MUAP modeling where accuracy and complexity of the modeling increased [65, 77, 78, 79, 80, 13]. In [77], the authors defined a monopolar electrode recording that is not a point-shaped electrode through a spatial integration with respect to the electrode area A.

$$S_e = \frac{1}{A} \int \int_A \phi(\rho, z) dA \tag{1.12}$$

Then in the early 90's, Gootzen and al. significantly incremented the electromyographic modeling by defining the conductor volume as finite [81, 14]. In fact, one major problem in former model was the infinite assumption of the conductor volume. This assumption was suitable with respect to nerve fibers because of their considerable length. Nevertheless, the extracellular action potential showed complex changes when approaching to the fiber end [82, 83]. For this purpose, authors proposed a method describing the generation and the extinction effect [81] of the SFAP at the end-plate and close to the fiber end, respectively. They represented the current density source as a spatio-temporal function, where the current density source is proportional to the second derivative of the intracellular AP along the fiber. The extinction of the AP is described as a current source compensation at the end of the fiber computed such that the total transmembrane current over the fiber is zero (see Fig. 1.18).

They also proposed a new transfer function of the conductor volume considering boundary conditions to account the finite dimension of the muscle expressed in the spatial frequency. The application of the boundary conditions often involves very ill-conditioning matrix equations that have to be solved to avoid numerical computer overflow or underflow occuring during the computation [14]. Finally, they proposed a geometrical model of the muscle as a cylinder with the inner compartment representing the muscle and a layer surrounding the muscle tissue representing the adipose tissue (see Fig. 1.19). It was the

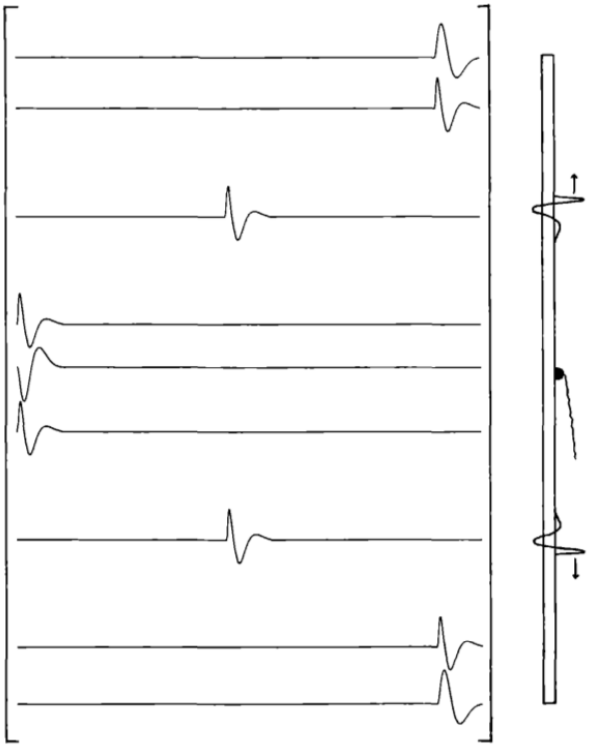

Figure 1.18: Muscle fiber current source density distribution represented by a spatio-temporal function [81].

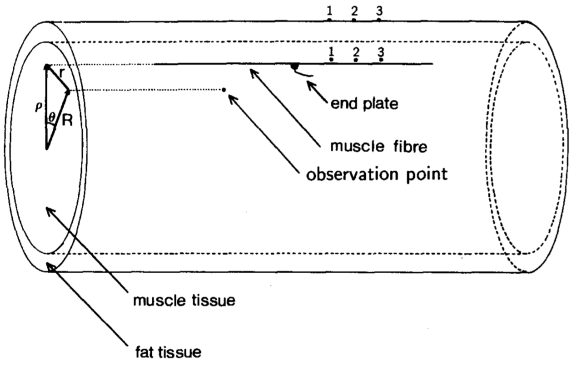

Figure 1.19: Volume conductor configuration with adipose layer tissue and finite length of the muscle [81].

first time that surrounding layer such as adipose or skin tissues were considered in the electromyographic modeling.

Finally, what we consider as the final major increments in the sEMG signal generation modeling are the several works of Merletti, Farina et al [84, 85, 7]. First major increment was to propose a continuous analytical spatio-temporal function that describes the generation, the propagation and the extinction of the action potential (see eq 1.13) at the

end-plate, along the fibre and at the fiber end [85], respectively.

$$i(z,t) = \frac{d}{dz}\left(\psi\left(z - z_i - vt\right) p_{L_1}\left(z - z_i - \frac{L_1}{2}\right) - \psi\left(-z + z_i - vt\right) p_{L_1}\left(z - z_i + \frac{L_1}{2}\right)\right) \tag{1.13}$$

where, $\psi(z)$ is the first derivative of eq (1.9), L_1 and L_2 are the semi-lengths of the fiber from the center of the muscle to the right and left tendon, respectively. z_i is the longitudinal coordinate of the fiber end-plate and $p_L(z)$ is a window function.

This description of the current density source (see eq (1.13)) as a continuous spatio-temporal function provides an important contribution of the sEMG signal generation modeling. This equation considers specific parameters at the fiber scale, such as the end-plate absolute position, propagation velocity and semi-lenghts of the fiber. The only other source modeling close to this description is the source proposed in [86]. Authors define the source as a time-shift invariant function according to an observation point. However, except of the extracellular description along the fiber, authors in [85] also distinctly defined all the computation step from the extracellular action potential to the recorded signals at the electrode. Nevertheless, this description was detailed for a 3 layers planar volume conductor as in Fig. 1.20.

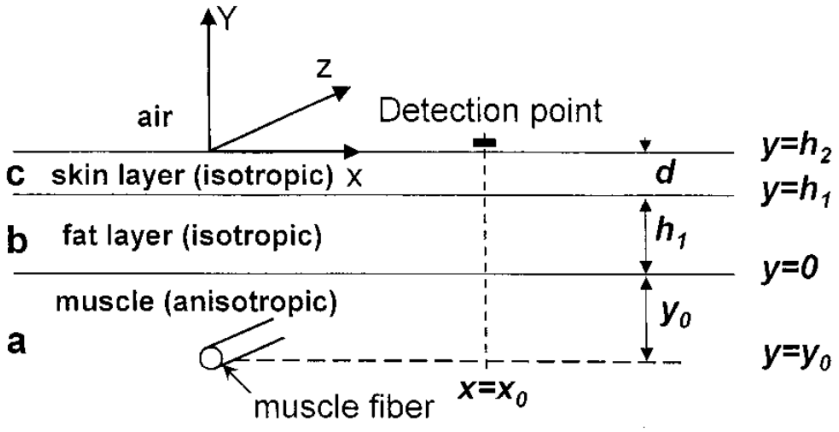

Figure 1.20: Planar volume conductor configuration with skin, adipose tissues and muscle [85]. d is the skin thickness. h_1 corresponds to the adipose tissue thickness and y_0 is the depth of the fiber within the muscle.

After this important work in sEMG signal generation modeling, same authors published another study where they detailed the computation for a multilayered cylindrical volume conductor [7]. The authors took inspiration from existing cylindrical model developed in [81] where the conductor volume was defined as a time invariant matrix in spatial frequency. The source is placed in the most internal layer which is the muscle.

More recently, we noticed some improvements in the proposed models such as definition of a triangular shape of the muscle [87] where the fibers are placed along the radial direction whereas it is placed according to the longitudinal direction in the based model [7]. Moreover, a model describing a bi-pinnate muscle [88] was proposed. In this model, the bi-pinnate muscle was assumed infinite and the fibers within are placed longitudinally along the muscle with a pinnate angle of $\theta^{\pm}$ (see Fig. 1.21).

Other models proposed to consider superficial bone or blood vessel within the muscle [89] or local and distributed inhomogeneity such as glands or vessels within any layer

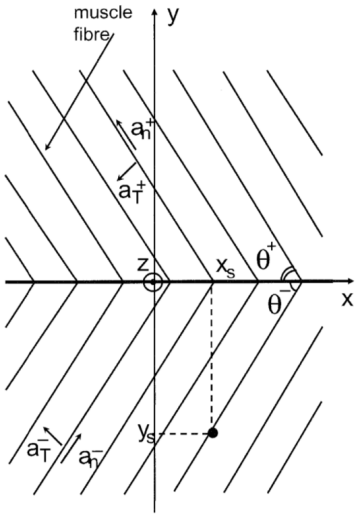

Figure 1.21: Radial view of the bi-pinnate muscle. The muscle fibers have two orientations defined by angles $\theta^{\pm}$ [88].

[90, 91].

Beside these analytical models of the sEMG signal generation, some researchers tried to formalize these equations using numerical models with the Finite Element Method (FEM). Defining numerical models allow an accurate representation of the geometry of the muscle. Thus, some complex geometry can be defined and induced more realistic sEMG signals [6]. In [11], they described the limb as in [81]. The extracellular potential is described as in [31]. The total number of elements used to describe the limb varied from 300000 to 600000 depending on the complexity of the geometry. One example of cylindrical multilayered limb can be seen on Fig. 1.22. Yet, this model can only compute one SFAP in 12 min. Modeling a muscle induces the simulation of hundreds of thousand fiber, this will increase the number of elements and thus, the computation time. Such description of the muscle will induce weeks of computation on a single computer and thus, can't have a direct application for clinicians for the moment.

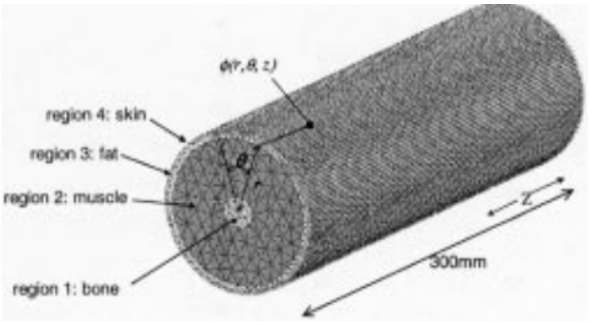

Figure 1.22: Finite element model of the limb with muscle, adipose and skin tissues [11].

Finally, Mesin and al. developed another FEM model of the muscle considering its shortening during isometric contractions [92]. Authors considered the conductivity of the muscle at each point dependent of the local fiber orientation which changed with

muscle shortening. They computed the fiber extracellular action potential as in [85] with a propagation path γ according to the inclination of the fiber. Only the myoelectric activity was modeled and the estimated muscle shortening isn't based on a mechanical model. In this model, authors never presented the computation time for the simulations (120 MUs and thousands of fibers).

1.5.3 Mechanical models

Modeling the mechanical activity of the neuro-muscular system and more specifically the force estimation generated by the muscle during a contraction has been widely studied since the early 20^{th} century. One of the first model describing the muscle as a visco-elastic material was developed by Hill [8]. The general Hill model type is composed of three elements (see Fig. 1.23):

- a contractile element which describes the muscle contraction and the force generation;
- a serial spring element which models the mechanical behavior of the tendon and describes the elasticity of the muscle;
- a parallel spring element which defines the mechanical behavior of the connective tissues surrounding the muscle fibers. This element produces passive force.

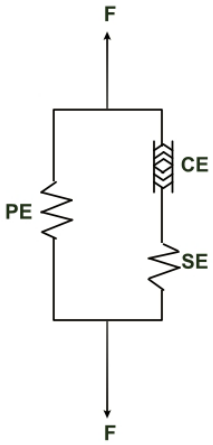

Figure 1.23: Rheological Hill model of the skeletal muscle [8].

According to this model, the total force F produced by the muscle is:

$$F = F^{PE} + F^{CE}, \quad F^{CE} = F^{SE} \tag{1.14}$$

where F^{PE}, F^{CE} and F^{SE} are the forces produced respectively by the parallel element, the contractile element and the serial element.

Similarly, the muscle length L is computed as:

$$L = L^{PE} = L^{CE} + L^{SE} \tag{1.15}$$

with, L^{PE}, L^{CE} and L^{SE} are the lengths of the parallel element, the contractile element and the serial element, respectively.

Basically, the muscle force produced by the contractile element is obtained from:

$$(v + b)(F + a) = b(F_0 + a) \tag{1.16}$$

where, F is the force produced from the muscle, v is the velocity of contraction, F_0 is the maximum isometric force generated in the muscle, a is a coefficient of shortening related to the heat and $b = \dfrac{av_0}{F_0}$ with v_0 the maximum velocity at $F = 0$.

Equation (1.16) can be rearranged to better exhibits the force-velocity relationship (see Fig.1.24).

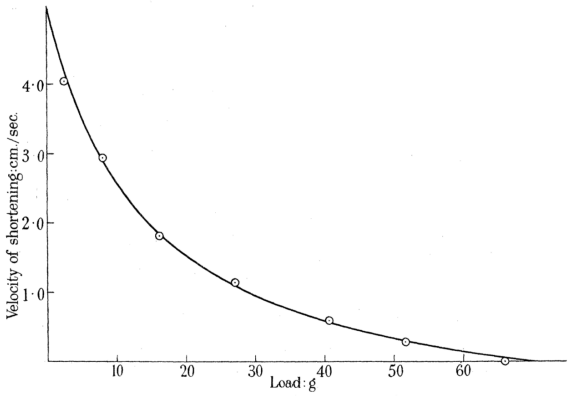

Figure 1.24: Force-velocity relationship of a tetanized muscle [8].

This equation is still widely used nowadays, with new specifications of the muscle behavior such as the force-length relationship [93], the stress-strain relationship [94], the active state description [95] or the fiber angle insertion with the tendon [27]. Nevertheless, all those features describing the muscle behavior during contraction are based on macroscopic studies considering the underlying phenomena without modeling them.

A modeling at the microscopic scale was proposed by Huxley with its well-known study [12] about the actin-myosin bridges attachment and detachment.

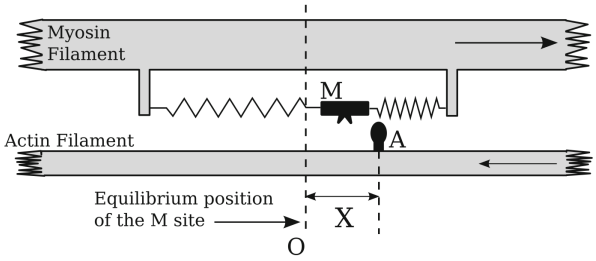

Figure 1.25: Sliding filaments (image taken from [9]) according to [12]. A represents the actin site, M the myosin site and X the distance between the actin site and the equilibrium site O.

The authors described the force generation by specifying the cross-bridge interactions at the sarcomere scale. According to Fig.1.25, during contraction, the actin filament moves to the left relative to the myosin filament and thus, the distance x decreases. The

authors proposed two rate constants f and g for the binding/breaking of actin and myosin following some hypothesis:

1. initially, A and M sites are detached;
2. if A site is within the range of position, there is a chance to create the binding;
3. when $A - M$ bridges are bound, there is a chance that this link breaks;

These hypothesis are described by the equation (see Fig. 1.26):

$$\begin{cases} f = 0 \texttt{ and } g = g_2 & \texttt{if } x < 0 \\ f = \frac{xf_1}{h} \texttt{ and } g = \frac{xg_1}{h} & \texttt{if } 0 < x < h \\ f = 0 \texttt{ and } g = \frac{xg_1}{h} & \texttt{if } x > h \end{cases} \tag{1.17}$$

Where, f_1, g_1 and g_2 are constant values that need to be identified for the system.

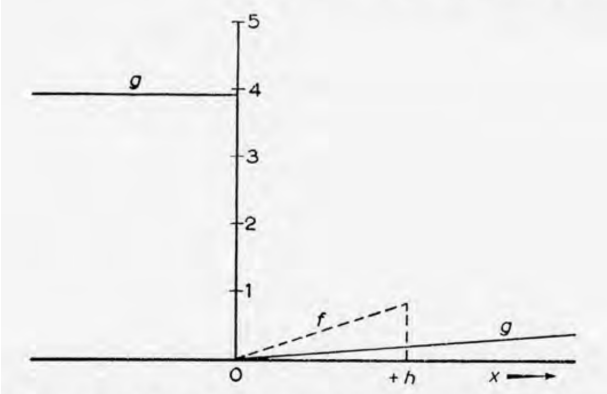

Figure 1.26: Dependence of the rate functions f and g according to x [12]. Formation of linking A and M sites is described by f (reaction 2). Breaking the bridge is described by g (reaction 3).

Assuming that all these A-M sites are placed in series in the sarcomere and considering the f and g functions proposed, the total force produced by a fiber is the sum of the force produced by the sites within one half-sarcomere, giving:

$$F_f = \frac{msk}{2l} \int_{-\infty}^{+\infty} nxdx \tag{1.18}$$

where, l is the separation of the A sites along the actin filament, k the muscle stiffness, n the number of formed actin-myosin cross-bridge and $\frac{ms}{2}$ is the number of bridge for a muscle of 1 cm^2 cross sectional area.

This modeling of the force production has more physiological reliability than the equation proposed by Hill [8]. Nevertheless, these equations are described at the fiber scale and are time consuming to solve. For a muscle composed of hundreds of thousand fibers, using these equations isn't feasible for muscle force simulation in a reasonable computing time.

Then, Zahalak developed the distribution-moment method for sarcomeres [96]. This method approximates the Huxley actin-myosin bridges model at the sarcomere scale for

the whole muscle. The author defined the ith moment of the bond-distribution function $n(x,t)$ as the function $M_i(t)$ and the ith moment of the bonding rate function $f(x)$ as the function $b_i(t)$:

$$\begin{array}{rcl} M_i(t) & = & \int_{-\infty}^{+\infty} x^i n(x,t)dx \\ b_i(t) & = & \int_{-\infty}^{+\infty} x^i f(x)dx \end{array} \tag{1.19}$$

Assuming that $n(x,t)$ is approximated by a Gaussian distribution. This assumption leads to:

$$\begin{array}{rcl} \dfrac{dM_0}{dt} & = & b_0 - F_0(M_0, M_1, M_2) \\ \dfrac{dM_1}{dt} & = & b_1 - F_1(M_0, M_1, M_2) - v(t)M_0 \\ \dfrac{dM_2}{dt} & = & b_2 - F_2(M_0, M_1, M_2) - 2v(t)M_1 \end{array} \tag{1.20}$$

The exact shape of functions F_0, F_1 and F_2 depend on the assumed shape of the rate functions f and g as well as the shape of $n(x,t)$. The produced force is related to the first-order moment of the bond distribution function and the stiffness to the zero-order moment of the bond distribution function.

This method presents the advantage to provide a direct mathematical connection from the microscopic parameters of contraction to the macroscopic parameters of the whole muscle. However, using the distribution moment theory restricts the model to the assumption that every muscle fiber have the same contractile properties and thus, generate the same mechanical contribution. Moreover, one remaining challenge in the mechanical modeling of the muscle is the definition of the muscle activation in order to understand what happens when two consecutive activation of the muscle arrive. This definition as well as the rate functions that are still uncorrelated to physiology and identified for the purpose of the studies.

Finally, the last major increment in the modeling of the muscle contraction based on physiological behaviour is the model proposed in [9].

In this model, the authors proposed a multi-scale model based on macroscopic Hill's and microscopic Huxley's theories using the distribution moment theory to upscale the sarcomere to the whole muscle without using the assumption of a Gaussian distribution. Also, the authors proposed another definition of the f and g rate functions. With this model, they could compute the force generated by the muscle as well as the active stiffness produced by the muscle.

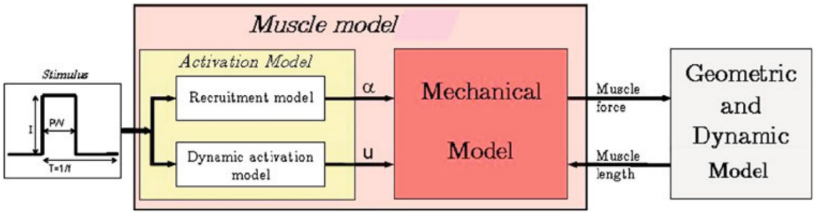

Figure 1.27: Muscle model proposed in [9] exhibiting three blocks.

This model is activated by an electrical stimulation (ES) defining the activation parameter $\alpha(t)$ corresponding to the percentage of recruited muscle fibers in the muscle according to the pulse width and the intensity of the stimulation.

The authors also described a chemical input $u(t)$ at the sarcomere scale synchronized with the stimulus events that will activate the muscle fibers and thus, the muscle (see Fig. 1.28).

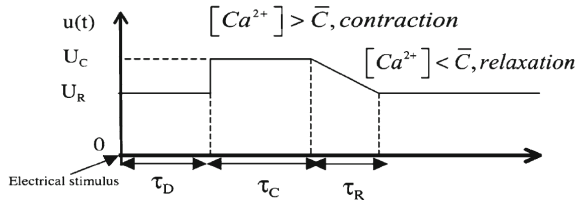

Figure 1.28: Calcium definition after an electrical stimulus [9].

Functions f and g are defined such as:

$$\left\{ \begin{array}{rcl} f(x,t) & = & \left\{ \begin{array}{ll} \Pi_c(t)U_c & \texttt{when } x \in [0;1] \\ 0 & \texttt{elsewhere} \end{array} \right. \\ g(x,t) & = & u(t) + a|\dot{\varepsilon}_c(t)| - f(x,t) \end{array} \right. \tag{1.21}$$

where, a is a dimensionless parameter describing the velocity contribution for creating cross-bridge and ε_c defines the relative length variation of the contractile element as $\varepsilon_c(t) = \dfrac{L_c - L_{c0}}{L_{c0}}$. The dynamic of the generated force F_c and the dynamic of the active stiffness k_c of the muscle can be determined from the fiber scale that are determined from the sarcomere scale.

Then, using the rheological model describing the muscle during isometric contraction proposed in [9] (see Fig.1.29), dynamic equations of the muscle are computed.

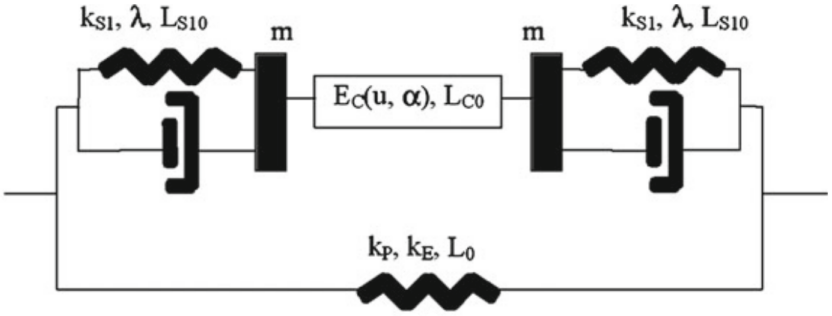

Figure 1.29: Mechanical model including masses and dampers inspired from the Hill–Maxwell model [9].

This model is validated on rabbits measures and also on humans recordings [9]. Nevertheless, this model doesn't describe the heterogeneity in the fiber types since only one type of fiber is described. Also, fatigue or potentiation phenomena cannot be reproduced with this model.

Besides those models focusing on the description of the muscle contraction based on the muscle physiological behavior, other researchers only focused on the force generation of the muscle during contraction and thus, had a closer focus on the heterogeneity of the muscle structure.

In those type of model, we noticed Coggshall and al. [64] being the first to describe analytically the twitch response of a MU. The muscle force is computed as:

$$F_M(t) = \sum_{-\infty}^{+\infty} \int_{-\infty}^{+\infty} f_k(t-u)\delta(u-t_k)du \tag{1.22}$$

where, $f_k(t)$ is the description of the twitch response and $\delta(t_k)$ are the discharge instant of the MU. The authors proposed the modeling of slow and fast twitches according to experimental measurements recorded from cat flexor hallucis longus (fast muscle) and cat soleus (slow muscle):

$$f_s(t) = 2109.7\left(\frac{1}{94.1}e^{-7.3t} - \frac{9.7t+1}{94.1}e^{-17t}\right) \tag{1.23}$$

$$f_f(t) = \frac{69^3}{2}t^2e^{-69t} \tag{1.24}$$

These approximations fairly estimate the twitch shape according to the MU type. Nevertheless, these equations describing the twitch has no connection with physiology except the type of the MU.

Considering the lack of realism in these equations, further studies were attempted to better describe the MU twitch response. Particularly, we noticed the work of Milner-Brown and al. [97] defining the twitch equation usually used nowadays:

$$f(t) = ate^{-\frac{t}{T}} \tag{1.25}$$

with, T the contraction time of the twitch and a a constant related to the peak amplitude P of twitch force such that $a = \dfrac{eP}{T}$.

Final equation of the twitch was proposed in [98] and identified from experimental recording on rats for each type of MU [99]. Here, MU twitch is described as:

$$F^i(t) = p^i t^{m^i} e^{-k^i t} \quad \texttt{if } t >= T_{imp} + T^i_{lead} \tag{1.26}$$

with, T_{imp} the instant of stimulus, T^i_{lead} the electro-mechanical delay, p^i, m^i and k^i are variables dependent of the MU's type. All those variables were identified for the four MU types: Slow, Fast Resistant, Fast Intermediate and Fast Fatigable (see Fig. 1.30).

1.5.4 Multi-physic models

Most of the models presented above only described one physical phenomenon induced during skeletal muscle contraction. Nevertheless, considering the muscle modifications arising during the contraction on its geometry and its properties, modeling only one phenomenon limits the realism of muscle contraction simulation. First attempt of multi-physics modeling of the muscle contraction is the model proposed by Fuglevand [20]. Even though, the electrical and mechanical models didn't "communicate" information, the two models are run with the same recruitment pattern and generate the corresponding electrical activity and force production.

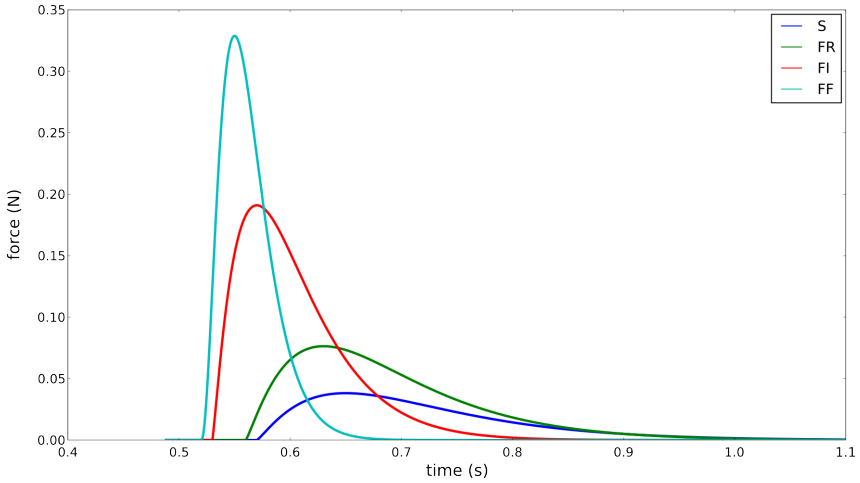

Figure 1.30: Twitch shape according to the MU type [99].

In muscle modeling, few research used this same formalism. It was mainly used for studying the sEMG/force relationship estimation [22, 57]. Considering the complex interactions taking place during the muscle contraction, it seems that numerical models can accurately transcribe these effects. A recent model was proposed by Heidlauf and al. [6] where they modeled the chemo-electro-mechanical behavior of skeletal muscle during contraction (see Fig.1.31).

This model is based on the open-source software library OpenCMISS [100]. This software allows the combination of different mesh regions with different dimension, i.e., 0D models (point or vertex) to describe the cellular behavior, 1D models (line or edge) to describe the AP propagation, and 3D models (volume) to describe the mechanical model. The proposed model in [6] is activated from simple definition of the MU discharge moments with a regular firing rate.

After the activation of a MU, all its fibers will contract and generate a coupled electrical and mechanical contribution. The electrical behavior of the muscle fiber is described at a single point representing a half-sarcormere through 51 Ordinary Differential Equations (ODEs). These ODEs define the changes of intracellular and extracellular ion concentrations as well as the binding states during cross-bridge kinetics. It describes the membrane electrophysiology, calcium release from the sarcoplasmic reticulum, calcium dynamic, cross-bridge dynamic, fatigue, sodium and potassium channels [101, 102, 103]. This bioreliable representation that can be adapted according to the fiber type, can also consider complex cellular behavior such as fatigue. Then, to extend this half-sarcomere 0D model to the propagation of an AP along the muscle fiber with 1D models, the authors used a reaction-diffusion equation giving by [104]:

$$\frac{\partial}{\partial s}\left(\sigma\frac{\partial V_m}{\partial s}\right) = A_m\left(C_m\frac{\partial V_m}{\partial t} + I_{ion}\right) \tag{1.27}$$

where s defines the spatial position along the path of the fiber, σ the conductivity, V_m the membrane voltage, A_m the ratio between the membrane surface area and the volume, C_m the capacitance of the cell membrane per unit area, I_{ion} represents the sum of ionic currents crossing the cell membrane of the sarcolemma and the T-tubule.

Concerning the 3D model describing the muscle deformation, it is commonly measured by the deformation gradient tensor:

$$F := \frac{\partial \chi(X,t)}{\partial X} = \frac{\partial x}{\partial X} \tag{1.28}$$

with, χ the placement function that assigns each point X in the reference configuration at time t_0 a corresponding point x in the deformed configuration at time t, thus $x = \chi(X,t)$. The strain is determined by Green-Lagrangian strain tensor $E := \frac{1}{2}(C - I)$, with $C = F^T F$ is the right Cauchy-Green deformation tensor and I the second-order identity tensor.

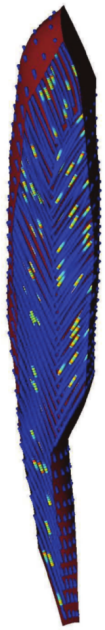

Figure 1.31: Geometry of the tibialis anterior muscle and the fiber distribution, where the fibers indicate the local membrane potential in color [6].

In fact, the authors proposed a highly complex multi-physic and multi-scale modeling of the skeletal muscle during contraction. Even if the model provides accurate and realist simulation of the muscle contraction, the major issue relates to the computing time. In fact, this is one of the major issue concerning models. In this model, simulation of 400 fibers for 200 ms of contraction lasted 49h22min using 1 processor and lasted 11h36min using 4 processors. This small number of fiber can't describe a whole muscle.

1.5.5 Summary

In all these models, we can distinguish different approaches to determine the physical responses to a muscle activation. Some models described the phenomenon based on mathematical equations describing assessed relationships. Using mathematical equations to describe the phenomenon often lead to necessary simplification to reduce the complexity of the equations and to insure the uniqueness as well as stability of the solution. Yet, some variability present in biological system can be considered, leading to the initialization of many variables using statistical equations. Those kind of model are usually described as **analytical models**.

Finally, some models used the Finite Element Method (FEM) to describe the phenomenon. This modeling approach often leads to reliable results considering the accurate description of the medium where the phenomenon arises. Nevertheless, these models are currently too complex to define and need considerable time for simulating the arising phenomena. These models are referred as the **numerical models**. The table below sums up the presented models as well as their approach.

Table 1.2: The presented models and the model approach used.

References	Described phenomenon	Model's class
Coggshall and al. [64]	Recruitment & Mechanical	Analytical
De Luca and al. [65]	Recruitment	Analytical
Fuglevand [20]	Multi-physics	Analytical
Rosenfalck [31]	Electrical	Analytical
Gootzen and al. [81]	Electrical	Analytical
Farina and al. [85, 7]	Electrical	Analytical
Mesin and al. [92]	Electrical	Numerical
Heidlauf and al. [6]	Multi-physics	Numerical
Hill [8]	Mechanical	Analytical
Huxley [12]	Mechanical	Analytical
Zahalak [96]	Mechanical	Analytical
El Makssoud and al. [9]	Recruitment & Mechanical	Analytical

1.6 Objectives of the thesis

As exposed in Table 1.2, there is only few models that describe the electrical and the mechanical outcomes to a muscle activation. And there is fewer, when it comes to consider the effects of the deformation determined from the mechanical model on the considered volume conductor used in the electrical model. Moreover, a second issue comes when the model computation time is investigated. In fact, the only known multi-physic model relating both physical phenomena lasts 11h30min for a simulation of the tibialis anterior muscle including only 400 fibers. This can't definitively be used for clinical applications and diagnosis purposes.

For this purpose, this thesis work is dedicated to develop a fast and bioreliable multi-scale and multi-physic modeling of the skeletal muscle during isometric non fatiguing contractions and introduce HD-sEMG signals simulation in an efficient manner. In addition, the underlying interaction arising in order to produce the force and the electrical activity such as the calcium dynamic will be described. We will propose a novel model based on several steps: (i) developing a generic model that computes the electrical activity of the skeletal muscle at the skin surface, (ii) developing a mechanical model of the muscle driven by the same recruitment pattern, (iii) making these two models communicate in order to consider the deformation in the electrical model.

Based on the literature, concerning the electrical and mechanical models of the skeletal muscle, the existing models lack a lot of important factors like biorealism, validation, reproducibility and optimization of the computing time. In fact, modeling implementation

has to be defined in a generic way in order to easily and quickly perform new simulations. Moreover, clear and human readable input(s) and output(s) have to be used for users. Following this approach enables to use of the model without having to modify the model program. As experimental protocols, the model program has to be: representative, reproducible and repeatable. Representativity corresponds to reliability of the model. Reproducibility corresponds to the possibility to use this model from other users with different computers and simulate the same results. Repeatability corresponds to simulate the same results using the same computer and the same input(s). Thus, in order to model the muscle during isometric contractions we need to understand and distinctly model several interactions that arise during muscle activation. The first modeling step is to define the muscle anatomy and the recruitment of the MUs from the PNS based on the studies of the literature. Second, we will define from this muscle anatomy, the electrical activity of the muscle based on mathematical equations in order to provide the HD-sEMG signals at the skin surface. Compare to the others electrical model that generate only the sEMG signals from single channel, we propose to simulate the complete electrical muscle activity over the skin surface as a 2D map and compute the sEMG signals as an integration of the electrical values under the electrode area. Third, the mechanical model will be modeled based on the same definition of the MUs recruitment previously defined. This modeling will use Huxley's research [12] combines with the moment method developed by Zahalak [96] in order to model the muscle at the MU scale. In the final part, a first presentation about the electro-mechanical muscle model will be exhibited where the deformation is considered under isovolumic assumption for electrical activity according to the mechanical model deformation. To do so, we will consider that only the muscle layer will swell whereas the adipose and skin tissues will be slimming. Thus, the MUs as well as the muscle fibers positions into the muscle layer are updated according to the muscle swelling. Moreover, in this part, we will present some sensitivity analysis of the models which is an important stage for the patient-specific modeling. Another application will be dedicated to the study of HD-sEMG/force modeling.

Thus, the following chapters of this thesis, as described in the general introduction, will address all these problems in order to model the muscle contraction in a biorealistic manner. The figure illustrating the general steps of the thesis work is presented in Fig.1.32.

Finally, the objectives of this work can be summarized by:

- Implementing the muscle anatomy definition and the muscle recruitment in a generic way. Some critical properties such as the homogeneity of the fiber density have to be managed. These properties should automatically be managed regardless of the number of simulated MUs and the MU distribution type;

- Developing and validating qualitatively the electrical model based on muscle physiology. The muscle will be considered as a multilayered cylinder where muscle, adipose and skin tissues are defined. The electrical model will simulate the muscle electrical activity at the skin surface and compute the induced HD-sEMG signals as an integration operator over the potential map allowing an infinity of electrode definition;

- Developing and validating the mechanical model based on muscle physiology. The mechanical model will be described at the MU scale and will be driven by the same recruitment pattern formalism as for the electrical model. The mechanical model has to follow the same format implementation as the electrical model;

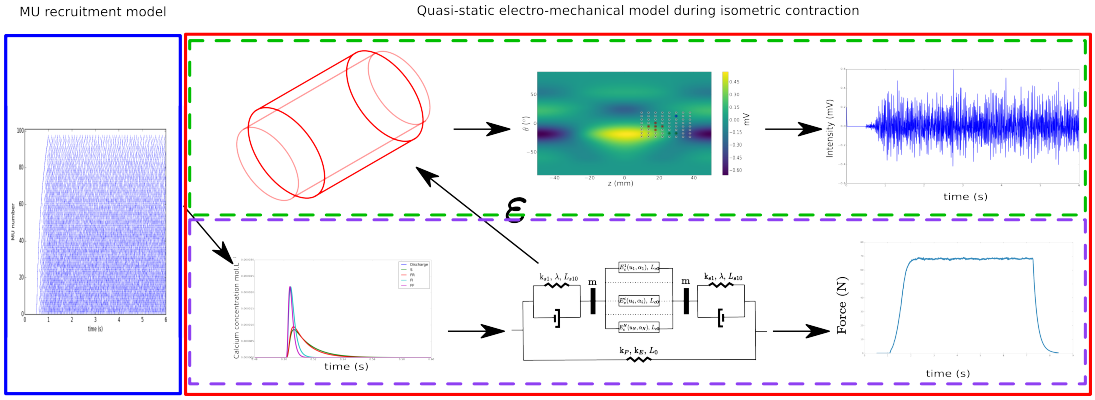

Figure 1.32: Scheme presenting the scheme for generating the electro-mechanical outcomes of the skeletal muscle during contraction (red box). A MU recruitment pattern is defined describing the firing times of each MU composing the muscle (blue box). Then, the mechanical model represented at the MU scale simulated the muscle force as well as its deformation (purple box). This deformation (ε) is considered in the electrical model where the limb is described as a multilayered cylinder. Once the muscle updated according to the deformation, the electrical model will compute the electrical activity of the muscle as the sum of the MUAPs at the skin surface (green box). Finally, the sEMG signals are simulated through a numerical integration of the values on the electrical surface under the electrode definition area.

- Developing a multi-physic deformable model including the two developed models that will perform the necessary communication to consider the deformation of the muscle in the electrical model. For this purpose, we will assume that the muscle volume remains stable, its length will shorten and its radius will raise. Thus, the MUs anatomical properties and position will be updated by an automatic algorithm;
- Providing a first sensitivity analysis of the HD-sEMG grid model helping the researchers to determine the feature sensitivity according to specific parameter or set of parameters;
- Modeling the HD-sEMG/force relationship using the proposed electrical model and a twitch model for a muscle imitating the Biceps Brachii. This study is one of the first to consider a multichannel recording system, i.e. the HD-sEMG technique.

Chapter 2

Modeling the muscle electrical activity

Contents

2.1 Introduction

The modeling of surface electromyogram (sEMG) signals generation has quickly expanded during the last twenty years [20, 85, 7, 81, 11] for purposes of testing decomposition approaches [105], local sensitivity analysis [47], studying the sEMG/force relationship [57], and assessing processing approaches among the numerous available applications. In fact, models can provide electromyographic data generated in specific physiological and neural configurations. Those configurations can be controlled in models whereas it is hardly estimated in experimental conditions. Important advances in sEMG modeling focused on the description of the volume conductor which can be planar [85] or cylindrical [81, 7, 11], the detection system [106, 10, 47] or the phenomena of generation and extinction of the intracellular action potentials at the end-plate and myotendinous junction [81, 85]. Also for more biological realism, some studies attempted to better describe the recruitment pattern of the MUs (spatial and rate coding) [20, 23, 41].

As introduced, analytical modeling approach is used in this work. Analytical models are usually computationally more efficient than their numerical counterparts but the latter models better describe the complex geometry of the muscle in a patient-specific manner. Investigation of the sEMG features changes according to physiological mechanisms is easier and faster with analytical models. Yet, analytical models are limited to a simplified non-realistic volume that can slightly distort the generated signals and their interpretation. Despite these limitations, analytical solutions are still valuable for the following reasons:

- to express the theoretical relationship of the generated signal according to a specific set of parameters (neural, anatomical and physiological);
- to benchmark the accuracy of numerical models in trivial configurations;
- to have an approximated solution in a reduced time compared to numerical model.

Even though, analytical computation is by definition faster than numerical one, computation time can significantly increase depending on its precision (ex: channel number and sampling frequency) and realism (ex: number of MU and fiber). However, this increasing complexity can be managed by optimal programming strategies. Unfortunately, these numerical aspects was never clearly explicited in previous analytical sEMG models with no or few indication of their numerical implementation cost [107, 7].

Recently, an electromyographic High Density (HD) recording technique has emerged, named HD-sEMG, that allows the direct and simultaneous access to a high number of channels (up to 256 channels). This technique significantly increases the spatial representativeness of the recorded data over the studied muscle. It opened the door to multi-channel analysis of muscle and brain activities (as for Electroencephalogram (EEG) recordings) and has already demonstrated promising abilities compared to classical recording routines [2, 58, 57]. Still, an efficient incorporation of this multidimensional view in the modeling process should be considered as complex to achieve. Some preliminary works have been proposed imposing a huge computational time [11, 6].

In a first place, we propose to overcome this computing complexity by efficient design and programming of a HD-sEMG generation model (see section 2.2). For this purpose, we propose a different and innovative computation scheme for a fast and optimized computation of the muscle electrical activity over the skin surface using 3D matrices in the Fourier domain and parallel computing. Nevertheless, when hundreds of thousand of fibers are

considered to generate the muscle electrical activity, the computation time remains too long to perform some important analysis such as global sensitivity analysis or inverse problems cannot be studied. For this purpose, we propose an upgrade of the initial model where the electrical source initially computed at the fiber scale is computed at the MU scale (see section 2.5). Finally, in order to validate the model for the generation of HD-sEMG signals, we detected the substantial effect of the position of the MUs within the muscle (see section 2.6). Most of the developped sEMG models [85, 7, 107] assumed a random territorial placement of the MUs as supposed in [20]. But, after some analysis, it was crucial to propose an algorithm that place the MUs within the muscle respecting an assumption over the fiber density homogeneity .

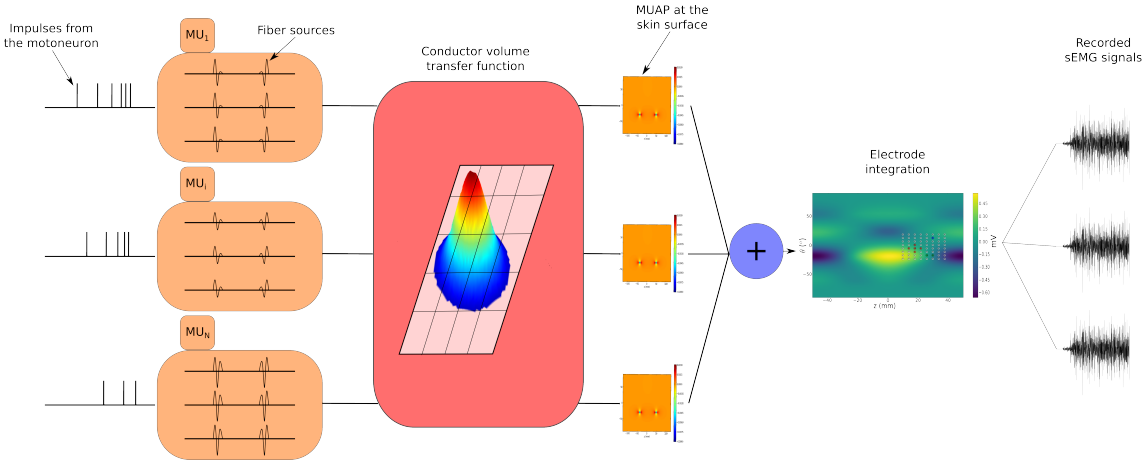

Figure 2.1: Muscle's electrical activity model scheme computation.

2.2 Fast generation model of high density surface EMG signals in a cylindrical conductor volume

2.2.1 Overview of the model geometry and computation

To develop the sEMG model, we took as a starting point the cylindrical representation of the model in [7]. Geometry of the limb is described in Fig. 2.2, where the cylindrical coordinates (ρ, θ, z) are used in this study. Origin of the cylinder limb is placed at its center. The cylindrical conductor volume is composed of three layers (muscle, adipose tissue, and skin) where sources are placed in the most internal layer, along z coordinate, whereas the recording system is placed at the most external boundary between layers (the skin-air interface). Thus, only fusiform muscle can be modeled with this representation, pinnate muscle modeling implies more complex description of the electrical source. The sources are defined at the microscopic scale and represent the fiber intracellular potential generation, propagation and extinction.

In [7], the authors considered four layers (bone, muscle, fat, and skin), yet the bone layer can be regarded as negligible influence on the simulated signals if the distance between muscle-bone and muscle-fat interfaces are high enough. In the case of a simulation of the Biceps Brachii muscle, this distance turns around 20 mm and therefore bone layer

has negligible impact (less than 1% on the simulated signals). This has been checked using the proposed model in a four layer configuration.

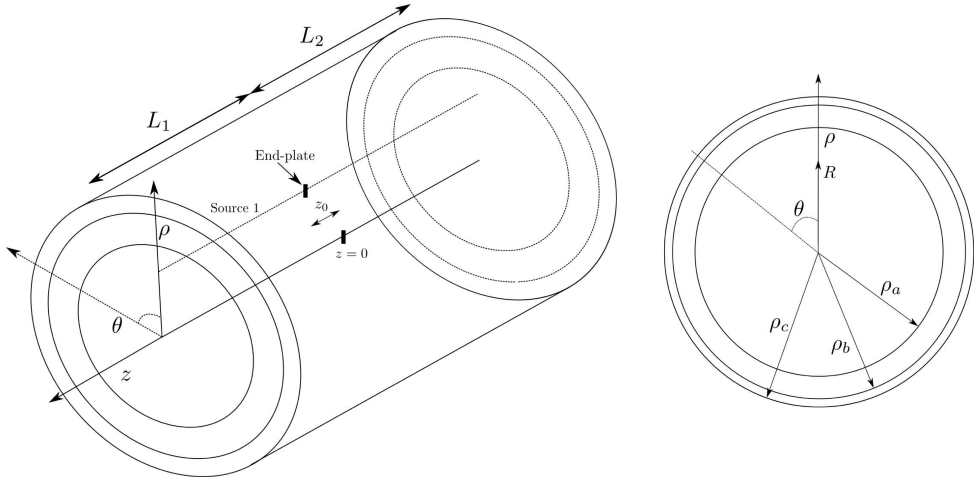

Figure 2.2: (L) Muscle geometry in cylindrical coordinates. (R) Longitudinal cross-section of the cylinder. R is the radial position of the fiber, ρ_a, ρ_b and ρ_c are the muscle, fat and skin radius, respectively.

In this model, all the layers have a finite thickness along the radial direction. Each layer composing the conductor volume is a homogeneous medium which can be anisotropic. Thus, the muscle layer is an anisotropic medium and has higher conductivity along the longitudinal direction than in the other directions. While, the adipose and the skin tissues are isotropic.

Computation of all the parts composing the model are optimized. Innovation of this work lies in the way the model does the computation. It uses the linear algebra properties of matrices in the Fourier domain to compute the electrical activity at the skin surface. Calculus diagram for the computation of one single fiber action potential (SFAP) can be observed in Fig. 2.3.

As shown in Fig. 2.3, computation is fully made in the Fourier frequency domain with matrices multiplication along the pertinent axis. Electrical activity over the skin surface is computed as the sum of the fiber electrical activities. The fiber electrical activity is computed from the multiplication between the Fourier transform of the MU discharge times and the 2D Fourier transform of the spatio-temporal signature of the fiber electrical source. Then, the result is multiplied with the volume conductor transfer function expressed in spatial frequency coordinates. Finally, 2D electrical activity over the skin surface is obtained with a 3D inverse Fourier transform (spatial and time coordinates). Sections below will detail how this computation is done and explain the necessity to do this computation in the frequency domain. In this model, Fourier transform will be performed with the Fast Fourier Transform algorithm implemented in the SciPy package available in Python.

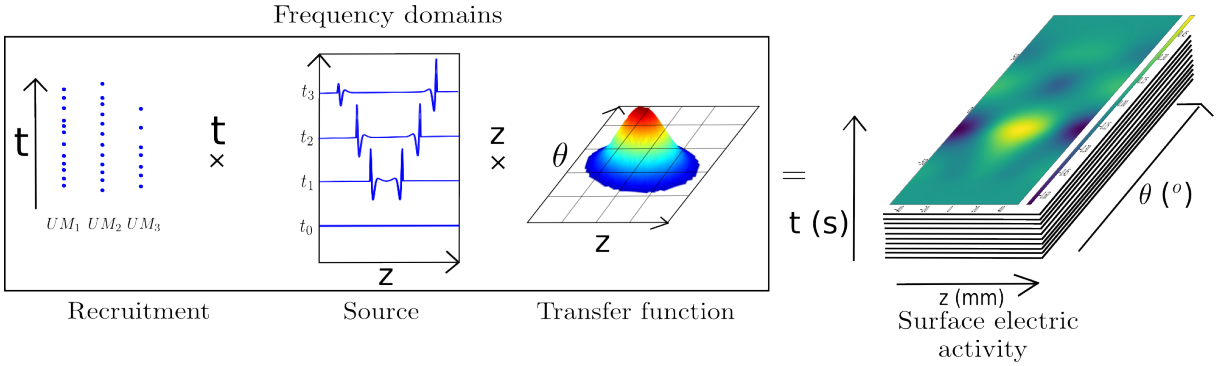

Figure 2.3: Model's calculus scheme to compute one SFAP. Recruitment represents the discharge times of the MU in time (t). A Fourier transform ($\mathcal{F}$) is applied for computing in frequency domain. Source depicted the intracellular action potential along the longitudinal direction of the fiber in time when a discharge time is triggered (z, t). A 2D Fourier transform ($\mathcal{F}^2$) is applied on it. Transfer function presents the volume conductor transfer function computed according to the composition of the volume conductor in spatial frequency domain (k_θ, k_z). Electrical activity over the skin surface is finally computed with a 3D inverse Fourier transform ($\mathcal{F}^{-3}$) and potential map is obtained in the spatio-temporal domain (θ, z, t).

2.2.2 Modeling the MU recruitment scheme

During contraction, MUs are recruited independently of others and in agreement with the size principle [18]. Each MU is activated at a specific threshold depicted in the Fuglevand model [20] and muscle specified in [41]:

$$RTE_i = \left(\frac{a.i}{N}\right) e^{i\frac{ln\left(\frac{RR}{a}\right)}{N}} \tag{2.1}$$

where RTE_i corresponds to the RTE of the i^{th} MU, RR is the recruitment range corresponding to the muscle force level where all the MUs are recruited, N is the number of motoneuron and a is a constant value describing the slope of the recruitment threshold function (see Fig. 2.4).

From observations of the Fig. 2.4, we can state that definition of the RTE is essential for the simulation. In fact, RTE definition will directly impact on the number and type of MUs recruited during the contraction. For example, for a contraction at 50% of the MVC with $a = 40$, MUs of type IIb or Fast Fatigable (FF) are recruited whereas for the same contraction level with $a = 80$ or 160 there aren't any FF MUs recruited. It is known that during high sustain contractions, these are the FF MUs that contribute the most in the sEMG signal composition [58, 57].

According to this representation, a MU remains inactive as long as the force level is below its RTE value. It is supposed that the first discharge occurs when the MU starts to be recruited. Each MU recruitment is regulated by a motoneuron firing rate (Fr_i) which linearly intensifies with force level, from its minimal (Fr_{min}) to its peak (PFR_i) firing rate.

$$FR_i(t) = g_i\left(E(t) - RTE_i\right) + Fr_{min} \quad \texttt{if} \quad E(t) \geq RTE_i \tag{2.2}$$

where $E(t)$ is the excitatory drive provided by the Central Nervous System (CNS) and g_i the linear gain according to force level defined as:

$$g_i = \frac{PFR_i - Fr_{min}}{100 - RTE_i} \tag{2.3}$$

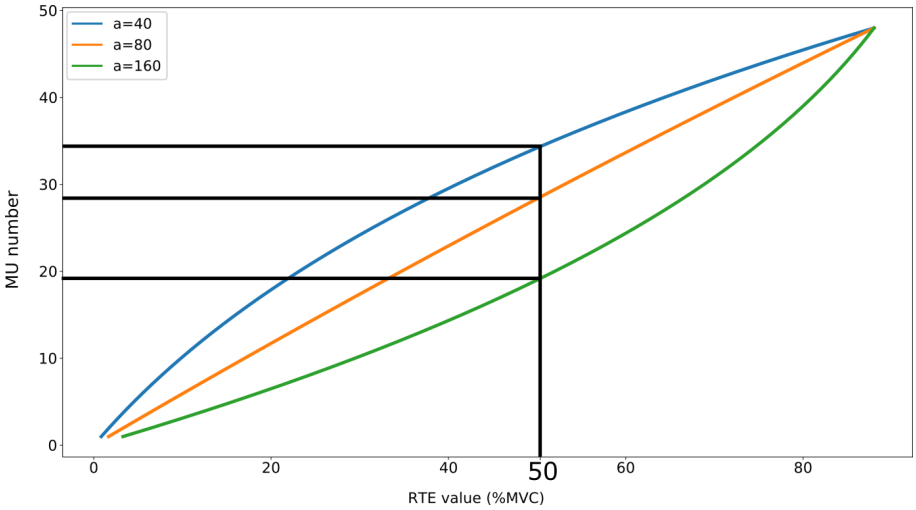

Figure 2.4: The recruitment threshold function for the same MU according to different values of parameter a.

Nevertheless, studies [71, 23] reported a non linear rate coding and proposed:

$$FR_i(t) = PFR_i\left(1 - e^{-\frac{E(t)-RTE_i}{\tau_i}}\right) + Fr_{min} \quad \texttt{if} \quad E(t) \geq RTE_i \tag{2.4}$$

where τ_i is a time constant specific to each MU defined as:

$$\tau_i = -\frac{100 - RTE_i}{ln\left(\frac{Fr_{min}}{PFR_i}\right)} \tag{2.5}$$

In this model, for each MU, its PFR is taken inversely proportional to the recruitment threshold.

$$PFR_i = PFR_1 - PFRD\frac{RTE_i}{RTE_N} \tag{2.6}$$

The firing frequencies Fr_{min} and PFR_1 are fixed to 8 and 35 Hz, respectively. PFRD is the peak firing rate difference and is fixed to 15 Hz in this study. Also, the "onion skin" phenomenon, observed in experimental study [70] following linear or non-linear MU firing rate slopes, is taken into account.

This representation of the motoneuron pool is generic and can differentiate each MU according to its size.

As we can see on Fig. 2.5, all the MUs are not recruited since the used RR value is 88%, thus all the MUs are not recruited for any contraction below 88% of the Maximal Voluntray Contraction (MVC). Moreover, we can also notice that the Inter-Spike Interval (ISI) decreases with force level showing the increase of the firing rate of the MUs according to force level.

2.2.3 Fiber electrical source modeling

The Intracellular Action Potential (IAP) $V_m(z)$ can be described in space domain as suggested in [31]. The fiber current density source travels at a velocity v_f along the longitudinal direction of the finite muscle fiber. It arises at the fiber end-plate, propagates

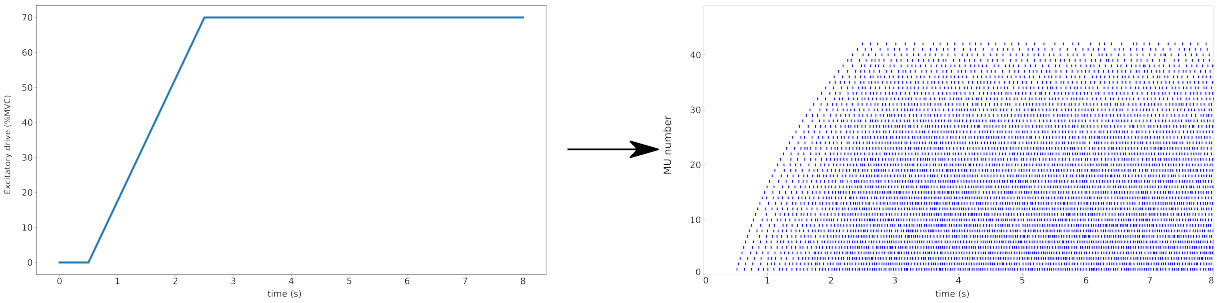

Figure 2.5: (L) The excitatory drive for a plateau contraction at 70% of the maximal voluntary contraction during 6s. (R) The corresponding discharge moments of a muscle composed of 50 MUs.

Table 2.1: Recruitment parameters needed to define the MUs recruitment

Parameter	Description	Unit
N	Number of MUs	
RR	Recruitment range	%MVC
a	Recruitment threshold slope	
lvl	Contraction level	%MVC
T_r	Resting time	s
T_h	Holding time	s
c_s	Contraction speed	%MVC.s^{-1}
f_s	Sampling frequency	Hz

along the fiber and extinguishes at the myotendinous junction. These phenomena are described in [85] by:

$$i_f(z,t) = \frac{d}{dz}\left(\varphi\left(z - z_0 - v_f t\right) p_{L_1}\left(z - z_0 - \frac{L_1}{2}\right) - \varphi\left(-z + z_0 - v_f t\right) p_{L_2}\left(z - z_0 + \frac{L_2}{2}\right)\right) \tag{2.7}$$

where, $\varphi(z)$ is the first derivative of $V_m(-z)$; z_0 is the position of the end-plate of the fiber; v_f is the propagation velocity of the fiber; $L_1 = \frac{L}{2} - z_0 - MTZ_L$ and $L_2 = \frac{L}{2} + z_0 - MTZ_R$ are the semi-lengths of the fiber from the end-plate to the right and to the left tendon, respectively; MTZ_L and MTZ_R are the left and right myotendinous length, respectively; $p_L(z)$ is the rectangular window defined as:

$$p_L(z) = \begin{cases} 1 & \texttt{if } |z| \leq \frac{L}{2} \\ 0 & \texttt{otherwise} \end{cases} \tag{2.8}$$

This description assumes a progressive generation and extinction of the first derivative of the IAP in order to simulate both end plate and end effect of the fiber without any approximation of the current density. A modified version of this description, with the use of Tukey window instead of rectangular window, is proposed below. This proposition follows previous works using exponential or conical decay of the electrical source [84] managing the decay using one parameter α. This proposition is motivated by the fact that generation and extinction of the electrical sources should be progressive and smooth which is not managed by the classical rectangular windowing in previous model [85] (see eq(2.7)). Thus:

$$i_f(z,t) = \frac{d}{dz}\left(\varphi\left(z - z_0 - v_f t\right)\omega_{L_1}\left(z - z_0 - \frac{L_1}{2}\right) - \varphi\left(-z + z_0 - v_f t\right)\omega_{L_2}\left(z - z_0 + \frac{L_2}{2}\right)\right) \tag{2.9}$$

With ω_L a Tukey window defined along fiber semi-lengths with $\alpha = 0.1$ such as:

$$\omega_L(z) = \begin{cases} \frac{1}{2}\left(1 + \cos\left(\frac{2\pi}{\alpha}\left(\frac{z+\frac{L}{2}}{L} - \frac{\alpha}{2}\right)\right)\right) & \texttt{if} \quad -\frac{L}{2} \leq z \leq \frac{\alpha}{2}L - \frac{L}{2} \\ 1 & \texttt{if} \quad \frac{\alpha}{2}L - \frac{L}{2} \leq z \leq \left(1 - \frac{\alpha}{2}\right)L - \frac{L}{2} \\ \frac{1}{2}\left(1 + \cos\left(\frac{2\pi}{\alpha}\left(\frac{z+\frac{L}{2}}{L} - 1 + \frac{\alpha}{2}\right)\right)\right) & \texttt{if} \quad \left(1 - \frac{\alpha}{2}\right)L - \frac{L}{2} \leq z \leq \frac{L}{2} \end{cases} \tag{2.10}$$

As mentioned above, the use of a Tukey window allows a smoother progressive generation and extinction of $\varphi(z)$. Thus, discontinuities produced by the rectangular window are attenuated (see Fig. 2.6). However, the classical rectangular windowing effect can be easily retrieved by setting the parameter α to 0.

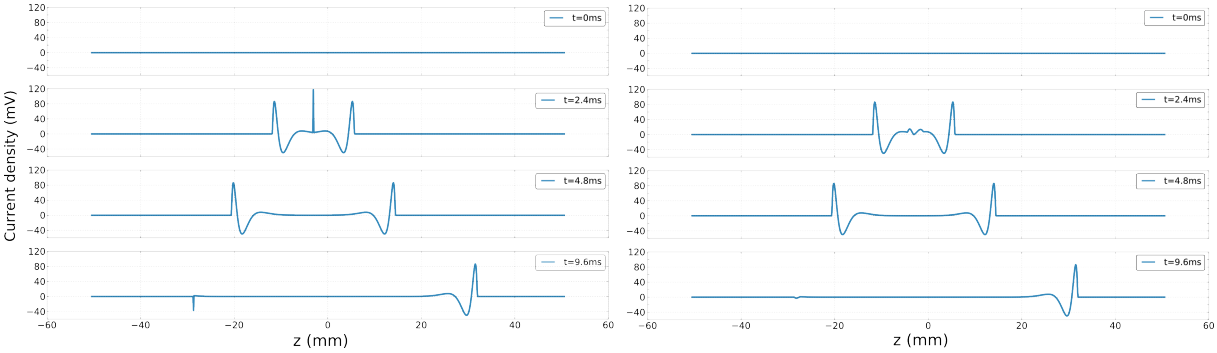

Figure 2.6: (L) A fiber current density source defined with the rectangular window at 4 different instants (t = 0ms, t = 2.4ms, t = 4.8ms and t = 9.6ms). (R) The same fiber current density source defined with the Tukey window at the same instants.

The IAP mathematical description will be computed once for each fiber in the muscle on 1s according to the time sampling and space domain. This impulse will be repeated each time when the motor unit, including its fibers, is recruited. Finally, to model the variability of myotendinous junction spreading, their positions will follow a uniform law at the extremities of the fiber as depicted in [84]. This modeling allows fiber electrical activities to extinguish at different instants and longitudinal positions as observed on real data [84].

2.2.4 Computation of the transfer function of a multilayer cylindrical volume conductor

Fig. 2.2 shows a cylindrical geometry of a three layers media which includes muscle, adipose and skin tissues. It has been shown in [7, 81] that the transfer function of a multilayered cylindrical conductor volume can be obtained by solving Poisson equation for the layer which contains sources and Laplace equation for the others. Boundary conditions must be defined for uniqueness and for the stability of the solution. Thus, these boundary conditions must be defined for the layer that is containing the source and for the common interface between layers. The main steps of calculation are summed

Table 2.2: Fiber parameters needed to define a fiber

Parameter	Description	Unit
L	Fiber length	mm
z_0	Fiber end-plate longitudinal position	
MTZ_R	Right myotendinous length	mm
MTZ_L	Left myotendinous length	mm
ρ_f	Radial position	mm
θ_f	Angular position	$^\circ$
v_f	Conduction velocity	$\mathrm{m.s^{-1}}$

up below. In a conductor volume, the electric potential in quasi-stationary conditions is retrieved from [108, 109]:

$$\nabla . J = -\nabla . \left(\underline{\underline{\sigma}} \nabla \varphi \right) = I \tag{2.11}$$

where, J is the current density ($\mathrm{A.m^{-2}}$); $\underline{\underline{\sigma}}$ is the conductivity tensor ($\mathrm{S.m^{-1}}$); φ is the potential (V) and I the density current of the source ($\mathrm{A.m^{-3}}$). Equation (2.11) can be written as:

$$-\underline{\underline{\sigma}} \nabla^2 \varphi = \int_{x'} I\left(x'\right) \delta\left(x - x'\right) dx' \tag{2.12}$$

With x a point in the space, and x' the position of the source. Using a Green function satisfying:

$$-\underline{\underline{\sigma}} \nabla^2 G\left(x, x'\right) = \delta\left(x - x'\right) \tag{2.13}$$

Subject to the constraint $G\left(x, x'\right) \to 0$ as $|x'| \to \infty$.

Considering cylindrical coordinates and symmetrical homogeneous medium equation (2.13) becomes:

$$\sigma_\rho \frac{\partial^2 G}{\partial \rho^2} + \sigma_\rho \frac{1}{\rho} \frac{\partial G}{\partial \rho} + \frac{\sigma_\theta}{\rho^2} \frac{\partial^2 G}{\partial \theta^2} + \sigma_z \frac{\partial^2 G}{\partial z^2} = -\frac{1}{\rho} \delta(\rho - R) \delta(\theta) \delta(z) \tag{2.14}$$

where, $x' = (R, 0, 0)$ is the cylindrical coordinate of the source, R is the radial position of the source, σ_ρ, σ_θ, σ_z are the conductivities in the three directions and $\delta(.)$ is a Dirac delta function. With the following variable change:

$$x = \rho k_z \sqrt{\frac{\sigma_z}{\sigma_\rho}} \tag{2.15}$$

where k_z is the spatial frequency in z direction. Equation (2.14) becomes after factorization:

$$\frac{\partial^2 G}{\partial x^2} + \frac{1}{x} \frac{\partial G}{\partial x} + \frac{\sigma_\theta}{\sigma_\rho x^2} \frac{\partial^2 G}{\partial \theta^2} + \frac{1}{k_z^2} \frac{\partial^2 G}{\partial z^2} = -\frac{1}{\sigma_\rho x} \delta(x - x') \delta(\theta) \delta(z) \tag{2.16}$$

where $x_0 = R k_z \sqrt{\frac{\sigma_z}{\sigma_\rho}}$.

In the present case, if the solution is written as a Green function:

$$G\left(x, \theta, z, x_0\right) = \sum_{k_\theta = -\infty}^{+\infty} \int_{-\infty}^{+\infty} e^{i z k_z} e^{i \theta k_\theta} K(x, x_0) dk_z \tag{2.17}$$

Then making use of equation (2.17), equation (2.16) becomes:

$$\frac{\partial^2 K}{\partial x^2} + \frac{1}{x}\frac{\partial K}{\partial x} - \left(1 + \frac{\sigma_\theta k_\theta^2}{\sigma_\rho^2 x^2}\right) = -\frac{1}{\sigma_\rho x}\delta(x - x') \tag{2.18}$$

The general solution of equation (2.18) (when $x \neq x'$) is the solution of Laplace equation along ρ coordinate that is the transfer function of the conductor volume:

$$K\left(x, k_\theta, k_z\right) = A_n(k_z) I_n(x) + B_n(k_z) K_n(x) \tag{2.19}$$

where A_n and B_n are arbitrary coefficients, $n = k_\theta \sqrt{\frac{\sigma_\theta}{\sigma_\rho}}$, I_n and K_n are modified Bessel functions of order n of the first and the second type, respectively.

Coefficients $A_n(k_z)$ and $B_n(k_z)$ in (2.19) have to be calculated to conform to the boundary conditions between the layers as well as the restrictions related to the source. There are two boundary conditions for each interface between two layers which are the continuity of the potential and its first derivative. Conditions at the interfaces are:

$$\begin{cases} K|_{\rho_0^+} & = & K|_{\rho_0^-} \\ \left[\sigma_0^+ \frac{\partial K}{\partial x}\right]_{\rho_0^+} & = & \left[\sigma_0^- \frac{\partial K}{\partial x}\right]_{\rho_0^-} \end{cases} \tag{2.20}$$

where ρ_0 designates the location of the considered interface and σ_0^+, σ_0^-, are the radial conductivities of the two considered layers.

Moreover, there are two conditions associated to the source which are the continuity of the potential and the discontinuity of its first derivative:

$$\begin{cases} K|_{x_0^+} & = & K|_{x_0^-} \\ K'|_{x_0^+} - K'|_{x_0^-} & = & -\frac{1}{x_0 \sigma_\rho} \end{cases} \tag{2.21}$$

with x_0 defined above and σ_ρ the radial conductivity of the layer enclosing the source. To compute a solution that is external to the source ($\rho > R$), coefficient A_n in (2.19) has to be set to 0 to take into account the finite dimension of the muscle because $I_n(x)$ diverges when $x \to +\infty$. Thus:

$$A_n|_{x_0^+} = 0 \;\; ; \;\; B_n|vert_{x_0^+} = \frac{1}{\rho} I_n(x_0) \tag{2.22}$$

Finally, the general transfer function of the conductor volume is retrieved in the spatial frequency domain according to the source position from (2.19), (2.21) and (2.22):

$$K\left(x, k_\theta, k_z, x_0\right) = A_n(k_z) I_n(x) + B_n(k_z) K_n(x) + \frac{1}{\sigma_\rho} I_n(x_0) K_n(x) \tag{2.23}$$

with, $x_0 = R k_z \sqrt{\frac{\sigma_z}{\sigma_\rho}}$. The last term of the equation in (2.23) is obtained from (2.19) and (2.21) and is only used for the layer that encloses the source.

Arbitrary coefficients in (2.23) are determined considering all the interfaces between layers. Usually, they are calculated with a linear system that uses the conditions described in (2.20) and (2.21). The general equation of a linear system is predicted by:

$$\underline{\underline{A}}.\underline{X} = \underline{b} \tag{2.24}$$

where $\underline{X}$ is the vector of coefficients to be determined, $\underline{\underline{A}}$ is a matrix based on the conductor volume composition and $\underline{b}$ is a vector related on the source position.

Then, unknown vector $\underline{X}$ is obtained by inverting matrix $\underline{\underline{A}}$. This inversion can induce numerical problems due to the ill-conditioning of the matrix that has a high conditioning number. However, this conditioning number can be reduced by using the substitution of the vector $\underline{X}$ proposed in [14]. In the case of a muscle with an anisotropic muscle layer (radius ρ_a, and conductivities $\sigma_{m\rho}$, $\sigma_{m\theta}$ and σ_{mz}), an isotropic adipose layer (radius ρ_b and conductivity σ_f) and an isotropic skin layer (radius ρ_c and conductivity σ_s), the following equation is obtained:

$$\underline{X} = \begin{pmatrix} A_n^m(k_z) I_n(\rho_{am} k_z) \\ A_n^f(k_z) I_n(\rho_b k_z) \\ B_n^f(k_z) K_n(\rho_b k_z) \\ A_n^s(k_z) I_n(\rho_c k_z) \\ B_n^s(k_z) I_n(\rho_c k_z) \end{pmatrix} \tag{2.25}$$

with $\rho_{am} = \rho_a \sqrt{\frac{\sigma_{mz}}{\sigma_{m\rho}}}$. Superscripts ^{m}, ^{f} and ^{s} represent the corresponding coefficient determinate in muscle, adipose and skin layer, respectively. Then, matrix $\underline{\underline{A}}$ becomes:

$$\underline{\underline{A}} = \begin{pmatrix} 1 & -\frac{I_n(\rho_a k_z)}{I_n(\rho_b k_z)} & -\frac{K_n(\rho_a k_z)}{K_n(\rho_b k_z)} & 0 & 0 \\ \sqrt{\sigma_{mz}\sigma_{m\rho}} \frac{I_n'(\rho_{am} k_z)}{I_n(\rho_{am} k_z)} & -\sigma_f \frac{I_n'(\rho_a k_z)}{I_n(\rho_b k_z)} & -\sigma_f \frac{K_n'(\rho_a k_z)}{K_n(\rho_b k_z)} & 0 & 0 \\ 0 & 1 & 1 & -\frac{I_n(\rho_b k_z)}{I_n(\rho_c k_z)} & -\frac{K_n(\rho_b k_z)}{K_n(\rho_c k_z)} \\ 0 & \sigma_f \frac{I_n'(\rho_b k_z)}{I_n(\rho_b k_z)} & \sigma_f \frac{K_n'(\rho_b k_z)}{K_n(\rho_b k_z)} & -\sigma_s \frac{I_n'(\rho_b k_z)}{I_n(\rho_c k_z)} & -\sigma_s \frac{K_n'(\rho_b k_z)}{K_n(\rho_c k_z)} \\ 0 & 0 & 0 & \sigma_s \frac{I_n'(\rho_c k_z)}{I_n(\rho_c k_z)} & \sigma_s \frac{K_n'(\rho_c k_z)}{K_n(\rho_c k_z)} \end{pmatrix} \tag{2.26}$$

And $\underline{b}$ is defined as follows:

$$\underline{b} = \begin{pmatrix} -\frac{1}{\sigma_{m\rho}} I_n(R_m k_z) K_n(\rho_{am} k_z) \\ -\sqrt{\frac{\sigma_{mz}}{\sigma_{m\rho}}} I_n(R_m k_z) K_n'(\rho_{am} k_z) \\ 0 \\ 0 \\ 0 \end{pmatrix} \tag{2.27}$$

where $R_m = R\sqrt{\frac{\sigma_{mz}}{\sigma_{m\rho}}}$. With this substitution, the conditioning number of matrix $\underline{\underline{A}}$ is reduced and provides more stable solutions, even for the case of multiple layers.

Due to the mathematical definition of $\underline{\underline{A}}$, it is clear that this matrix is invariant in time. Then, the matrix $\underline{\underline{A}}$ is computed once for every values of k_θ and k_z. On the other hand, vector $\underline{b}$ is specific to the fiber radial position and is also invariant in time domain. After, the vector $\underline{b}$ is computed once for every value in the spatial frequency domain and for each fiber.

2.2.5 Spatial frequency sampling

Sampling of the angular frequency k_θ has to be imposed due to the restriction of the angular coordinate θ to the interval $[-\theta_{max}; \theta_{max}]$. Spatial coordinate θ is independent of z, t and ρ, thus, this dimension can be sampled in a decoupled manner respecting the Nyquist condition. With $\theta_{max} = \frac{\pi}{2}$, only the upper part of the cylinder will be represented.

Parameter	Description	Unit
k_θ	Number of angular bins	
N_l	Number of layers	

(a) Conductor volume parameters needed to define the conductor volume

Parameter	Description	Unit
σ_ρ	Radial conductivity	$S.m^{-1}$
σ_θ	Angular conductivity	$S.m^{-1}$
σ_z	Longitudinal conductivity	$S.m^{-1}$
R	Layer radius	mm

(b) Layer parameters needed to define a layer

If this cylinder approximates an arm, one can suppose that this upper part can represent the Biceps Brachii muscle. Then we put $k_\theta \in [-50; 50]$ with a step of $\Delta k_\theta = 1$. Thus, the number of angular frequency bins and its discretization are $w_\theta = 101$ and $\Delta\theta = \frac{\pi}{w_\theta}$, respectively.

Considering the longitudinal frequency sampling, we know that the longitudinal coordinate z and time are linked by the propagation velocity.

$$z = vt \tag{2.28}$$

Thus, we have the relation in spatial and time frequency domains such as:

$$k_z = \frac{k_t}{v} \tag{2.29}$$

with, $k_t = 2\pi f_s$ the angular time frequency and f_s the sampling frequency. In time frequency domain, the frequency bandwidth is limited to the interval $\left[-\frac{f_s}{2}, \frac{f_s}{2}\right]$ respecting the Nyquist theorem. Thus, we can deduce the maximal longitudinal frequency as:

$$k_{zmax} = \frac{\pi f_s}{v} \tag{2.30}$$

By definition, the spatial frequency discretization respects:

$$\Delta k_z = \frac{2k_{zmax}}{w_z} \tag{2.31}$$

with, w_z the number of spatial frequency bins needed in the numerical implementation. These relations also arise in the spatial domain such as:

$$z_{max} = \frac{1}{\pi \Delta k_z} \tag{2.32}$$

$$\Delta_z = \frac{1}{\pi k_{zmax}} \tag{2.33}$$

Thus from these equations, we can deduce the number of longitudinal bins needed such as:

$$w_z = \frac{2z_{max} f_s}{v} \tag{2.34}$$

In this model and for improving physiological realism [110], fiber conduction velocity v_f is slightly different for each fiber, according to its type and its radius, which is not the case in most of the sEMG generation models. Then, in order to avoid the loss of information in the longitudinal frequency domain, the number of spatial frequency bins w_z is computed with the lowest fiber conduction velocity (v_f^{min}). This will define the highest longitudinal sampling frequency and in this way, loss of information will be minimized.

Finally, electrical activity can be computed for every position $(\theta, z) \in [-\theta_{max}, \theta_{max}] \times [-z_{max}, z_{max}]$ at the skin surface and for every time step $t \in [0, T]$.

2.2.6 Computing the electrical activity

SFAP and MUAP computation

The SFAP is computed according to its source description, position, and propagation in the conductor volume. SFAP is obtained from eq (2.12):

$$-\underline{\underline{\sigma}}\nabla^2\varphi\left(x\right) = I\left(x\right) \tag{2.35}$$

Leading to:

$$\underline{\underline{\sigma}}\nabla^2\varphi\left(x\right) = -\int_V I\left(x'\right)\delta\left(x-x'\right)dx' \tag{2.36}$$

Considering the solution computed from eq (2.13), we have:

$$\underline{\underline{\sigma}}\nabla^2\varphi\left(x\right) = \int_V I\left(x'\right)\left(\underline{\underline{\sigma}}\nabla^2 G\left(x,x'\right)\right)dx' \tag{2.37}$$

Due to the linearity of the operator $\underline{\underline{\sigma}}\nabla^2$, eq (2.37) can be written as:

$$\varphi(x) = \int_V I\left(x'\right)G\left(x,x'\right)dx' \tag{2.38}$$

Thus, we define the SFAP at the skin–air interface in time domain as:

$$\varphi\left(\rho_c,\theta,z,t\right) = \left(I * G\left(\rho_c,\theta,z,R\right)\right) \tag{2.39}$$

with, $*$ being the convolution operation and ρ_c the radial position of the skin–air interface. Due to the complex calculation and computation of the convolution product, the computation of the SFAP is done in frequency domain and then 3D inverse Fourier transform is performed in order to return to the 3D spatio-temporal domain. Finally, SFAP of a fiber placed at position (R,θ_f,z) is given in spatial and time domain by:

$$\varphi\left(\rho_c,\theta,z,t\right) = \mathcal{F}^{-3}\left(\mathcal{F}^2\left(i_f(z,t)\right)\mathcal{F}\left(\delta\left(\theta_f\right)\right)G\left(\rho_c,k_\theta,k_z,R\right)\right) \tag{2.40}$$

where, $\mathcal{F}^{-3}$ is the 3D inverse Fourier transform (in k_θ, k_z and k_t) defined as:

$$\mathcal{F}^{-3}\left(f\left(k_\theta,k_z,k_t\right)\right) = \int_{-k_{\theta_{max}}}^{k_{\theta_{max}}}\int_{-d_{k_{z_{max}}}}^{d_{k_{z_{max}}}}\int_{-d_{k_{t_{max}}}}^{d_{k_{t_{max}}}} e^{i\theta k_\theta}e^{izk_z}e^{itk_t}f\left(k_\theta,k_z,k_t\right)dk_{theta}dk_z dk_t \tag{2.41}$$

$\mathcal{F}\left(\delta\left(\theta_f\right)\right)$ is the 1D Fourier transform of the angular position θ_f of the fiber. $I_f\left(k_z,k_t\right)$ is the 2D Fourier transform of $i_f(z,t)$ presented in section 2.2.3. And $G\left(\rho_c,k_\theta,k_z,R\right)$ is the transfer function of the conductor volume presented in section 2.2.4.

As we know, the MUAP is described as the sum of the SFAP from all fibers of this MU. Thus, from eq (2.40) we have the MUAP defined at the skin–air interface:

$$MUAP\left(\rho_c,\theta,z,t\right) = \sum_{i=1}^{N}\varphi_i\left(\rho_c,\theta,z,t\right) \tag{2.42}$$

where N is the number of fibers which constitute the MU. In this model, for a better physiological description of the muscle, four types of MU are described as in [111]. These types are defined according to the muscle fiber type composing the MU, we assumed that all the fiber in the same MU have the same type. Therefore, we have the:

- slow MU (SMU) exclusively composes of muscle fiber of type I;
- fast resistant MU (FRMU) composes of muscle fiber of type IIa;
- fast intermediate MU (FIMU) composes of muscle fiber of type IIx;
- fast fatigable MU (FFMU) composes of muscle fiber of type IIb.

Area of the MUs is supposed circular and MU territory superposition is considered in the model. Different physiological properties, according to the MU's type, are used and are described in [111].

Finally, fibers within the MU are defined in agreement to its MU's type. MU's fibers are uniformly positioned within MU area and fibers conduction velocities are defined as in [111]. The end-plate region width is set to 10 mm for each MU as in [84].

Table 2.3: MU parameters needed to define a MU

Parameter	Description	Unit
L	MU length	mm
ρ_{MU}	MU center radial position	mm
θ_{MU}	MU center angular position	°
type	MU type	
N	Number of fibers	
R	MU radius	mm

Muscle electrical activity determination

The muscle electrical activity can be described as the sum of MUAPs at the air–skin interface recorded under the electrode area. Furthermore, a MUAP can be described as the sum of its corresponding SFAPs (see Section 2.2.6). Thus, the muscle electrical activity in spatial and time domain is given by the following equation:

$$\begin{aligned} mEA\left(\rho_c,\theta,z,t\right) &= \sum_{i=1}^{N}\left(MUAP_i\left(\rho_c,\theta,z,t\right) * \sum_{k=1}^{P_i}\delta\left(t_k\right)\right) \\ &= \sum_{i=1}^{N}\left(\sum_{j=1}^{M_i}\varphi_{i,j}\left(\rho_c,\theta,z,t\right) * \sum_{k=1}^{P_i}\delta\left(t_k\right)\right) \\ &= \mathcal{F}^{-3}\left(\sum_{i=1}^{N}\left(\sum_{j=1}^{M_i}\mathcal{F}^{2}\left(i_f(z,t)\right)\mathcal{F}\left(\delta\left(\theta_f\right)\right)G\left(\rho_c,k_\theta,k_z,R_{f_j}\right)\right)\right. \\ &\quad \left.\mathcal{F}\left(\sum_{k=1}^{P_i}\delta\left(t_k\right)\right)\right) \end{aligned} \tag{2.43}$$

where ρ_c is the radial position of the skin–air interface; M_i is the number of fibers in the i^{th} MU and P_i is the number of discharge instants of the i^{th} MU. Once again, due to the complex numerical computation of the convolution product, this calculation is done

in the frequency domain with $\mathcal{F}\left(\sum_{k=1}^{P_i}\delta\left(t_k\right)\right)$ is the Fourier transform of the MU discharge instant defined as:

$$\mathcal{F}\left(\sum_{k=1}^{P_i}\delta\left(t_k\right)\right)=\sum_{k=1}^{P_i}\mathcal{F}\left(\delta\left(t_k\right)\right)=\sum_{k=1}^{P_i}e^{-it_kk_t} \tag{2.44}$$

2.2.7 Modeling the recording system and the sEMG signal generation

From the muscle electrical activity definition in eq (2.43), the sEMG signal recorded by the electrode at the skin surface is simulated with an integration operator of the electric current values over the numerical electrode area definition. In fact, at a time t_i, signal of electrode j will be obtained with this following equation:

$$S_j\left(\theta_j,z_j,t_i\right)=\int\int_{\mathbb{S}_j}mEA\left(\rho_c,\theta,z,t_i\right)d_\theta d_z \tag{2.45}$$

where (θ_j, z_j) is the cylindrical coordinates of the center of electrode j and $\mathbb{S}_j$ is the electrode area. For circular shape electrode, we obtain:

$$\mathbb{S}_j=\left\{(\theta,z)\ \mid\ z^2-2zz_j\cos\left(\theta-\theta_j\right)+z_j^2\leq r_j^2\right\} \tag{2.46}$$

where r_j is the radius of electrode j. The potential map is integrated numerically under the electrodes and the signal is normalized by the number of pixels forming the electrode surface.

In [7], a 2D transfer function has been developed for analytical description of the detection system effect. Both transfer functions are implemented in the proposed model. In order to validate the spatial transfer function defined above, a comparison study using both surface integration and analytical transfer function definition will be exposed later (see section 2.2.9). This numerical integration enables us to compute HD-sEMG signals from a given potential map without simulating it again, for any electrode configurations (number or shape).

The use of the integration under electrode area has been exposed for computing the corresponding electrical signal. In the models in [7, 112], the authors exhibited an analytical transfer function for different electrode shapes as circular and concentric-ring electrodes. As depicted before, this subsection illustrates the possibility, thanks to the modular programming of the proposed model, to generate a large diversity of electrode shapes driven by user's needs. Almost any type of electrode can be implemented in the proposed model, if the area under the electrode can be represented as an analytical surface integration operation.

Modeling the shape diversity of the electrode system

In [112], the authors developed a transfer function for concentric-ring electrode with the possibility of simulating multiple rings. Implementation of those electrodes can also be managed by a simple 2D integration over the high resolution potential map generated by the proposed model. Geometry of concentric-ring circular electrode is presented in Fig. 2.7c. In this figure, the area of this electrode can be observed. This area can be divided into two parts, the central circular electrode (A_1) with center (θ_e, z_e) and radius r_1 which

will be weighting with the weight 1, and the ring around A_1, named A_2, with center (θ_e, z_e), internal radius of r_2 and external radius r_3 with the weight -1. Multiple rings can also be easily managed in this model. Thanks to this definition, surface integration boundaries and equation can be easily obtained.

A rectangular electrode with rounded corners is implemented in the model and reproduces electrode geometry used in some experimental studies [2]. The geometry of this electrode is put forward in Fig. 2.7b. The corresponding area of this shape can be divided into three parts: A_1, A_2 and A_3. Area A_1 represents a rectangular area with (l_θ, l_z) lengths, A_2 and A_3 represent semi-circular areas with $\left(\theta_e, z_e + \frac{l_z}{2}\right)$, $r = \frac{l_\theta}{2}$ and $\left(\theta_e, z_e - \frac{l_z}{2}\right)$, $r = \frac{l_\theta}{2}$ as center and radius, respectively. As for previous shape configuration, surface integration equation can be easily derived.

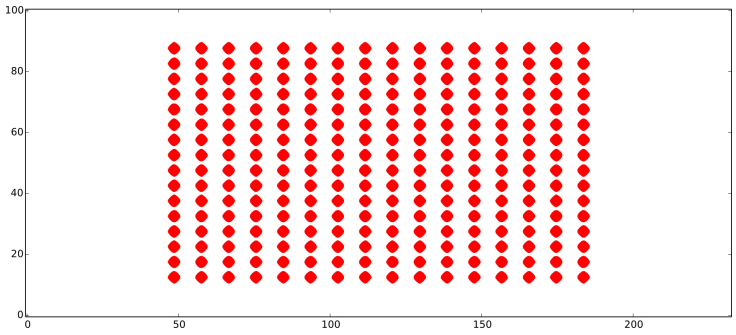

(a) HD-sEMG electrode grid of 16×16 circular electrodes placed at the skin surface of the muscle

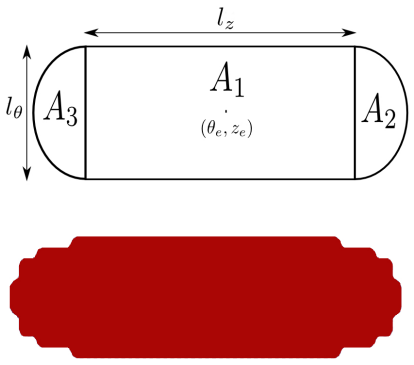

(b) Specifications and numerical area of a rectangular electrode with rounded corners

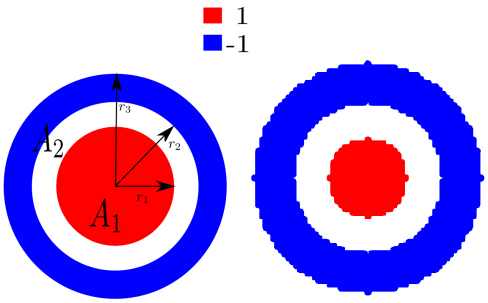

(c) Specifications and numerical area of a concentric-ring circular electrode

Figure 2.7: Grid description, rectangular electrode with rounded corners and circular concentric-ring electrode shapes.

As we can see on Fig. 2.7a, we can also define in this model an electrode grid. We can use any type of electrode in this grid, yet only one type at a time. However, thanks to the decoupling modeling between the electrical activity and the recording instruments, multiple electrode grids can be applied on the same computed electrical activity in a small amount of time. Thus, comparison and analysis of the instrumental recording are easy and fast to perform excluding the possible variability between subjects in experimental studies.

Defining the electrode grid needs several parameters. All these parameters are directly linked to instrumentation design. Thus, the electrode grid center (θ_{eg}, z_{eg}) is required as well as the number of electrode in both directions (n_θ, n_z) and their radius r_e. Moreover, the inter-electrode distances in both directions (d_θ, d_z) can also be managed in this model. Finally, rotation of the grid d_e according to the muscle fiber orientation is also considered since it has a wild interest in experimental studies.

Definition of a single electrode is managed with this formalism of the electrode grid since the total number of electrode managed is equal to $n_\theta \times n_z$.

Table 2.4: Electrode grid parameters needed to define an electrode grid

Parameter	Description	Unit
n_θ	Number of electrode in θ direction	
n_z	Number of electrode in z direction	
d_θ	Inter-electrode distance in θ direction	mm
d_z	Inter-electrode distance in z direction	mm
(θ_{eg}, z_{eg})	Center position of the grid	(°,mm)
r_e	Electrode radius	mm
d_e	Rotation of the grid according to z direction	°

2.2.8 Model implementation

For programming efficiency and flexibility, the proposed model is implemented in *Python* (v2.7 or v3) with an object-oriented approach. *Python* is a generic high-level programming language which features dynamic typing system and automatic memory management. It provides an easier and faster programming than for instance *C++* or *Java*. Time spent to program this model has been widely reduced thanks to the *Python* paradigms. *Python* strength also lies in the large scientific ecosystem that provides such comprehensive libraries and tools such as *NumPy* which supports large, multi-dimensional arrays or matrices, or *SciPy* which supports Fourier transform, signal and image processing and ODE solvers. Moreover, some tools like code profiling or multiprocessing allow users to optimize and minimize the computation time of a complex program.

As previously mentioned, the proposed model in this study is implemented through an object-oriented approach. This approach with structured programming provides a modular code. The code of the model is split into independent modules, in a way that each module clearly represents a specific part of the model presented in the previous sections. This modular approach also allows for modifications or extensions of a specific module easily without having an impact on the other modules. All the model modules are documented and a whole documentation presenting the different features of the model is generated with tools available in *Python*. Furthermore, a *Python* user-friendly Human Machine Interface (HMI), using the *PyQt* library, has been developed to easily use the model without mastering *Python* language and visualize the simulated results. It allows users to easily define the simulation information (purpose of the simulation, date, etc.), the simulation parameters for the model (see Fig. 2.8), simulation features (number of processes to use) as well as the desired outputs (data, image or movie).

The implemented model needs two inputs to perform a simulation. These two files are *JSON* files where one gathers all the parameters needed by the model and the other,

provided in the model, defines standard units for all the needed parameters. It indicates the name of the parameter with an associated unit. Hence, users can define parameters with any unit as long as this unit can be converted into the aimed unit (for example, a length in meter or inches), model will do the conversion itself if it is possible, otherwise it means that a unit parameter is ill-defined, then the model will catch this error and specify the error to the user.

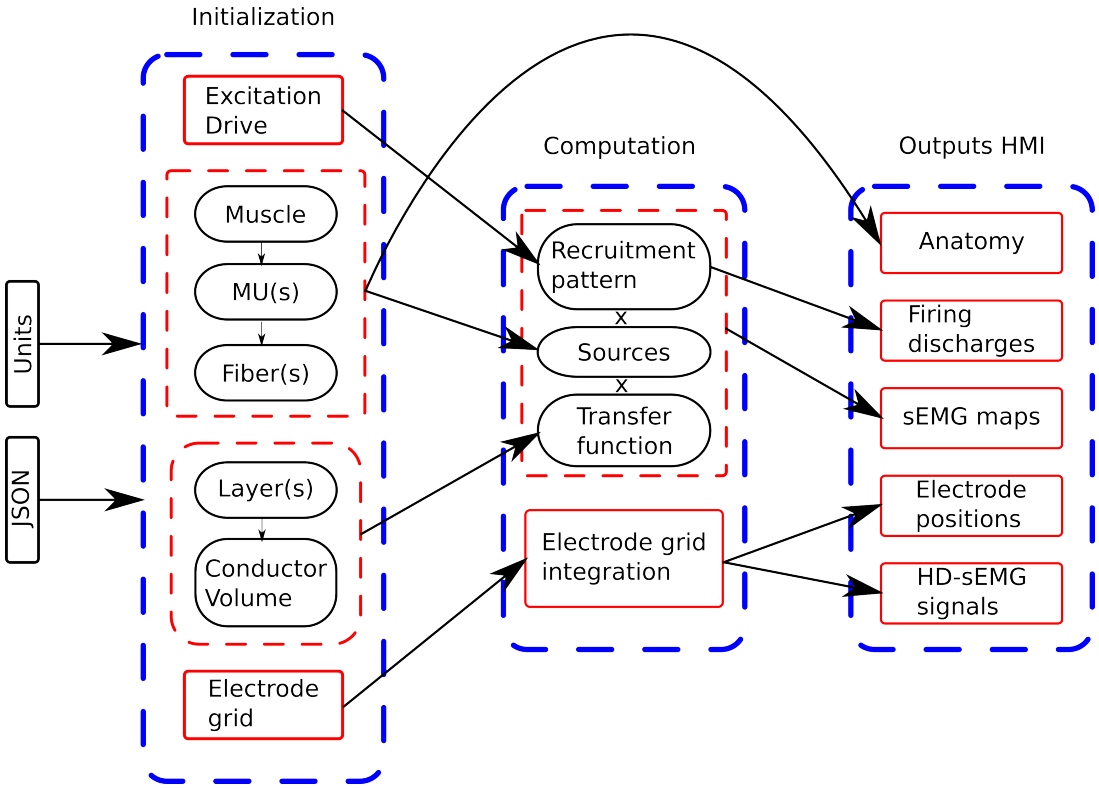

Figure 2.8: Model implementation block diagram describing the dependencies between modules.

As presented above, model is separated into independent modules. Users can define composition of the muscle at different scales through three modules: Muscle, MU and Fiber. The Muscle module defines an entire muscle with the desired number of MU and the MU distribution according to their type. MUs and fibers are automatically generated according to the number of MUs defined and the MU type distribution. The MU module (see Table 2.3) defines a single MU with a specific position in the muscle $(\rho_{MU}; \theta_{MU})$ and its type. Fibers within the MU will be initialized automatically according to the MU type. Fiber module (see Table 2.2) is like the MU module but only for the definition of a single fiber. Users must provide more parameters like the conduction velocity of the fiber.

The conductor volume structure is defined through two modules. The layer module (see Table 2.3b) defines one layer with its different spatial conductivities and its radius in the conductor volume. Then, the ConductorVolume module (see Table 2.3a) gathers all the layers definitions in order to build the conductor volume. It is also in this module that the sampling of k_θ will be imposed.

An electrode grid is implemented in elec grids module. It defines an electrode grid with the number of electrodes according to θ and z axis, the inter-electrode distances in the two directions, the electrode radius and the position of the grid center (see Table 2.4).

Recruitment pattern is defined through the excitation drive in the module RecrutPattern. This excitation drive is defined with the rest time, the holding time, the contraction level, the goal of the contraction, the contraction slope, the recruitment range and the sampling frequency (see Table 2.1). All these modules and their connections are illustrated in Table 2.8.

The proposed model is designed to furnish different outputs in order to provide available information and facilitate a better understanding of the relationship between the sEMG signal features and the physiological mechanisms (ex: sensitivity analysis purpose). The anatomy of the muscle can be plotted illustrating the muscle area in the cylinder with its different layers and the position of the MUs within it. Moreover, MUs recruitment pattern can also be plotted (see Fig. 2.5) and presents the different firing times for a specific MU. Finally, electrode positions over the skin (see Fig. 2.7a), 2D electrical activity at each time step and the signal recorded at each electrode can also be saved in a manageable format (*HDF5*) and reused later.

2.2.9 Simulation results

In this section, the model proposed above will be used for several simulations that illustrate its relevance and efficiency. Moreover, as all models, this one should be validated before trying to interpret the simulations results. For this purpose, a first simulation study will concern a qualitative validation on the MUAP longitudinal propagation and angular attenuation in order to assess the model realism using different electrode shapes presented earlier. Next, the accuracy of the numerical integration under the electrode areas will be also assessed using analytical transfer function formulation. In order to exhibit the easy and fast reproducibility of the model, we will present a simulation study where we define the volume detection for a circular monopolar electrode.

Finally, considering the analysis of the computing time, we will present the computation time in different case: computation of a single MUAP and computation of a muscle contraction at 70% MVC for a muscle with 700 MUs in serial and parallel computing.

All simulations have been run on the same workstation with the following specifications: 2×8 cores Intel Xeon 2.40GHz with hyperthreading (32 threads), 128Go RAM, Ubuntu 14.04 64bits. Concerning all the simulations presented below, some parameters concerning the simulations are defined and will not change among simulation (see Table 2.5) for clarity purpose.

Qualitative validation on the MUAP/SFAP behavior

In this section, two simulation cases are presented, a MUAP recorded with concentric-ring electrodes and a SFAP recorded with circular electrodes in a muscle with three layers (muscle, adipose and skin tissues). For this purpose, the two simulations have been made with the same muscle anatomy definition. Some parameters were specified for this simulation in addition to the parameters from Table 2.5: muscle length is 100mm, muscle radius is 25mm, adipous tissue thickness is 3mm and skin thickness is 2mm. Considering the signal sampling frequency fixed to 4096 Hz, the longitudinal discretization is $dz = 0.76mm$ and the angular discretization is $d\theta = 0.75mm = 1.78°$.

The simulated MUAP is computed from one FF MU placed at $(\rho; \theta) = (21.8; 0)$ corresponding to a MU radius of 3.2 mm and is composed of 214 fibers. It is recorded using

Table 2.5: Configuration of simulation

Parameter	Value (unit)
Radius S MU	$\mathcal{N}(2.5, 0.5)$ (mm)
Number of fibers S MU	$\mathcal{N}(100, 10)$ (mm)
S fiber diameter	$\mathcal{N}(45, 1)$ (μm)
Radius FR MU	$\mathcal{N}(2.75, 0.5)$ (mm)
Number of fibers FR MU	$\mathcal{N}(150, 15)$ (mm)
FR fiber diameter	$\mathcal{N}(50, 1)$ (μm)
Radius FI MU	$\mathcal{N}(3.0, 0.5)$ (mm)
Number of fibers FI MU	$\mathcal{N}(200, 20)$ (mm)
FI fiber diameter	$\mathcal{N}(55, 1)$ (μm)
Radius FF MU	$\mathcal{N}(3.25, 0.5)$ (mm)
Number of fibers FF MU	$\mathcal{N}(250, 25)$ (mm)
FF fiber diameter	$\mathcal{N}(60, 1)$ (μm)
Sampling frequency (f_t)	4096 (Hz)
Radial muscle conductivity ($\sigma_{m\rho}$)	0.1 ($S.m^{-1}$)
Angular muscle conductivity ($\sigma_{m\theta}$)	0.1 ($S.m^{-1}$)
Longitudinal muscle conductivity (σ_{mz})	0.5 ($S.m^{-1}$)
Adipose tissue conductivity (σ_f)	0.05 ($S.m^{-1}$)
Skin conductivity (σ_s)	1 ($S.m^{-1}$)
MU NMJ position (z_{MU})	$\mathcal{U}(-15, 15)$ (mm)
Fiber NMJ position within MU (z_0)	$\mathcal{U}(z_{MU} - 5, z_{MU} + 5)$ (mm)
Fiber left MTZ length (MTZ_L)	$\mathcal{N}\left(-\frac{L}{2} + 15, 2\right)$ (mm)
Fiber right MTZ length (MTZ_R)	$\mathcal{N}\left(\frac{L}{2} - 15, 2\right)$ (mm)
Tukey window parameter (α)	0.1

where, $\mathcal{N}(\mu, \sigma)$ corresponds to a normal distribution with its mean μ and its standard deviation σ. $\mathcal{U}(a, b)$ represents an uniform distribution between a and b (with $a < b$).

concentric-ring electrodes defined with the following radii (r_1; r_2; r_3) (1; 2; 3) mm.

The simulated SFAP was obtained from a single fiber placed at $(\rho; \theta) = (24; 0)$, corresponding to a depth of 1mm in the muscle tissue with conduction velocity fixed at 4 m.s^{-1}, NMJ is at $z_0 = 0$ and MTZ lenghts are fixed to 5mm and 15mm from the right and left side of the NMJ, respectively. The monopolar circular electrodes are defined with a radius of 1mm. Both longitudinal and angular attenuation have been assessed for both simulations.

Electrodes are centered in the longitudinal middle of the muscle ($z_0 = 0$), thus, there are 2 electrodes on each side of the MU and fiber innervation zone. Longitudinal propagation of the MUAP and SFAP on Fig. 2.9a clearly shows a symmetry of the obtained action potential shapes in respect to the position of the innervation zone (around $z_0 = 0$) and a time support correlated to the mean velocity (4 m.s$^-$1) of the fibers within the simulated MU.

Moreover, Fig. 2.9a (Left) also shows the disappearance, due to the high-pass filtering, of the end-plate effect (non propagating component) when a MUAP is recorded with a concentric-ring electrode. On Fig. 2.9a (Right), SFAP recorded with a circular electrode shows the two end-plate effects at z = 0 at two different times. It is coherent with the

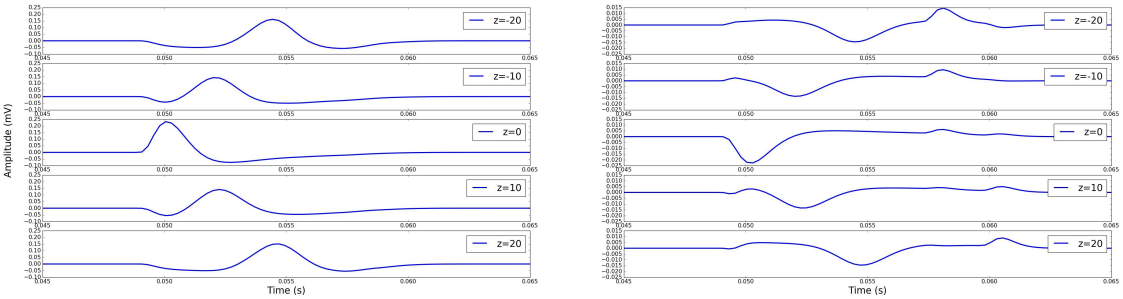

(a) Signals recorded along z axis at $\theta = 0°$. Signals are recorded at five different positions using specific electrodes placed along the z axis with an interelectrode distance of 10 mm. (Left) MUAP longitudinal propagation recorded on 5 concentric-ring electrodes. (Right) SFAP longitudinal propagation recorded on 5 circular monopolar electrodes.

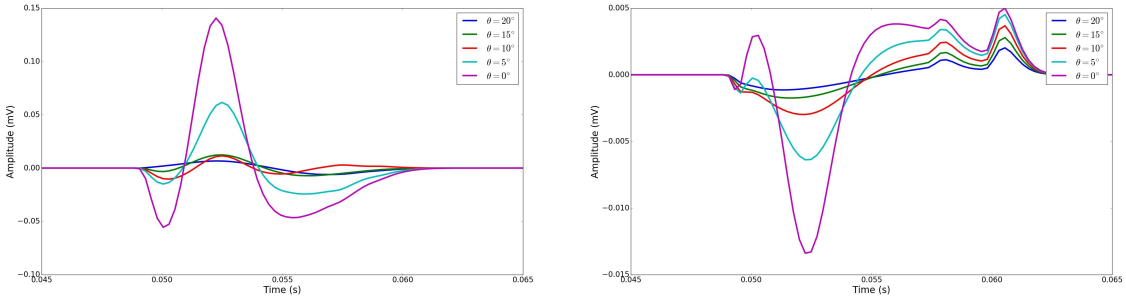

(b) Signals recorded along θ axis at $z = 10$. Signals are recorded at five different positions using specific electrodes placed along the θ axis with an interelectrode distance of 5° (corresponding to 2.6mm). The MUAP angular attenuation recorded on 5 concentric-ring electrodes (Left) and the SFAP angular attenuation recorded on 5 circular monopolar electrodes (Right).

Figure 2.9: Examples of simulated MUAP and SFAP recorded with 2 different electrode shapes at different angular and longitudinal positions for a muscle with three layers (muscle, adipose and skin tissues).

fact that muscle semi-lengths are different on each side of the muscle.

The Fig. 2.9b shows the angular attenuation of the MUAP and SFAP along axis θ. Electrodes are centered in the angular middle of the muscle ($\theta = 0°$) with angular distance steps of 5° corresponding to an inter-electrode distance of 2.6mm. One can observe the strong attenuation of recorded signals as the angular (lateral) distance increases according to the reference position for both the MU and the fiber.

Integration recording evaluation

In this section, a comparison of the sEMG signals recorded by electrodes with the technique exhibited in section 2.2.7 is presented using the spatial integration defined by the surface under electrode area and the 2D inverse Fourier Transform of the electrode transfer function presented in [7].

For this purpose, we did one simulation (50 MUs, 2048 Hz on 6 s) where we defined one electrode grid formed of 8×8 circular electrodes with a radius of 2 mm. Therefore, Normalized-Root-Mean-Square-Error (NRMSE) between signals obtained by both spatial transfer function, considering the analytical one as the reference, is computed in order to check the accuracy of the method proposed compared to the transfer function used in [7].

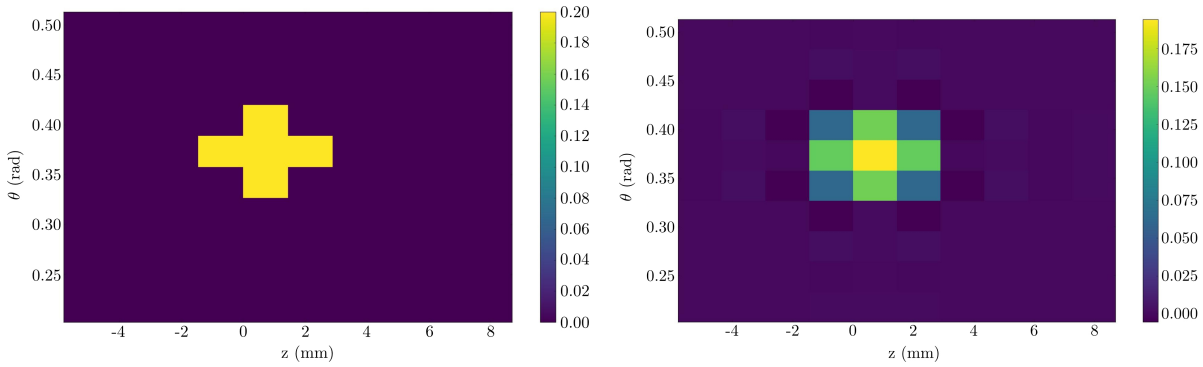

(a) The spatial 2D area of the electrode defined through numerical integration.

(b) The spatial 2D area of the electrode defined in frequency domain [7].

Figure 2.10: Defined areas with both electrode definitions.

On Fig. 2.10 the area of both electrode definitions is exhibited in the spatial domain. A 2D inverse Fourier transform was applied on the analytical definition of the electrode whereas the numerical area is directly defined in spatial domain. We can see that both areas are alike, points with the highest weight are at the same position (under the defined electrode area) and magnitude of the weights are almost similar. On Fig. 2.10b weights decrease from the center of the electrode. It represents a 2D sinc function whereas on Fig. 2.10a integration points have the same weight and represents a 2D cross window. Mean of the computed NRMSE on the 64 sEMG signals is 5%. This difference is explained by the slight divergence between both spatial area definitions.

Volume detection for circular monopolar electrode

In this section, we present a first study about the volume detection of a circular electrode according to its radius in a cylindrical representation of the muscle. Such an analysis has been proposed in [74], but in a planar representation of the muscle. The muscle length is 100mm, muscle radius is 41mm, adipose tissue thickness 3mm and skin thickness 1mm. Four differents electrode radii have been used: 1 mm, 2 mm, 3 mm and 10 mm. These electrodes are placed at $(\theta; z) = (0; 0)$. In order to determine the volume detection of an electrode, we first placed a reference fiber at $(\rho; \theta) = (40.95; 0)$ and compute its SFAP recorded with the four different electrodes. Then, SFAP are computed for deeper fibers with the same parameters of the reference fiber with a step of 0.25 mm along ρ axis, then $\rho \in [10; 40]$. Finally, SFAP are computed for fibers by varying θ with a step of 0.25° for each value of defined ρ. As in [74], amplitude ratio between the other SFAPs and the reference SFAP is computed. The electrode volume detection is defined as the region where this ratio is above 1% [74]. Overall, 19169 fiber simulations were performed, using the proposed model, to precisely cover the detection volume and determinate isoenergetic regions depicted on Fig. 2.11.

On Fig. 2.11 the limit of the detection volume for the 1 mm electrode radius is exhibited. Moreover, thanks to all the simulations we were able to make 10 detection levels of the electrode according to the amplitude ratio between the reference SFAP and other SFAP recordings. The first observation between the different detection volumes is that the electrode radius doesn't significantly change the volume detection of the electrode. On Fig. 2.11, detection volume has a radial maximal depth of 28 mm (distance between the electrode and the fiber with adipose and skin tissue thicknesses) and an angular minimal

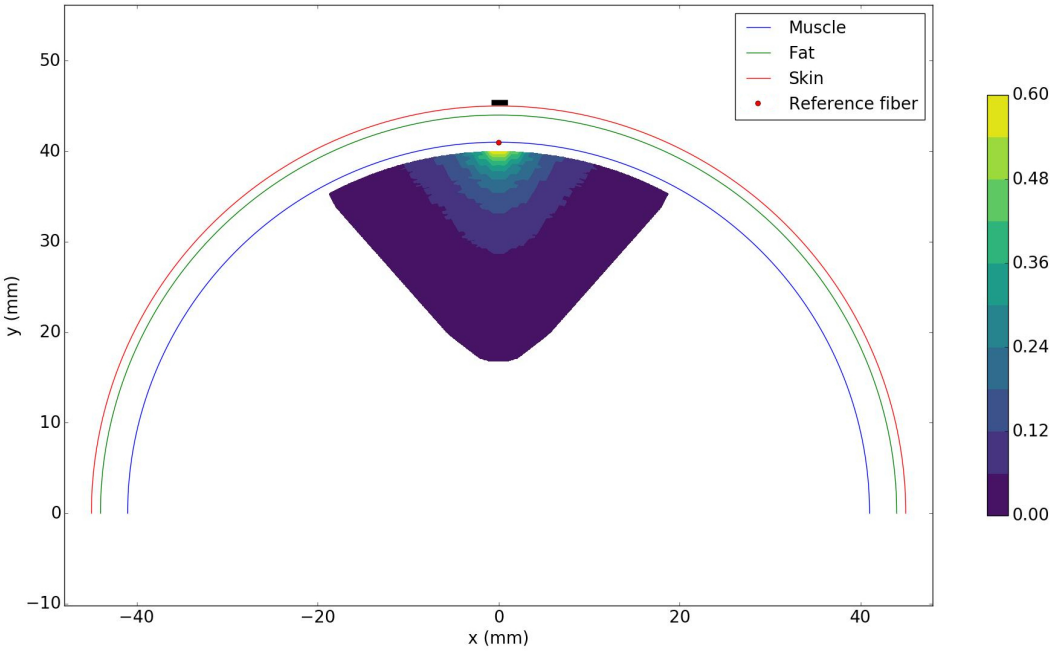

Figure 2.11: Detection volume for a 1mm electrode radius placed at $(\theta, z) = (0, 0)$; color scale indicates the corresponding amplitude ratio range.

distance of 21.24 mm (distance between the electrode and the fiber at the maximal angle and the maximal radial values). Whereas, for an electrode radius of 10 mm, the detection volume has a radial depth of 27 mm and an angular minimal distance of 23.32 mm. For the three electrode radii (1, 2, 3 mm) we don't observe a significant variation in the depth or the size of the detection volume of the electrode. However, a 10 mm electrode radius has a smaller depth and a larger angular detection than the 1 mm electrode radius. In fact, important increase of the electrode radius will reduce the maximal detection depth but will increase the angular detection in the muscle volume.

Related computation time

One crucial feature about modeling is its computation time. This analysis can be seen as a quantitative validation where a good compromise should be found between the model simplifying assumptions and model computation time. For this purpose, we proposed to compare the model computation time for the same simulations in two different computing configurations. These configurations are: computation in serial (using one process) and computation in parallel (using several processes).

Since several research only focus on the MUAP, we propose to compare the computation time for a MUAP generation as well as for muscle contraction. In Table 2.6 is presented the related computation for the computation of a MUAP. 40 different MUs (10 for each type) are defined for the comparison.

As we can see in Table 2.6, the computation time is the same in serial and in parallel. This is coherent since the parallel computing is defined on the MU computation, then if only one MUAP is computed, parallel computing doesn't reduce the computation time.

Then, in Table 2.7 is presented the computation time for 5 simulations of a muscle contraction using different number of CPUs for the parallel computing. Model computed

Table 2.6: Related computation time according to the MU type (mean ± std)

Number of process	S	FR	FI	FF
Serial (1 CPU)	6min58s ± 35s	9min8s ± 2min15s	9min32s ± 34s	14min56s ± 5min52s
Parallel (10 CPUs)	6min51s ± 34s	9min5s ± 2min13s	9min24s ± 36s	14min59s ± 4min55s

a simulation of 50 MUs for 4s of contraction at 70% MVC respecting the parameters configuration of Table 2.5.

Table 2.7: Computation time according to the number of processes used

	Initialization	Electrical activity computation	Electrode recording
Serial (1 CPU)	$4.23s \pm 0.33s$	15h27min ± 1h19min	0.37s ± 9.5ms
5 CPUs	$3.77s \pm 0.06$s	3h30min ± 59min	0.39s ± 0.01s
10 CPUs	$3.96s \pm 0.09$s	1h57min ± 31min	0.36s ± 9.2ms
14 CPUs	$3.85s \pm 0.11$s	1h36min ± 12min	0.40s ± 0.02s

Computation time of the initialization stage represents the time for instantiating the MUs and the fibers positions. Furthermore, during the initialization part, matrix A and vectors b are computed once according to the defined conductor volume configuration. Computation time of the electrical activity computation stage represents the addition of the time needed to compute SFAPs and the use of 3D inverse Fourier transform in order to obtain simulated surface potential map in 2D space and time domain. Electrode recording computation time represents the time for the integration of the potential map over the electrode area defined for every step in time of the simulation (in this case, generation of 128 sEMG signals from the surface potential map).

According to Table 2.7, initialization and electrode recording computation times are negligible compared to the surface potential map computation time. Those computation times remain stable compared to the number of process used as these steps are implemented in a serial manner (managed by one processor).

Computing time for the electrical activity, implemented in parallel, is clearly reduced by the number of used processes. This time reduction seems to follow approximately a linear relationship according to the number of processes. In fact, for 5 processes used, computation time is reduced by 4.4 compared to using one process, whereas for 14 processes, time is reduced by 9.7.

Beyond the use of 10 processes, model speedup begins to diverge from the ideal linear time reduction law according to process number. This divergence is inherent to the model. Firstly, because all the model calculus cannot be run in parallel. Then, overhead induced at the initialization of processes and at the reduction of those processes increases the computation time with the increasing number of process used.

Moreover, the same simulation is also performed on 10 processes but for 6 s of simulation. This time simulation increases of 2 s (+50% of reference simulation time) does not change the computing time significantly compared to the reference computation time of 4 s ($\simeq$ 15 min +13% of computing time). This is mainly due to the intensive use of parallel computation on the 3D inverse Fourier transform for each additional seconds of simulation where the same MUAP representation in the frequency domain is used and already stored in the volatile memory. In addition, the 3D inverse Fourier transform can

be performed independently for each time slice and then can be computed for different time slices (each slice managed by one process) of the 3D matrix at the same time.

Large scale simulation

In this section, a large scale simulation using the proposed model is presented to evaluate the higher computing time that should be encountered during simulations. In this simulation, number of MUs is set to 300 ($\approx$ 52200 fibers) and an electrode grid with 256 circular electrodes is used (see Fig. 2.7a). Moreover, three different excitatory drives are simulated during a global simulation time of 12 s. It means that three different contractions are simulated corresponding to a first plateau at 80% MVC followed by a contraction in ramp from 0 to 80% MVC and a last plateau at 40% MVC (see Fig. 2.12b). To our knowledge, this is the first time that a grid with this high number of electrode is simulated for generating such long time sequence (12 sec.) with a high number of simulated MUs (300) at high sampling frequency (4 kHz). In fact, in [51], simulations with planar model have been performed [85], at 4 kHz for one contraction with 120 MUs. And in [74], 65 MUs at 1024Hz for 3 s have been simulated.

This simulation has been run on 10 processes and it lasted 14h48min. The other previously presented simulation with 10 processes has been generated for 4 seconds of contraction with 50 MUs (see third line in table 2.7) and has lasted around 2 h. In this simulation there are six times more MUs and the contraction time is three times longer. By linear interpolation, we can suppose that sEMG computation time for 4 seconds of contraction with 300 MUs should last around 12h with the use of 10 processes. Here, it is clear that it is much faster, using this model, to simulate several contractions in a serial manner in time and embedded in the same simulation than to simulate each contraction separately if they concern the same muscle anatomy. On the recorded signals, we can observe few artefacts with small amplitudes between each contraction due to the inherent periodicity in time domain introduced by the 3D inverse Fourier transform for each time slice of the defined 3D matrix. Those artefacts can be easily removed thanks to a simple post-processing algorithm. An illustration of the electrode surfacic integration on the large scale simulation with the corresponding signal recording is available at `http://www.utc.fr/~jlaforet/Suppl/sEMG_300MU.mp4`.

2.3 Discussion

In this part, we presented a generation model using multilayered cylindrical volume for simulating HD-sEMG signals by efficient theoretical computation, program coding, and parallel computing. In fact, by using 3D Fourier transform to avoid convolution computation, the proposed model is able to quickly simulate high resolution surface potential map (101×131 samples (θ;z) for a muscle length of 120 mm, 25 mm of muscle radius, 3 mm of fat thickness, 1 mm of skin thickness and on 180°) at the skin surface of the simulated muscle. This surface potential map allows the simulation of an infinite electrode number and shape configurations with tiny additional computing cost since the obtained signals are gathered by numerical integration under the electrode areas without simulating again the surface potential map.

For this purpose, the theoretical formalism of the propagation of electrical current inside a multilayered cylindrical volume has been demonstrated in details. Following as-

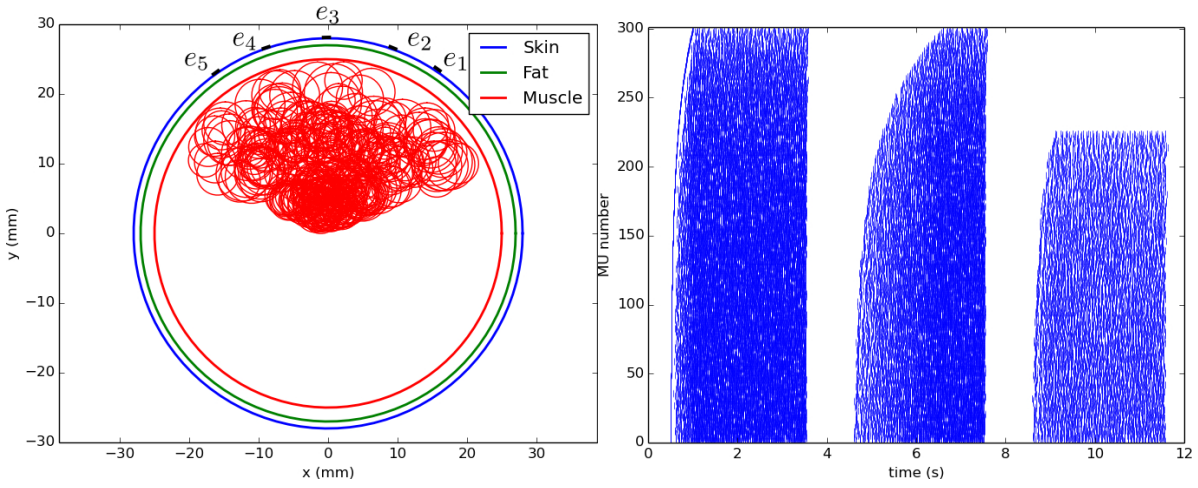

(a) Simulated muscle anatomy.

(b) Simulated MU recruitment pattern sequence.

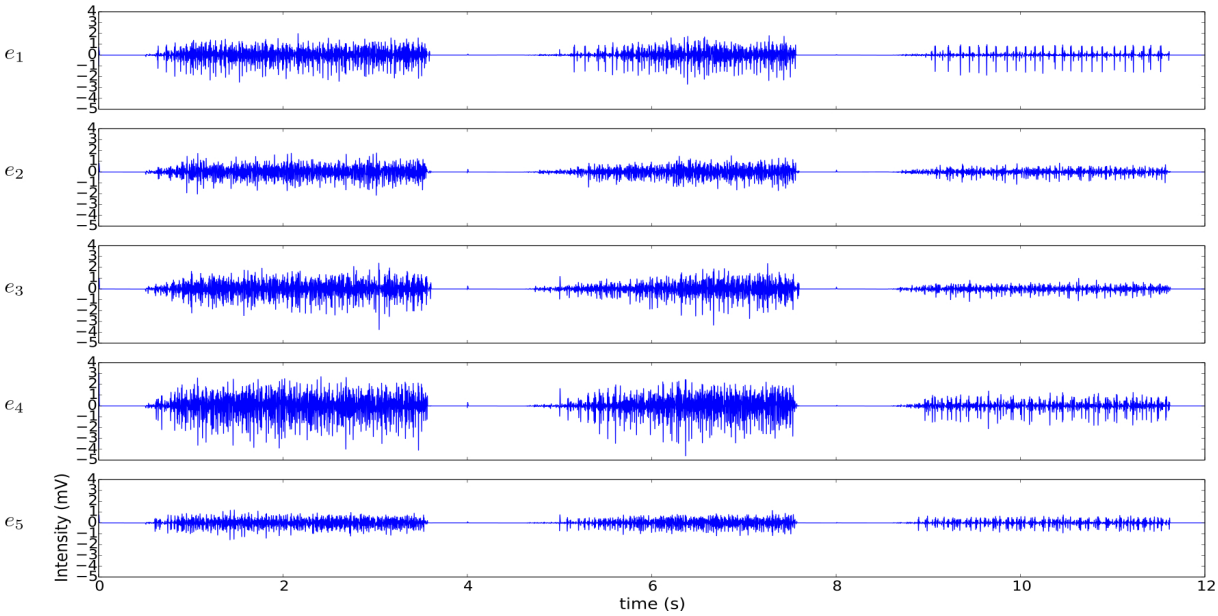

(c) Recorded sEMG signals according to electrode position.

Figure 2.12: Large scale simulation. First contraction represents a high plateau (80 % MVC) held for 2.5 s of simulation; second contraction describes a ramp on 2 s kept for 1 s (from 0 to 80 % MVC); Last contraction illustrates a low plateau (40 % MVC) helds for 2.5 s.

sumptions of a previous published model [7] concerning four layers, the calculus leaded to similar results concerning the proposed model that deals with three layers. This configuration is realistic for simulating Biceps Brachii muscle where the bone layer has negligible impact on the simulated signals. However, the four layers version of the proposed model is also available for other purposes. The principal innovations in this work are:

- The proposed model allows to specify conduction velocities for each fiber;
- A smoothing window is proposed to better describe the generation and extinction of the current sources traveling along the fibers;
- Precise mathematical and numerical implementation description of the model is

provided;

- All calculus are done in the Fourier domain exploiting intensive parallel computing;
- HD-sEMG signals are obtained from numerical integration under the electrode area from a high resolution potential map allowing electrode shape diversity and infinite combinations of electrode number and position with no need of re-simulation.

Concerning the Tukey window that is tuned by one parameter that fixes the smoothness applied on the generation and extinction phenomena. Its influence on the generated sEMG signals has been checked at different contraction levels with Root-Mean-Square value differences lower than 1% for $\alpha = 0.1$. In addition, propagating versus non propagating component ratio has been also verified for several MUAP configurations with no observation of significant difference. However, this parameter has to be carefully fixed to reduce the frequency leakage without altering the amplitude and power of the generated signals.

The proposed model was numerically implemented using *Python* language. This object-oriented language, by its flexibility and compatibility with existing software, offers interesting abilities for scientific computing. A particular effort was given in regards to collect the model inputs using a graphical interface and *JSON* file, and for providing model outputs (signal file, anatomy and recruitment images, surface potential map movie).

To assess the efficiency and possible limitations of the proposed model, several simulations were run. First, the parallel computing strategy impact has been evaluated. It clearly appears that increasing the number of used processes (up to 10) significantly decreases the computing time in a quasi-linear relation (processes/computing time). Above this limit, the speed gain declines. Furthermore, it is also possible to simulate longer sequence, using the same generated muscle anatomy, with a negligible computing time cost.

Another important point, is the small computing time concerning the sEMG signal generation using the numerical integration under the electrode area compared to the use of analytical transfer function. In fact, the numerical integration allows a total decoupling between the high resolution surface potential map and the calculus of the recorded sEMG signals. This important property authorizes the generation of an infinite number and shape of electrodes in a short time and by using the same surface potential map. A limitation of this methodology is rooted in the necessity of the use of a spatial resolution sufficiently high to maintain the electrode simulation accuracy compared to a fully analytical solution as the 2D transfer function proposed in [85]. For this purpose, a simulation has been proposed to check the accuracy of the numerical integration under a 2 mm radius electrode area with both definitions of the electrode transfer function. According to the obtained results, both electrode transfer function definitions are almost equivalent.

In this work, the detection volume with a cylindrical configuration was evaluated, for the first time, using a circular electrode with radius variation. It appears that the radius variation has negligible effect in the range of few millimeters. The effect is more observable using larger electrodes (radius of 10 mm). One can notice that, as for the planar configuration [74], the estimated detection volume is not semi-circular. The obtained volume is larger than the one exposed in [74]. This should be explained by the difference in both volume shape and used electrode arrangements (single differential in [74] and monopolar

in this study). According to this observation, it seems that a grid of small electrodes will have an important muscle volume coverage and the deeper MUs should not be neglected in the simulation process.

Another crucial point is the validation of the proposed model. In the ideal case, this validation should be done using exact knowledge of physiological and anatomical parameters as MU and fiber position and number. Also, several electrical parameters such as the media conductivity should be exactly determined experimentally to perform more reliable simulations. Then, realistic model configuration should be fixed including neural command, and artificial sEMG signals should be compared to experimental sEMG signal using the same simulated electrode paradigm. In reality, these multiple tasks are genuinely complex to realize. An alternative option can however be found in the qualitative evaluation of MUAP shapes compared to real data as in [85] and [7] or simulating data using previous models.

When varying angular position, one can observe MUAP and SFAP attenuation as depicted on Fig. 2.9. Similar effect has been observed on both simulation and experimentation in [7]. In the same figure, we can observe the electrical propagation along the longitudinal axis at each side of the end plate region. To illustrate the capabilities of the proposed model to simulate different electrode configuration according to specific task, we simulated concentric-ring electrode and rectangular with rounded corners electrode used in many experimental studies. Pinnate muscle wasn't managed in this study but should be considered in future works.

Finally, we simulated a large-scale configuration to push the computing process to its limit by using a configuration with 300 MUs and 256 electrodes for a total simulation time of 12 seconds. To our knowledge, this simulation is the first that concerns a grid with 256 electrodes with such long simulation time. The obtained computing time was 14h48min (same time that the simulation of 50 MUs electrical activity for 128 electrodes computed in series). These promising results indicate strong potential of the proposed model to simulate, with high spatial and time resolution, electrical phenomena that occur at the skin surface of a muscle and relate to the recruitment of important MU number with reasonable computing cost using the proposed programming paradigm. However, computation strongly bears on the use of multidimensional Fourier transforms to speedup simulations. One limitation of this use is the possible appearance of artifacts due to the periodicity effect in the Fourier transform in both spatial and time domain. This is the reason why MU positions were constrained in an angular interval $\left[-\frac{\pi}{2}+\frac{\pi}{10},\frac{\pi}{2}-\frac{\pi}{10}\right]$ smaller than $\left[-\frac{\pi}{2},\frac{\pi}{2}\right]$ to avoid this problem. Similarly, some artifacts also appeared in the time representation of the obtained signals for the same reason. This limitation has to be overcome in the next model version.

In addition, the proposed model should be enhanced by incorporating a procedure to save/load data of 2D Fourier representations of electrical activity for a specific anatomy and MU configuration. Thus, the HD-sEMG signals should be obtained faster by matrix multiplication with a specific Fourier representation of recruitment pattern for a specific stored muscle anatomy without regenerating the 2D Fourier representations of the all corresponding SFAPs. For this purpose, two simulations was performed with and without saving the 3D Fourier representations of MUAPs. Precisely, simulations have been run with 50 MUs at 2048Hz. Firstly, a simulation on 2 processes lasted 55min30s, MUAP Fourier maps were saved during this simulation. Then, the same simulation has been

run loading these maps and lasted 1min06s on serial (one thread) and provided the same signals as the first simulation.

The reuse of saved MUAP Fourier maps can be clearly useful in order to make up the HD-sEMG signals in a, by far, less time. However, it will freeze the computation of the electromyographical signals to a specific muscle configuration and discretization (muscle anatomy, time and spatial sampling frequency). Moreover, this use needs high storage capabilities. Indeed, for the previous simulation, the 50 MUAP frequency maps need for storage about 10GB on the hard drive. One can easily imagine the important requested space for hundreds of MUs for one anatomy.

In this study, we also tried, with the presentation of the numerical implementation of the model, to provide to users a methodology for efficient programming using recent tools as Python language and multiprocessor programming. These computing technologies offer interesting abilities for programming complex models linked to physiological processes. We foresee a generalization of their use and the rising of new model generation that combines both realistic behavior (patient-specific) and optimized computing. Such models, as in electromyography, will certainly help scientists and clinicians to achieve better comprehension and diagnosis of pathology.

2.4 Conclusion

In this study, we proposed a fast model which can simulate accurate HD-sEMG signals generated from electrical propagation inside a three layered conductor volume. Thanks to optimized and modular programming that rely on object-oriented language (Python) and parallel computing, the proposed model is able to compute several configurations within acceptable computing time.

In fact, all the complex calculus involved in the proposed model are done in the Fourier domain. In addition, a high resolution potential map at the skin surface is generated for each time step of simulation. This important characteristic supports the possibility of post-computing of sEMG signals, using numerical surface integration, for any combination of electrode number and shape for the same simulated muscle anatomy. To assess the model abilities, several simulations have been run that illustrate the available electrode shape diversity (concentric-ring, circular and rectangular with rounded corners shapes) and the efficiency of the parallel computing strategies (used processor number) in reducing the computing time in a significant manner. These simulations are in agreement with previous published works. Furthermore, both detection volume and accuracy of the numerical integration operation, comparing to the use of analytical transfer function, have been assessed.

Finally, for illustrating the model efficiency, a large scale simulation concerning 256 electrodes and a muscle that contains 300 MU for 12s (sampled at 4096 Hz) and representing 3 different isometric contractions is realized in less than 15 hours. However, some limitations of the model should be overcome in future works as artifacts generated by Fourier periodicity property in both time and space domain. Also, it should be interesting to save/load 2D electrical MUAP representations to constitute a muscle library which would accordingly further put down the computing time.

Nevertheless, some studies such as global sensitivity analysis or inverse problem that are very useful for clinical applications cannot be performed since it requires thousands of simulations for a specific muscle definition to have consistent results. As previously

depicted, the main time consuming part of the sEMG signals generation models is the hundreds thousand of sources to compute. With a view to using this model for clinical diagnosis and better understanding of the neuromuscular system, we need to reduce this computation time of the model.

2.5 Speedup computation of HD-sEMG signals using a motor unit specific electrical source model

The modeling of surface electromyogram (sEMG) generation is of great interest in many applications especially for understanding how specific physiological mechanisms and phenomena can influence the generation process under various contexts. It can also help researchers and clinicians in the interpretation of experimental sEMG data in pathological situations. Various sEMG models have been proposed since the late 70's [85, 7, 107, 10, 109, 40, 14, 113, 114, 11, 86] and particularly during the last decade. Simulating sEMG signal implies different stages starting by the modeling of the Motor Units (MUs) recruitment [20]. Afterwards, the description of the fiber Intracellular Action Potential (IAP) [31] must be described. Then, there is the volume conductor filtering step [85, 10]. Finally, the sEMG signals are obtained after the individual or multiple surface electrodes recording stage [7, 10]. Modeling all these steps of the generation process provides a bio-reliable model that is faithful to the human neuromuscular physiology and physics. Moreover, the variabilities among skeletal muscle properties have to be considered in the modeling which will add complexity but makes the model more reliable. This type of model provides an important insight into physiological processes that are hard to investigate in experimental conditions. Nevertheless, due to the high complexity of the electrical phenomenon, the model computation time is long. This problem prevents the use of these models in certain applications and studies such as the inverse problem related to the identification of the parameters. This is the reason why nowadays, most of the existing models only focus on the properties of few Motor Unit Action Potentials (MUAP) recorded by a single electrode. According to [10, 6], the use of these intricate models to study the impact of specific input parameters on the sEMG generation seems genuinely hard and lengthy [47]. This high computation time comes from the significant number of electrical sources to compute in order to generate the sEMG signals. These sources are simulated at the fiber scale. Thus, hundreds of thousands of fiber sources have to be computed. This leads to several hours or days of computation even when parallel computing and optimization are used to significantly reduce the computation time [10]. In [10], we performed a simulation of 300 MUs ($\approx$ 52200 fibers) for 12s of contraction at 4096 Hz in $\approx$ 15h. However, in this model, we significantly optimized the computation time by setting all the computation in a 3D Fourier domain and using parallel computing.

To overcome this modeling issue, we propose in this study an upscale computation of the MUAP that can significantly reduce the model computation time. In the literature, there is no research that attempted to reduce the MUAP modeling time. However, in [73], the authors underlined that the MUAP is not equal to N times the corresponding FAP wave shape. In this study, a generic method is presented to compute a single electrical source at the MU scale specifically to the fibers composing it. This macro electrical source generation will be adapted according to the fiber properties belonging to the MU (see section 2.5.1). In fact, modeling the electrical source at the MU scale will remarkably reduce the computation time of the model. However, it will also induce some errors in the

generated signals due to the approximation process. The main challenge of such modeling is to preserve the bio-reliability of the model, variability as well as realism.

One of these modeling error that will arise from this simplification are extinction synchrony of the source at the MyoTendinous Zone (MTZ). However, a MU specific temporal frequency filtering over the MUAP is proposed in order to remove the high frequencies induced by this synchrony. Using this MU source approximation, global sensitivity analysis over the whole physiological parameters as well as inverse problem studies will become feasible in short computation time and with minimal alterations on the sEMG statistics and spectral content (see section 2.5.1).

In order to assess the efficiency as well as the accuracy of the proposed MU macro electrical source, we present in section 2.5.2 comparisons including single MUAP as well as sEMG simulations involving hundreds of simulated MUAPs. This section is concluded by a comparison of the computation time using the two different electrical sources models. Next, the abilities and limitations of the proposed model are discussed (see section 2.5.3). A final section (see section 2.5.4) concludes and brushes over the perspectives of futures works.

2.5.1 Macro-scale motor unit electrical source

Simulating the electrical activity of the muscle implies the computation of all the recruited fiber current density sources as described in previous subsection (see section 2.2.3), thus hundreds of thousands fiber electrical sources have to be computed leading to several hours or days of computation. Since the model computation time is too long, global sensitivity analysis study of all the input parameters of the model or parameters identification to develop new diagnosis tools for clinicians or researchers aren't feasible. In order to overcome this complex modeling issue, we propose, through an upscale computation of the electrical source, to significantly reduce the model computation time.

As introduced in chapter 1, the Motor Unit Action Potential (MUAP) is the sum of its corresponding Single Fiber Action Potential (SFAP) innervated by the same α-motoneuron. Yet, a MUAP of a specific MU composed of N fibers is not simply N times the SFAP wave shape [73]. The anatomical and physiological differences between individual fibers have a strong impact on the spatial and temporal properties of the generated MUAP. In this context, anatomical regions such as the NeuroMuscular Junction (NMJ) position, both MyoTendinous Zone (MTZ), relative positions of muscle fibers within the MU and the location of corresponding MU within a muscle are all significant and have to be considered in any attempt of upscaling (from fiber to MU) the electrical source.

Source positioning

For this purpose, we propose a specific modeling of the MU electrical source based on its fibers. Initially, considering the position of the MU macro electrical source, we decided to place it at the isobarycenter position of the fibers within the MU. This assumption is motivated by the fact that the positioning of the MU macro electrical source is strongly dependent on the distribution of its fibers within the MU area. Examples of the isobarycenter position compared to the initial referenced position of the MU and its fibers are exhibited on Fig 2.13. We can see that the referenced center of the MU is different from the computed isobarycenter. Thus, polar position of the MU macro electrical source

center of the ith MU is determined as:

$$\begin{cases} \rho_i &= \frac{1}{N_i}\sum_{j=1}^{N_i}\rho_{i,j} \\ \theta_i &= \frac{1}{N_i}\sum_{j=1}^{N_i}\theta_{i,j} \end{cases} \tag{2.47}$$

Where $\rho_{i,j}$ and $\theta_{i,j}$ are the corresponding polar coordinates of the fiber j within the i^{th} MU.

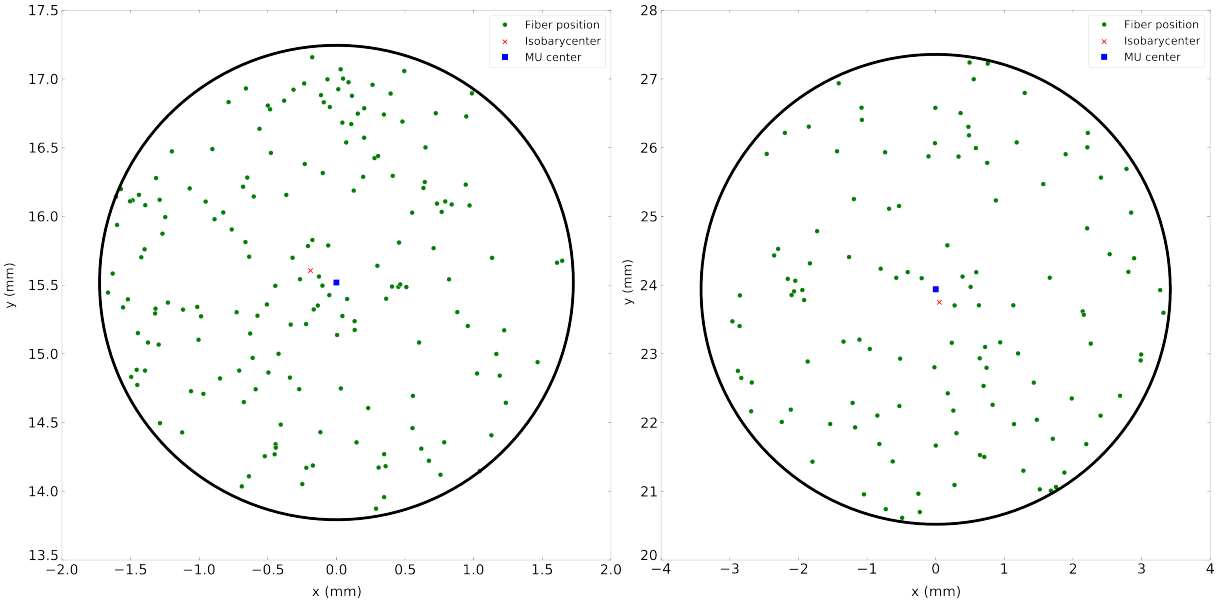

Figure 2.13: Two different isobarycenters computed for the MU macro electrical source model based on the fibers position within the corresponding MU.

Source description and parametrization

Furthermore, as mentioned above, all the parameters describing the fiber have to be considered. Depending on its fibers, the position of the NMJ for the MU specific macro electrical source is computed from the average position of the NMJ fibers following the distribution presented in Table 2.8. Similarly, the position of both MZT and the electrical source conduction velocity are obtained from the average of the fibers MTZ positions and conduction velocities respectively, as indicated in the equations below.

$$\begin{cases} NMJ_i &= \dfrac{1}{N_i}\displaystyle\sum_{j=0}^{N_i} NMJ_{i,j} \\ MZT_{L_i} &= \dfrac{1}{N_i}\displaystyle\sum_{j=0}^{N_i} MTZ_{L_{i,j}} \\ MZT_{R_i} &= \dfrac{1}{N_i}\displaystyle\sum_{j=0}^{N_i} MTZ_{R_{i,j}} \\ v_i &= \dfrac{1}{N_i}\displaystyle\sum_{j=0}^{N_i} v_{i,j} \end{cases} \tag{2.48}$$

Where, $NMJ_{i,j}$ is the NMJ position of the fiber j in the ith MU, $MTZ_{L_{i,j}}$ and $MTZ_{R_{i,j}}$ are the fiber corresponding MTZ from left and right side of the muscle, $v_{i,j}$ corresponds to the conduction velocity of the fiber and N_i is the number of fibers within the ith MU.

Table 2.8: Anatomical MU parameters

Parameter	Value (unit)
MU NMJ position z_{UM} (in z coordinate)	$\mathcal{U}$(-10,10) (mm)
Fiber NMJ position z_{0f} within MU (in z coordinate)	$\mathcal{U}(z_{UM}-5, z_{UM}+5)$ (mm)
Fiber MTZ left length MTZ_{Lf}	$\mathcal{N}\left(-\frac{L}{2}+15, 2\right)$ (mm)
Fiber MTZ right length MTZ_{Rf}	$\mathcal{N}\left(\frac{L}{2}-15, 2\right)$ (mm)

As we considered the isobarycenter and the average of the fiber parameters, the MU macro source current density is represented as N_i times the current density defined in (2.7).

The MU macro electrical source model will induce a synchronization of the fibers sources during the generation, propagation and extinction. This artificial synchrony at the time of action potential extinction leads to a sharper Non-Propagating Component (NPC) (see Fig. 2.15) compared to the one modeled at the fiber scale (see section 2.5.2). This difference in the NPC shape distinctly appears on the MUAP. The smoothing (low-pass filtering) of the NPC of the MUAP is principally due to the jitter effect (delay dispersion from asynchronous extinction) among all the fiber NPCs. After analyzing the temporal spectral content of the MU macro electrical source action potential, we observed that this sharper NPC is mostly represented in the high frequencies. Thus, in order to remove it and make the proposed MU macro electrical source approximation more realistic, we propose to filter the spectral content of the generated MU macro source action potential. This will be done using a MU specific filter, defined in frequency domain, in order to smooth the high frequencies of the MUAP corresponding to the NPC without altering the low frequencies representing the generation and propagation of the MUAP (see eq (2.49)).

$$MUAP_{fil}\left(k_t, k_z\right) = \mathcal{F}^2\left(MUAP\left(k_t, k_z\right)\right).\Lambda\left(k_t\right) \tag{2.49}$$

With MUAP_{fil}, the MUAP spectral representation computed after filtering in frequency domain, $\mathcal{F}^2$ is the 2D Fourier transform applied on the current density defined in eq (2.7) with the macro electrical source parameters and $\Lambda(k_t)$ is the filter that will be define below. $k_t = 2.\pi.f_s$, with f_s the sampling frequency, and k_z is the longitudinal angular frequency.

Considering the design constraints on the filtering operation presented above, we decided to use a Gaussian filter with its standard deviation (σ_{MU}) tuned by several parameters of the macro electrical source.

$$\Lambda_i\left(k_t, \mu, \sigma_{MU}\right) = e^{-\frac{(k_t-\mu)^2}{2\sigma_{MU}^2}} \tag{2.50}$$

With, k_t is the angular temporal frequency, μ is the mean (here it will be 0) and σ_{MU}, the std of the Gaussian distribution that will tune its low-pass filtering behavior.

σ_{MU} was determined through several steps. At first, following an identification procedure, we performed various simulations on the same MU with the fiber source model at different depths where we only changed one parameter that we suspected to have an effect

on σ_{MU} (namely, the macro electrical source conduction velocity v_{MU}, the muscle layer radius ρ_m, the number of fiber within the MU nbF_{MU} and the MTZ dispersion σ_{MTZ}). Then, we computed the same simulations with the macro electrical source by numerically optimizing σ_{MU} according to the MU depth. The final objective was to find the suited function of σ_{MU} related to the MU parameter set that better mimics the referenced MUAP computed with the fiber electrical sources.

Since the MUAP is represented in spatio-temporal domain (θ, z, t) [10] (see section 2.2.6), an optimization procedure of σ_{MU} was performed in order to minimize the Normalized Root Mean Square Error (NRMSE) between the spatio-temporal MUAP generated with the fiber and MU electrical models during one MUAP propagation time (see eq (2.51)). This optimization was done using the Nelder-Mead algorithm [115] available in the Python SciPy package where the tolerance error was set to 10^{-6}. This procedure was repeated for each MU depth varying between 20 and 44 mm with a step of 1 mm. Thus, 24 optimizations for each MU type were performed to find the optimal curve. This curve is depicted in Fig. 2.14.

$$NRMSE(MUAP, MUAP_{fil}) = \frac{\sqrt{\sum_{i=1}^{M}\sum_{j=1}^{N}\sum_{k=1}^{P}\left(MUAP(i,j,k) - MUAP_{fil}(i,j,k)\right)^2}}{\sqrt{M.N.P}.\left(max(MUAP) - min(MUAP)\right)} \tag{2.51}$$

With, $MUAP_{fil}$ and $MUAP$ are the spatio-temporal MUAP representation computed with the MU and fiber electrical source models, respectively. M, N and P are the considered number of samples in the transversal direction, longitudinal direction and in time during the MUAP propagation, respectively.

By analyzing the optimized σ_{MU} values with respect to different MU parameters variation, we noticed that these parameters have only an effect on the magnitude of the σ_{MU} values. We also concluded from this analysis that the relationship between σ_{MU} and the MU depth is nonlinear (see Fig. 2.14).

For this purpose, we tried to propose some nonlinear relationship models to fit the trend obtained by the optimization procedure (Fig. 2.14). As a first attempt, we proposed to use a 2^{nd} order polynomial equation specific to the MU description:

$$\sigma_{MU}\left(v_{MU}, \rho_{MU}, \rho_m\right) = \frac{v_{MU}}{3} + \left(\rho_{MU} - \frac{3\rho_m}{5}\right)^2 \tag{2.52}$$

Where, σ_{MU} is the std used for eq (2.50), v_{MU} (in mm.s^{-1}) is the conduction velocity of the macro electrical source, ρ_{MU} (in mm) the radial position of the isobarycenter and ρ_m (in mm) the muscle layer radius. The formalism of this equation was obtained heuristically after many trials. Nevertheless, this equation wasn't able to consider the major inter-variability existing within MU of the same type [116].

At the beginning, this equation gave good approximation of σ_{MU} when the MU propagation velocity, the MU depth and the muscle radius were considered. However, when we started to consider the effect of the parameters σ_{MU}^{MTZ} and N_{MU}, equation (2.52) was inadequate.

Therefore, considering the shape of the relationship (see Fig.2.14) obtained numerically on 24 depth values of the MU, we decided to use the following Gaussian filter formalism including the suspected parameters that interact in the relationship. After testing different formalism by the evaluation of the obtained trends as in Fig. 2.14, we selected the following equation:

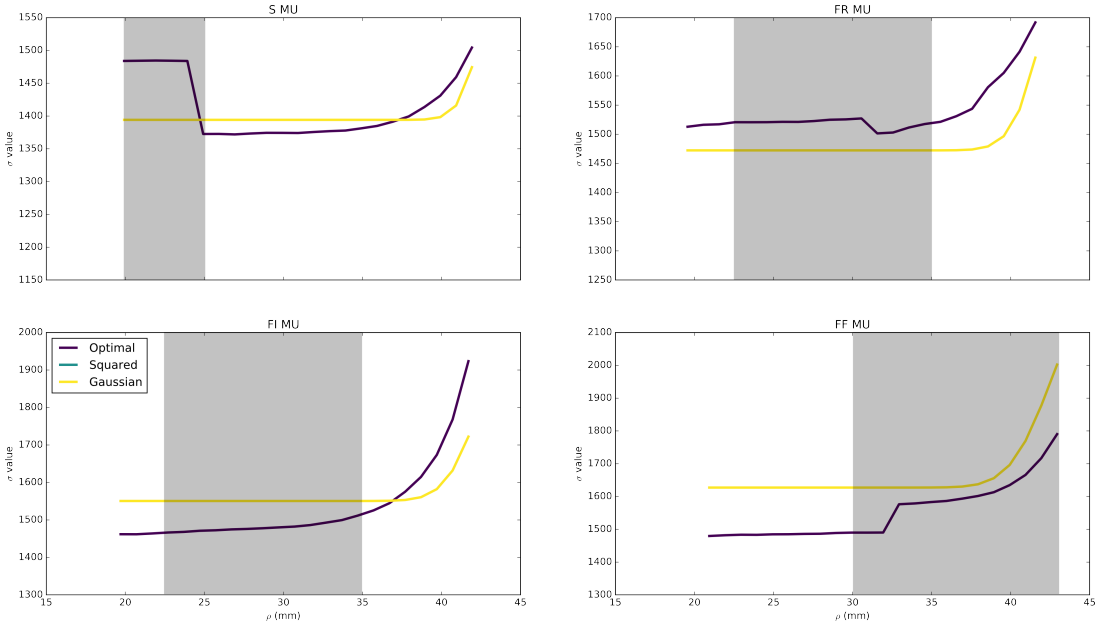

Figure 2.14: Example of σ_{MU} values according to MU type and MU depth computed by the described optimization algorithm (optimal) and equation (2.53) (Gaussian). Grey boxes define the MU physiological position according to its type (see Table 2.13). Areas in white mean that the MU cannot be physiologically placed at this position for a Biceps Brachii muscle. Even though, simulations were computed on all the possible radial position to study the global trend.

$$\sigma_{MU}\left(v_{MU}, \rho_{MU}, \rho_m, N_{MU}, \sigma_{MTZ}\right) = \frac{v_{MU}}{8} e^{-\frac{4 v_{MU}\left(1-\frac{\rho_{MU}}{\rho_m}\right)^2}{9 N_{MU}^2}} + v_{MU}\left(a + \frac{b}{\sigma_{MTZ}}\right) \tag{2.53}$$

Where, σ_{MU} is the computed std used for the filter in eq (2.50), v_{MU} (in mm.s^{-1}) is the conduction velocity of the macro electrical source based on the fibers within the MU (see 2.48), ρ_{MU} (in mm) is the radial position of the isobarycenter (see 2.47), ρ_m (in mm) is the muscle layer radius, N_{MU} is the number of fibers within the MU, a and b are determined coefficient which are equals to $\frac{42.5}{120}$ and $\frac{1}{60}$ respectively. σ_{MTZ} (in mm) is the MTZ dispersion used to define both MZT of the MU fibers.

This equation has been built by analyzing the effect of the 4 parameters: v_{MU}, ρ_{MU}, N_{MU} and σ_{MTZ}^{MU} by considering 3 values for each. Also, the relative position of the MU NMJ has been analyzed but is not considered in this work since it does not seem to have an effect on the temporal spectrum of the MUAP. This spectrum becomes asymmetric but remains centered. Thus, the use of an asymmetric filter can improve the results. But, defining this filter is too complex considering the MU variability. Nevertheless, results presented in section 2.5.2 show satisfying approximation of the MUAP using the formalism of eq (2.53).

2.5.2 Results

Evaluation of the MU electrical source

First part of this section will present some simulations where we will evaluate the efficiency of the methods proposed on single MUAP generation. Second part will present some results computed on the outputs of the model (sEMG signals and statistics) with the two source models presented in sections 2.2.3 and 2.5.1.

Single MUAP

In this part, all the generated anatomies have fixed parameters described in Table 2.9. Concerning the MU and the fibers parameters, they followed the distributions proposed in Table 2.5.

Table 2.9: Configuration of simulation

Parameter	Value (unit)
Muscle length (L)	101.0 (mm)
Muscle radius (ρ_m)	45.0 (mm)
Bone radius (ρ_b)	15.0 (mm)
Adipous tissue thickness	2.0 (mm)
Skin thickness	1.0 (mm)

The gold standard simulations will be the simulations computed with the fiber electrical source model as described in section 2.2.3. The MU electrical source model will be evaluated by computing the NRMSE between the generated spatio-temporal MUAPs according to both electrical source models. To assess the robustness of our MU electrical source modeling, we randomly generated 20 MUs per type using the corresponding distributions presented in Table 2.5. Then, corresponding MUAP is computed with the fiber electrical source and the proposed MU electrical source with and without filtering operation. Results about the NRMSE are presented in Table 2.10. Time support is reduced to the propagation time of the MUAP as well as the angular support which is reduced to the angular propagation of the MUAP.

Table 2.10: Mean NRMSE between the generated MUAP

MU type	Without filtering	With filtering
S	4.29 ± 0.57 %	2.64 ± 0.26%
FR	3.66 ± 0.74%	2.42 ± 0.42%
FI	3.69 ± 0.63%	2.43 ± 0.45%
FF	2.77 ± 0.53%	1.87 ± 0.26%

As we can see in Table 2.10, all NRMSE values are below 5%. However, we can see that mean and std of the NRMSE are lower for all the types of MU with the filtered MU electrical source modeling than without.

On Fig. 2.15, we can see the electric activity, over the time, on one position of the spatial electrical map (it illustrates the results in Table 2.10). The MUAP modeling with

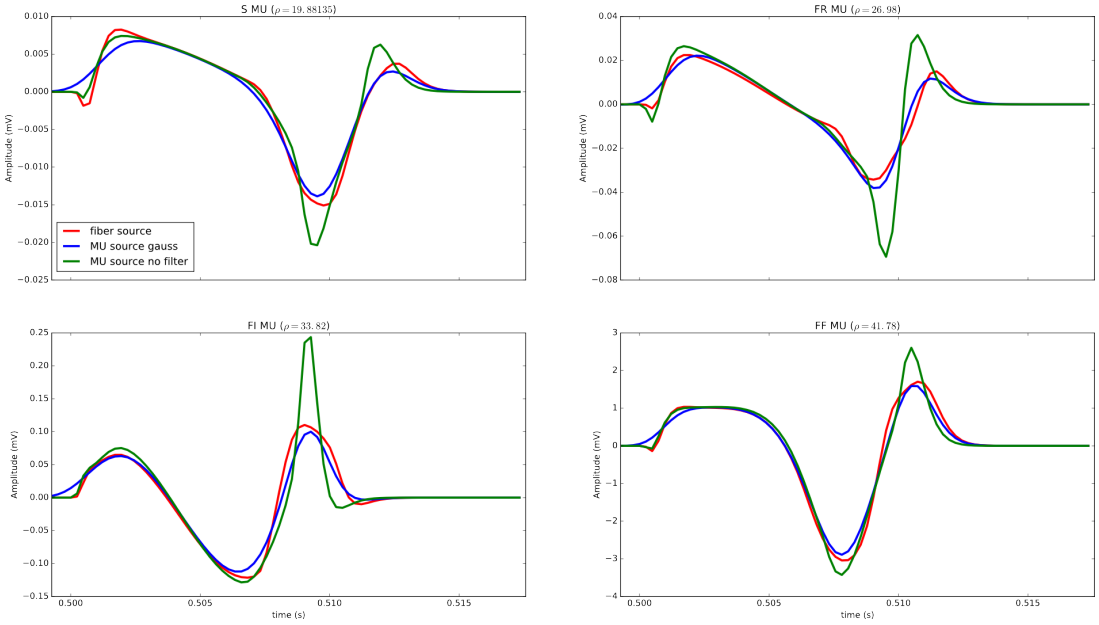

Figure 2.15: Electric time representation of a MU on one position of the spatial electrical map according to the MU type. In red the signal computed with the fiber electrical source model. In blue the signal computed with the filtered MU electrical source model. In green the signal computed with the MU electrical source model without filtering.

a MU electrical source without applying a filter has a sharper NPC than with filtering and should leads to non realistic sEMG signals. As explained before, this issue is due to the synchrony of the extinction of the macro electrical source using the isobarycenter and eq (2.49). One can observe on Fig. 2.15 that the simple averaging operation of spatial and anatomical fiber parameters according to equations (2.47) and (2.48) gives similar propagated component of the MUAP than the classical fiber modeling of the MU electrical source. Moreover, we can see that the signal using a Gaussian filter with its std defined as in eq (2.53) give good results in this simulation configuration. To conclude this section, we can assess for the further simulations that the use of a centered Gaussian filter with its std defined through the equation (2.53) seems to be pertinent to approximate the MUAP with a macro electrical source paradigm.

Simulated HD-sEMG signals

To evaluate the proposed MU electrical source model on a large scale MU recruitment scheme, we decided to simulate HD-sEMG signals over a 8×8 electrode grid and to compute the NRMSE on the recorded signals, on the amplitude statistics (Average Rectified Value, Root Mean Square value and High Order Statistics) and on the estimated Power Spectral Density (PSD) of these simulated signals.

For this purpose, we simulated a potential map of five anatomies defined with 300 MUs ($\approx$ 50000 fibers) at 30, 50 and 70% of the Maximal Voluntray Contraction (MVC) during 4s of holding contraction. The five anatomies are generated with the same parameters, only the MUs positions and definitions changed among the anatomies. For model comparison, simulation parameters and grid position are the same, only the electrical source computation is different between the two simulations. The MU spatio-temporal recruitment scheme is also the same for each simulated muscle anatomy and contraction

level.

Errors are computed as the NRMSE computed between the signals recorded by the same electrode with the two electrical source models as:

$$NRMSE\left(s_f, s_{MU}\right) = \frac{\sqrt{\frac{\sum_{k=1}^{P}\left(s_f(k) - s_{MU}(k)\right)^2}{P}}}{max\left(s_f\right) - min\left(s_f\right)} \tag{2.54}$$

Where, s_f and s_{MU} are the signal recorded by the same electrode with the fiber source and the MU macro electrical source model, respectively. P is the number of time samples (here $P = 4 \times 4096$). Then, NRMSE is also computed between the statistics computed on the same signal with the two source models as:

$$NRMSE_{ST}\left(s_f, s_{MU}\right) = \frac{\sqrt{\frac{\sum_{k=1}^{N}\left(ST\left(s_f(k),k\right) - ST(s_{MU}(k),k)\right)^2}{P}}}{max\left(s_f\right) - min\left(s_f\right)} \tag{2.55}$$

Where, ST is the corresponding computed statistics (ARV, RMS or HOS), $ST\left(s_f\right)$ and $ST\left(s_{MU}\right)$ are the corresponding statistics computed on the same electrode with the fiber and MU electrical source models, respectively. N is the number of electrode (here $N = 64$). Finally, we computed the mean $\pm$ standard deviation of this NRMSE over the HD-sEMG grid. Results are exhibited in Table 2.11.

Table 2.11: NRMSE computed on the signals between the fiber electrical source model and the filtered MU electrical source model, the PSD and the statistics (mean $\pm$ std) over the five anatomies at 30, 50 and 70% of the MVC

	30% MVC	50% MVC	70% MVC
Signals	1.82 ± 0.29 %	1.68 ± 0.37%	1.75 ± 0.29%
ARV	7.14 ± 1.84 %	4.89 ± 2.00%	7.95 ± 2.68%
RMS	6.16 ± 2.37 %	3.59 ± 1.93%	6.99 ± 2.36%
Kurtosis	7.84 ± 1.98 %	5.55 ± 1.21%	7.50 ± 1.21%
Skewness	7.75 ± 2.77 %	6.24 ± 1.65%	9.08 ± 1.98%
PSD	1.01 ± 0.40 %	1.07 ± 0.49%	1.27 ± 0.56%

As we can see in Table 2.11, all the errors computed on the statistics are smaller than 10%. However, this error is a magnitude error and slightly alters the estimated dynamic according to contraction level increase. NRMSE is less than 1% if we computed the NRMSE on the normalized amplitude descriptors as well as on the centered reduced statistic descriptors. It is important to note that HD-sEMG simulated data are not normalized to better estimate the effect of the MU macro electrical source modeling on the HD-sEMG signal amplitude. Using a Gaussian filter will reduced the high frequency and thus smooth the non propagating component. But it will also slightly reduce the power of the overall signal giving less amplitude to the generated MUAPs. One can also observe that the error is more important on statistics based on cumulative measure as ARV, RMS and HOS leading to error increase. But, the statistic descriptor trends according to muscle contraction level remain stable.

In addition to these statistics, Student T-test and Levene test [117] were performed on the descriptors. Student T-test determining if the mean values of the statistics are significantly different exhibits that there are significant differences between the mean

values for each statistic ($p^* < 0.2$). Levene test compares the equality of the variances from the statistics. It shows no significant difference between the variance of these statistics among the grid ($p^* > 0.8$). However, we can deduce that upscaling the source just have a scaling effect on the amplitude descriptors values since we reduce the power of the obtained signals in a homogeneous manner. Compromises have to be found between the signal amplitude descriptors and the Probability Density Function (PDF) shape descriptors. As we can see on Fig. 2.16, the HD-sEMG signals generated don't diverge in their shape along time even if large number of MUs are recruited. We have less precision with the macro electrical source but it is expected by significant reduction of the number of source.

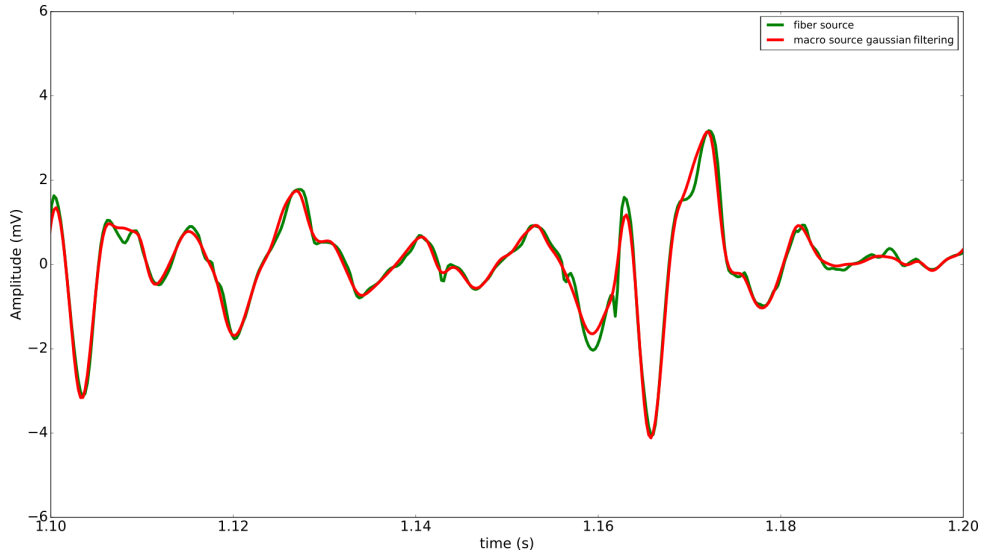

Figure 2.16: sEMG signal observed on a time window (100 ms) and generated at 70% MVC with the two electrical source models recorded on the same electrode.

Related computation time

To conclude the presentation of the results, we performed an analysis of the time computation over the large scale simulations. Three computation time are presented according to the electrical source model used and the number of process.

Table 2.12: Computation time for the five anatomies (mean ± std) at 30, 50 and 70% of the MVC for both electrical source models using serial and parallel configurations

	30% MVC	50% MVC	70% MVC
Fiber sources (with 1 CPU)	38h43min ± 2h9min	63h4min ± 2h45min	88h21min ± 3h51min
Fiber sources (with 10 CPUs)	3h52min ± 13min	6h48min ± 17min	9h51min ± 23min
MU sources (with 1 CPU)	23min27s ± 44s	32min22 ± 57s	39min28s ± 1min7s

According to Table 2.12, computation time of the HD-sEMG signals at 30% MVC using the electrical macro source model corresponds to 1% of the micro source computation time in series and to 11% of the micro source computation time in parallel with 10 threads. At 50% MVC the MU scale electrical source computation time falls to 0.8% of the micro source model computation time in series and to 8% of the parallel computation

time, respectively. Finally, at 70% MVC the MU scale electrical source model computation time represents 0.7% of the serial micro source computation time and to 7% of the parallel computation time. One can observe that both computing time according to a contraction level and computing time increase with contraction level increase are dramatically reduced using the electrical macro source model.

2.5.3 Discussion

In this study, we proposed to model a MU specific electrical source based on the fibers within the corresponding MU in order to significantly reduce the computation time of the HD-sEMG generation models with a reduced alteration of the original MUAP computed with the fiber electrical sources. The use of a MU specific macro electrical source formalism is a novel approach compared to other studies [7, 107, 111] where the MUAP is modeled as the sum of the corresponding FAP. In fact, modeling the muscle electrical activity at the fiber scale is very lengthy. Here we used a cylindrical multilayered analytical model of the limb [10] where the computation is optimized and parallelized. Even though the model is optimized and computes a FAP in 4s, the simulation of the electrical activity of a realistic muscle like the Biceps Brachii (around 240000 fibers [118]) lasts several days. Such computation time does not allow us to perform studies like global sensitivity analysis on the generated signals while varying all the parameters of the muscle or inverse problems where thousands of simulations need to be achieved. However, these studies are necessary for patient-specific modeling to help practitioners in diagnosis purposes or for designing rehabilitation therapies.

From the observation that a MUAP is the sum of the FAPs generated by the fibers innervated by the same motoneuron, we presented a method that estimates a MU specific electrical source according to its fibers. First of all, the position of this macro electrical source is considered at the isobarycenter position of the fiber positions within the corresponding MU. According to the obtained results, this hypothesis seems appropriate given the uniform position of the fibers within the MU. The isobarycenter position will be placed where the fiber density is the highest in the MU area. Also, parameters describing the MU specific electrical source are determined from the average of the parameters of the fibers used to defined their fiber source. Since all the fibers within the MU are different but of the same type and thus are only slightly different, considering the average of the parameters as well as the isobarycenter seem suitable to define a MU electrical source.

The MUAP computed from this MU electrical source has almost similar amplitude and shape compared to the MUAP computed from the fiber sources. However, a problem arises at the extinction of the MU electrical source. In fact, a single source definition corresponds to the synchronization during extinction of the FAPs at the same position and time. It induces significant error on the NPC of the generated MUAP and also on the high frequencies of its spectrum. Based on this observation, we proposed to multiply the MU electrical source with a centered Gaussian filter which preserves the low frequencies of the signal and reduces its high frequencies. The determination of the filter standard deviation needed an identification process. We started to compute the best standard deviation σ_{MU} of the filter according to the MU depth by minimizing the NRMSE computed between the MUAP with the fiber electrical source and the MUAP with the macro electrical source (see Fig (2.14)). This analysis has been performed considering three values of the MU electrical source parameters that we suspected to have an influence on the MUAP spectrum. Some

anatomical parameters such as the adipose and skin thicknesses or conductivity which have an effect on the computed signals [45] are not considered here since their influences have been considered in the conductor volume transfer function definition [10]. Considering the relationship shape relating σ_{MU} with the MU depth, we proposed two nonlinear equations (see eq (2.52) and (2.53)) defining σ_{MU} based on some parameters related to the electrical source. These two equations have been built heuristically after many trials and the observation of the relationship obtained by optimization procedure. According to the shape of the optimal σ_{MU} (see Fig. 2.14), only very complex equation seems to be able to perfectly describe the σ_{MU} variation based on the electrical parameters. Nonetheless, the equation (2.53) gives good and robust approximation and can be improved in future works. Suggesting such a robust and generic equation based on the electrical source model parameters is a complex task. Furthermore, the constant coefficients used in the equation (2.53) can be optimized using a numerical method to minimize the deviation with the optimized σ_{MU} and thus, minimize the computed NRMSE. This study is beyond the scope of this article which focuses on the proposition to model a MU specific electrical source to significantly reduce the computation time of the electrical activity of a muscle without altering the HD-sEMG signal information.

To assess the modeling of this MU specific source, several simulations have been performed. We investigated the effectiveness of the filter by computing the NRMSE between the MUAP generated by the fiber electrical sources and the MUAP generated from the MU specific electrical source with and without filtering. We found that σ_{MU} defined by a Gaussian probability density function better approximates the MUAP than defined by a 2^{nd} order polynomial. Moreover, some simulations investigated the effect of the MU position according to its type and exhibited the significant influence of the radial position of the MU on the error whereas angular position of the MU does not alter the estimation error. Finally, we performed simulations with 300 MUs and an 8×8 HD-sEMG grid at 30, 50 and 70% MVC. Thus, NRMSE were computed over the generated signals, the corresponding PSD and the amplitude descriptors (ARV, RMS and HOS) computed on these signals. All the NRMSE computed using the Gaussian filter and σ_{MU} from eq (2.53) are lower than 10%. Moreover, using the MU specific electrical source radically reduces the computation time of the electrical activity of the muscle. In fact, computation time is reduced about 10 times compared to the computation using the fiber sources even with parallel computing. However, studying single MUAP generation should continue to use the fiber sources model in order to have more accurate results if needed. Computation of the single MUAP with the fiber sources model lasts around 15 min and thus, is still reachable. Finally, the proposed MU specific electrical model seems to be relevant in designing large scale simulations (number of MUs and number of simulations) to fulfill to a better physiological realism. It will open the door to global sensitivity analysis and identification applications that are needed to design patient-specific neuromuscular model and more effective signal processing tools.

2.5.4 Conclusion

In this study, we presented a MU specific electrical source based on the fibers composing the MU which significantly speedup the computation of the HD-sEMG generation model. Previously, a MUAP was computed as the sum of the FAP generated by its fibers. Due to the high computation time induced by the large number of fibers within a single muscle, we proposed to compute this MUAP using a single electrical source defined on

the fibers arranging the corresponding MU. Thus, placement of this source is determined as the isobarycenter of the fibers in the MU. Moreover, MU electrical source parameters are defined as the mean of the fibers parameters. Some rough approximation induced by the modeling of a single source such as the synchronization of the electrical source extinction has been considered. In order to overcome this major issue, we proposed to apply a MU specific Gaussian filter to the corresponding MUAP in the Fourier domain. This filtering will reduce the temporal high frequencies in the MUAP spectrum related to the NPC and preserve the energy in the low frequencies related to the propagating component. Thus, the synchronized NPC is smoother but the signal amplitude will also be slightly reduced. However, NRMSE computed between HD-sEMG simulations using the two sources methods exhibited an approximation error less than 2% on the simulated signals, a magnitude deviation on the amplitude and statistic descriptors less than 10%. Then, considering the computed errors with the MU specific electrical source compared to the significant time-saving on the computation time (at least 99% of time reduction compared to the fiber sources computed using one CPU), we definitively believe that this study will open new possibilities for the HD-sEMG generation model studies. Thanks to this important speed-up in the HD-sEMG computation without altering the signal information, future works can be finally initiated, thanks to the proposed model, to focus on global sensitivity analysis of the HD-sEMG signal generation according to potentially an important number of anatomical, instrumental and neural parameters. When the inverse problem or global sensitivity analysis are considered, thousands of simulations have to be performed to find a stable solution. Since we have overcome the complex modeling of a MUAP from one source to significantly reduce the model computing time by an upscaling procedure, such studies as presented above are reachable and open new perspectives for the use of sEMG generation models to help practitioners for diagnosis purposes.

2.6 Realistic motor unit placement in a cylindrical HD-sEMG generation model

Several sEMG generation models have been developped in order to better understand how the sEMG signal is generated in skeletal muscle [10]. Analytical models describe the muscle in a simple way but allow us the access to electromyographic data corresponding to several physiological contexts and specific motor control strategies that are complicated to evaluate in experimental conditions. Thus, the investigation of the changes of sEMG signal features according to physiological mechanisms and instrumentation parameters are easier and faster with analytical models rather than numerical models [10, 45].

However, none of these models cited above have carefully evaluated the Motor Units (MUs) position within the muscle (see section 1.5.2). The main hypothesis used is the unconstrained uniform distribution of the MUs according to their types [119]. Implementation of this hypothesis has never been presented in details in previous models. Thus, we can assume that some studies used random MUs placement without any other constraints. However, some models adopted a specific fiber density but did not mention how they incorporated it with the MU structure [45, 51].

MU position within the muscle has a huge influence on the generated sEMG signals. In fact, a realistic muscle simulation would insure a constant fiber density in the muscle. If the muscle has a higher fiber density somewhere, it will directly impact the sEMG

signals because of the accumulation of electrical sources in this area. Thus, it may induce artifacts on the amplitude descriptors of the sEMG signals which can lead to inaccurate interpretations of the studied phenomenon.

In this study, we attempt to assess the necessity to use a specific algorithm for the positioning of the MUs. This was done by comparing the anatomies, the fiber density and the Root-Mean-Square (RMS) values map computed over 64 monopolar electrodes using two placement algorithms.

2.6.1 Unconstrained MU positionning

According to Fuglevand model [20], MU territories have circular cross-sectional profiles and are randomly spread with uniform distribution within the muscular area according to the MU type. To mimic the Biceps Brachii muscle, fast and large MUs are placed closer to the muscle surface than slow and small MUs. MU fibers can be mixed with others within the muscle. Moreover, possible MU area superposition is also considered in the model. MU types have different properties. MU radial position follows the distribution described in Table 2.13 without any other constraint. Each random number draw is produced by the random function from the Python package NumPy.

Table 2.13: Radial MU position distribution according to MU type

MU type	Radial MU position
Slow (S)	$\rho_b + \left(R_i + \mathcal{U}(0,1).\frac{\rho_m}{3}\right)$
Fast Resistant (FR)	$\rho_b + \frac{\rho_m}{4} + \mathcal{U}(0,1).\left(R_i + \frac{\rho_m}{2}\right)$
Fast Intermediate (FI)	$\rho_b + \frac{\rho_m}{4} + \mathcal{U}(0,1).\left(R_i + \frac{\rho_m}{2}\right)$
Fast Fatigable (FF)	$\rho_b + \frac{\rho_m}{2} + \mathcal{U}(0,1).\left(\frac{\rho_m}{2} - R_i\right)$

where, ρ_b is the bone radius, R_i is the radius of the corresponding i^{th} MU according to its type, ρ_m is the muscle radius and $\mathcal{U}(0,1)$ is an uniform distribution between 0 and 1.

As we can see on Fig. 2.17, even with a high number of MUs within the muscle there is still some space where the fiber density is zero. Those holes in the fiber density will induce some errors on the output signals. For this purpose, we proposed an algorithm that can quickly place the MUs in order to avoid this major issue.

2.6.2 Best Candidate MU positionning

All the models cited in the introduction (see section 1.5.2) didn't carefully evaluate the MUs positions within the muscle. The main hypothesis used is the unconstrained uniform distribution of the MUs position according to their types [119] presented above. Thus, we can assume that some studies used random MUs placement without any other constraints. However, some models adopted a specific fiber density but did not mention how they incorporated it with the MU structure [45, 51]. Recently, Navallas and al. [120] proposed an identification algorithm allowing to control the MU fiber density distributions. This algorithm accurately mimics the muscle architecture. Yet, computation time of this algorithm was not exhibited and then can last several hours to place hundreds of

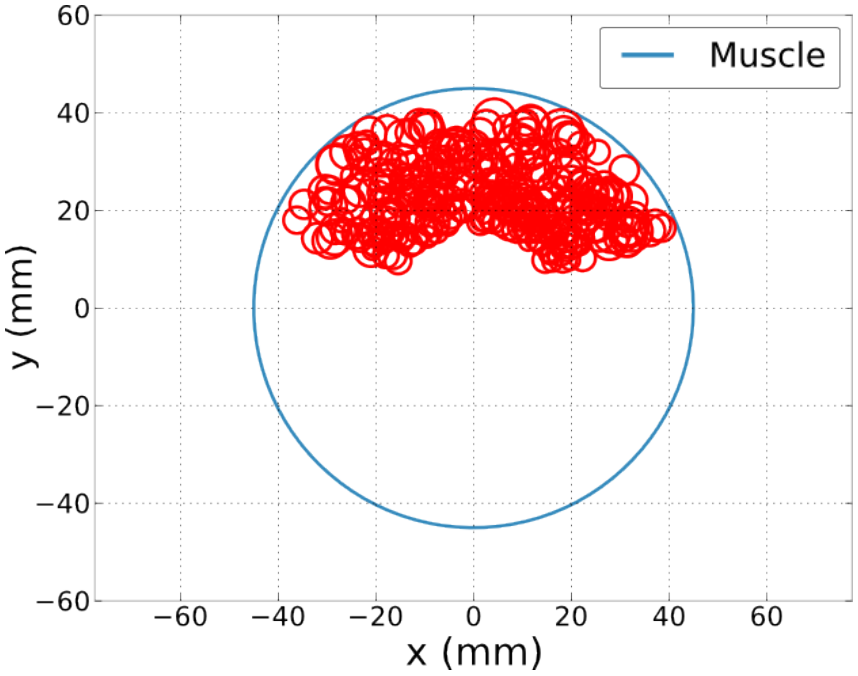

Figure 2.17: Anatomy composed of 300 MUs generated with unconstrained uniform distribution.

MUs. Moreover, this algorithm assumes the same fiber density within MUs that is an oversimplification of the problem. Then, Robertson and al. [121] updated this algorithm in order to consider the relationship between the fiber type and its radial position in the muscle giving more accurate muscle architecture.

We decided to do not use this algorithm in this work since implementation as well as the approach didn't seem suited for the model. Nevertheless, we still considered this major issue in the muscle anatomy definition. For this purpose, we propose an algorithm based on the algorithm proposed by Mitchell [122] named Best Candidate (BC) algorithm.

Compared to the unconstrained random placement of the MUs, the BC algorithm adds a constraint in order to maximize the minimal distance between MUs (see algorithm 1). Moreover as [121], we regionalized the MUs position within the muscle according to their type (see Table 2.13) as suspected in physiological studies [123, 30].

Where, N is the number of MUs within the muscle, N_p is the number of MUs already placed (it starts at 0), (ρ_k, θ_k) is the position of the placed MUs and (ρ_i, θ_i) is the position of the processes MUs.

This algorithm is applied for each non placed MU to ensure an optimal filling of the muscle. Moreover, the MUs positioning order is random, to insure MUs types diversity in each zone.

Compared to anatomy generated with the unconstrained algorithm (see Fig. 2.17), the anatomy generated with the best candidate algorithm has less hole in the fiber density according to the placement of the MUs (see Fig. 2.18). Assessment of the effectivness of this result is provided in section 2.6.3.

input : A muscle with its parameters
output: Positions of all MUs

for $i \leftarrow 1$ **to** N **do**
  $d_m = 2$;
  for $j \leftarrow 1$ **to** 100 **do**
    $d = zeros[N_p]$;
    Draw a position of the MU according to its type $(\rho_{i,j}, \theta_{i,j})$ using Table 2.13;
    for $k \leftarrow 1$ **to** N_p **do**
      $d[k] = \sqrt{(\rho_{i,j}.\cos(\theta_{i,j}) - \rho_k.\cos(\theta_k))^2 - (\rho_{i,j}.\sin(\theta_{i,j}) - \rho_k.\sin(\theta_k))^2}$;
    end
    $d_{min} = min(d)$;
    if $d_{min} > d_m$ **then**
      $(\rho_i, \theta_i) = (\rho_{i,j}, \theta_{i,j})$;
      $d_m = d_{min}$;
    end
  end
end

Algorithm 1: Best Candidate algorithm

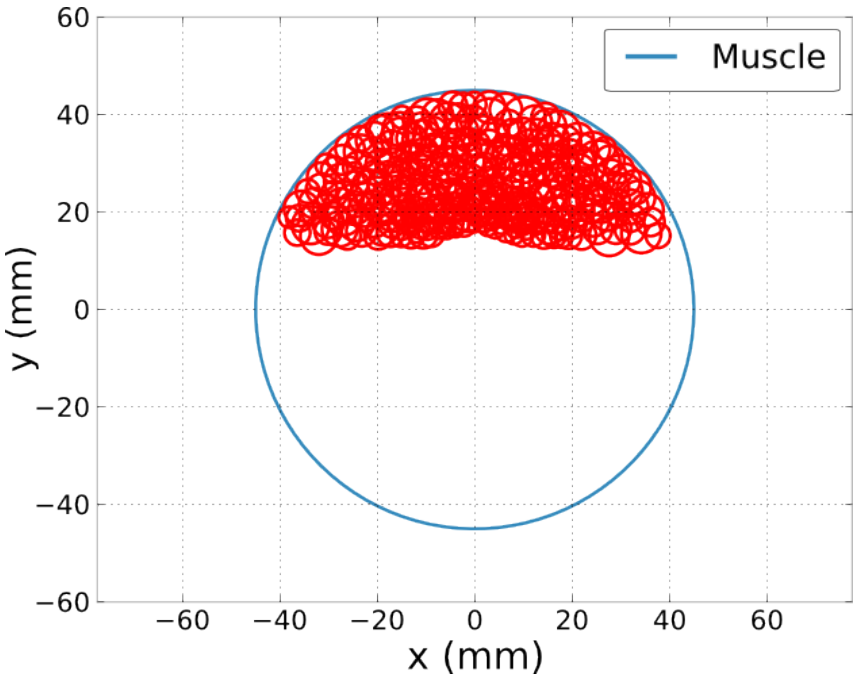

Figure 2.18: Anatomy composed of 300 MUs generated with constrained uniform distribution.

2.6.3 Results

In order to compare the anatomies generated by both algorithms (see section 2.6.1), we will use two indicators: the fiber density within the muscle and a classical amplitude descriptor of the sEMG signals, namely the Root Mean Square value.

For this purpose, we simulate a contraction at 70% MVC for each generated anatomy by both algorithms presented above. Parameters related to simulations are presented

in Table 2.14. Both generated anatomies have the same MUs and fiber properties with same discharge instants. Only the MUs and thus the fiber positions change between both anatomies.

Table 2.14: Configuration of simulation

Parameter	Value (unit)
Number of MUs & fibers	300 & 52313
MU distribution (S, FR, FI, FF)	$(0.33, 0.17, 0.17, 0.33)$ (%)
Muscle radius	41.0 (mm)
Adipose tissue thickness	1.5 (mm)
Skin thickness	1.2 (mm)
Electrode radius	1.0 (mm)
Electrode grid center (θ, z)	$(0, 26)$ (^{o},mm)

Fig. 2.19 shows the fiber density distribution in the muscle. By comparing the two anatomies, we can clearly emphasize the necessity to use a realistic placement algorithm at least for the MU position. On Fig. 2.19a, fiber density is (mean ± std ; [min;max]) 28 ± 20 ; [0;110] fibers.mm^{-2} whereas fiber density with MBC algorithm is 28 ± 16 ; [0;75] fibers.mm^{-2} (see Fig. 2.19b). Normally, fiber density should be approximately uniform within the muscle [119]. With parameters from Table 2.14, muscle area defined by both anatomies is 1853.056 mm^2 with 52313 fibers. Thus, perfect fiber density should be equal to 28 fibers per mm^2 with a small standard deviation. Fiber density mean is the same for both, but this is logical since there is the same number of fibers within the same muscle area. However, as expected, the standard deviation of the MBC anatomy is significantly lower than the random anatomy (-25%). Physiologically, this standard deviation should be small in order to have a realistic distribution. Moreover, maximum number of fibers in 1 mm^2 is also lower with the MBC placement than the random placement (-32%). This maximum should converge on the mean fiber density. However, compared to simple unconstrained random positioning, fiber density is homogeneously distributed with MBC algorithm.

For those two anatomies, 64 HD-sEMG signals have been generated at 70% MVC. Fig. 2.20 represents the RMS values maps computed over 4s plateaus for both simulated and experimental HD-sEMG signals. Both grid are aligned along the longitudinal axis z with respect the with the muscle fiber orientation within the muscle. Axis θ represents the angular orientation. Here again, it clearly underlines the necessity to use realistic algorithm for the MU placement. In Fig. 2.20a, the computed experimental RMS value map is obtained from the mean RMS value map of the Biceps Brachii from 5 healthy subjects (age: 27.2±1.3 years; stature: 176.8±5.1 cm; mass: 73.8±7.3 kg) respecting the declaration of Helsinki. All participants provided their written consent and did not relate any history of muscular or neurophysiological problem at the upper limbs. We followed the HD-sEMG recording procotol described in [6], electrode grid has been placed 1 cm above the Biceps NMJ. Final observation on Fig. 2.20a is about the homogeneity of the RMS value map. Experimental RMS value map (Fig. 2.20a) is homogeneously spread on the electrodes with a slight increase on the electrodes next to the NMJ. In order to compare the RMS value maps, they have been normalized by their maximum RMS value. Mean normalized RMS value on all the electrodes is about 0.82±0.06. On the MBC RMS value map (Fig. 2.20b), RMS value is also homogeneously dispersed on the electrodes

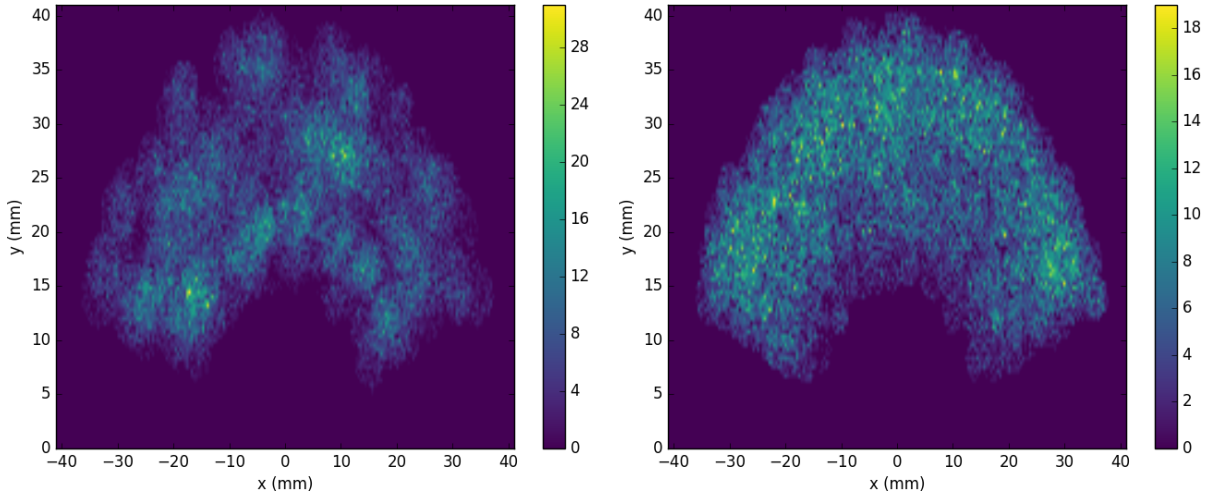

(a) Fiber density using the unconstrained uniform algorithm.

(b) Fiber density using the best candidate algorithm.

Figure 2.19: Fiber density by both algorithms and fibers histograms in ρ and θ axis. Each case is about 0.1681 mm^2.

but with a decrease at the halfway between neuromuscular junction and myotendinous junction. Mean normalized RMS value on all the electrodes is about 0.79±0.09. On the uniform RMS value map (Fig. 2.20c), RMS value is heterogeneously distributed on the electrodes. Mean normalized RMS value on all the electrodes is about 0.64±0.16. A Student's t-test has been performed between experimental and both simulated normalized RMS amplitude value. We obtain $p* = 4.0.10^{-12}$ and $p* = 0.035$ for experimental/random and experimental/MBC couple, respectively. Thus, we observe more significant difference with the random placement than with the MBC placement, according to experimental data and visual observation on the RMS value maps.

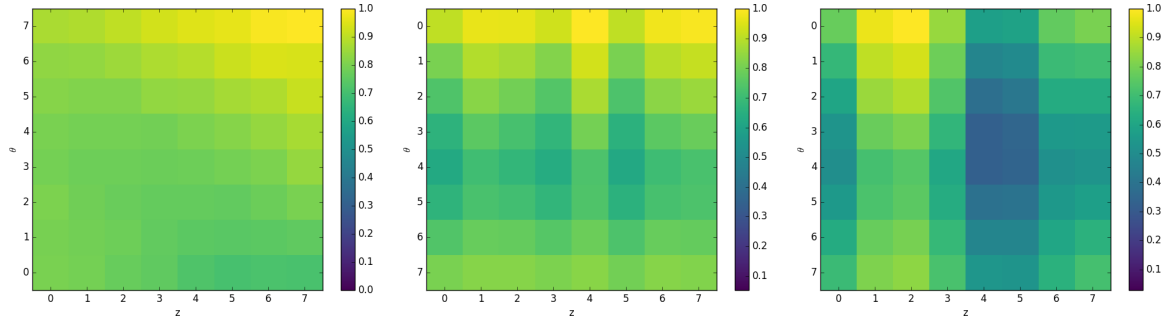

(a) Experimental RMS values map.

(b) RMS values with the best candidate placement algorithm.

(c) RMS values map with the unconstrained uniform algorithm.

Figure 2.20: Normalized experimental and simulated RMS values map on the 64 electrodes at 70% MVC.

To conclude, using the best candidate algorithm for the positioning of the MUs provides more realistic simulation of the muscle contraction. A particular focus needs to be on the fibers and MUs placement in the muscle. We have shown that MU positioning is crucial in HD-sEMG signal simulation. In fact, statistics computed from the sEMG

signals are used in several cases: the force estimation [121, 57] or the decomposition of the sEMG in order to identify the MUs recruitment pattern for the sources detection [124]. If the signals are not generated respecting physiological realism, it can alter these statistics and their interpretation.

2.6.4 Conclusion

The objective of this study was to assess the use of a realistic algorithm in sEMG modelling for the position of the MUs within the muscle. According to the obtained results, the trivial hypothesis to use an unconstrained random algorithm for the MU positioning is not sufficient. In order to simulate realistic contraction of a muscle, several parameters need to be tuned according to the muscle anatomy. However, most muscles have a homogeneous fiber density [119]. A particular focus needs to be on the fibers and MUs positioning in the muscle. We have shown that MU positioning is crucial in HD-sEMG signal simulation. In fact, statistics computed from the sEMG signals are used in several cases: the force estimation [125], the decomposition of the sEMG in order to identify the MUs recruitment pattern for the sources detection [124], etc. If the signals are not generated respecting physiological realism, it can alter these statistics and their interpretation. For this purpose, we presented an automatic optimized algorithm for the MUs position within a muscle providing more realistic muscle anatomy. It can be applied on the fiber positions in order to have an almost homogeneous fiber density but will last several hours. In future simulation studies, this algorithm should be used instead of the random unconstrained positioning in the HD-sEMG signal generation process.

2.7 General conclusion

This part of the thesis work aims for proposing a bio-reliable model of the skeletal muscles that can help researchers as well as practitioners. For this purpose, we developed a fast model that can simulate accurate HD-sEMG signals generated from electrical propagation inside a three layered cylindrical conductor volume. All the main stages of the muscle electrical activity generation are considered, from the motoneuron pool model describing the firing instants of the recruited MUs, the spatio-temporal electrical sources description generated by the muscle fibers, to the filtering of these sources by the conductor volume. Thanks to optimized and modular programming that relies on object-oriented language (Python) and parallel computing, the proposed model is able to compute several realistic muscle configurations within acceptable computing time.

In a first time, we developed a model where all the complex computation were performed in the Fourier frequency domain. Moreover, compared to the literature of sEMG signals generation, we proposed to disconnect the muscle electrical activity and the recording system. This decoupling allows us to define an infinite number of electrode grid for the same electrical activity without computing again this one.

Nevertheless, computation time of the model was too long when bio-reliable simulation of muscle contraction was considered. This way, some model analysis such as global sensitivity analysis or inverse problem aren't reachable. This high computation time was induced by the large number of fibers within the muscle leading to the computation of hundreds of thousands electrical sources representing several hours of computation to provide the simulation. For this purpose, we presented a MU specific electrical source based on the fibers composing the MU which significantly speed-up the computation of

the HD-sEMG generation model. In the literature [85, 7, 81, 107, 11, 6], the MUAP was always computed as the sum of the SFAP generated by its fibers. Reducing the number of electrical sources to a single one for each MUAP generation induced some alterations on the original signals computed with fiber sources. For this purpose, we propose to filter the frequency MUAP computed with the single source with a MU specific Gaussian probability function. NRMSE computed between HD-sEMG simulations using the two source models (fiber and MU) exhibited an approximation error less than 2% on the simulated signals and a magnitude deviation on the statistic descriptors less than 10%. Even with this deviation, we definitively believe that this study will open new perspectives for the HD-sEMG signal generation model thanks to the important computation time reduction (about 99% compared to fiber source model).

Finally, we proposed an automatic and realistic algorithm that place the MUs in order to have a homogeneous fiber density. In fact, after several simulations we observed a significant impact of the MUs placement within the muscle. In the literature [45, 51, 105], the MUs are placed according to an unconstrained uniform distribution. Using this placement will induce non homogeneous fiber density within the muscle even if high number of MUs is considered. The proposed algorithm doesn't perfectly simulate a perfect homogeneous fiber density, yet the fiber density estimation with this algorithm gives correct results.

Future works, using this model, are envisaged for realistic simulation of the Biceps Brachii electrical activity for deeper exploration of the relationship between recent sEMG amplitude descriptors, extracted from HD-sEMG signals, and muscle activation (see Chapter 4). In addition, data generated by the proposed model should be used as reference one, e.g. for faster solutions for solving related inverse problems as electrical source localization. To conclude, we believe that the proposed fast, reliable and generic model should help researchers to perform more realistic multichannel sEMG simulations with large configuration possibilities using a workstation at a reasonable time and financial cost.

Chapter 3

Mechanical multiscale modeling of the skeletal muscle

Contents

3.1 Introduction

From the middle of the 19^{th} century until now, researchers attempted to better understand how the motion of the human body is generated. They found that the movement is the result of several interactions between complex mechanisms in the body [126]. At the macroscopic scale, the muscle contraction is in charge of the movement through the joints. In fact, during contraction the muscle length shortens and thus will stretch the connected tendons to provide the movement of bones around a specific joint.

Thus, several studies have been focused on the understanding of the activation [127, 128, 129] and the mechanical phenomena of the muscle contraction [8, 12]. Due to the complex feasibility to study the human muscles in vivo, the muscle needs to be described through mathematical model. These models can help us to get a better understanding of the motor control and the different mechanisms of the muscle contraction. Moreover, by controlling all the parameters of the model, users can investigate precisely the impacts of the phenomena on the outputs of the model to simulate physiological or pathological conditions.

Modeling of the muscle contraction has been widely developed and used [8, 12, 27, 96, 9]. These models can be separated by the scale and the approach considered. The phenomenological macroscopic models are governed by Hill-Maxwell or Hill-Voigt models, inherited from the Hill model [8], which is generally credited as the first model describing the muscle contraction. The Hill models describe a muscle as an active contractile component with series and parallel passive elastic components. Furthermore, the author considered the muscle as a visco-elastic material and thus, described the well-known force/length relationship of the muscle. Yet, this systemic macroscopic model is often described as a "black-box" driven by fitted non-physiological parameters. Some models integrate after the pennation angle of the muscle with the tendon [27] and macroscopic features of the muscle. Beside these models, some biochemical microscopic models were developed. The most widely used is the model proposed by Huxley [12] who considered the muscle at the sarcomere scale. The authors proposed an interpretation of the cross-bridges dynamic through mathematical equations and attempted to determine the muscle force from the rates of attachment and detachment of these cross-bridges. From these two classes of muscle models, Zahalak proposed a model that bridges the microscopic and macroscopic models [96]. From the cross-bridges model, the author computed the muscle force through mathematical approximation with the distribution-moment technique [96, 9]. Finally, twitch type model introduced by Coggshall and al. [64] are also used where the authors only described the muscle force as the sum of the convolution operation between the firing times of the Motor Units (MUs) and a function defining the MU twitch. This type of model doesn't consider the induced muscle deformation or the underlying processes arising between the recruitment and the force generation.

All these models provided some information about the muscle contraction and brought crucial knowledge about the muscle rehabilitation and control. However, models other than twitch models have an issue about the muscle activation. Hill-type models use an identified parameter input enclosed in $[0; 1]$ interval representing the activation percentage of the muscle. This parameter has no physiological meaning and is hard to experimentally estimate. Other models attempted to give a sense to this activation parameter through the Functional Electrical Stimulation (FES) [9, 129, 130] where this parameter represented the percentage of muscle fiber recruited during stimulation. Yet, the recruitment pattern induced by FES does not follow voluntary contraction [130]. It reverses

the natural sequence, larger MUs are recruited the first and smaller the last. Also the FES synchronizes the firing times of all recruited MUs whereas the voluntary recruitment pattern is asynchronous. Riener et al [130] attempted to keep the muscle representation at the MU scale. The authors tried to describe the muscle force from the summation of all active MUs. They described the depolarization of the T-Tubule membrane dynamics induced by the neural activation as well as the calcium release from the sarcoplasmic reticulum in order to compute the MUs twitch. This model was the first twitch type model describing physiological processes. Another type of model combining the microscopic sarcomere model of Huxley [12] with the distribution moment theory of Zahalak [96] defined a macroscopic muscle model [9] based on the sarcomere model formalism and avoided the costly computation time model at the sarcomere scale. From the description of the muscle with one contractile element, only one type of fiber can constitute the muscle model. Moreover, the authors also proposed a visco-elastic model describing the muscle-tendon contraction during isometric contraction. This model was validated on both animal and human subjects [9, 129].

Considering the major increment brought by the model proposed in [9], we propose in this study a mechanical model of the muscle based on the previous work of El Makssoud et al. [9]. Instead of using the FES input for muscle contraction, we will use a voluntary recruitment pattern defined in [20] as input. Compared to the original model, the muscle will be represented at the MU scale while it was depicted at the muscle scale. Firstly, we will detail the different models used for the simulation (see sections 3.3 and 3.4). Then, some results showing the efficiency of our model will be presented and discussed (see section 3.5). Finally, we will conclude on the main contribution of this study and on the possible perspectives.

3.2 Model overview

As introduced, the main purpose of this study is to propose a mechanical multiscale modeling of the skeletal muscle driven by a voluntary command. This model would be an improvment of the model presented above [8, 12, 96, 130, 9]. The underlying purpose is also to provide a bio-reliable model which is based on physiological parameters to get significant results. In fact, each MU will be modeled by one specific contractile element placed in parallel to model the whole muscle. Thus, the proposed muscle model is divided into two parts as presented in Fig. 3.1:

- first part represents the activation model of the muscle and gives a physiologic meaning of the input of the mechanical model;
- second part is the muscle mechanical model at the MU scale based on the distributed moment technique inspired from [9].

First challenge of this model was to provide an activation model based on the firing times of the MUs.

3.3 Activation model

Previously, the mechanical model input was the percentage of recruited muscle fibers determined with FES [9]. This input description can't be applied for voluntary contractions

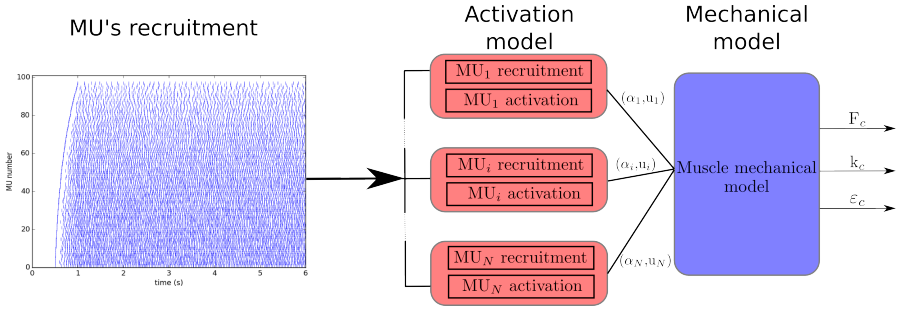

Figure 3.1: Model block diagram. On the left there is the input of the model corresponding to the recruitment pattern describing the discharge instant of the recruited MUs. On the right the mechanical model scheme, determining the contribution of each MUs then, processes at the muscle scale in order to determine the muscle force (F_c), the muscle stiffness (k_c) and its deformation (ε_c).

and thus, restricts the use of this model type. Purpose of this study is to simulate accurate contractile behaviors of the muscle governed by a MU voluntary or elicited recruitment pattern. We based our model development on physiological processes arising during the contraction [130]. Firstly, it is well known that skeletal muscles are composed of four types of fiber and thus, of MU:

- Slow or type I MUs (SMUs) that provide low force with a slow contraction speed and has a high resistance to fatigue;
- Fast Resistant or type IIa MUs (FRMUs) that provide intermediate force, with fast contraction speed and are resistant to fatigue;
- Fast Intermediate or type IIx MUs (FIMUs) that provide intermediate force (more than FRMU), with fast contraction speed and are less resistant to fatigue than FRMU;
- Fast Fatigable or type IIb MUs (FFMUs) that provide high force, with very fast contraction speed but are quickly fatigued.

Each MU type will have its own set of parameters for both activation and mechanical characteristics corresponding to their different properties. As in [12, 130, 9], we considered that the fiber contraction is dependent of the calcium ion (Ca^{2+}) concentration presents in the cytoplasm. From this hypothesis, MUs can be in one of these three states during the muscle contraction: in contraction, in relaxation or relaxed. When a MU is recruited, it will contract during a determined time, according to the Ca^{2+} concentration. If it does not receive a new impulse during the contraction time, the MU starts to be in relaxation according to the Ca^{2+} uptake time. Finally, if it still doesn't receive a new impulse it goes in relaxed state when its Ca^{2+} concentration reaches the concentration at rest. Thus, these states will be defined according to the intracellular Ca^{2+} concentration.

3.3.1 MU recruitment

Voluntary recruitment

During contraction, MUs are recruited independently of others and in agreement with the size principle [131]. Each MU is activated at a specific threshold depicted in the Fuglevand

model [20]. However, Kukulka and Clamann [68] have provided evidence that the distribution of recruitment threshold for larger proximal muscles, such as the Biceps Brachii, is less skewed compared with the exponential distribution of others muscle. Therefore, we decided to use the following equation from [41]:

$$RTE_i = \left(\frac{a.i}{N}\right) e^{i\frac{ln\left(\frac{RR}{a}\right)}{N}}$$

where, RTE_i is the recruitment threshold for the i^{th} MU, N is the total number of MU and $a = 40$ is a constant value describing the slope of the recruitment threshold function [41]. It is also tuned by the recruitment range ($RR = 88\%$ [68]) which describes the percentage when all MUs are recruited in the muscle.

Each MU recruitment is regulated by a motoneuron firing rate (Fr_i) which increases linearly or non linealy with force level, from its minimal firing rate (Fr_{min}) to its peak firing rate (PFR_i). In this model, for each MU, PFR_i is taken inversely proportional to the recruitment threshold for the linear increase of firing rate. This model was previously developed in section 2.2.2 and more details can be found in it.

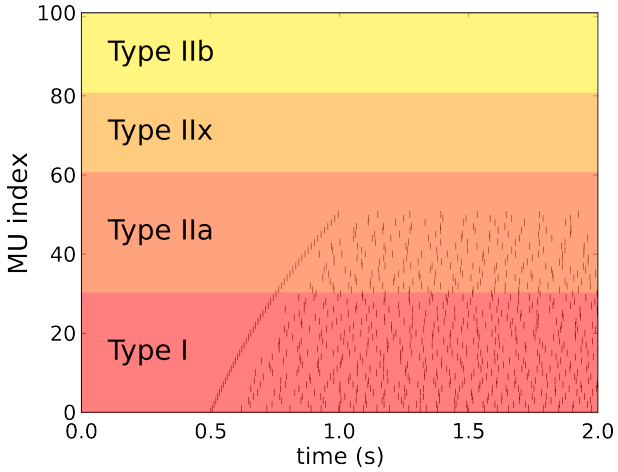

Figure 3.2: Example of simulated voluntary MU recruitment at 30% of the Maximum Voluntary Contraction (MVC) for a muscle composed of 100 MUs with the following MUs distribution type: 33% type I, 33% type IIa, 17% type IIx and 17% type IIb.

Elicited recruitment

In addition to the voluntary recruitment, an elicited recruitment of the MUs simulating a Neural Electrical Stimulation (NES) is also developed in this model. In fact, this type of recruitment is often used in mechanical muscle study to exactly quantify the muscle activation parameter [130, 9]. During a NES, the MUs are recruited synchronously in respect with the diameter size of their motoneuron and the area of electrical spread. Larger motoneurons, representing larger MU radius, are hired first in a descending order [132]. Number of recruited MUs mostly depends on the current intensity and on the pulse width of the NES [127]. The number of contracting MUs is bigger with a higher intensity and a longer pulse width. For this purpose, we have used the same equation as in [129] that describes a recruitment, corresponding to the recruited percentage of the muscle, (noted α) according to the pulse width.

$$\alpha(pw) = \frac{c_1}{1 + e^{c_2\left(c_3 - \frac{pw}{pw_{max}}\right)}} \tag{3.1}$$

with pw_{max} is the maximal pulse width depending on the stimulator. c_1, c_2 and c_3 are parameters that represent the plateau level, maximum slope and inflection point, respectively. This description ensures a monotonic increase of eq (3.1) assuring function α increase according to the input pulse width pw. Moreover, this equation can be adapted considering the current intensity. Function α is no longer a function of the pulse width but of the current intensity giving:

$$\alpha(i) = \frac{c_1}{1 + e^{c_2\left(c_3 - \frac{i}{i_{max}}\right)}} \tag{3.2}$$

where, i_{max} is the maximal current intensity depending on the stimulator.

Then, from the recruitment α representing the percentage of recruited fibers in the muscle, we generated the corresponding elicited recruitment pattern (see Fig. 3.3). Since we know the total number of fibers in the muscle and the number of fibers per MU from the anatomy generated by [10], we can create the corresponding recruitment pattern of the NES.

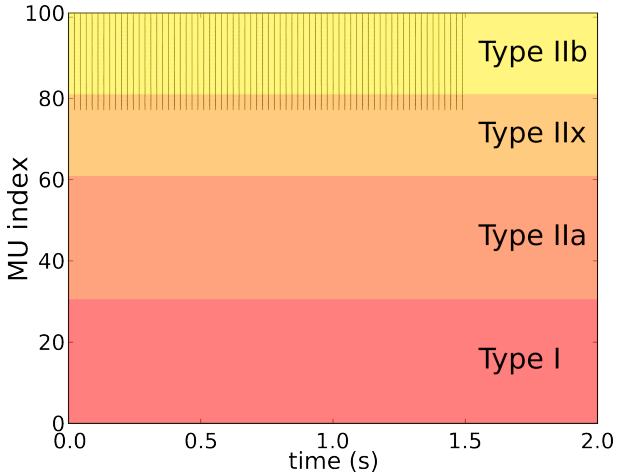

Figure 3.3: Example of elicited recruitment where 32.4% of the muscle fibers are recruited for the same muscle as in Fig. 3.2.

3.3.2 Modeling the calcium dynamic of the fiber

Radioactive function description

When a neural Action Potential (AP) reaches the fibers of a MU, the sarcoplasmic reticulum (SR) releases Ca^{2+} into the myoplasm [133]. When this concentration exceeds a specific threshold, the fibers within the MU begin to contract. The contraction remains until this concentration decreases below the threshold. Detailed models of the calcium concentration dynamic are presented in [134, 135, 130, 136]. However, we decided to use the definition of the SR Ca^{2+} release in response to an AP from [136] adapted to the MU

type.

$$u_i(t) = \begin{cases} U_{r,i} & \texttt{if} \quad t < \tau_D \\ R_i . \left(1 - e^{-\left(\frac{t-\tau_D}{\tau_{1,i}}\right)}\right)^5 . e^{-\left(\frac{t-\tau_D}{\tau_{2,i}}\right)} & \texttt{if} \quad t \geq \tau_D \end{cases} \tag{3.3}$$

Where i represents the type of the MU, $U_{r,i}$ is the Ca^{2+} concentration at rest for the MU of type i, τ_D is the time delay response to the Ca^{2+} release which is the same for all type of MU, R_i is an amplitude parameter to be in agreement with the calcium amplitude according to the type of the MU and $\tau_{1,i}$ and $\tau_{2,i}$ are specific parameters according to the MU type and representing the rise and the descent of the Ca^{2+} dynamic, respectively. This calcium dynamic is depicted in Fig 3.4.

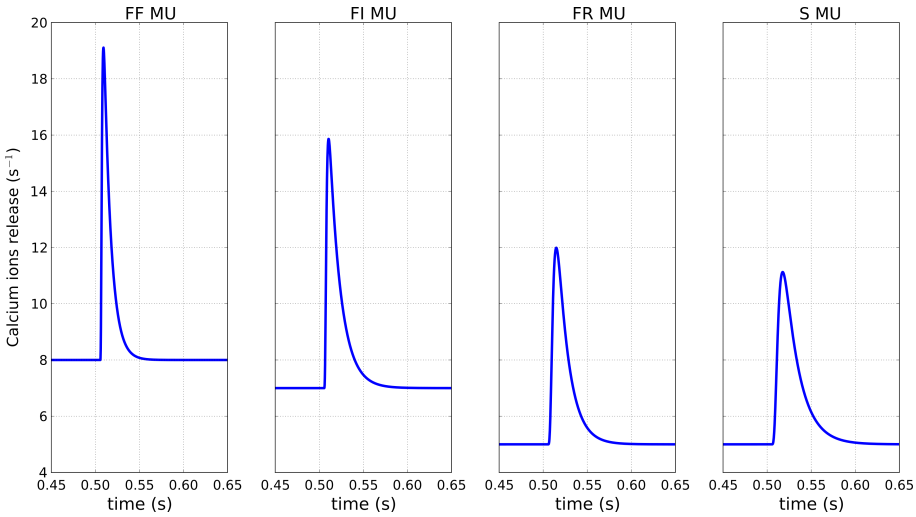

Figure 3.4: Calcium dynamic of MU according to its type. The neural AP reaches the MUs at 0.5s.

The contraction-relaxation cycle is formed to follow two phases: every time an AP reaches a MU, a contraction begins with a time delay of τ_D for taking into account the propagation time of the AP and the average time delay due to the calcium dynamic. After this delay, a contraction phase takes place and Ca^{2+} concentration ups above the calcium threshold ($U_{c,i}$) during a few moment according to the MU type. After this, if no other AP has been received in the mean time, an active relaxation follows until the rest Ca^{2+} concentration $U_{r,i}$. The calcium release is fast enough in skeletal muscle to be considered quasi-instantaneous (see Fig. 3.4). This dynamics will be determined using the convolution operator between the firing times of the corresponding MU and the calcium function.

3.3.3 MU activation

During muscle contraction, the MU can be in one of these three states: activated ($\alpha_i(t)$), in relaxation ($\beta_i(t)$) and relaxed ($\gamma_i(t)$). This activation can be determined from the calcium dynamics of the MU defined above (see section 3.3.2). From this definition, we proposed these activation equations describing MU state in time:

$$\alpha_i(t) = \begin{cases} 1 & \texttt{if} \quad u(t) \geq U_{c,i} \\ 0 & \texttt{otherwise} \end{cases} \tag{3.4}$$

$$\beta_i(t) = \begin{cases} 1 & \texttt{if} \quad U_{r,i} < u(t) < U_{c,i} \\ 0 & \texttt{otherwise} \end{cases} \tag{3.5}$$

$$\gamma_i(t) = \begin{cases} 1 & \texttt{if} \quad u(t) = U_{r,i} \\ 0 & \texttt{otherwise} \end{cases} \tag{3.6}$$

By weighting the MU activation with its number of fibers divided by the total number of fibers within the muscle, we can obtain the percentage of the muscle that is contracted, in relaxation and relaxed during time as we can see on Fig. 3.5.

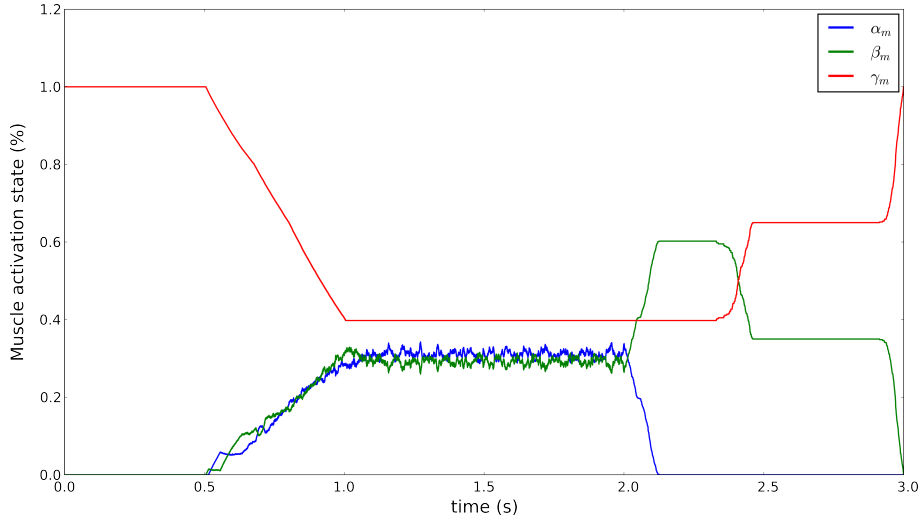

Figure 3.5: Muscle activation states α, β and γ according to a voluntary contraction at 50% MVC.

3.4 Mechanical model of the muscle during isometric contraction

Previously, the muscle mechanical model was developed only at the muscle scale. Here, we attempt to provide a mechanical model at the MU scale. Unlike models in [8, 27, 96, 9], the muscle is modeled by N contractile elements with the same length L_c placed in parallel. Each contractile element will describe mechanical dynamics of one MU.

This model presented on Fig. 3.6 is composed of macroscopic passive elements interacting with N contractile elements E_c^i that contract independently and with its own local activation described in section 3.3.3. We assume the left and right tendons having the same properties. To stay close to the structure proposed by Hill, the springs are assumed to be linear (k_{s1} N.m^{-1}). L_{s10} is the length of the springs at rest condition, when no force is generated and L_{s1} is the springs length at any time. L is the length of the parallel spring and L_{c0} is defined as the length at which the muscle produces the maximum isometric force. From this model we have:

$$\begin{cases} m\ddot{x_1} &= F_c + k_{s1}(X_1 - x_1) + \lambda(\dot{X_1} - \dot{x_1}) \\ m\ddot{x_2} &= -F_c + k_{s1}\,(X_2 - x_2) - \lambda(\dot{X_2} - \dot{x_2}) \end{cases} \tag{3.7}$$

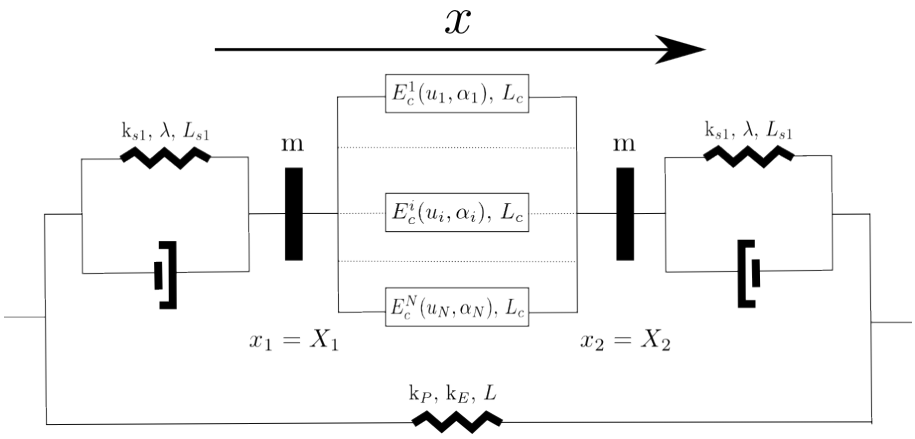

Figure 3.6: Mechanical rheological model of the muscle, including masses and dampers derived from [9] with N parallel contractile elements representing the MU.

Substracting these two dynamics leads to:

$$m\left(\ddot{x_2} - \ddot{x_1}\right) = -2F_c + k_{s1}\left(X_2 - x_2 - X_1 + x_1\right) + \lambda\left(\dot{x_1} - \dot{x_2}\right) \tag{3.8}$$

Knowing that : $(x_2 - x_1) = L_c$ and $(X_2 - X_1) = L_c^0$, the rest length of the muscle, we obtain:

$$m\ddot{L_c} = -2F_c + k_{s1}\left(L_c^0 - L_c\right) - \lambda\dot{L_c} \tag{3.9}$$

with $\varepsilon_c = \dfrac{L_c - L_{c0}}{L_{c0}} \Rightarrow L_c = \varepsilon_c L_{c0} + L_{c0}$.
Equation (3.9) becomes:

$$mL_{c0}\ddot{\varepsilon_c} = -2F_c - k_{s1}\left(L_c^0 - \varepsilon_c L_{c0} - L_{c0}\right) - \lambda\dot{\varepsilon_c}L_{c0} \tag{3.10}$$

$$\Rightarrow \ddot{\varepsilon_c} = -\frac{2F_c}{mL_{c0}} - \frac{k_{s1}}{m}\varepsilon_c - \frac{\lambda}{m}\dot{\varepsilon_c} - \frac{k_{s1}}{m} + \frac{k_{s1}L_c^0}{mL_{c0}} \tag{3.11}$$

Moreover, by definition we have: $L_c^0 = \varepsilon_c^0 L_{c0} + L_{c0}$. Where ε_c, defined above, represents the relative deformation of the muscle compared to L_{c0}. Thus equation (3.11) becomes:

$$\Rightarrow \ddot{\varepsilon_c} = -\frac{2F_c}{mL_{c0}} - \frac{k_{s1}}{m}\varepsilon_c - \frac{\lambda}{m}\dot{\varepsilon_c} - \frac{k_{s1}}{m} + \frac{k_{s1}\left(\varepsilon_c^0 L_{c0} + L_{c0}\right)}{mL_{c0}} \tag{3.12}$$

Finally,

$$\Rightarrow \ddot{\varepsilon_c} = -\frac{2F_c}{mL_{c0}} - \frac{k_{s1}}{m}\varepsilon_c - \frac{\lambda}{m}\dot{\varepsilon_c} + \frac{k_{s1}}{m}\varepsilon_c^0 \tag{3.13}$$

Then, from (3.8), we also have:

$$2F_c = -mL_{c0}\ddot{\varepsilon_c} + k_{s1}\left(L_c^0 - L_c\right) - \lambda\dot{L_c} \tag{3.14}$$

Knowing that in isometric contraction we have: $L_c + 2L_{s1} = L = L_c^0 + 2L_{s10}$ and $L_{c0}\varepsilon_c + 2L_{s10}\varepsilon_{s1} - 2L_{s10}\varepsilon_{s1}^0 = 0$. With $\varepsilon_{s1}^0 = \frac{L_{s1}^0 - L_{s10}}{L_{s10}}$ is the relative deformation of the

tendon between its length at rest (L_{s10}) and its optimal length (L^0_{s1}), equation (3.14) becomes:

$$2F_c = 2mL_{s10}\ddot{\varepsilon}_{s1} + 2k_{s1}\left(L_{s1} - L_{s10}\right) + 2\lambda\dot{L}_{s1} \tag{3.15}$$

$$\Rightarrow F_c = mL_{s10}\ddot{\varepsilon}_{s1} + k_{s1}L_{s10}\varepsilon_{s1} + \lambda L_{s10}\dot{\varepsilon_{s1}} \tag{3.16}$$

Moreover, the force F_e of the visco-elastic component representing the tendon is the sum of the spring force F_s and the damper force F_d. Thus, $F_e = F_s + F_d = k_{s1}L_{s10}\varepsilon_{s1} + \lambda L_{s10}\dot{\varepsilon}_{s1}$. When the ratio of F_c and F_e is considered using Laplace transform, we have:

$$\frac{\mathcal{L}\left[F_c\right]}{\mathcal{L}\left[F_e\right]} = \frac{ms^2\Upsilon(s) + \lambda s\Upsilon(s) + k_{s1}\Upsilon(s)}{\lambda s\Upsilon(s) + k_{s1}\Upsilon(s)}$$

With $\Upsilon(s)$ is the Laplace transform of $L_{s10}\varepsilon_{s1}(t)$. Thus, we can write:

$$\lambda s\mathcal{L}\left[F_c\right] + k_{s1}\mathcal{L}\left[F_c\right] = ms^2\mathcal{L}\left[F_e\right] + \lambda s\mathcal{L}\left[F_e\right] + k_{s1}\mathcal{L}\left[F_e\right] \tag{3.17}$$

Giving, after inverse Laplace transform use, the following differential equation:

$$m\ddot{F}_e + \lambda\dot{F}_e + k_{s1}F_e = \lambda\dot{F}_c + k_{s1}F_c \tag{3.18}$$

$$\Rightarrow \ddot{F}_e = -\frac{\lambda}{m}\dot{F}_e - \frac{k_{s1}}{m}F_e + \frac{\lambda}{m}\dot{F}_c + \frac{k_{s1}}{m}F_c \tag{3.19}$$

Finally, we have this system at the muscle scale:

$$\begin{cases} \ddot{\varepsilon}_c &= \frac{k_{s1}}{m}\varepsilon^0_c - \frac{2F_c}{mL_{c0}} - \frac{k_{s1}}{m}\varepsilon_c - \frac{\lambda}{m}\dot{\varepsilon_c} \\ \ddot{F}_e &= -\frac{\lambda}{m}\dot{F}_e - \frac{k_{s1}}{m}F_e + \frac{\lambda}{m}\dot{F}_c + \frac{k_{s1}}{m}F_c \end{cases} \tag{3.20}$$

An equation system is also needed for each contractile element representing a MU. According to [9], we have, for each contractile element, the dynamic of its stiffness $k_{c,i}$ and its force $F_{c,i}$:

$$\begin{cases} \dot{k}_{c,i}(t) &= -\left(u_i(t) + a|\dot{\varepsilon}_c(t)|\right)k_{c,i}(t) + \alpha_i(t)k_{max,i}(t)\Pi_{c,i}(t)U_{c,i} \\ \dot{F}_{c,i}(t) &= -\left(u_i(t) + a|\dot{\varepsilon}_c(t)|\right)F_{c,i}(t) + \alpha_i(t)F_{max,i}(t)\Pi_{c,i}(t)U_{c,i} + \omega\left(F_{c,i}(t)\right)k_c(t)L_{c0}\dot{\varepsilon}_c(t) \end{cases} \tag{3.21}$$

With, $F_c = \sum_{i=0}^{N} F_{c,i}$ and $k_c = \sum_{i=0}^{N} k_{c,i}$ the muscle force and stiffness, respectively. u_i is the calcium dynamic described in section 3.3.2, a is a parameter describing the velocity contribution between the actin and myosin filaments, α_i is the activation described in section 3.3.3, $k_{max,i}$ and $F_{max,i}$ are the maximum stiffness and force produced by the i^{th} MU. $U_{c,i}$ is the calcium concentration threshold of the ith MU determining when the contraction occurs. Moreover, $\Pi_{c,i}$ is a function following the normalized calcium dynamic according to the MU type (see eq 3.3). Assuming that all the fibers have the same mechanical contribution, $k_{max,i}(t)$ and $F_{max,i}(t)$ are determined as a percentage of the maximal stiffness (k_{max}) and force (F_{max}) produced by the muscle according to the

number of innervated fiber in the MU. Moreover, $k_{max,i}(t)$ and $F_{max,i}(t)$ are function of the deformation ε_c described as follow:

$$\left\{ \begin{array}{rcl} F_{max,i}(t) & = & F_{max,i} f_l\left(\varepsilon_c\right) \\ k_{max,i}(t) & = & k_{max,i} f_l\left(\varepsilon_c\right) \end{array} \right. \tag{3.22}$$

with $f_l\left(\varepsilon_c\right) = e^{\frac{-\varepsilon_c^2}{b}}$, where b is a scale parameter. Finally, $\omega\left(F_c\right)$ (in equation (3.21)) is defined as follows:

$$\omega\left(F_c\right) = \left\{ \begin{array}{ll} 1 & \texttt{if } F_c > 0.0001 \\ 0 & \texttt{otherwise} \end{array} \right. \tag{3.23}$$

This window function is used in order to prevent the passive force generated by the non recruited MUs that shouldn't produce active force. Details of the calculus to obtain the system (3.21) can be obtained from [9].

3.5 Results

In all the results present below, some parameters were set. These parameters are presented in the table below.

Table 3.1: Fixed parameters

Parameter	Value (unit)
Sampling frequency (f_s)	4096 (Hz)
Time delay response (τ_D)	5 (ms)
SMU Ca^{2+} concentration at rest ($U_{r,S}$)	5 (μmol.L^{-1})
SMU Ca^{2}+ concentration activated threshold ($U_{c,S}$)	10 (μmol.L^{-1})
FRMU Ca^{2+} concentration at rest ($U_{r,FR}$)	5 (μmol.L^{-1})
FRMU Ca^{2}+ concentration activated threshold ($U_{c,FR}$)	11 (μmol.L^{-1})
FIMU Ca^{2+} concentration at rest ($U_{r,FI}$)	7 (μmol.L^{-1})
FIMU Ca^{2}+ concentration activated threshold ($U_{c,FI}$)	14 (μmol.L^{-1})
FFMU Ca^{2+} concentration at rest ($U_{r,FF}$)	8 (μmol.L^{-1})
FFMU Ca^{2}+ concentration activated threshold ($U_{c,FF}$)	15 (μmol.L^{-1})
SMU rise slope ($\tau_{1,S}$)	4 (ms)
SMU descent slope ($\tau_{2,S}$)	20 (ms)
SMU amplitude calcium dynamics (R_S)	16
FRMU rise slope ($\tau_{1,FR}$)	3 (ms)
FRMU descent slope ($\tau_{2,FR}$)	17 (ms)
FRMU amplitude calcium dynamics (R_S)	16
FIMU rise slope ($\tau_{1,FI}$)	1.3 (ms)
FIMU descent slope ($\tau_{2,FI}$)	13 (ms)
FIMU amplitude calcium dynamics (R_S)	14.5
FFMU rise slope ($\tau_{1,FF}$)	1 (ms)
FFMU descent slope ($\tau_{2,FF}$)	8 (ms)
FFMU amplitude calcium dynamics (R_S)	20.0

3.5.1 Fusion frequency study

In this subsection, we will present some results concerning the fusion frequency needed to simulate the twitch fusion according to the MU type. For this purpose, we simulated two muscles composed of 500 MUs using the following distributions of MU type: 33% SMU, 17% FRMU, 17% FIMU and 33% FFMU for the first muscle (M_1) and 33% SMU, 33% FRMU, 17% FIMU and 17% FFMU for the second muscle (M_2). This difference between these two muscles is the number of what is considered as slow (or fast) MU. In M_1 there are 250 MUs that are considered slow (S and FR MUs) whereas 330 are defined in M_2. Concerning the recruitment, it was defined using the description in section 3.3.1 and equation (3.1). Parameters of this equation was set in order to recruit all the MUs at each stimulation (see Table 3.2).

Different frequencies of stimulation were used in this study, according to [99, 137], the frequency fusion of MU mechanical response to a stimulus is correlated to its type. Thus, we proposed to simulate for the same muscle and parameters of the model, 5 different fusion frequencies, 5, 20, 50, 100 and 120 Hz. Moreover, the complete simulation parameters set is presented in Tables 3.1 and 3.2.

Table 3.2: Parameters used for the fusion frequency

Parameter	Value (unit)
Maximal intensity (i_{max})	3.15 (mA)
Intensity (i)	3.15 (mA)
Ellicited recruitment parameters (c_1, c_2, c_3)	1.15, 8.12, 0.75
Optimal muscle length (L_{c0})	9.18 (cm)
Rest muscle length (L_c^0)	10.0 (cm)
Velocity contribution (a)	1.0
Force-length parameter (b)	0.54
Tendon viscosity (λ)	19.0 (kg.s^{-1})
Muscle weight (m)	0.5 (kg)
Maximal force (F_{max})	300 (N)
Maximal stiffness (k_{max})	100 N.mm^{-1}
Tendon stiffness (k_{s1})	120 N.mm^{-1}

The fusion frequency comparison can be made on different mechanical behavior of the muscle (force, stiffness or deformation). In this section, we decided to compare the force generation according to the stimulation frequency.

On Fig. 3.7, we can observe an increase of the generated force according to the stimulation frequency increase. Yet, one can see a lower generated force at 120 Hz than at 100 Hz. Moreover, we also observe the force fusion increasing with the frequency from the amplitude reduction between impulses. Thus, the optimal fusion frequency for this muscle is around 100 Hz.

As on Fig. 3.7, we can observe on Fig. 3.8 the relationship between the generated force and the stimulation frequency. Yet, we observe lower generated force with M_2 muscle than M_1 at 100 and 120 Hz. In fact, M_2 that has more slow MUs generates less force than M_1 that has more fast MUs. This difference could be explained by the MU type repartition, knowing that SMUs generate less force than FFMUs. Yet, at 50 Hz the M_2 generates more force than M_1. Thus, we can suppose that the optimal fusion frequency

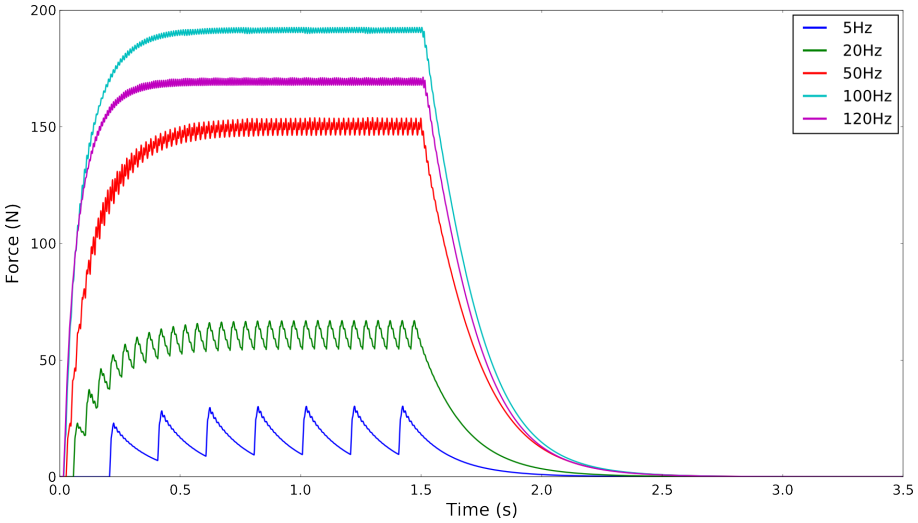

Figure 3.7: Fusion frequency evaluation for M_1.

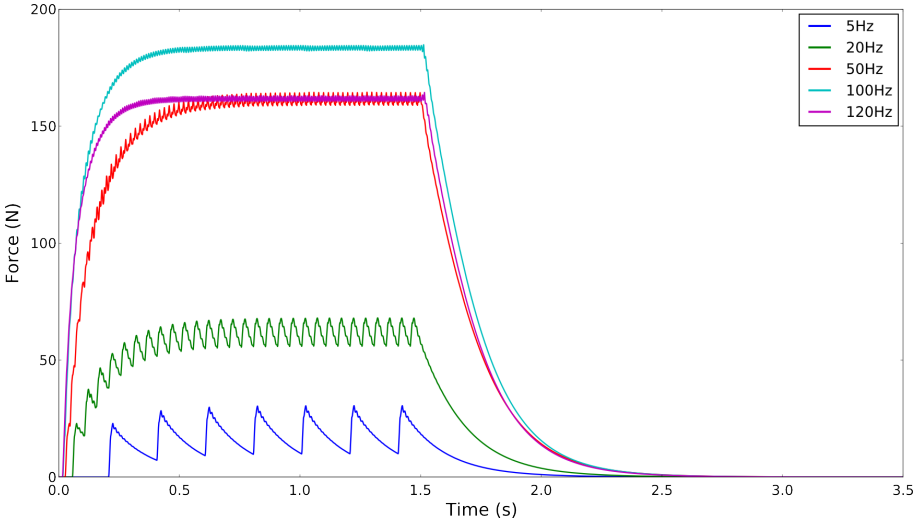

Figure 3.8: Fusion frequency evaluation for M_2.

for this muscle is around 50 Hz. Finally, at 5 and 20 Hz only partial fusion arises and gives the same results for both muscles.

This decrease in force generation while the stimulation frequency increases, can be explained from the twitch shape of the MUs. Determination of the optimal frequency stimulation can be computed from the related time of the corresponding MU twitch as in [138]. In those simulations, the stimulation frequency at 120 Hz is too high and will induce a diminution of the force generation compared to a stimulation at 100 Hz. These simulation results are in agreement with previous experimental studies [137] that observed an optimal frequency stimulation.

3.5.2 Motor unit scale

Considering the model description, we have access to the mechanical contribution developed by each MU. Thus, deeper investigation about the muscle mechanical behavior is

feasible. In this section, we propose to dissect these muscles at the MU scale in order to give some insights about the underlying mechanical phenomena.

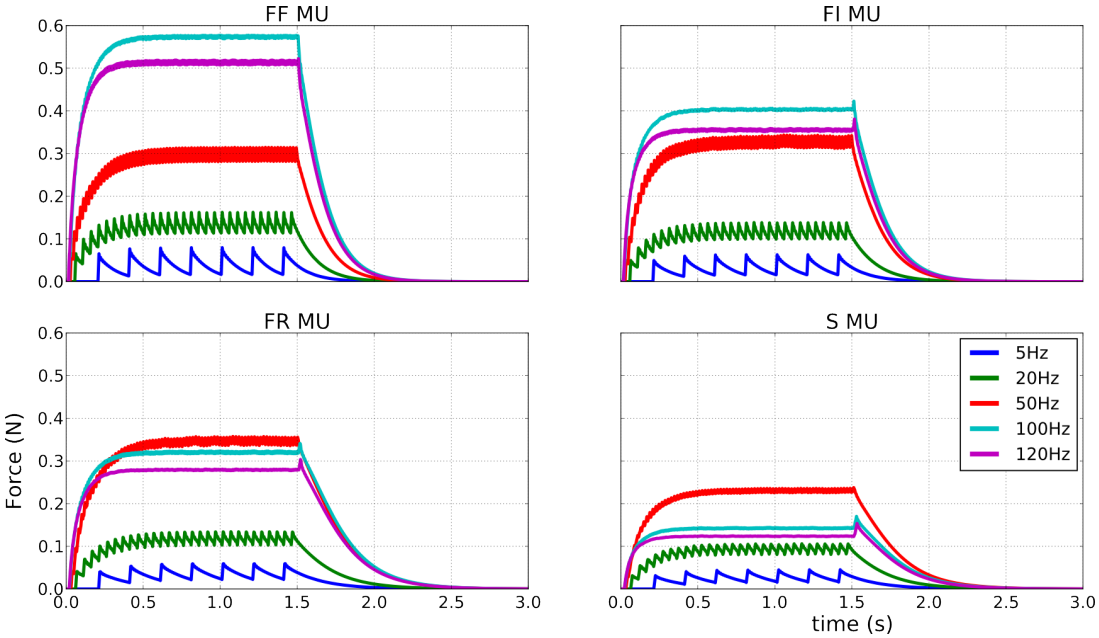

Figure 3.9: MU force response to the stimulation frequency according to its type.

On Fig. 3.9, the generated force according to the stimulation frequency and the MU type is presented. As one can see on this figure, the SMUs generate more force at 50 Hz than at 100 and 120 Hz. Considering the slow contraction of such MUs, the tetanus contraction is obtained around 50 Hz. Same effect can be observed on the FRMU type, yet its optimal stimulation frequency is higher than the one for SMU. On the other hand, FIMU and FFMU have also this effect but with even a higher fusion frequency than SMU and FRMU. In this model, the optimal stimulation frequency is highly correlated to the calcium dynamic presented in 3.3.2.

3.5.3 Comparison with the twitch model

In this section, we will compare the force generated from a classical twitch model [99] using the same anatomy and stimulation frequency as before (see Figs. 3.10 and 3.11). In [99], the twitch is function of 6 parameters identified from experimental study.

$$F(t) = pt^m e^{-kt} \tag{3.24}$$

with, $p = F_{max} e^{-kT_c(ln(T_c)-1)}$, $m = kT_c$ and $k = \dfrac{ln(2)}{-T_c ln\left(\frac{T_{hr}}{T_c}\right) + T_{hr} - T_c}$. T_c represents the contraction time, the time from the start of MU force generation to the time where MU reaches its peak value F_{max}. T_{hr} describes the half time relaxation corresponding to the time from the start of MU force generation to the time where MU force decreases to half of its peak. Moreover, a time delay T_{lead} representing the electro-mechanical delay is given to delay the response. Value of the parameters governing this model is presented in Table 3.3.

Table 3.3: Parameters used for the twitch model

MU type	T_{lead} (ms)	T_c (ms)	T_{hr} (ms)	F_{max} (N)
S	70	80	200	0.0382
FR	60	70	175	0.0764
FI	30	40	100	0.191
FF	20	30	60	0.328

From this definition, the muscle force is computed as:

$$F_m = \sum_{i=1}^{N} F_i(t) * \sum_{j=0}^{M} t_k \tag{3.25}$$

where F_m is the muscle force, F_i is the twitch definition (see eq 3.24) of the ith MU, N is the number of MU, t_k is the kth discharge time of the MU and M is the number of discharge.

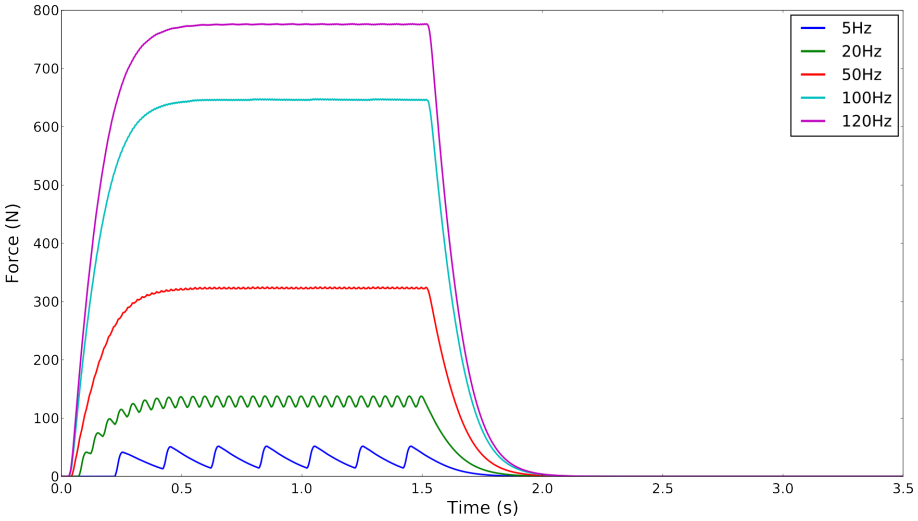

Figure 3.10: Fusion frequency for M_2 with twitch model.

On Fig. 3.10, we can see a continuous increasing of the generated force while increasing the stimulation frequency. Compared to Fig. 3.8, where we observe an optimal frequency, the twitch model cannot describe this optimal frequency in this range of stimulation frequency. No saturation of the tetanus can be visible with the twitch model. In fact, in the twitch model, the muscle force is computed from the sum of the convolution between the firing times of the MU and their corresponding twitch. Because of this convolution operator and the definition of the firing times of the MUs (Dirac impulse), it doesn't exist a limit if $M \to \infty$. Thus, increase the stimulation frequency will defined ∞ number of firing times.

At the MU scale, same trend is observed on the generated force, which continuously increasing with the stimulation frequency whatever the MU type (see Fig. 3.11). Compared to Fig. 3.9, the FRMU generates more force than FF or FIMUs that isn't in agreement with the literature since the FFMUs are the MU that produce the highest force. Thus, we can assess that the twitch model cannot transcribe an optimal stimulation frequency and has no meaning when high stimulation frequency (>100 Hz) are considered.

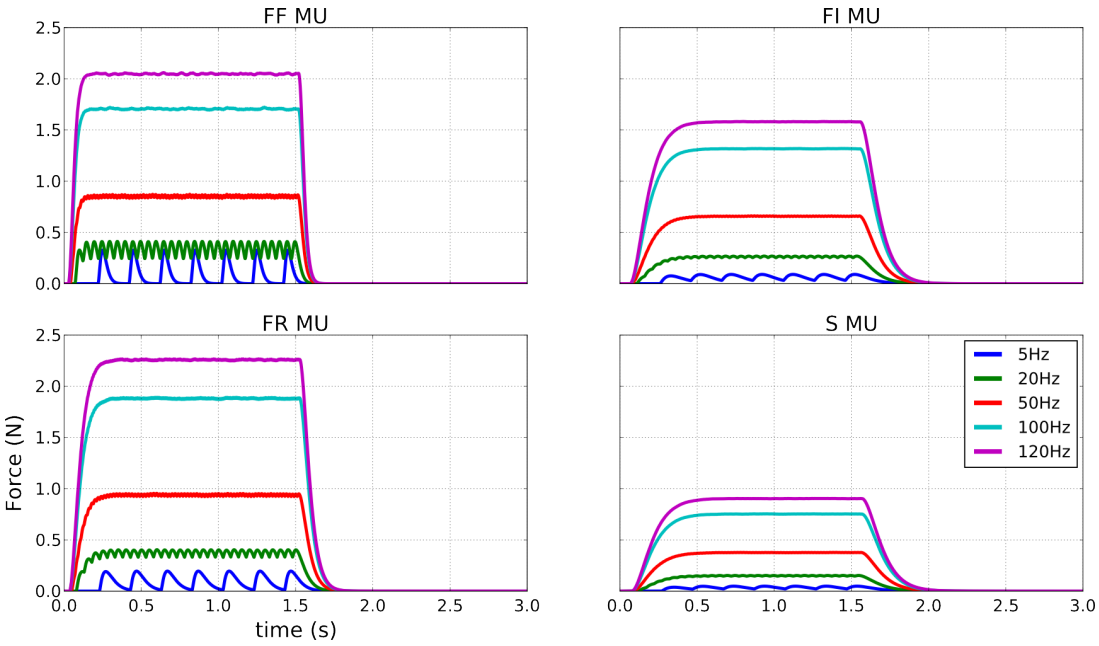

Figure 3.11: MU force response to the stimulation frequency according to its type using the twitch model.

3.5.4 Model validation

Experimental data used in this study come from the study [129]. Particularly, these data were used to identify the parameters of a multiscale musculo-skeletal model controlled by electrical stimulation. Details about the experimental setup and the identification process can be found in [129]. In this study, we used one force profile from isometric measurements recorded from the subject implanted with an electrical stimulation device [139]. During the stimulation, the knee joint was fixed at the position at which the torque was maximum. The quadriceps muscle was stimulated with 8 stimulation trains (duration 1.5s), separated by a 2s rest time. The neural stimulation was performed using an implanted FES system [140]. The stimulation frequency was set at 20Hz for the subject. Pulse widths were fixed during the stimulation, but the intensity increased between trains from 0.4mA to maximum i_{max} = 3.15mA with a constant step.

Simulation of a quadriceps bulk

Aim of this section is to validate the presented model according to experimental recording. For this purpose, simulation parameters concerning the simulation are presented in Tables 3.1 and 3.4. Some of these parameters were extracted from [129] while others were defined based on the literature [141, 142, 143, 30].

Considering that the stimulated muscle is the quadriceps, we decided in a first step to simulate a quadriceps bulk regrouping the four muscles composing the quadriceps as in [129]. For this purpose, we defined a muscle composed of 3250 MUs with the following distribution 40% SMU, 13% FRMU, 16% FIMU and 31% FFMU. This distribution is determined as a weighted average according to each muscle composition based on [30, 145] and number of MU. Here, we assumed that rectus femoris (RF) muscle is composed of 750 MUs with an innervation ratio $\simeq$ 750. This innervation ratio represents the average number of fiber innervated by the MUs. Thus, FF and FI MUs innervate more than 750

Table 3.4: Parameters used for the fusion frequency

Parameter	Value (unit)
Maximal intensity (i_{max})	3.15 (mA) [129]
Intensities (i)	0.4, 0.8, 1.2, 1.6, 2.0, 2.4, 2.8, 3.15 (mA) [129]
Ellicited recruitment parameters (c_1, c_2, c_3)	1.15, 8.12, 0.75 [129]
Optimal muscle length (L_{c0})	9.18 (cm) [129]
Rest muscle length (L_c^0)	10.5 (cm)
Velocity contribution (a)	1.0 [129]
Force-length parameter (b)	0.54 [129]
Tendon viscosity (λ)	19 (kg.s^{-1}) [9]
Muscle weight (m)	1.6 (kg) [142]
Maximal force (F_{max})	1000 (N)
Maximal stiffness (k_{max})	10000 (N.m^{-1}) [144]
Tendon stiffness (k_{s1})	40000 (N.m^{-1}) [144]

fibers and FR and S MUs less. The vastus intermedius (VI) has 500 MUs innervating around 750 fibers each. The vastus medialis (VM) has 1000 MUs innervating around 1000 fibers each. And the vastus lateralis (VL) has 1000 MUs innervating around 1000 fibers each. In total, the defined muscle is composed of $\simeq$ 2,500,000 muscle fibers.

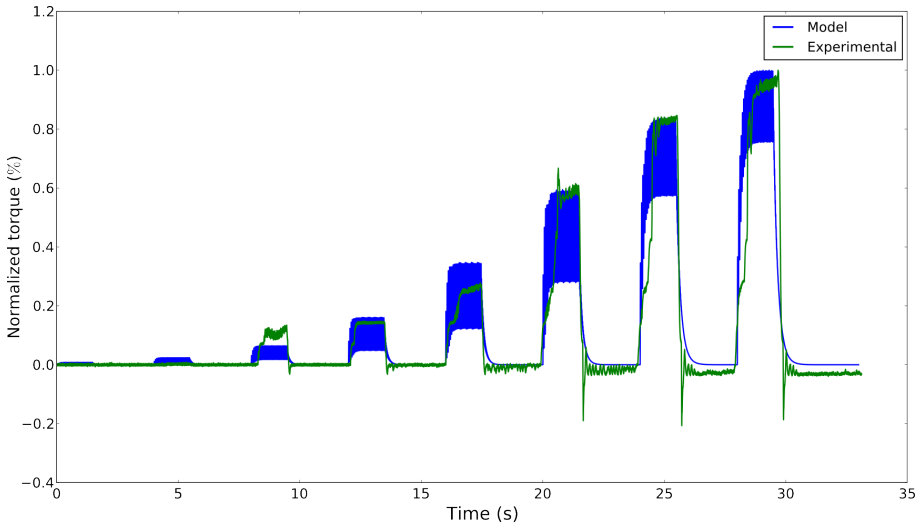

Figure 3.12: Normalized generated force in experimental conditions following the protocol presented above (data extracted from [129]) compares to simulated force from the proposed mechanical muscle model.

Both force profiles were normalized according to their respective maximum. First observation on Fig. 3.12 concerns the global dynamic of the force generation according to the stimulation intensity. Compared to experimental recording, the simulated force correctly describes the trend of experimental force. Only one force generation according to the stimulations (the 3^{rd}) is under estimated while the 5^{th} stimulation is over estimated. Moreover, we can observe on the experimental recording a two steps increase of the force. After few stimulations the muscle force increases and stabilizes during few hundreds of

milliseconds and then continue to rise. This sidestepping rise is always the same between the stimulation whatever the intensity. To assess the effectiveness of the model, the Normalized Root Mean Square Error was computed as follow:

$$NRMSE = \frac{\sqrt{\sum_{i=1}^{P}\left(\widehat{F}_i - F_i\right)^2}}{\sqrt{P}\left(max(\widehat{F}) - min(\widehat{F})\right)} \tag{3.26}$$

where, P is the number of time sample of the force, $\hat{F}$ is the experimental force and F is the simulated force. Using this equation, computed NRMSE indicates that the error between experimental and simulated force is 8.7%. Major error comes from the almost perfectly synchronization of the muscle contraction since we only simulated one muscle representing the quadriceps. Finally, concerning the computation time of the model, this simulation lasts 57min using a dedicated workstation (2x8 cores Intel Xeon 2.40Ghz with hyperthreading, 128Gb Ram, Ubuntu 14.04 64bits) without parallel computation.

Simulation of a quadriceps

In this part, we will simulate four muscles corresponding to each muscle composing the quadriceps. For this purpose, we needed the values describing the anatomical parameters described in Table 3.5 for each muscle. Some parameters such as the maximal muscle force or the rest muscle length cannot be found and thus had to be fix with a physiological value.

Table 3.5: Parameters used for the fusion frequency

Parameter (name) unit	RF	VI	VM	VL
Optimal muscle length (L_{c0}) cm	8.4 [129]	8.7 [129]	8.9 [129]	8.4 [129]
Rest muscle length (L_c^0) cm	10.4 [141]	10.5 [142]	10.5 [142]	9.1 [142]
Velocity contribution (a)	1.0 [129]	1.0 [129]	1.0 [129]	1.0 [129]
Force-length parameter (b)	0.4 [129]	0.45 [129]	0.45 [129]	0.45 [129]
Muscle weight (m) kg	0.358 [142]	0.612 [142]	0.487 [142]	0.712 [142]
Maximal force (F_{max}) N	200	225	270	250
Maximal stiffness (k_{max}) N.m^{-1}	2000	2000	2000	2000
Tendon stiffness (k_{s1}) N.m^{-1}	7000	7000	7000	7000
Pennation angle (θ) ^{o}	27.9 [142]	9.8 [142]	17.3 [143]	16.5 [143]

Considering the specifications of each muscle, the quadriceps muscle force is obtained as:

$$F = F_{RF}cos\left(\theta_{RF}\right) + F_{VI}cos\left(\theta_{VI}\right) + F_{VL}cos\left(\theta_{VL}\right) + F_{VM}cos\left(\theta_{VM}\right) \tag{3.27}$$

where, F is the quadriceps force, F_X is the corresponding muscle force simulated, θ_X the corresponding pennation angle and RF, VI, VM and VL represent each muscle composing the quadriceps.

Compared to the validation results presented above, the force profile is worse estimated defining the four muscles with an NRMSE of 21.5%. Yet, the force trend remains stable compare to the quadriceps bulk simulation. With this modeling, we can have access to each muscle contribution to the force (see Fig. 3.13).

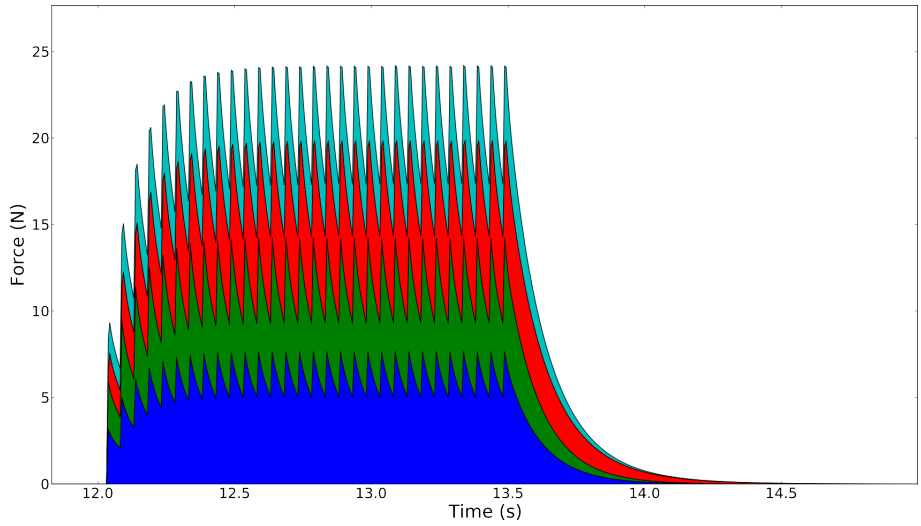

Figure 3.13: Cumulative plot representing the force contribution for each muscle composing the quadriceps muscle presented above at the stimulation intensity 1.6mA (corresponding to the fourth stimulation). In blue the VL force contribution, in green the VM force contribution, in red the VI force contribution and in cyan the RF force contribution.

First observation on Fig. 3.13 is the contribution of the VL muscle. This muscle is only composed of S and FR MUs and we can observe a smaller amplitude in the force generation than the other which is coherent with the muscles definitions. Moreover, one can notice few contribution of the RF since it is the muscle with the less contribution according to its definition. Both VL and VM contributed almost equally since their definitions are almost alike. This simulation illustrates the ability of the proposed model to represent in an accurate way the mechanical contribution and synergy of muscle group around a joint. Further works are planned to increase its physiological realism.

3.5.5 Voluntary contraction simulation

In the proposed model, the input parameter α describing the activation of the muscle is also adapted to MU voluntary recruitment. This formalism also allows us to simulate voluntary contraction as presented in Fig. 3.14.

Force profiles were generated using the same voluntary recruitment patterns defining force plateaus from 10 to 100% MVC. Knowing that only twitch type model allow the simulation of voluntary force profiles, we are comparing the force profiles generated using the defined twitch model and the proposed mechanical model from the same recruitment pattern. The anatomy used is the M_1 muscle described in previous section 3.5.1. Moreover, we notice that the parameters remain the same among the simulations for both models, only the recruitment pattern changes at each contraction.

As you can see on Fig. 3.14, the plateau remains stable along the contraction with slight variability due to the MU recruitment rolling. Yet, the proposed model correctly represents the same force profiles generated from the validated twitch model [99]. Only for the 10 and 20% MVC contractions, the proposed model simulates higher force than the twitch model. Comparison of the mean and the standard deviation (std) computed over the force plateau for both models is presented in Fig. 3.15a.

On Fig. 3.15a, we can observe almost the same mean computed over the force profiles

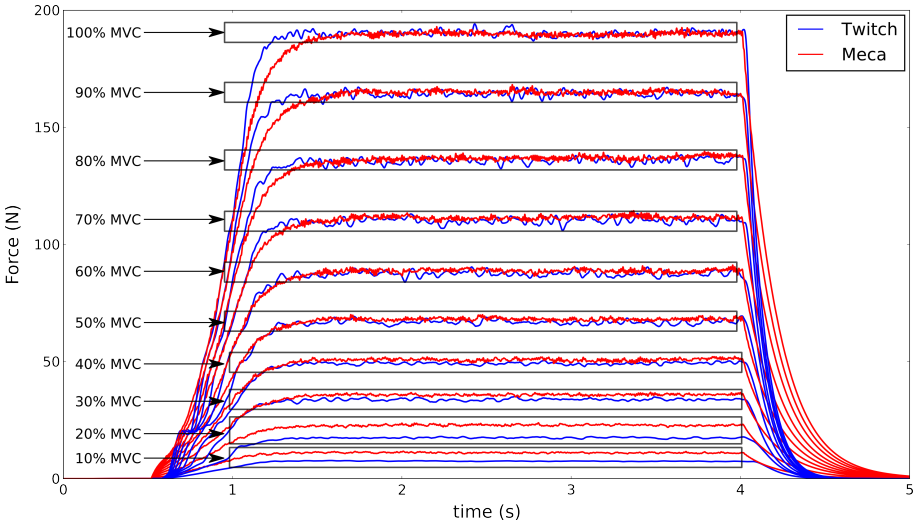

Figure 3.14: Force profiles for voluntary contractions from 10 to 100% MVC using the defined twitch model and the proposed muscle mechanical model.

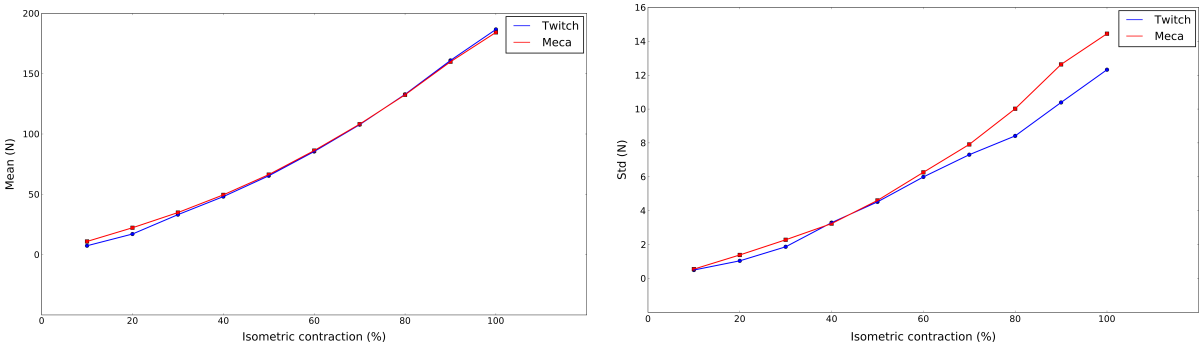

(a) Computed mean for each contraction level according to both models

(b) Computed standard deviation (std) for each contraction level according to both models

Figure 3.15: Mean and std computed from both models from 10 to 100% MVC.

plateau from both models. Only the mean computed with the proposed model at 10 and 20% MVC is overestimated compared to the twitch model. Moreover on Fig. 3.15b is presented the standard deviation computed for both models. As we can see, more dispersion of the generated force is observed with the proposed model compared to the twitch model. Yet, the trend remains the same, the std increases according to increase of the contraction level.

Increasing the mean and std according to the contraction level is also observed in experimental recording. Nevertheless, we estimated that a comparison with experimental recordings isn't suitable yet. In fact, experimental recordings describe the global force applied to a specific joint. In the case of upper limb force recording for the elbow joint, this force represents forces generated by the Biceps Brachii, the Brachialis and the Brachioralialis. Moreover, noises in the recorded signals and lack of training for force sustaining induces unsteady force plateaus (even for low contraction level) and thus, bias the comparison. Since studies [22, 146, 147, 99] trying to estimate a single muscle force contribution based their analysis using the twitch model, we decided to limit this comparison with the

twitch model that is related to one simulated muscle.

3.6 Discussion

In this study, we proposed to model the mechanical behavior of the skeletal muscle during isometric contraction. This modeling is described at the MU scale, which are assumed to be placed in parallel in the muscle as N contractile elements. Modeling the mechanical contribution of the muscle at the MU scale had previously been used in [130, 99]. Yet, these models only computed the force contribution of each MU individually. In [130], the authors also described the calcium dynamic induced by the recruitment of the MU. Nevertheless, some important relationships such as the force-length relationship weren't considered in this work.

Determining the muscle force contribution is an assembly of several mechanisms and interactions. Most of these mechanisms are well described in [8, 12, 27]. However, in [8, 27] the muscle was described only as one contractile element where its activation didn't have any physiological meaning. In [12], the muscle was described at the fiber scale and accurately characterized the underlying processes arising during muscle fiber contraction. Yet, using this model to define each fiber in the muscle isn't feasible in terms of computation time for our application.

The distribution moment theory, proposed in [96], allowed to upscale from the fiber scale to the muscle scale and thus, preserved the fiber accurate modeling to the muscle scale. This modeling gives promising results and some studies upgraded this modeling [9]. In [9], the authors also defined the input parameter α according to the functional electrical stimulation. Nevertheless, using the formalism proposed by Zahalak implies modeling simplification such as the muscle composition. In fact, using the distribution moment theory will consider that the muscle is composed of the N (number of fibers) times the same muscle fiber.

In the proposed model, we used the formalisms proposed in [9] since this model was validated on human recordings. Now the main improvement is the description of the muscle as N (number of MUs) contractile elements placed in parallel (see Fig. 3.6) where each contractile element is activated independently from the others. Actually, except the activation, there is a strong dependence between the contractile element contraction and the global muscle contraction since muscle force-length and muscle force-velocity relationships are considered. The contractile element mechanical dynamic considered local variables as well as global variable at the muscle scale. We also specified the activation dynamic according to the MU type and also the mechanical contribution of each MU. In the anatomical model, we supposed different number of fiber according to the MU type. Thus, FFMUs have more fiber than SMUs in order to provide more contribution to the muscle contraction.

Apart from the twitch model [99], this is the first model that considers the mechanical relationships and is able to simulate voluntary contractions at the MU scale. Moreover, compared to the twitch model, the proposed dynamic model is more complex and can simulate physiological behaviors that the twitch model can't (see section 3.5.1). In fact, it has been assessed that it exists an optimal frequency stimulation [148] where the muscle generates the maximum of force. The twitch model can't represent this optimal frequency compared to the proposed mechanical model (see section 3.5.1). The twitch model also doesn't represent the muscle stiffness and the muscle deformation which have an effect on

the muscle force dynamic where our proposed model does. Yet, as we can see on Fig. 3.9 we observe a sudden raising of the generated force when the muscle starts to relax.

The proposed model has been validated with experimental data [129]. A specific set of parameters representing the quadriceps bulk based on the literature was used in order to validate the proposed model. According to Fig. 3.12 and the small computed NRMSE, we can assess that the proposed model is validated. It has to be noticed that no identification algorithm was used to identify the parameter values, these values were extracted from the literature and experimental studies. Most of the parameters values were found but a major issue came during their collect: some parameters values were significantly different between studies representing the subjects' inter-variability and recording technique. On the other hand, some parameters values couldn't be found in the literature. Thus, for the simulations we tried to define these values with a physiological meaning but, a parameter identification algorithm is needed to provide better results and subject's specific parameter tuning. We also tried to simulate the four muscles composing the quadriceps bulk instead of only one. This simulation performed worse result than simulating one muscle representing the quadriceps. Nevertheless, simulating the four muscles composing the quadriceps allows the access to each muscle contribution in the contraction. We believe that this simulation can better estimate the quadriceps force using an identification procedure and deeper investigation of the parameters defining each muscle.

The developed model doesn't consider the muscle fatigue. Yet, it is known that the electrical stimulation induced an intense fatigue compared to voluntary contractions [149]. This fatigue phenomenon is described at two different levels [150]:

- the neural fatigue representing the limitation of the nerves to generate sustained action potential;
- the muscular fatigue (or metabolic fatigue) representing the reduction of force generation by the muscle fibers.

Thus, the fatigue will induce a significant decrease in muscle force generation due to repeated muscular activation [151]. Considering the successive stimulations used in the experimental protocol (see section 3.5.4), the fatigue phenomenon has probably arose during the recording. This phenomenon isn't considered in the proposed model, but can be defined at the neural level as well as at the muscle level thanks to the decoupling of the neural input describing the MU firing times and the muscle definition.

3.7 Conclusion

In this study, we proposed a mechanical model representing the muscle at the MU scale. Modeling the muscle at the MU scale allows us to have more information than the modeling at the muscle scale and also permits us to simulate a whole muscle compare to the fiber scale modeling. It also allows the simulation of mechanical behavior according to various muscle compositions.

This modeling at the MU scale can also provide the activation level of the muscle through the MUs firing times. This description provides us the possibility to define elicited contractions as well as voluntary contractions. To assess the validity of our model, we performed a validation comparison with experimental data recorded in a former study where we know exactly the recruitment induced by the electrical stimulation. The muscle force was simulated from a single muscle representing the quadriceps bulk composed of

3250 MUs with the suspected fiber type distribution. The results exhibit reliable results compare to experimental recording with a NRMSE of 8.7%. The relationship between the muscle force with intensity of the stimulation is respected.

Moreover, thanks to the definition of the model, we simulated the four muscles composing the quadriceps where each muscle has a specific set of parameters extract from the literature. This preliminary modeling allows us to access to the contribution of each muscle during the quadriceps contraction. Yet, some parameters defining those muscles are unknown and thus, biased the results.

Future works, using this model, are envisaged for more realistic study of the sEMG/force relationship as in section 4.3. In fact, this model can easily be used in parallel of an electrical model of the muscle contraction [10] where the input representing the MUs firing times and the muscle composition are the same. This model can also be used for the definition of a quasi-dynamic electro-mechanical model of the skeletal muscle during isometric contractions (see section 4.4 for details). Since the muscle deformation is determined with the corresponding MU recruitment pattern, we can use this deformation information in the electrical model to have better representation of the muscle anatomy during contraction. Moreover, studies concerning the contribution of agonist and antagonist muscles can be performed using identification algorithm and adapted MU recruitment pattern. Also, several clinical applications are envisaged, using the proposed model, after parameter identification and model personalization, such as sarcopenia evaluation where one can simulate a sarcopenic muscle with both mechanical and electrical manifestations.

Chapter 4

Applications of the proposed models

Contents

4.1 Introduction

In chapters 2 and 3 we proposed two models describing the electrical and mechanical activities of the muscle during isometric contraction. To illustrate model implementation reliability, reproductibility and usefulness two main applications will be presented in this chapter.

A global sensitivity analysis of the electrode grid recording system used in the electrical model 4.2 is performed. Thanks to the decoupling of the electrical model and the recording system model, it is easy and fast to perform this sensitivity analysis with only variations of the recording system parameters. This study enables to assess the effect of the recording system parameters on the statistics computed on the sEMG signals. Thus, it can help clinicians and researchers to design efficient protocols using HD-sEMG grid considering the results of this study.

Then, a study of the sEMG/force relationship, where the electrical model is used 4.3, is performed. Thanks to the model implementation, it is feasible to perform, for the same recruitment pattern, electrical and mechanical activities of the a single muscle during contraction. Modeling the sEMG/force relationship is important to better understand and estimate individual force muscle contribution in experimental studies with non invasive protocol.

Finally, this chapter ends with a first overview of the quasi-dynamic model of muscle contraction during isometric contraction that includes both electrical and mechanical models 4.4. Thanks to the models structure, it is fast to do the communication between the electrical and mechanical models. This study investigates the effect of the contraction on the generated signals and the statistics computed on them.

4.2 Global sensitivity analysis

Mathematical models of surface electromyogram (sEMG) generation consist of a series of equations describing the generation and the propagation of an action potential (AP) along the muscle fibers and within the muscle, respectively [10].

Actually, models allow us the access to electromyographic data corresponding to several physiological contexts and specific motor control strategies that are hardly evaluated in experimental conditions. The investigation of the changes of sEMG signal features according to physiological mechanisms and instrumentation parameters are easier and faster with analytical models rather than numerical models [10, 6].

Recently, a High Density sEMG (HD-sEMG) recording technique has emerged. This technique allows the direct and simultaneous access to a high number of channels (up to 256 channels). This technique significantly increases the spatial representativeness of the recorded data over the studied muscle. It opened the door to multi-channel analysis of muscle activity (as for EEG recordings) and has already demonstrated promising abilities comparing to classical recording techniques [2].

For this purpose, we used a HD-sEMG generation model inspired from a recently published work described in [10]. In this model, the muscle is considered as a cylinder with the possibility of multiple anisotropic layers. The source is described as a progressive generation of the intracellular action potential at the end plate, a propagation along the fiber and its extinction at the ends of the fiber.

Identifying the most influential parameters of the models through some sensitivity

analysis is an important task, as it allows one to know (1) where experimental efforts should focus, (2) which parameters are important to identify by inverse methods and (3) on which parameter it is important to perform an uncertainty analysis.

Commonly, the standard deviation of the sEMG signal is used to estimate the magnitude of the muscle activation [152]. Other amplitude estimators, such as Root Mean Square value (RMS) and mean Average Rectified Values (ARV) have been extensively investigated as means of controlling prosthetic devices, ergonomic assessments, biofeedback systems, as well as for a better understanding of healthy and pathological neuromuscular systems [2]. In addition to these classical amplitude parameters, we propose to study features linked to the shape of the sEMG Probability Density Function (PDF), namely, the HOS parameters.

In a previous study, these features have demonstrated, by simulation, promising sensitivity to some sEMG generation parameters [153]. Two High Order Statistics (HOS) will be considered, the Skewness related to the PDF asymmetry and the Kurtosis linked to its flatness.

In this study, we present a global sensitivity analysis of four HD-sEMG amplitude parameters to assess their robustness/sensitiveness, with a parameter ranking, toward the variation of the grid parameters. This task is done using the Elementary Effect Method (EEM) [154] that allows the precise quantification of varying each tested parameters on a specific set of output features [47].

4.2.1 Electrode grid recording

Muscle electrical activity is recorded by the electrode at the skin surface with a surfacic integration of the electric activity values over the sampled positions under the electrode. This surface integration is done numericaly and is normalized by the number of sampled positions under the simulated electrode area.

$$S_j(\theta_j, z_j, t_i) = \int\int_{\mathbb{S}_j} sEMG(\rho_c, \theta, z, t_i) d\theta dz \tag{4.1}$$

where t_i is an instant point during the simulation, (θ_j, z_j) are the cylindrical coordinates of the center of electrode j, $\mathbb{S}_j$ is the electrode area and ρ_c is the skin radius. For circular shape electrode, we have:

$$\mathbb{S}_j = \left\{(\theta, z) \mid z^2 - 2z.z_j.\cos(\theta - \theta_j) + z_j^2 \leq r_j^2\right\} \tag{4.2}$$

where, r_j is the radius of electrode j.

Once the electrode shape is defined, we also have to define an electrode grid. For this purpose, several parameters are needed (see Fig. 4.1):

- the center of the electrode grid (centerX; centerZ). With centerX the angular center of the electrode grid and centerZ the center according to the longitudinal axis;
- the inter-electrode distances (dx, dz). With dx the inter-electrode distance in the angular direction and dz the longitudinal inter-electrode distance;
- the number of electrode (n_x, n_z). With n_x the number of electrode along the angular axis and n_z the number of electrode in the longitudinal direction;
- the rotation of the grid according to the longitudinal axis z.

A particular care needs to be considered on the values of the inter-electrode distances and the electrode radius. In fact, if the electrode radius is larger than one of the inter-electrode distance it will mean that the electrode are overlapped.

In this model, the first electrode is placed at the top left of the electrode grid (see Fig. 4.1) incrementing along the angular axis x leading to the last electrode placed at the bottom right of the electrode grid.

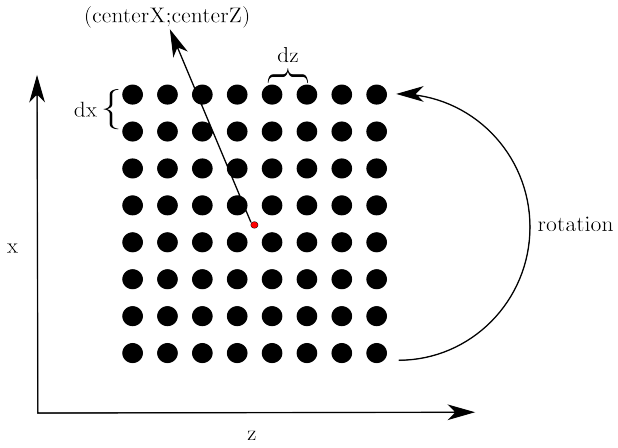

Figure 4.1: A 8×8 electrode grid representation with the studied grid parameters.

The principal advantage of the numerical electrode simulation is the total decoupling between the potential map generation and, after, the computing of HD-sEMG signals in an infinite number of electrode configurations (number, shape, positions and rotation) without the need of simulating again the potential maps (one for every contraction levels) [10]. All the grids in this paper will be composed of 8x8 electrodes. From this composition we can arrange the monopolar electrodes in the bipolar and laplacian arrangements as we can see on Fig.4.2.

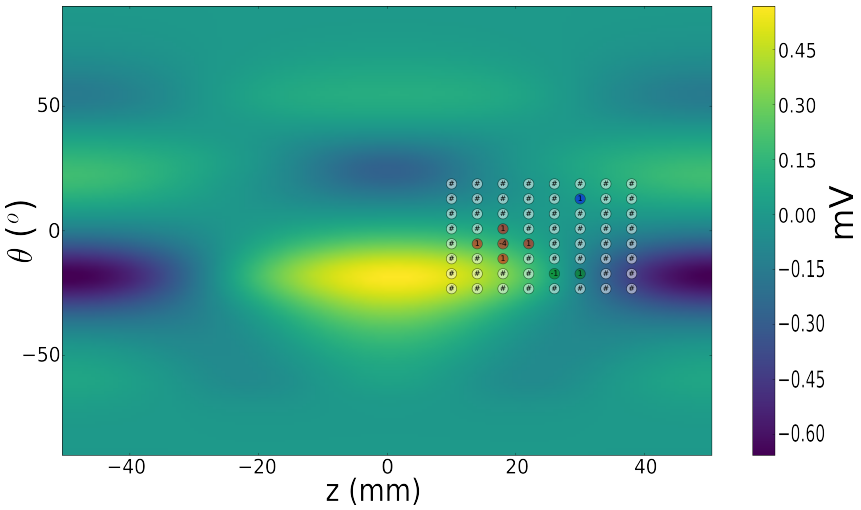

Figure 4.2: 8×8 electrode grid placed on the surface of the muscle skin. Blue electrode shows the monopolar arrangement (64 signals). Green electrodes shows the bipolar arrangement with corresponding weight on the electrode (56 signals). Red electrodes sh ows the laplacian arrangement with corresponding weight on the electrode (36 signals).

4.2.2 Global sensitivity analysis

The Elementary Effect Method (EEM), that identifies elementary effects of parameters, is used as a preliminary analysis [154]. This screening method is based on a "one factor at a time" design. It uses local variations (the elementary effects) and averages them over several points in the parameters space in order to obtain a global analysis (see Figure 4.3). EEM also provides a specific Design Of Experiment (DOE) of the grid parameters from their distributions [154, 155]. In the HD-sEMG model described above, an electrode grid is defined by 6 parameters (see Table 4.1). Thus, according to [155] 16 electrode grids are defined from the DOE by taking 3 values from the distribution of the parameters. For each simulation, EEM changes the value for one parameter and all the others remain the same. Then, it calculates the outputs changes compared to the other simulation outputs. Finally, EEM determines which parameter is the most sensitive parameter according to the outputs.

The elementary effects are computed this way:

$$EE(X_i^{(j)}) = \frac{f(X_1, \ldots, X_i + \Delta, \ldots, X_n) - f(\mathbf{X}^{(j)})}{\Delta} \tag{4.3}$$

with $\mathbf{X}^{(j)} = X_1, \ldots, X_i, \ldots, X_n$ is one vector of parameters, f the electrode grid definition and Δ the parameter variation.

As suggested by [156], we computed the 3 indicators μ^*, μ and σ as follow for a given parameter i:

$$\mu_i^* = \frac{1}{r} \sum_{j=0}^{r} \left| EE(X_i^{(j)}) \right| \tag{4.4}$$

$$\mu_i = \frac{1}{r} \sum_{j=0}^{r} EE(X_i^{(j)}) \tag{4.5}$$

$$\sigma_i = \sqrt{\frac{1}{r-1} \sum_{j=0}^{r} \left(EE(X_i^{(j)}) - \mu_i \right)^2} \tag{4.6}$$

with r the number of electrode grid on which the elementary effect is computed. Indicators μ^* and μ represent the direct interaction of the parameter on the outputs of the model and σ defines the possible indirect interaction of the parameter on the outputs through interactions with the other parameters.

The Figure 4.4 exhibits a simple example of Sensitivity Index (SI) for three parameters. The parameters p_1, p_2 and p_3 have (5;1), (1;5) and (5;5) for (μ^*;σ) values, respectively. By computing the SI for each parameters, we see that the most sensitive parameter is p_3 with a SI of 7.07. Moreover, parameters p_1 and p_2 have the same SI of 5.10 but have different values of (μ^*;σ) and thus different effects on the features. On the Figure 4.4 it is not clear that the parameters p_1 and p_2 have the same SI. Thus, this kind of representation can be hard to interpret due to the scales of the axes. If the axes scales are not the same, two parameters can have the same SI but distance from origin can appear different on this type of figure (as on the figure 4.4 between parameters p_1 and p_2). Finally, this representation loses information from the sensitivity analysis such as the monotonous effect of a parameter if $\mu^* = |\mu|$.

As indicated above, the parameters of the electrode grid have to be defined using specific distribution for each parameter. These parameters with their variation ranges for the sensitivity analysis are summarized in table 4.1.

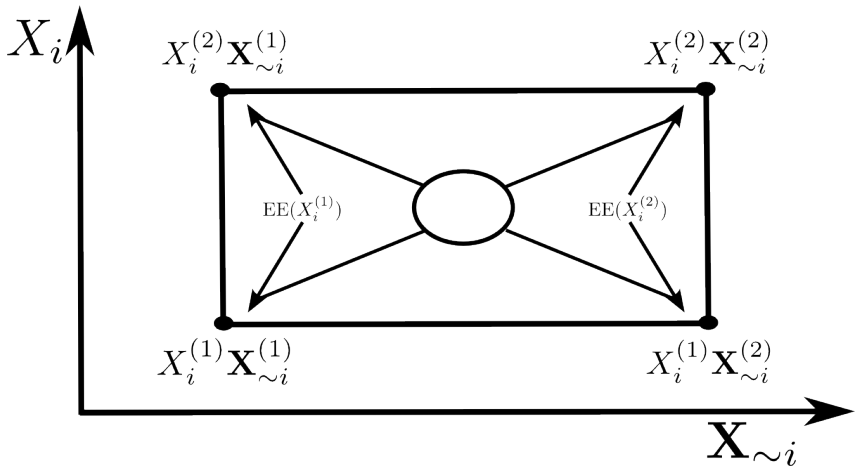

Figure 4.3: Elementary Effect (EE) computation diagram. X_i^1 and X_i^2 are two different values of the parameter X_i. $\mathbf{X}_{\sim i}^{(1)}$ and $\mathbf{X}_{\sim i}^{(2)}$ are two different parameter sets excluding parameter X_i. $EE(X_i^{(j)})$ is the Elementary Effect of the tested parameter $X_i^{(j)}$ value with the j^{th} value of the parameter set. $X_i^{(1)}\mathbf{X}_{\sim i}^{(1)}$ corresponds to one set of parameter, $X_i^{(2)}\mathbf{X}_{\sim i}^{(1)}$ is equivalent to the same set of parameter with a different value of the parameter X_i.

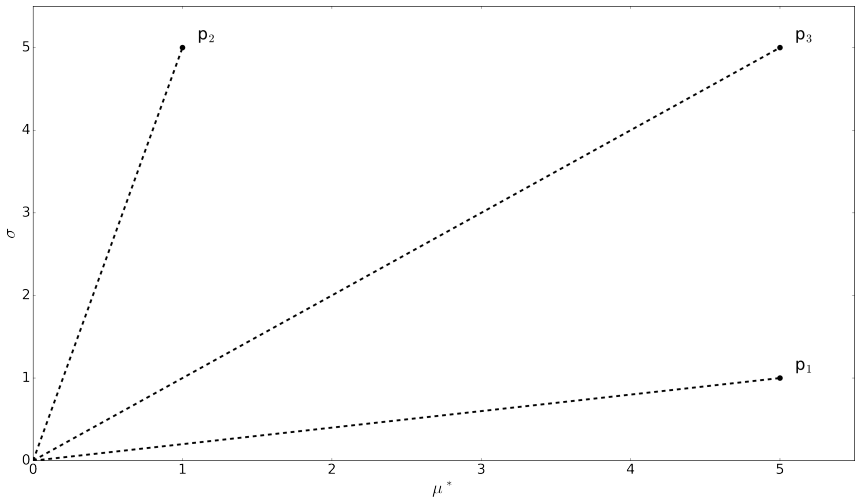

Figure 4.4: Example of sensitivity index for 3 parameters. The parameter p_1 has a higher direct impact on the outputs of the simulation than the parameter p_2 ($\mu_1^* > \mu_2^*$). Conversely, the parameter p_2 has an higher impact through the other parameters of the simulation on the outputs than the parameter p_1 ($\sigma_2 > \sigma_1$). However, the most sensitive parameter here is the parameter p_3.

Where, U(a ; b) represents the uniform distribution on $[a; b]$. T(a ; b ; c) represents the triangular distribution on $[a; b]$ with a peak at $c \in [a; b]$.

As presented in the introduction, the purpose of this study is to assess which parameter of the grid has the higher impact on the signal features and thus which study can be compared with others.

We assume no prior knowledge on the possible variations of the layout parameters of the grid (inter-electrode distances and electrode radius), hence we use uniform distributions. Nevertheless, we assume a realistic range of values for these parameters. We used

Name	Description	Variables distribution	Unit
dx	Angular inter-electrode distance	U(4.0 ; 6.0)	mm
dz	Longitudinal inter-electrode distance	U(4.0 ; 6.0)	mm
r	Electrode radius	U(0.5 ; 2.0)	mm
centerX	Angular electrode grid center	T(-10 ; 10 ; 0)	^{o}
centerZ	Longitudinal electrode grid center	T(23.25 ; 27.25 ; 25.25)	mm
rotation	Electrode grid rotation	T(-15 ; 15 ; 0)	^{o}

Table 4.1: Parameters used for sensitivity analysis and their variation range.

a triangular distribution for the position parameters of the grid (grid center position and rotation). This kind of distribution assess the highest probability for the value c with linear decreasing probability to the values a and b. We used this distribution to model the possible deviation of the grid position according to a desired position. Range of values chosen for these parameters is in respect to the protocol for the HD-sEMG recording on the Biceps Brachii [58].

4.2.3 Signal features

We computed the elementary effects not on the signals themselves but on features extracted from these signals. Root Mean Square (RMS), Average Rectified Value (ARV) and High Order Statistics (HOS) are used as output features. Outputs of the model used for the analysis are statistical criteria on the signal recorded by the electrodes.

- RMS amplitude of signal Y: $RMS(Y) = \sqrt{\frac{1}{n}\sum_{j=0}^{n} Y(j)^2}$;
- ARV amplitude of signal Y: $ARV(Y) = \frac{1}{n}\sum_{j=0}^{n} |Y(j)|$;
- Kurtosis of signal Y: $Kur(Y) = \frac{E(Y-\mu_Y)^4}{\sigma_Y^4} - 3$;
- Skewness of signal Y: $Skew(Y) = \frac{E(Y-\mu_Y)^3}{\sigma_Y^3}$.

With n the number of sampling points in the signal, $E(.)$ the expectation operator and μ_Y, σ_Y the expected values and standard deviation of the signal Y, respectively.

Those features have been used in previous studies [157] and are classical amplitude statistic descriptors on the sEMG signals.

4.2.4 Parameter sensitivity results

All the simulations were performed on a dedicated workstation (2x8 cores Intel Xeon 2.40Ghz with hyperthreading, 128Gb Ram, Ubuntu 14.04 64bits). The 16 grid definitions needed to compute the elementary effects of all parameters were obtained in a few seconds. Signals recorded by the 16 electrode grids are performed on the same simulated 2D surfacic potential maps. Statistics are computed for monopolar, bipolar and laplacian electrode arrangements. Then, statistics are computed for the 64 monopolar (56 bipolar and 36

laplacian) signals of the grid and the mean value over the electrodes is used. Ten anatomies with the same properties presented in table 4.2 were computed to have robust results. The ANOVA test is computed for the 10 anatomies for each features and proves that there is no significant influence of the anatomies on the mean value of the studied features. Thus, the sensitivity measures are computed for the features for each anatomy and then the mean value of the features is computed from the 10 anatomies. Since, the sensitivity measures give almost the same results in these two cases, we will only present the results for the mean value of the features on the 10 anatomies.

Name	**Description**	**Parameter Value** (Unit)
nMUs	Number of MUs	352
nFibs	Number of fibers	60862
ρ_m	Muscle radius	42 (mm)
σ^m	Radial and angular muscle conductivity	0.1 ($S.m^{-1}$)
σ_z^m	Longitudinal muscle conductivity	0.5 ($S.m^{-1}$)
ρ_{ap}	Adipose tissue thickness	2 (mm)
σ^{ap}	Adipose tissue conductivity	0.05 ($S.m^{-1}$)
ρ_s	Skin thickness	1 (mm)
σ^s	Skin conductivity	1 ($S.m^{-1}$)

Table 4.2: Parameters used for the generation of the ten anatomies.

Monopolar sensitivity ranking

We present in tables 4.3 and 4.4 all the parameter sensitivities computed for each signal features by the elementary effect method previously described. Signal features are computed from the mean of the corresponding features of the ten anatomies. For nearly all parameters μ^* equals to $|\mu|$, regardless of the feature. This means that the EE computed at different points of the parameter space have the same sign, indicating monotonous effects.

The Fig.4.5 presents the ranked parameters according to their sensitivity in descending order for each features for the monopolar arrangement. All the features agree that the three most sensitive parameters are the rotation, the lateral center of the grid and the electrode radius. Moreover, the two least sensitive parameters are the lateral and the longitudinal inter-electrode distance variation. Only the Skewness at 30 %MVC shows different ranking for the parameter. This can be linked to the less number of recruited MUs at this contraction level which seems to highly interfer with the PDF assymmetry.

Parameters are not considered sensitive when their μ^* is a 100 times smaller than the maximal μ^* for the given feature [154, 155]. According to the values presented in tables 4.3 and 4.4, we don't observe significant difference between the μ^* values which means that all the parameters are sensitive for the given features. For monopolar arrangement, the rotation, the electrode radius and the lateral inter-electrode distance (dx) show a difference between μ^* and $|\mu|$ for the Skewness at 30%MVC only (see values highlight in red). This means that those parameters have non-monotonous effects on the feature. Moreover, no parameter has a high σ value. It means that there is no indirect effects on the features through interactions with other parameters.

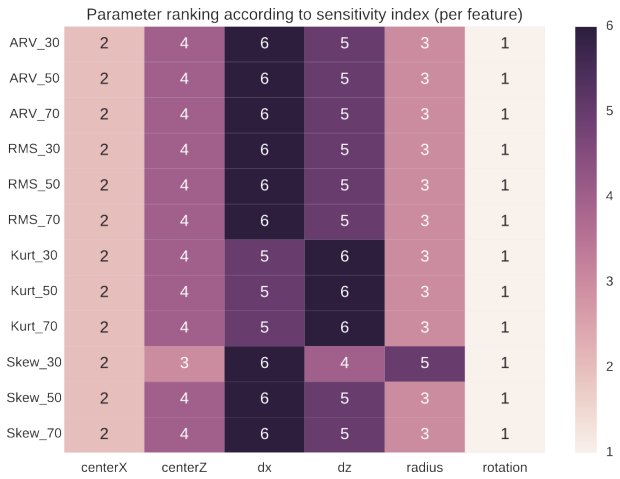

Figure 4.5: Parameters ranking according to the features for monopolar arrangement on the grid.

To conclude on the monopolar arrangement, ARV and RMS features show very similar sensitivity ranking and measures for monopolar arrangement, showing that these two features are equivalent for our study. Moreover, sensitivity measure tables by anatomies show different ranking for the rotation and the lateral center of the grid (centerX) for the Skewness at 30%MVC feature. Thus, they present differences in the parameters ranking, the longitudinal center of the grid (centerZ) has a higher impact than the lateral center (centerX) for one anatomy for the Skewness at 30%MVC.

rk	Param.	μ^*	μ	σ
1	rotation	0.2014	0.2014	$7.66.10^{-5}$
2	centerX	0.1870	0.1870	$2.23.10^{-5}$
3	radius	0.1097	-0.1097	$4.06.10^{-6}$
4	centerZ	0.0615	0.0615	$1.28.10^{-6}$
5	dz	0.0344	-0.0344	$1.42.10^{-7}$
6	dx	0.0247	-0.0247	$8.02.10^{-7}$

(a) ARV at 30 %MVC.

rk	Param.	μ^*	μ	σ
1	rotation	0.3877	0.3877	$6.80.10^{-5}$
2	centerX	0.3630	0.3630	$1.99.10^{-5}$
3	radius	0.2078	-0.2078	$3.95.10^{-6}$
4	centerZ	0.1181	0.1181	$3.02.10^{-6}$
5	dz	0.0584	-0.0584	$6.16.10^{-7}$
6	dx	0.0470	-0.0470	$1.67.10^{-8}$

(b) ARV at 50 %MVC.

rk	Param.	μ^*	μ	σ
1	rotation	0.5334	0.5334	$6.12.10^{-5}$
2	centerX	0.5016	0.5016	$1.87.10^{-5}$
3	radius	0.2842	-0.2842	$3.36.10^{-6}$
4	centerZ	0.1618	0.1618	$2.92.10^{-6}$
5	dz	0.0780	-0.0780	$1.07.10^{-6}$
6	dx	0.0649	-0.0649	$5.56.10^{-7}$

(c) ARV at 70 %MVC.

rk	Param.	μ^*	μ	σ
1	rotation	0.0660	0.0660	$3.40.10^{-5}$
2	centerX	0.0600	0.0600	$9.06.10^{-6}$
3	radius	0.0366	-0.0366	$1.99.10^{-6}$
4	centerZ	0.0206	0.0206	$6.13.10^{-7}$
5	dz	0.0146	-0.0146	$5.47.10^{-8}$
6	dx	0.0081	-0.0081	$3.93.10^{-7}$

(d) RMS at 30 %MVC.

rk	Param.	μ^*	μ	σ
1	rotation	0.2624	0.2624	$6.40.10^{-5}$
2	centerX	0.2441	0.2441	$1.61.10^{-5}$
3	radius	0.1391	-0.1391	$4.52.10^{-6}$
4	centerZ	0.0814	0.0814	$5.17.10^{-6}$
5	dz	0.0443	-0.0443	$1.71.10^{-6}$
6	dx	0.0318	-0.0318	$3.52.10^{-8}$

(e) RMS at 50 %MVC.

rk	Param.	μ^*	μ	σ
1	rotation	0.4459	0.4459	$1.37.10^{-4}$
2	centerX	0.4169	0.4169	$3.78.10^{-5}$
3	radius	0.2359	-0.2359	$8.83.10^{-6}$
4	centerZ	0.1377	0.1377	$9.34.10^{-6}$
5	dz	0.0749	-0.0749	$3.87.10^{-6}$
6	dx	0.0538	-0.0538	$8.55.10^{-7}$

(f) RMS at 70 %MVC.

Table 4.3: Detailed monopolar ARV and RMS features sensitivity for all parameters on the mean features of the ten anatomies.

Bipolar sensitivity ranking

On Fig. 4.6 is presented the ranking of the most sensitive parameters acoording to the features. As in the monopolar ranking (see Fig. 4.5), the rotation, the lateral center of the grid and the electrode radius are the three most sensitive parameters. Also, the inter-electrode distances are the two less sensitive according to the results. However, there are some differences about the skewness feature at 50 and 70%MVC. The longitudinal center and the longitudinal inter-electrode distance is more sensitive with the bipolar arrangement than in the monopolar and laplacian. It can be explained by the longitudinal bipolar arrangement of the electrode and also because it is supposed to be aligned with muscle fibers.

According to the tables 4.5 and 4.6, we can assess that all the grid parameters are sensitive for the features. As in the monopolar results, no parameter has a high value of σ. With a deeper insight into the results by anatomies, we observe several differences in the ranking of the parameters for the skewness features at 50 and 70%MVC. In fact, there is only a factor of around 4 and 6 between the most sensitive parameter and the less at 50 and 70 %MVC, respectively. Thus, the skewness features at 50 and 70 %MVC seem to be sensitive to the anatomy with the longitudinal bipolar arrangement.

rk	Param.	μ^*	μ	σ
1	rotation	1.4678	1.4678	$2.02.10^{-4}$
2	centerX	1.3583	1.3583	$2.80.10^{-4}$
3	radius	0.7635	-0.7635	$2.39.10^{-4}$
4	centerZ	0.4205	0.4205	$8.81.10^{-7}$
5	dx	0.1772	-0.1772	$6.80.10^{-5}$
6	dz	0.1591	-0.1591	$4.15.10^{-5}$

(a) Kurtosis at 30 %MVC.

rk	Param.	μ^*	μ	σ
1	rotation	3.7488	3.7488	0.0342
2	centerX	3.5567	3.5567	0.0249
3	radius	1.8030	-1.8030	$1.98.10^{-4}$
4	centerZ	1.0699	1.0699	$1.01.10^{-4}$
5	dx	0.4271	-0.4271	$7.40.10^{-5}$
6	dz	0.2878	-0.2878	$3.21.10^{-4}$

(b) Kurtosis at 50 %MVC.

rk	Param.	μ^*	μ	σ
1	rotation	1.4192	1.4192	$2.12.10^{-3}$
2	centerX	1.3424	1.3424	$1.55.10^{-3}$
3	radius	0.6906	-0.6906	$1.00.10^{-6}$
4	centerZ	0.4080	0.4080	$1.00.10^{-5}$
5	dx	0.1697	-0.1697	$9.10.10^{-5}$
6	dz	0.1299	-0.1299	$3.10.10^{-5}$

(c) Kurtosis at 70 %MVC.

rk	Param.	μ^*	μ	σ
1	rotation	0.0560	0.0195	$3.14.10^{-3}$
2	centerX	0.0468	0.0468	$5.62.10^{-4}$
3	centerZ	0.0350	0.0350	$1.44.10^{-4}$
4	dz	0.0299	0.0299	$1.00.10^{-6}$
5	radius	0.0162	0.0012	$2.61.10^{-4}$
6	dx	0.0090	−0.0062	$8.20.10^{-5}$

(d) Skewness at 30 %MVC.

rk	Param.	μ^*	μ	σ
1	rotation	0.7000	-0.7000	$1.90.10^{-5}$
2	centerX	0.6469	-0.6469	$8.00.10^{-5}$
3	radius	0.3439	0.3439	$4.80.10^{-5}$
4	centerZ	0.1972	-0.1972	$9.50.10^{-5}$
5	dz	0.0889	0.0889	$8.40.10^{-5}$
6	dx	0.0784	0.0784	$2.60.10^{-5}$

(e) Skewness at 50 %MVC.

rk	Param.	μ^*	μ	σ
1	rotation	0.4176	-0.4176	$1.73.10^{-5}$
2	centerX	0.3895	-0.3895	$5.86.10^{-7}$
3	radius	0.2040	0.2040	$1.01.10^{-5}$
4	centerZ	0.1184	-0.1184	$2.09.10^{-5}$
5	dz	0.0562	0.0562	$3.52.10^{-5}$
6	dx	0.0491	0.0491	$2.43.10^{-6}$

(f) Skewness at 70 %MVC.

Table 4.4: Detailed monopolar kurtosis and skewness features sensitivity for all parameters on the mean features of the ten anatomies. Highlighted values in red correspond to values indicating a non monotonous effect of the parameter.

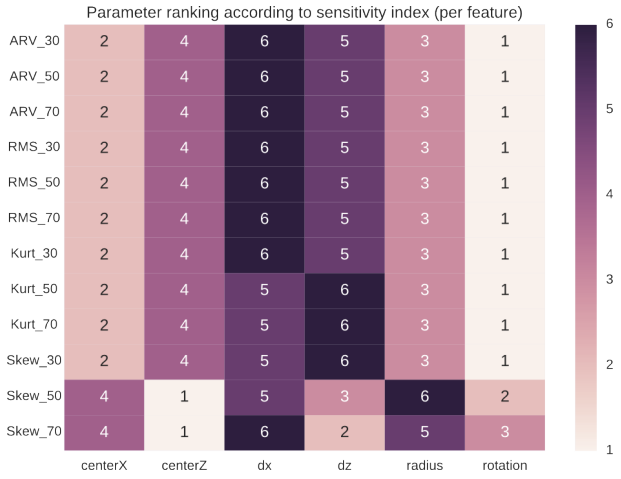

Figure 4.6: Parameters ranking according to the features for bipolar arrangement on the grid.

rk	Param.	μ^*	μ	σ
1	rotation	0.1417	0.1417	$4.28.10^{-5}$
2	centerX	0.1311	0.1311	$1.07.10^{-5}$
3	radius	0.0770	-0.0770	$2.53.10^{-6}$
4	centerZ	0.0438	0.0438	$7.20.10^{-7}$
5	dz	0.0244	-0.0244	$1.00.10^{-7}$
6	dx	0.0175	-0.0175	$1.18.10^{-6}$

(a) ARV at 30 %MVC.

rk	Param.	μ^*	μ	σ
1	rotation	0.2889	0.2889	$8.83.10^{-5}$
2	centerX	0.2666	0.2666	$8.68.10^{-6}$
3	radius	0.1538	-0.1538	$1.01.10^{-5}$
4	centerZ	0.0916	0.0916	$5.14.10^{-6}$
5	dz	0.0496	-0.0496	$6.54.10^{-7}$
6	dx	0.0351	-0.0351	$3.02.10^{-6}$

(b) ARV at 50 %MVC.

rk	Param.	μ^*	μ	σ
1	rotation	0.4055	0.4055	$1.24.10^{-4}$
2	centerX	0.3763	0.3763	$1.30.10^{-5}$
3	radius	0.2149	-0.2149	$1.30.10^{-5}$
4	centerZ	0.1294	0.1294	$7.00.10^{-6}$
5	dz	0.0696	-0.0696	$1.00.10^{-6}$
6	dx	0.0491	-0.0491	$8.00.10^{-6}$

(c) ARV at 70 %MVC.

rk	Param.	μ^*	μ	σ
1	rotation	0.0314	0.0314	$9.66.10^{-6}$
2	centerX	0.0282	0.0282	$2.10.10^{-6}$
3	radius	0.0174	-0.0174	$6.58.10^{-7}$
4	centerZ	0.0100	0.0100	$1.80.10^{-7}$
5	dz	0.0073	-0.0073	$1.14.10^{-8}$
6	dx	0.0039	-0.0039	$2.24.10^{-7}$

(d) RMS at 30 %MVC.

rk	Param.	μ^*	μ	σ
1	rotation	0.1615	0.1615	$1.15.10^{-4}$
2	centerX	0.1453	0.1453	$1.16.10^{-5}$
3	radius	0.0843	-0.0843	$1.23.10^{-5}$
4	centerZ	0.0546	0.0546	$7.64.10^{-6}$
5	dz	0.0378	-0.0378	$7.51.10^{-7}$
6	dx	0.0192	-0.0192	$2.06.10^{-6}$

(e) RMS at 50 %MVC.

rk	Param.	μ^*	μ	σ
1	rotation	0.2725	0.2725	$2.97.10^{-4}$
2	centerX	0.2473	0.2473	$3.90.10^{-5}$
3	radius	0.1425	-0.1425	$2.80.10^{-5}$
4	centerZ	0.0922	0.0922	$1.60.10^{-5}$
5	dz	0.0638	-0.0638	$2.00.10^{-6}$
6	dx	0.0320	-0.0320	$9.00.10^{-6}$

(f) RMS at 70 %MVC.

Table 4.5: Detailed bipolar ARV and RMS features sensitivity for all parameters on the mean features of the ten anatomies.

Laplacian sensitivity ranking

As we can see on the Fig 4.7, like the monopolar and bipolar arrangements, the features are less sensitive to the lateral and longitudinal inter-electrode distance and the most sensitive to the rotation, the lateral center of the grid and the electrode radius. However, we observe different ranking of the parameters according to the anatomies. All the HOS features present different ranking for the two most sensitive parameters, the rotation and the lateral center of the grid.

On tables 4.7 and 4.8, are presented the sensitivities values with their rank for all the parameters. We don't observe significant difference between the μ^* values, meaning that all the parameters have an impact on the given features. Also, no parameter has an important σ value.

One can observe the values presented in tables 4.3 and 4.4, we see that the lateral center of the grid has higher impact on the HOS features (Kurtosis and Skewness) at 50 and 70%MVC with the laplacian arrangement than with the monopolar and bipolar displays. However, according to the Table 4.8 the difference on the μ^* values between the parameters centerX and the rotation is minimal for all the HOS features for all contraction levels. Thus, the lateral center and the rotation of the grid are the two parameters with

rk	Param.	μ^*	μ	σ
1	rotation	1.4955	1.4955	$5.33.10^{-3}$
2	centerX	1.3621	1.3621	$2.62.10^{-4}$
3	radius	0.7947	-0.7947	$8.00.10^{-4}$
4	centerZ	0.4419	0.4419	$5.00.10^{-6}$
5	dz	0.2453	-0.2453	$2.10.10^{-5}$
6	dx	0.1769	-0.1769	$2.97.10^{-4}$

(a) Kurtosis at 30 %MVC.

rk	Param.	μ^*	μ	σ
1	rotation	5.3278	5.3278	$8.04.10^{-2}$
2	centerX	5.0865	5.0865	$5.11.10^{-2}$
3	radius	2.5234	-2.5234	$1.21.10^{-3}$
4	centerZ	1.7485	1.7485	$2.08.10^{-4}$
5	dx	0.6006	-0.6006	$6.33.10^{-4}$
6	dz	0.5714	-0.5714	$1.54.10^{-3}$

(b) Kurtosis at 50 %MVC.

rk	Param.	μ^*	μ	σ
1	rotation	1.9702	1.9702	$7.50.10^{-3}$
2	centerX	1.9050	1.9050	$2.00.10^{-3}$
3	radius	0.9363	-0.9363	$2.65.10^{-4}$
4	centerZ	0.6460	0.6460	$1.00.10^{-6}$
5	dx	0.2443	-0.2443	$1.08.10^{-3}$
6	dz	0.2248	-0.2248	$2.69.10^{-4}$

(c) Kurtosis at 70 %MVC.

rk	Param.	μ^*	μ	σ
1	rotation	0.2886	0.2886	$7.33.10^{-4}$
2	centerX	0.2459	0.2459	$2.64.10^{-6}$
3	radius	0.1538	-0.1538	$1.61.10^{-4}$
4	centerZ	0.0410	0.0410	$2.03.10^{-8}$
5	dx	0.0332	-0.0332	$1.15.10^{-5}$
6	dz	0.0118	-0.0118	$8.34.10^{-6}$

(d) Skewness at 30 %MVC.

rk	Param.	μ^*	μ	σ
1	centerZ	0.0436	-0.0436	$9.60.10^{-5}$
2	rotation	0.0383	0.0383	$1.00.10^{-5}$
3	dz	0.0303	0.0303	$2.64.10^{-4}$
4	centerX	0.0276	0.0073	$7.60.10^{-4}$
5	dx	0.0144	0.0144	$2.60.10^{-5}$
6	radius	0.0129	−0.0078	$1.67.10^{-4}$

(e) Skewness at 50 %MVC.

rk	Param.	μ^*	μ	σ
1	centerZ	0.0287	-0.0287	$4.80.10^{-5}$
2	dz	0.0152	0.0152	$8.30.10^{-5}$
3	rotation	0.0151	0.0151	$1.13.10^{-4}$
4	centerX	0.0116	−0.0073	$1.35.10^{-4}$
5	radius	0.0099	−0.0026	$9.80.10^{-5}$
6	dx	0.0051	0.0051	$2.50.10^{-5}$

(f) Skewness at 70 %MVC.

Table 4.6: Detailed bipolar kurtosis and skewness features sensitivity for all parameters on the mean features of the ten anatomies. Highlighted values in red correspond to values indicating a non monotonous effect of the parameter.

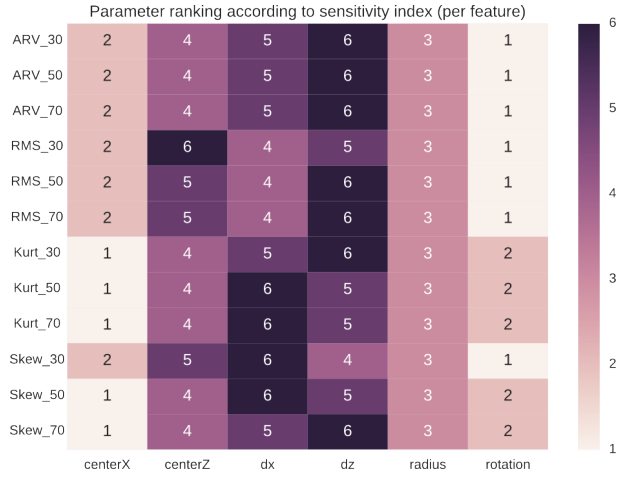

Figure 4.7: Parameters ranking according to the features for laplacian arrangement on the grid.

the highest impact on the HOS features for the laplacian configuration of the grid.

rk	Param.	μ^*	μ	σ
1	rotation	0.1199	0.1199	$3.67.10^{-4}$
2	centerX	0.1011	0.1011	$4.21.10^{-5}$
3	radius	0.0663	-0.0663	$4.31.10^{-5}$
4	centerZ	0.0344	0.0344	$2.84.10^{-7}$
5	dx	0.0259	-0.0259	$1.73.10^{-7}$
6	dz	0.0257	-0.0257	$1.17.10^{-6}$

(a) ARV at 30 %MVC.

rk	Param.	μ^*	μ	σ
1	rotation	0.3389	0.3389	$2.00.10^{-3}$
2	centerX	0.2969	0.2969	$3.87.10^{-4}$
3	radius	0.1843	-0.1843	$1.59.10^{-4}$
4	centerZ	0.0999	0.0999	$4.00.10^{-6}$
5	dx	0.0822	-0.0822	$7.00.10^{-6}$
6	dz	0.0582	-0.0582	$3.00.10^{-6}$

(b) ARV at 50 %MVC.

rk	Param.	μ^*	μ	σ
1	rotation	0.4999	0.4999	$3.54.10^{-3}$
2	centerX	0.4416	0.4416	$6.66.10^{-4}$
3	radius	0.2691	-0.2691	$2.85.10^{-4}$
4	centerZ	0.1481	0.1481	$8.00.10^{-6}$
5	dx	0.1136	-0.1136	$1.40.10^{-5}$
6	dz	0.0862	-0.0862	$4.00.10^{-6}$

(c) ARV at 70 %MVC.

rk	Param.	μ^*	μ	σ
1	rotation	0.0249	0.0249	$5.99.10^{-5}$
2	centerX	0.0185	0.0185	$6.04.10^{-6}$
3	radius	0.0141	-0.0141	$7.09.10^{-6}$
4	dx	0.0074	-0.0074	$3.43.10^{-7}$
5	dz	0.0072	-0.0072	$1.82.10^{-10}$
6	centerZ	0.0067	0.0067	$1.17.10^{-8}$

(d) RMS at 30 %MVC.

rk	Param.	μ^*	μ	σ
1	rotation	0.2702	0.2702	$3.70.10^{-3}$
2	centerX	0.2242	0.2242	$7.25.10^{-4}$
3	radius	0.1430	-0.1430	$2.56.10^{-4}$
4	dx	0.0851	-0.0851	$4.53.10^{-9}$
5	centerZ	0.0802	0.0802	$1.15.10^{-5}$
6	dz	0.0588	-0.0588	$4.17.10^{-7}$

(e) RMS at 50 %MVC.

rk	Param.	μ^*	μ	σ
1	rotation	0.4587	0.4587	$9.89.10^{-3}$
2	centerX	0.3810	0.3810	$1.78.10^{-3}$
3	radius	0.2409	-0.2409	$7.48.10^{-4}$
4	dx	0.1385	-0.1385	$4.16.10^{-6}$
5	centerZ	0.1355	0.1355	$2.66.10^{-5}$
6	dz	0.1008	-0.1008	$2.38.10^{-7}$

(f) RMS at 70 %MVC.

Table 4.7: Detailed laplacian ARV and RMS features sensitivity for all parameters on the mean features of the ten anatomies. Highlighted values in red correspond to values indicating a non monotonous effect of the parameter.

According to all these results, the specific parameters about the layout of the HD grid (inter-electrode distances) have a minor effect compared to parameters specific to the HD grid position (rotation and center of the grid) for monopolar, bipolar and laplacian arrangements. Therefore, HD-sEMG applications should have a specific focus on the right alignment with the muscle fibers and on the good positioning of the lateral center of the grid. Finally, we saw that the parameter sensitiveness is also depending on the anatomy. According to the obtained results, HOS features seem to be able to provide some information about the nature of the activated muscle region.

4.2.5 Discussion & Conclusion

The objective of this study was to investigate and to precisely quantify the sensitivity of HD-sEMG amplitude descriptors according to varying parameters related to the HD-sEMG grid design and position. This interest is motivated by recent studies using HD-sEMG grid [125, 158]. For this purpose, we proposed a first global sensitivity anal-

rk	Param.	μ^*	μ	σ
1	centerX	2.6132	2.6132	$5.27.10^{-3}$
2	rotation	2.6039	2.6039	$2.57.10^{-4}$
3	radius	1.4080	-1.4080	$4.27.10^{-3}$
4	centerZ	0.7421	0.7421	$5.10.10^{-3}$
5	dx	0.3921	-0.3921	$3.54.10^{-3}$
6	dz	0.1984	-0.1984	$6.08.10^{-4}$

(a) Kurtosis at 30 %MVC.

rk	Param.	μ^*	μ	σ
1	centerX	9.6200	9.6200	$2.32.10^{-2}$
2	rotation	9.6013	9.6013	$3.79.10^{-1}$
3	radius	4.7833	-4.7833	$7.59.10^{-2}$
4	centerZ	3.0745	3.0745	$1.00.10^{-6}$
5	dz	1.0773	-1.0773	$1.39.10^{-2}$
6	dx	0.5127	-0.5127	$1.72.10^{-2}$

(b) Kurtosis at 50 %MVC.

rk	Param.	μ^*	μ	σ
1	centerX	4.2755	4.2755	$1.62.10^{-2}$
2	rotation	4.1861	4.1861	$1.99.10^{-1}$
3	radius	1.9711	-1.9711	$2.21.10^{-2}$
4	centerZ	1.3503	1.3503	$4.74.10^{-4}$
5	dz	0.4327	-0.4327	$8.31.10^{-4}$
6	dx	0.2104	-0.2104	$7.17.10^{-4}$

(c) Kurtosis at 70 %MVC.

rk	Param.	μ^*	μ	σ
1	rotation	0.1995	0.1995	$1.98.10^{-3}$
2	centerX	0.1884	0.1884	$1.29.10^{-3}$
3	radius	0.1184	-0.1184	$6.00.10^{-6}$
4	dz	0.0498	-0.0498	$1.20.10^{-5}$
5	centerZ	0.0306	0.0306	$8.00.10^{-5}$
6	dx	0.0175	0.0059	$3.05.10^{-4}$

(d) Skewness at 30 %MVC.

rk	Param.	μ^*	μ	σ
1	centerX	1.5228	1.5228	$1.65.10^{-7}$
2	rotation	1.5109	1.5109	$7.28.10^{-3}$
3	radius	0.7995	-0.7995	$2.32.10^{-3}$
4	centerZ	0.4971	0.4971	$1.67.10^{-5}$
5	dz	0.1617	-0.1617	$1.71.10^{-3}$
6	dx	0.1022	-0.1022	$3.71.10^{-3}$

(e) Skewness at 50 %MVC.

rk	Param.	μ^*	μ	σ
1	centerX	1.1506	1.1506	$6.49.10^{-4}$
2	rotation	1.1398	1.1398	$9.24.10^{-3}$
3	radius	0.5641	-0.5641	$1.27.10^{-3}$
4	centerZ	0.3626	0.3626	$1.52.10^{-4}$
5	dx	0.1055	-0.1055	$3.94.10^{-4}$
6	dz	0.0999	-0.0999	$4.04.10^{-4}$

(f) Skewness at 70 %MVC.

Table 4.8: Detailed laplacian kurtosis and skewness features sensitivity for all parameters on the mean features of the ten anatomies. Highlighted values in red correspond to values indicating a non monotonous effect of the parameter.

ysis based on the EEM. The 64 simulated signals per grid are generated using a recent multilayered cylinder muscle model [10]. This model allowed us to compute all the signals on the same potential surface map provided by the DOE definition which describes the different electrode grid to model, from the EEM. This modeling formalism allows us to study only the electrode grid effect on the generated signals. In total, 16 electrode grid composed of 64 electrodes are defined and computed for each contraction level and anatomy. This gave us $5 \times 16 \times 64$ signals for this study. Also, monopolar, bipolar and laplacian arrangements on the grid are tested for this analysis. Moreover, 10 different anatomies were generated with the same properties (number of MUs, adipose and skin tissue conductivities and thicknesses) but with different position of the MUs within the muscle. We did this in order to do a robust analysis of the parameters sensitivity and to investigate the possible influence of the MU positions on the sensitivity measures. The main result of this study is the identification of the tested parameter that has the higher impact on the amplitude descriptors: the grid rotation. A misalignment of the grid with muscle fibers will have much more effect on the recorded HD-sEMG signals than having an increase of the lateral inter-electrode distance. Other parameters with high impact are

the lateral grid position and the electrode radius variation. Thus, we assessed that the HD-sEMG grid layout (inter-electrode distances) induces lower significant deviations on the signals than the grid position. Furthermore, placement of MUs within the muscle has a little effect on the classical parameters sensitivity. However, HOS features, especially at lower contraction levels, seem to be sensitive to the MU placement particularly with monopolar and laplacian configurations. According to the results, we also assessed that the ARV and RMS features in monopolar arrangement have the same sensitivity and thus are equivalent for our study. Finally, future works will focus on the testing of frequency features in complement of the amplitude descriptors of the HD-sEMG signals. Actually, those features have also desmonstrated their usefulness in assessing muscle fatigue and neuromuscular diseases [159].

This study has been performed with an analytical model using a multilayered cylinder muscle with a high spatial resolution of the surface maps and a high number of simulated MUs [10]. This kind of study is useful for helping practitioners in designing efficient instrumental protocols that take into account the results of such sensitivity analysis. In fact, they have to be careful about the grid placement according to the muscle fibers orientation. A misalignment of a few degree will bias the recording signals between the subjects and thus, give false interpretation of the results. This result is in agreement with a previous study [160] where authors only studied the rotation effect of the grid according to the fiber orientation. Also, the lateral center of the grid has to be carefully chosen. On the same subject, an other adjustement of the lateral grid center between two recordings will induce a different investigation region of the muscle. Thus, different MUs will be examined and different results will be obtained. Future sensitivity analysis studies, using the described HD-sEMG model, will focus on both anatomical and neural parameters of the muscle to evaluate their effects on the amplitude descriptors.

4.3 sEMG/force relationship estimation

In parallel to this thesis, another thesis was realized in the same laboratory focusing on the modeling of the sEMG/Force relationship by data analysis of high resolution sensor network [53]. Considering the close relationship between these two theses, collaborations were performed [57, 47]. Signal processing, data fusion and experimental recordings were performed within the framework of the other thesis [53] and simulation procedure were performed in this thesis framework. This study was mainly performed by Al Harrach [57], yet we believe this study is a good illustration of the applications that can be performed using the proposed models.

We know that a direct relationship exists between the sEMG and the exerted force [161]. In addition to the information contain in the sEMG signal [162] and its features [163, 164, 165], we can register anatomical facts like the location and the shift of the Neuromuscular Junction (NMJ) [42], mechanical behaviors [27] as well as fatigue evaluation [166, 167, 165]. In fact, the sEMG/force relationship has been a controversial topic of inspection for researchers since the early 70s [168, 169]. The reason behind this grown interest in this relationship is motivated by the fact that a better understanding can contribute to a great extent in the force estimation [170] and modeling paradigms in both healthy and pathological contexts [171, 172].

The study of the relationship between the sEMG signal and the muscle force in isometric non fatiguing voluntary contractions, and understanding the factors and mechanisms

that affect it, are essential to the modeling and estimation steps. There are several studies in the literature that explore the shape of the relationship between sEMG signal and muscle force [22]. However, this relationship is usually based on the sEMG recorded from an individual muscle and the global force of a certain joint due to the high complexity of the experimental evaluation and thus, has a lack of realism. According to papers from the literature [168, 173, 174], the sEMG/force relationship shape is muscle specific. It can be either linear [174] for the first dorsal interosseous or non linear [174] for the Biceps Brachii (BB) for example. We have to insist here on the fact that the muscle force measured experimentally for the BB is not the individual muscle force but the summation of forces produced by the group of muscles that cocontract with these muscles. Thus, aside from small muscles like the interosseous muscles of the hand, it is complex to perform a reliable investigation of an individual muscle sEMG/force relationship using experimental studies. Based on these observations, numerical simulation could help to identify and analyze this relationship. In such a way, we need to use simulation in order to have a reliable analysis of the form variation of this relationship since we would have a direct access to the individual force and corresponding sEMG signals generated by the same MU recruitment pattern. However, the efficiency of this approach in assessing more precisely the HD-sEMG/force relationship is strongly related to the physiological realism of the employed generation models. Along these lines, Zhou and Rymer [22], presented a simulation study that tested the effect of different parameters on the shape of the obtained normalized sEMG/force relationship [22]. They used the motoneuron pool and force models developed in [20] and adapted them to fit the first dorsal interosseous muscle. To model the sEMG signal, they used Hermite Rodriguez (HR) functions [22]. They tested different recruitment and firing rate strategies and two different types of MUAP-twitch relations as well as the effect of MU firing synchrony that is supposed to occur during fatigue [22]. They found that the firing rate had an influence on the shape of the relationship but the MUAP/twitch relation had the major influence. The synchrony did not have an impact of the HD-sEMG/force relation form [22]. Even though this study proposed to test the factors governing the HD-sEMG/force relationship shape, it lacks realism in the sEMG signal simulation model as well as MU firing rate strategies and force generation. Some important parameters describing the skeletal muscle are missing such as the MU type distribution where it is well known that the MU type has a significant impact on the generated twitch force as well as its corresponding MUAP.

Then, based on these linear and nonlinear relationship hypothesis, Botter et al. [175] tried to asses this relationship by classing the sEMG/force relationship into three patterns: Linear, Nonlinear with downward concavity and Nonlinear with upward concavity. Thus, they defined the sEMG/Force relationship for each muscle by a nonlinear relationship with two coefficients: one that defines the muscle contribution and the other defines the nonlinearity degree. However, there is no simulation study to test the accuracy of this type of function. Moreover, they used the instantaneous averaged envelope of all the grid sEMG signals which is not necessarily representative of muscle activation.

In this study, we propose to study in details, through a focused sensitivity analysis, the effect of different neural (recruitment strategy and firing rate), functional (MUs type percentages in the muscle) and physiological (subcutaneous tissue thickness, skin tissue thickness and muscle length) parameters on the shape of the sEMG/force relationship function for the purpose of a better sEMG/force relationship modeling and estimation. After the selection of the suitable mathematical model, a simple sensitivity analysis is performed to evaluate the influence of neural, anatomical and physiological parameters

on the model coefficients.

4.3.1 HD-sEMG generation model

The 8×8 HD-sEMG signals were simulated using the fast multilayered cylindrical model [10] developed in chapter 1. The limb is depicted as a three layered cylinder (muscle, adipose and skin tissues) in which the sources are located longitudinally within the muscle layer. The source is portrayed as a spatio-temporal function which describes the generation, propagation and extinction of the intracellular action potential at the end plate, along the fiber and at the myotendinous area, respectively. sEMG signal recordings are computed by surface integration under each electrode area of the generated potential map. This approach allows us to simulate a wide variety of electrode shapes and grids without simulating again the muscle's electrical activity. This electrical activity analytical calculus is fully performed in frequency domain and parallel computing is implemented in order to achieve optimal speed. The global parameter values used for the simulation are presented in Table 4.9. These parameters are based on existing data and are constant throughout this study. The studied parameters involved in the shape analysis of the sEMG/force relationship will be detailed in section 4.3.4. We should note that the bone radius as well as the Brachialis (BR) are considered for the placement of the MUs in the muscle layer as exhibited in Figure 4.8b. The value of the bone and BR radius is the mean value measured using ultrasound from 6 different subjects (see section 4.3.3). Mitchell's best-candidate algorithm (see section 2.6.2) was used for the placement of the MUs in order to position the MUs homogeneously and mimic the BB anatomy in a more realistic manner than the unconstrained uniform law [176]. For the positioning of the 8 × 8 HD-sEMG grid it was placed, as presented in Fig. 4.8a, at 1 cm below the Neuromuscular Junction (NMJ). The details of the channels (diameter and inter-electrode distance) are depicted in Fig. 4.8c and presented in Table 4.9.

Table 4.9: Fixed parameters of the cylindrical HD-sEMG simulation model.

Parameter	**Value (unit)**
Number of MU (n_{UM})	400
Time frequency sample (f_t)	2048 (Hz)
Radius (ρ_a)	46.48 (mm)
Bone + Brachialis radius (ρ_d)	18.23 (mm)
Radial muscle conductivity ($\sigma_{m\rho}$)	0.1 ($S.m^{-1}$)
Angular muscle conductivity ($\sigma_{m\theta}$)	0.1 ($S.m^{-1}$)
Longitudinal muscle conductivity (σ_{mz})	0.5 ($S.m^{-1}$)
Adipose tissue conductivity (σ_f)	0.05 ($S.m^{-1}$)
Skin conductivity (σ_s)	1 ($S.m^{-1}$)
Center of electrode grid (θ, z)	(0, 30) (°, mm)
Number of electrodes ($n_\theta; n_z$)	8 × 8
Electrode radius (r_e)	1.5 (mm)
Inter-electrode distances (d_θ, d_z)	(4, 4) (mm, mm)
Simulation time (T)	5 (s)
Angular discretization (k_θ)	101

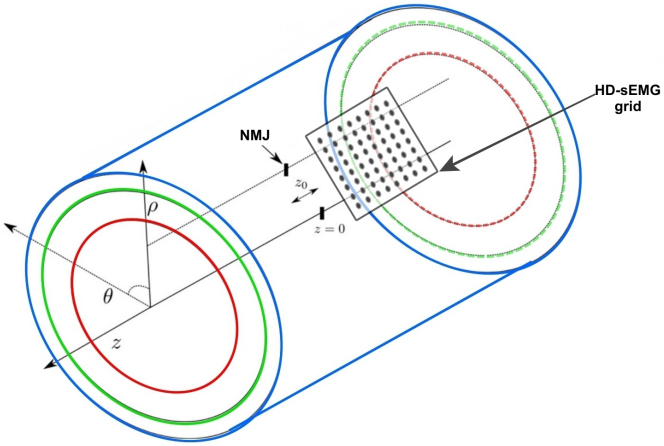

(a) The position of the HD-sEMG grid with respect to the cylinder parameters.

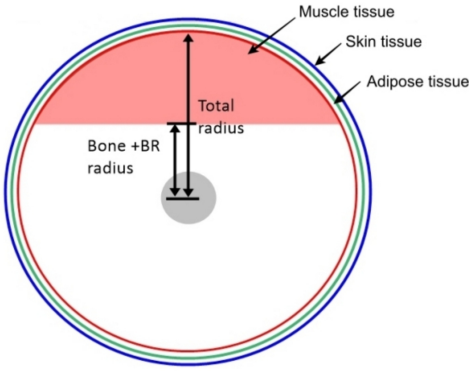

(b) The cross section of the cylindrical model with the different layers: muscle, adipose and skin tissues.

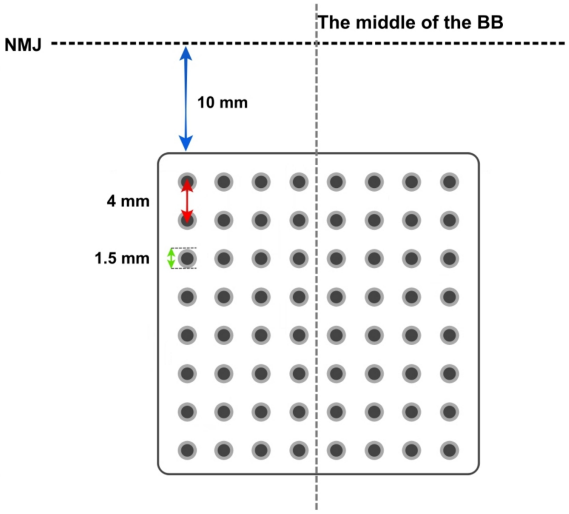

(c) The HD-sEMG grid parameters and position.

Figure 4.8: The cylindrical limb model and HD-sEMG grid.

4.3.2 Muscle force generation model

Each MU responds to an impulse from the Central Nervous System (CNS) by producing a mechanical response, namely, a twitch. The twitch characteristics depend on the MU type generating it [99]. Thus, in order to simulate the force produced by an individual muscle, we need to model the summation of particular twitches for the different types of MUs according to their shapes. In [98], authors proposed an analytical model of the twitches identified using hierarchical genetic algorithm. This model can estimate the individual muscle force contribution of the elbow joint. Consequently, in this work we will use this model in order to simulate the force produced by the BB. The twitch parameters and their values for the different MUs are presented in Table 4.10.

The analytical function describing the MU twitch response to a neural stimulus is described by [98]:

$$F_{MU}(t) = pt^m e^{-kt} \tag{4.7}$$

Table 4.10: Twitch parameters from [98].

MU type	T_d (ms)	T_c (ms)	T_{hr} (ms)	F_{max} (N)
S	70	80	200	0.0382
FR	30	40	100	0.191
FI	60	70	175	0.0764
FF	20	30	60	0.328

With T_d as the electromechanical delay between the time the stimulus is received and the start of the contraction, F_{max} the twitch maximum value, T_c the contraction time between the start of the contraction and when it reaches F_{max}, T_{hr} the duration between the start of the contractile response and the moment the force decreases to half the maximum value.

with p, m and k are constants defined as:

$$k = \frac{ln\,(2)}{-T_c ln\left(\left(\frac{T_{hr}}{T_c}\right) + T_{hr} - Tc\right.}$$

$$m = kT_c, \qquad p = F_{max} e^{-kT_c(ln(T_c)-1)}$$

Accordingly, the total force $F(t)$ developed by the muscle is obtained as follow:

$$F(t) = \sum_{i=1}^{N} (F_{MU_i}(t) * \sum_{k=1}^{P_i} \delta\,(t_k)) \tag{4.8}$$

Where δ is the Dirac function, t_k is the discharge instant, P_i the number of impulses in the $i^{th} MU$ discharge impulses train, N is the total number of active MUs in the muscle for a specific contraction level and $*$ is the convolution operator. It is important to note that the twitch parameter set is fixed for all the proposed simulations.

4.3.3 Model personalization using experimental data

In this subsection, an experimental protocol is described to extract data that will be used to personalize the HD-sEMG generation model in order to provide more bioreliable simulations. For this purpose, six healthy male subjects (mean ± std, age: 27.2 ± 1.3 years; stature: 176.8 ± 5.1 cm; body mass: 73.8 ± 7.3 kg; Body Mass Indicator (BMI): 22.6 ± 1.6) participated in the study respecting the declaration of Helsinki. All participants provided their written consent and did not relate any history of muscular or neurophysiological problem at the upper limbs. First, an electrostimulation device (Compex Sprt-P, Medicompex SA, Ecullens, Switzerland) was used to locate the NMJ of the BB [177]. This NMJ position is then used to place the grid and to measure the physiological parameters with ultrasound, by placing the probe at the same location as the grid, with elbow angle fixed at 90°. Then, an ultrasound device (Siemens ACUSON Antares 5.0 Ultrasound System) with a 7.5 MHz probe was used to scan the specified site of the BB. For each subject, a cross sectional transversal ultrasound image was taken at 1 cm below the NMJ (position of the HD-sEMG grid) in order to measure the skin and adipose tissue thickness (see Fig. 4.9c). Then a longitudinal image of all the BB was taken by sliding the probe starting from the deltoid insertion to the elbow tracing a straight line outlined at the middle of the muscle (see Fig. 4.9a). Finally, a panoramic image for the quantification of

the muscle section was taken by also sliding the probe around the muscle at 1 cm below the NMJ (see Figure 4.9b). These three images were taken at rest position (no muscular contraction) for all subjects. This protocol was repeated twice, and the average value was considered for further analysis. All measurements were performed by a skilled experimenter with elbow angle fixed at 90°. We computed the IntraClass Correlation (ICC) for one of the subject for which we repeated the measurements three times. We obtained an ICC > 0.95 which indicates the reproducibility of the ultrasound measurements. We also repeated these measurements at approximately 50 %MVC for several subjects in order to determine the BB diameter increase percentage. We found it equal to $\simeq 30\%$ of the original value.

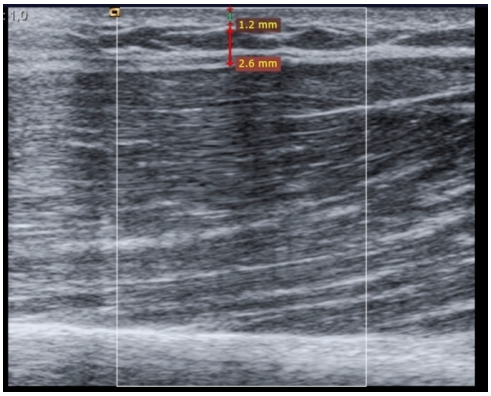

(a) The longitudinal ultrasound image.

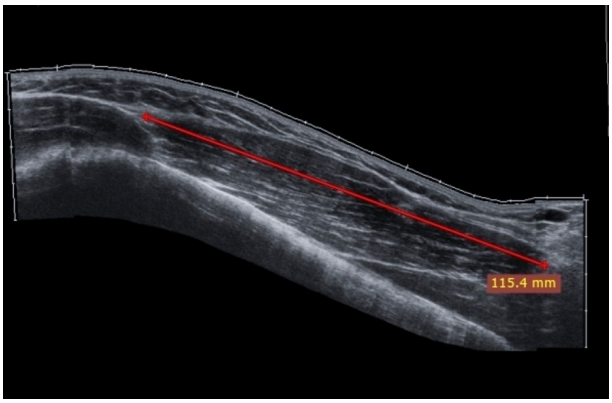

(b) The panoramic ultrasound image.

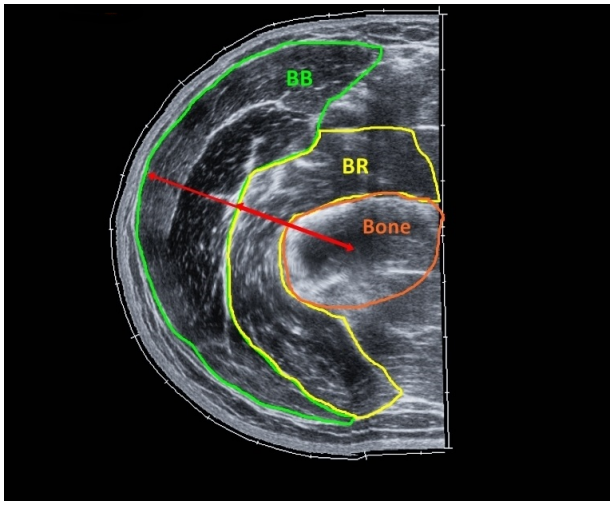

(c) The cross section ultrasound image.

Figure 4.9: The three ultrasound images of the BB muscle taken for the extraction of morphological parameters for one of the subjects.

The parameters values extracted from the ultrasound images are presented in Table 4.11 for the six subjects where ρ_b describes the adipose tissue thickness, ρ_c the skin tissue thickness and L the muscle length.

Table 4.11: The measured morphological parameters using ultrasound images for each subject

Subject	ρ_b (mm)	ρ_c (mm)	L (mm)
1	2.33	1.45	89.8
2	3.40	1.20	126.1
3	2.70	1.30	97.4
4	3.58	1.55	95.6
5	1.68	1.75	93.3
6	2.30	1.13	98.4

4.3.4 Simulation procedure

For each parameter set, we generated five anatomies with different MU placements. For each anatomy, 10 isometric contractions were simulated at: 10, 20, 30, 40, 50, 60, 70, 90 and 100% MVC. The duration of the simulation for each force level was 5 s. The sEMG and force signals were simulated at a sampling frequency of 2048 Hz. As previously described, we targeted the effect of three types of parameters: anatomical, neural and physiological.

For the anatomical parameters we distinguished between three realistic MU distribution percentages as shown in Table 4.12.

Table 4.12: MU percentages for each distribution.

MUs distribution	**SMU** (%)	**FRMU** (%)	**FIMU** (%)	**FFMU** (%)
BB_{Int}	33	17	17	33
BB_{Slow}	43	15	15	27
BB_{Fast}	37	10	10	43

Where BB_{Int} defines an "intermediate" muscle, BB_{Slow} describes a "slow" muscle and BB_{Fast} a "fast" muscle. These percentages were chosen in order to obtain a realistic distribution of MUs types in the muscle by respecting the total percentage of slow ($\sim$ 40%) and fast ($\sim$ 60%) MUs within the BB [118, 28]. We have to recall the four types of MUs present in the muscle: Slow (S), Fast Resistant (FR), Fast Intermediate (FI) and FF.

Concerning the neural parameters, we defined two different recruitment strategies that we called High Recruitment Strategy (HRS) and Low Recruitment strategy (LRS). The LRS implies that there isn't FF MUs recruited before 50% MVC (see Fig. 4.10). On the other hand, the HRS indicates that FF MUs recruitment threshold is below 50% MVC and thus, some FF MUs are recruited at 50% MVC (see Fig. 4.10). These relationship are equivalent for all MUs type distributions.

Moreover, we also tested the linear and a nonlinear rate coding strategies. Usually, the linear rate coding is adopted in simulation. It was proposed by Fuglevand et al. [20], where he considered that motoneuron firing rate increases linearly with the excitatory drive between recruitment threshold and peak firing rate levels [20]. However, in a recent experimental study [21], it was observed, using sEMG decomposition techniques, that

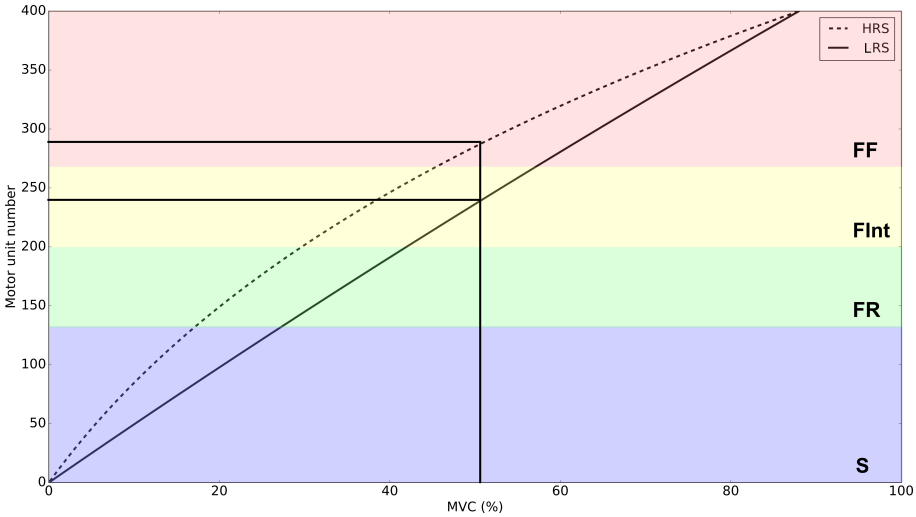

Figure 4.10: The profiles of recruitment threshold with respect to the MUS for the LRS and HRS.

the MU firing rate follows a nonlinear law. For the two types of firing rates presented above, the "onion skin" phenomenon described in [70] that defines a MU specific firing rate increasing with respect to excitation is used in the MU recruitment scheme model. This implies that MUs have specific firing rate/excitation slopes [23, 21].

Lastly, for the morphological parameters, we tested the influence of the adipose tissue thickness, skin tissue thickness and muscle length by simulating the HD-sEMG signals using the values obtained from ultrasound images and comparing the influence of each one of them. The schematic representation of the simulations with respect to the parameters variation is presented in Fig. 4.11 with the morphological parameters corresponding to each simulation are detailed in Table 4.13.

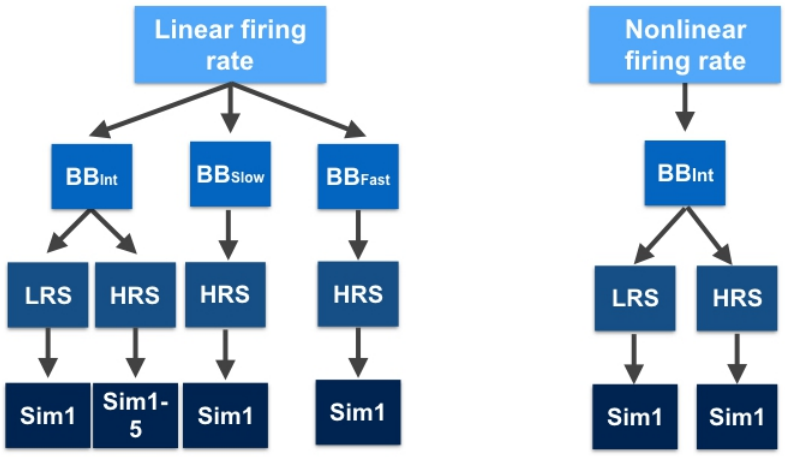

Figure 4.11: Schematic diagram presenting the configurations of parameters used for the different simulations where Sim defines the different morphological values defined in Table 4.13.

Table 4.13: Morphological parameters used for simulations

Sim	ρ_b (mm)	ρ_c (mm)	L (mm)
1	2.74	1.42	101.0
2	1.68	1.42	101.0
3	3.58	1.42	101.0
4	2.74	1.75	101.0
5	2.74	1.42	126.1

Where Sim 1, Sim 2 and Sim 3 represent the average, minimum and maximum values for the adipose tissue thickness and the average values for the skin tissue thickness and muscle length respectively. And Sim 4 and 5 represent the maximum values for the skin thickness and muscle length with average value for the adipose tissue thickness respectively.

Subsequently, we have in total 10 different configuration of parameters $\times$ 5 different anatomies $\times$ 10 levels of muscle contractions corresponding to 500 different simulations. For both HD-sEMG and force signals, we simulated a plateau of a constant force that lasted 5s at each contraction level (2048 Hz sampling frequency).

4.3.5 Data fusion & HD-sEMG/force relationship fitting

The HD-sEMG technique can be considered as an imaging tool [61] in complement to ultrasound technique and Magnetic Resonance Imaging (MRI) for assessing muscle architecture and functionality. Therefore, we propose to use an automatic and personalized channel selection method based on image segmentation. This method is obtained using a previously validated HD-sEMG image segmentation method, the watershed algorithm [178]. This approach is a non parametric unsupervised segmentation method that selects an optimal threshold based on discriminant analysis to maximize the separability of the classes in grey levels [179, 180]. This thresholding was determined on monopolar Root Mean Square (RMS) value maps for the ten studied contraction levels (10% to 100% MVC). We chose to use the Root Mean Square (RMS) parameter as an amplitude descriptor since it has shown robustness to spatial aliasing in comparison with the Average Rectified Value (ARV) which is usually used in similar studies [181]. For each contraction level, different filters are computed according to the RMS values map. This way, the chosen filter is a compromise of all the filters by multiplying the computed binary matrices. This filter is then applied to the RMS value maps in order to remove the unneeded channels. Finally, the final RMS value is obtained by averaging the values of the remaining channels. This RMS value will be used for the estimation of the force.

Based on the literature, there are different types of proposed HD-sEMG/force relationships, the linear relationship ($F = aRMS + b$) [182], the polynomial relationship ($F = \sum_{i=0}^{n} p_n RMS^n$) [183, 184], the power relationship ($F = aRMS^b$) [175] or the exponential one ($F = a \exp^{bRMS}$) [185]. Thus in this section, we propose to test these hypothesis on our database of 500 couples of signals (HD-sEMG, force) in order to assess the best fit. The fitting will be done by least square minimization. Which means that based on a predefined parametric model, the outcome of the fitting is an estimate of the model

coefficients. In order to do so, the difference between the simulated and estimated force by the model is minimized by the least square algorithm.

In order to evaluate the fitting models, we will compute the Normalized Root Mean Squared Error (NRMSE) between the simulated force and the estimated force by fitting for each one the ten simulations (parameter configurations discussed in the previous section) and five anatomies. This NRMSE is defined by:

$$NRMSE = \frac{1}{\hat{F}}\sqrt{\frac{1}{N_c}\sum_{i=1}^{N_c}\left(F_i - F_{e_i}\right)^2} \tag{4.9}$$

Where N_c is the total number of contraction levels, F_i is the averaged simulated force at the i^{th} contraction level over the 5 s of contraction, F_{e_i} is the estimated force by fitting at the i^{th} contraction level and $\hat{F}$ is the deviation between the maximum and the minimum value of F ($F_{max} - F(0)$).

Moreover we used the R-square value expressed by:

$$\text{R-square} = \frac{SS}{SST} - 1 \tag{4.10}$$

with $SS = \sum_{i=1}^{N_c}\left(F_i - \hat{F}\right)^2$ and $SST = \sum_{i=1}^{N_c}\left(F_{e_i} - \hat{F}\right)^2$

The R-square value can take on any value between 0 and 1, with a value closer to 1 indicating that a greater proportion of variance is accounted for by the model. It indicates how successful the fitting is in explaining the variation of the data.

4.3.6 Results

sEMG/force relationship shape variation with the different parameters

The two simulation models along with the processing (data fusion) stage allowed the computing of the sEMG RMS in mV and the corresponding force value in Newton (N) at a given excitation level. As previously explained, three morphological parameters that are suspected to affect the HD-sEMG/force relationship were tested. These parameters are the adipose tissue thickness (ρ_b), skin tissue thickness (ρ_c) and muscle length (L). Figure 4.12 illustrates the HD-sEMG/force relationships corresponding to different values of these parameters for the linear rate coding, HRS recruitment strategy and first MU type distribution BB_{Int}. For the adipose tissue thickness we compared between the minimum, average and maximum values obtained from ultrasound (see section 4.3.3). As for the skin tissue thickness and the muscle length, the average and the maximum values (see table 4.11) were compared.

Concerning the variation of the relations for different adipose and skin tissue thicknesses, we can clearly state that these parameters have a direct effect on the HD-sEMG/force relationship dynamic. Furthermore, the variation of these two parameters have the same effect on the relation curve. This effect manifests by shifting the curve toward smaller RMS values with increasing thickness value. On the contrary, no noticeable impact was observed from the muscle length variation.

Afterwards, the effect of both anatomical and neural parameters on the HD-sEMG/force relationship was considered. Figure 4.13 exhibits the relations relative to different types of these parameters. First, the relations for the three considered MU type distribution percentages BB_{Int}, BB_{Slow} and BB_{Fast} (see Table 4.12) illustrated for the five different

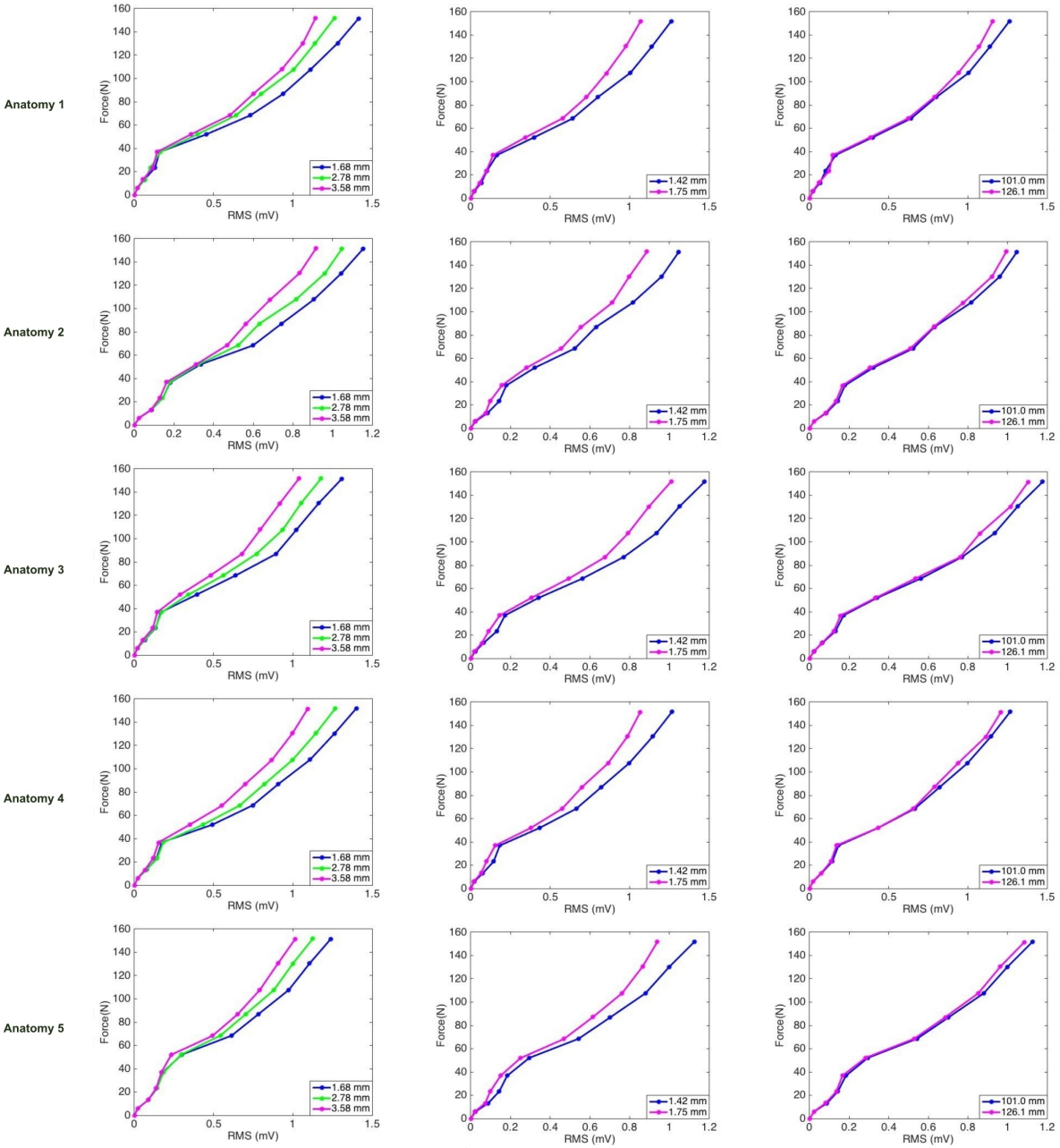

(a) Adipose tissue thickness. (b) Skin tissue thickness. (c) Muscle length.

Figure 4.12: The HD-sEMG/force relations for the five anatomies relative to different morphological parameters.

anatomies for the linear rate coding, HRS and average values of the morphological parameters were presented. Then, the two different rate coding types: L and NL as well as the two recruitment strategies: LRS and HRS were considered. For the MU type distributions, we can see an impact on the shape of the relationship, especially for the BB_{Fast} (Figure 4.13a). The main effect is the change of the curve inflection point position (see Figure 4.13).

If we consider now the neural parameters influence (Figures 4.13b and 4.13c), small variation between the relations for linear and nonlinear rate coding can be noticed in both

LRS and HRS cases. Also, there is a shift in the position of the curve inflection point between LRS and HRS.

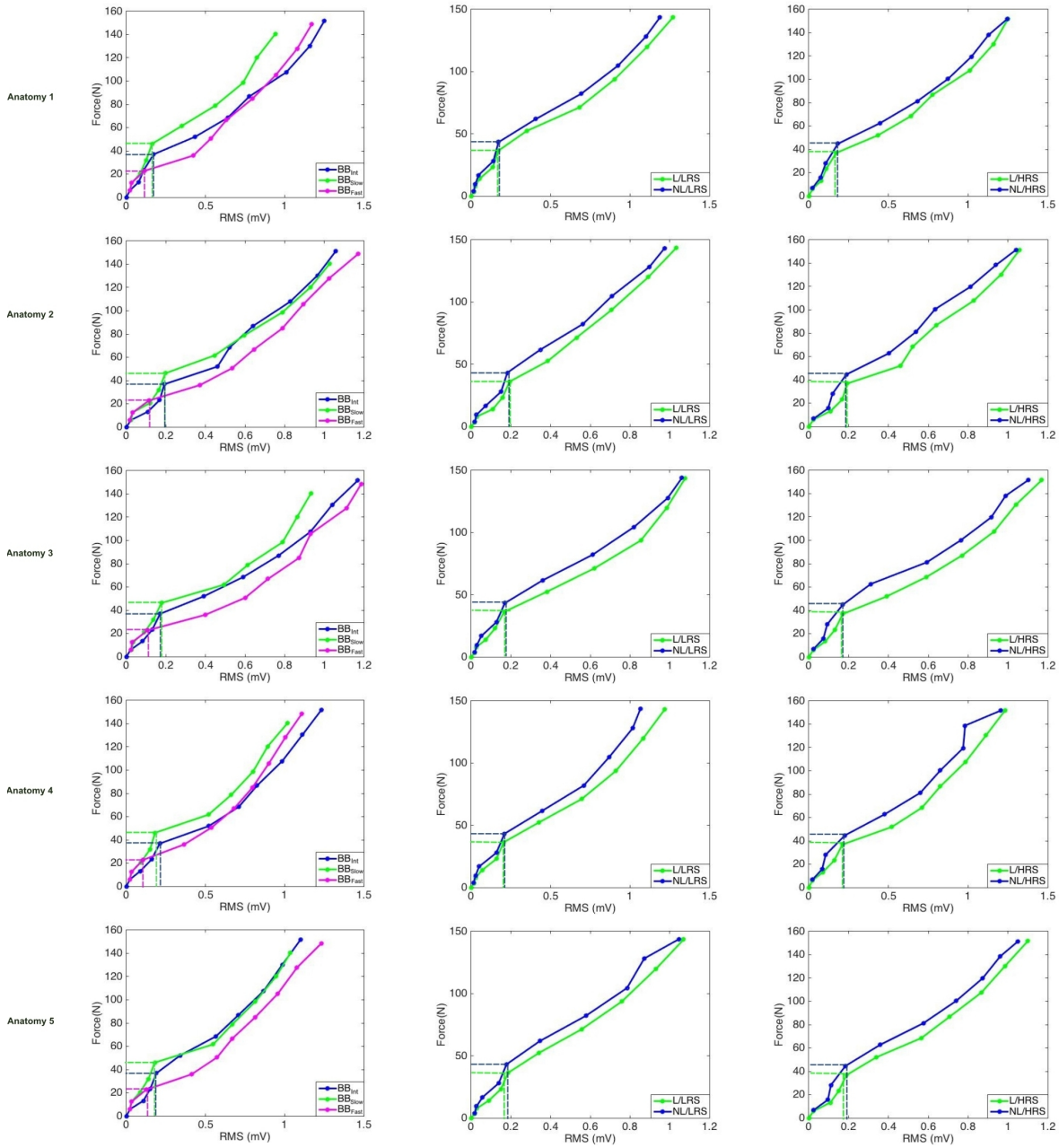

(a) MU type distributions. (b) Firing rates for the LRS. (c) Firing rates for the LRS.

Figure 4.13: The HD-sEMG/force relations for the five anatomies relative to anatomical and neural parameters (see Table 4.12) with the points indicated on the curves are the inflection points).

sEMG/force relationship modeling

The results of the fitting for the different functions mentioned in section 4.3.5 are presented in Figure 4.14. Figures 4.14a and 4.14b present the box plots of the NRMSE and the

R-square computed for the ten simulation cases respectively (see section 4.3.4). We can see that we have maximum NRMSE values for the exponential type fitting. We also have similar results for the power type as well as linear fittings. However, we have the minimal error and maximal correlation between the simulated force values and the predicted force values for the polynomial fittings (from order 3 to order 9).

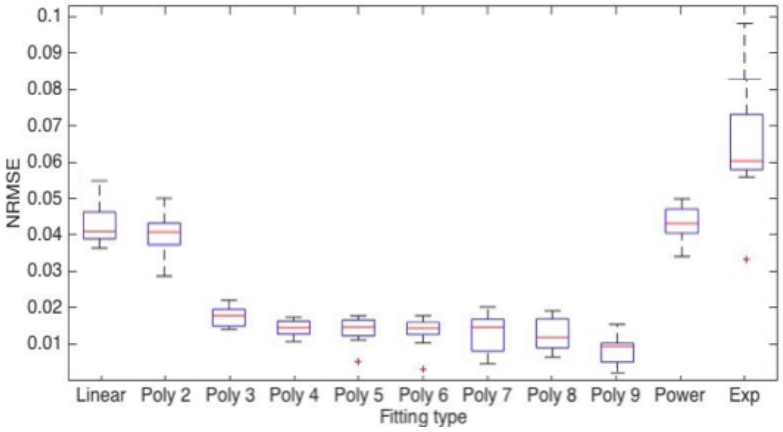

(a) The variation of the NRMSE relative to the fitting method for the different simulations.

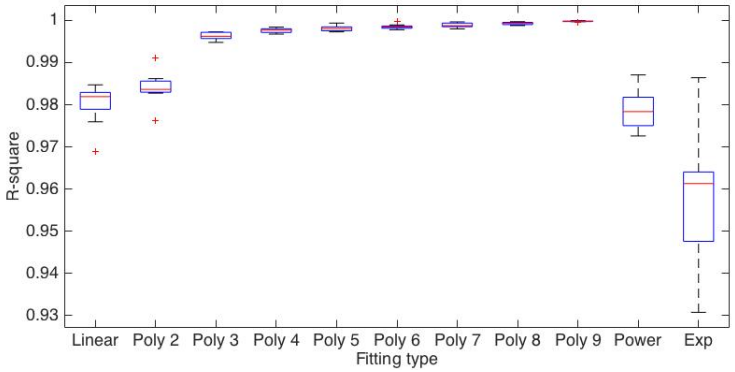

(b) The variation of the R-square value relative to the fitting method for the different simulations.

Figure 4.14: The variation of the evaluation values with respect to the fitting type.

Afterwards, a Kruskal Wallis nonparametric one-way ANOVA was performed on both NRMSE and R-square value. This test revealed significant differences for the NRMSE (χ^2(df= 10) = 86.32, $p < 10^{-6}$) as well as for the R-square value (χ^2(df= 10) = 101.56, $p < 10^{-6}$) between the ten methods used to describe the shape of the HD-sEMG/force relationship. Then, Post-hoc tests revealed maximal difference between the linear, exponential and power type fittings with 3^{th} to 9^{th} order polynomial fittings. These tests allows us to chose the best way to characterize the variation of the individual force with the RMS value. Whereof, we found the best regression type model to be the polynomial fitting (from order 3 to order 9). Moreover, we can notice that with increasing polynomial order, we have decreasing NRMSE and increasing R-square value. These values decrease significantly from the second to the third order polynom, where it attains a minimal value of 2.4 % of error, then it remains near this value as far as the 9^{th} order polynom where it decreases to 1.6 %.

Based on the study presented above, the polynomial fitting seems to be the most adequate for the studied relationship. The choice of the polynom degree should be a compromise between minimal error and complexity (number of coefficient to estimate). Thus, the 3^{rd} order polynom presents a good compromise from the number of unknown parameters to find point of view, since we have to consider the direct application of this polynom in the force estimation model (where the aim will be to estimate the parameters of the polynom). The corresponding model equation is given by:

$$F = P_3 RMS^3 + P_2 RMS^2 + P_1 RMS + P_0 \tag{4.11}$$

Where P_3, P_2, P_1 and P_0 are the polynomial coefficients obtained by the least square algorithm.

Based on the choice of the 3^{rd} order polynom, the NRMSE between the force value obtained through the polynom and the simulated value were computed. An error that varies between 0.99 and 2.35% with a mean ± std = 1.64±0.17% was found.

In presence of residual muscle activity and noise, the force level is assumed to be equal to 0 for an almost 0 RMS value, giving $P_0 = 0$. Therefore, the fitting procedure should be adapted in order to take into account the first point of the relationship (0 mV, 0 N). Thus, an adapted version of the least square algorithm presented above was used, where the curve was forced to pass by the origin point. This was done through the use of a linear constraint with the linear least square algorithm. The error results obtained using the optimization method are depicted in Tables 4.14 for the different configurations of parameters and the five MU anatomies. The new mean error is equal to 1.80 ± 0.26% which indicates an increase of 0.15% of fitting error in comparison with the original fitting algorithm with no constraint.

Table 4.14: The NRMSE computed for the 3^{rd} degree polynom fitting by optimization for the different morphological, anatomical and neural parameter values in %.

Anatomy	BB_{Int}								BB_{Slow}	BB_{Fast}
	LRS/L	HRS/L	LRS/NL	HRS/NL	LRS/L				LRS/L	LRS/L
	Sim1				Sim2	Sim3	Sim4	Sim5	Sim1	Sim1
1	2.20	2.31	2.21	2.48	2.31	1.61	1.65	1.54	1.82	1.23
2	1.65	1.54	1.33	1.78	1.54	1.57	1.39	1.71	1.66	1.51
3	1.94	1.34	1.37	1.70	1.34	1.75	1.70	1.38	1.89	1.65
4	2.15	1.77	1.24	2.14	1.77	1.42	1.71	1.93	2.19	2.31
5	1.90	1.73	1.77	1.55	1.73	2.29	1.10	1.83	2.21	2.35

Using the relationship obtained from the fitting study above, we performed a focused sensitivity analysis of the variation of the polynomial coefficients according to the previously discussed parameters. Therefore, the same data obtained from the models described previously, was exploited to study each parameter effect on the polynomial coefficients. Figures 4.15 and 4.16 illustrate the variation of the coefficients P_3, P_2 and P_1 according to adipose and skin tissue thickness variation respectively. These results confirms our previous observation that all the coefficients change in the same manner. By inspecting further the plots in Figures 4.15 and 4.16, we can notice that we have the same sign for the coefficients, P_3 and P_1 that are always positive in contrast to P_2 which is always negative.

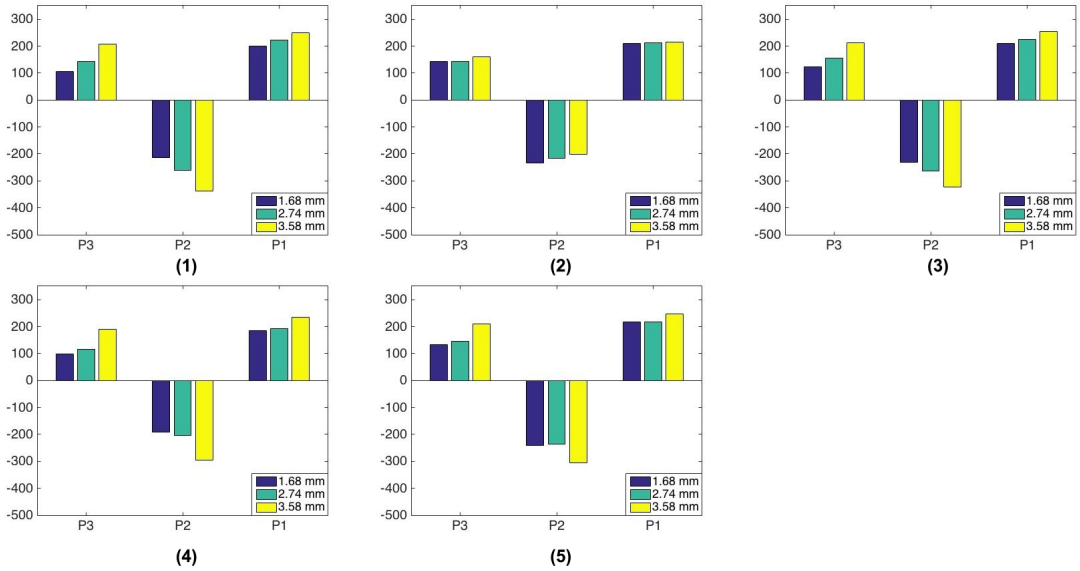

Figure 4.15: P_3, P_2 and P_1 coefficients variation according to adipose tissue thickness value for the five anatomies.

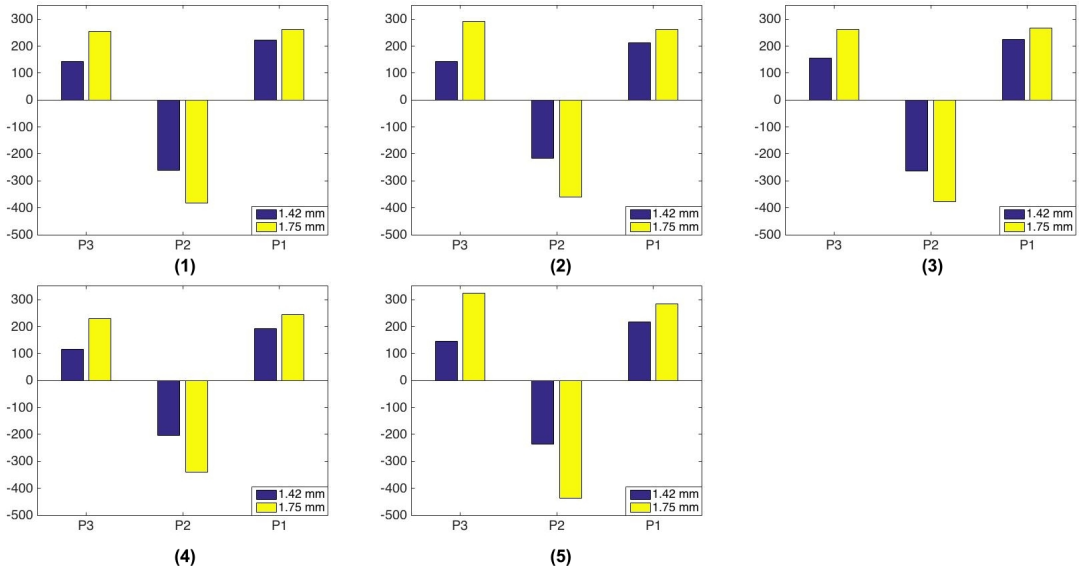

Figure 4.16: P_3, P_2 and P_1 coefficients variation according to skin tissue thickness value for the five anatomies.

Also, we can observe that the parameters amplitude increase while increasing skin and adipose tissue thickness. This means that when the skin or adipose tissue increases, we obtain the same force for less RMS value due the spatial filtering of the sEMG signals caused by these tissue conductivities.

Considering now the MU type distributions, the variation of the polynom coefficients with respect to the MU type percentages in the muscle are presented in Figure 4.17. The first observation from Figure 4.17 is that we have the same signs for the polynomial coefficients in the three MU type distributions cases. If we compare between BB_{Int} and BB_{Slow}, we can see that we have an increase in the polynom coefficients for BB_{Slow},

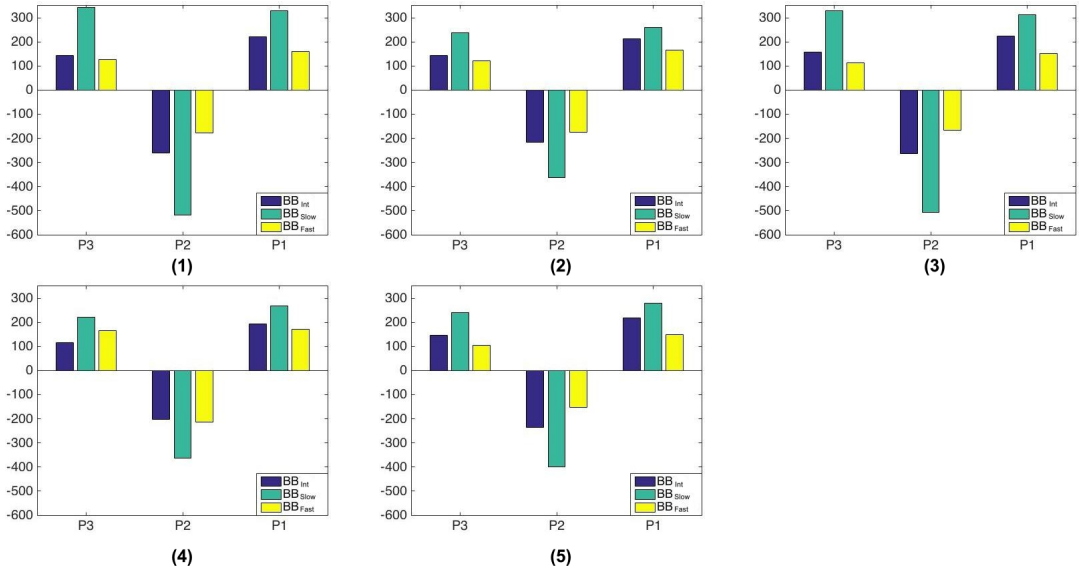

Figure 4.17: P_3, P_2 and P_1 coefficients variation according to the different MU type distributions for the five anatomies.

where we have more SMUs than FFMUs, in comparison with BB_{Int} where we have the equal numbers of SMUs and FFMUs. On the contrary, if we compare between BB_{Int} and BB_{Fast}, where we have more FFMUs that SMUs, we can see a decrease in all parameters.

Finally, for the neural parameters evaluation, if we look at the polynom coefficients presented in Figure 4.18, we can see the influence of the recruitment strategy. For almost all the different anatomies we have a decrease in the value of the coefficients when we go from LRS to HRS. This is true in both linear and nonlinear rate coding cases. Differently, if we compare between the polynomial coefficient for the linear and the nonlinear rate codings, we can see that we have slightly higher coefficient values for the nonlinear rate coding.

4.3.7 Discussion & Conclusion

This simulation study based on muscle modeling allowed us to explore the parameters that affect the HD-sEMG/force relationship. In addition, using this realistic personalized HD-sEMG simulation model along with an individual force generation model, we were able to find the most adequate equation that can describe this relationship in isometric non fatiguing voluntary contraction context.

The first part of this study, as previously explained, was aimed towards analyzing the different types of parameters that can influence the shape of the sEMG/force relationship. Starting by the morphological parameters, we found that the adipose and the skin tissue thicknesses have an impact on the dynamic of the relationship. This effect is expected due to the filtering effect of these tissues on the sEMG signals [186]. This filtering effect is more pronounced for the skin tissue as for the adipose tissue.

For the functional parameters, we observed a change in the position of the relationship curve inflection point for the different distributions of MU types in the BB muscle. The inflection point position has the highest force value (>45 N) for the BB_{Slow} muscle type and the lowest force value (<25 N) for the BB_{Fast} muscle type. As for the BB_{Int} muscle

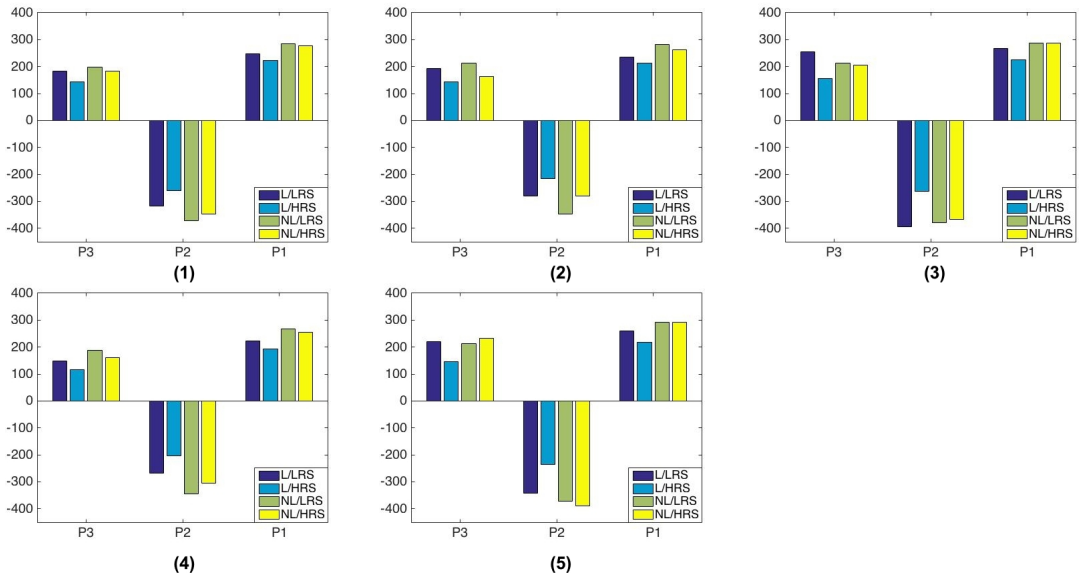

Figure 4.18: P_3, P_2 and P_1 coefficients variation according to the different spatial recruitment strategies (LRS vs HRS) and firing rates (linear vs nonlinear) for the five anatomies.

type distribution the position of the inflection point is between 30 and 40 N. This observation is similar in all five anatomy cases. These variations can be explained according to the MU distribution types. For example, for BB_{Fast} distribution, we have more FFMUs, therefore it is expected for the relationship to change shape earlier than in the BB_{Int} case where we have equal number of SMUs and FFMUs which means FFMUs are recruited later on, even more so for the BB_{Slow} where we have more SMUs than FFMUs which explains the inflection point at 50% MVC (i.e: the fifth point on the plots). One can also observe that the BB_{Int} strategy reaches the higher force value at 100% followed by BB_{Fast} and BB_{Slow} strategies respectively. This important observation put a focus on the role of both SMUs and FFMUs in building the force output.

Lastly for the neural parameters, we found a variation in the position of the inflection point between LRS and HRS. If we compare between the first plot in Figure 4.13b and 4.13c, we can see that the inflection point of the HRS curves are positioned at 50% MVC instead of 40% MVC for the LRS. This can be explained by the fact that for the HRS strategy, we have FFMUs that are recruited before 50% MVC which is not the case for the LRS strategy. Now, if we compare between the rate coding schemes we can see that the NL rate coding corresponds to a higher force value ($\sim$ 44 N) than the L rate coding scheme ($\sim$36 N). For the rate coding scheme effect (Figs. 4.13b and 4.13c), we can notice that for the same RMS values, we have more produced force for the nonlinear rate coding in comparison with the linear which is expected since the discharge frequency per MU is higher in the nonlinear case than the linear one for the same excitation level.

In the second part of this study, we tested different fitting algorithms in order to find the best equation that describes the HD-sEMG/force relationship. Thus, we compared between four different types of models: linear, polynomial, power and exponential (see section 4.3.5). These models were previously mentioned in literature. However, this is the first study where they are employed in a simulation context. After computing the NRMSE results for these different equations, we found the 3^{rd} order polynom to be the best to

describe the observed relations in terms of NRMSE and number of unknown coefficients.

Afterwards, we used this relation type (3^{rd} order polynom) in order to study in depth the impact of the morphological, anatomical and neural parameters on the shape of the relationship. Among the tested morphological parameters, we found an important impact of the adipose and skin tissue thickness. This impact revealed a monotonic variation of the polynom coefficient values with the thicknesses values (Figs. 4.15 and 4.16). Where we have an increase of the coefficients amplitude with increasing skin and adipose tissue thicknesses. These variations in the values of the polynomial coefficients are dependent on the muscle's anatomy. For the MU type distribution in the muscle, we found a consistency in the variation of the polynomial coefficient values with the shape of the relationship variation that was analyzed in section 4.3.6. Since this type of functional parameters has a significant effect of the relationship shape, thence it impacts the coefficients of the 3^{rd} degree polynom. In fact, we obtained the minimal coefficients for the BB_{Fast} distribution (Fig. 4.15) which is logical since we have maximum number of FFMUs, which mean that we have larger muscle fibers that produce more force [168]. However, these large fibers conduct faster and ergo their amplitude will be reduced [168] which explains that we have less force for same values of RMS. The same explanation could made toward the BB_{Slow} distribution in order to justify the high coefficient values. The last type of parameters that we tested was the neural parameters, we observed that the major influence was due to the rate coding. If we compare between the L and NL rate coding schemes in Fig. 4.18, we can see that we have almost for the five anatomies an increase in values of the coefficients when we switch from L to NL rate coding. In contrast, we have a decrease of the coefficient values from LRS to HRS. It was shown by Lawrence and De Luca that the BB relies essentially on the spatial recruitment to increase its force not on the rate coding scheme [174]. This was observed in Figs. 4.13b and 4.13c where we have higher produced force in N in the HRS case for the save $\%MVC$.

Further, we found that the spatial positioning of the MUs in the muscle has an influence on the relation even when all other parameters are fixed to certain values. This observation was clearly demonstrated when we generated five different anatomies of muscle (different MU placements) for each configuration of parameters and we found that we have an important standard deviation among the observed polynomial coefficient set. This means that the HD-sEMG/force relationship is subject specific and should be adapted to each subject's personal morphological, neural and anatomical properties. We also have to mention, that we tested the effect of different simulations of the recruitment patterns for the same MU anatomy and muscle configuration. However, we did not find a variation in the relationship between five different recruitment patterns with the same spatial recruitment law and rate coding (std = 0.0768 N).

This work presents a reliable and realistic study of the sEMG/force relationship shape as well as some of the factors that can affect it. One of the closest studies to our paper was that of Zhou and Rymer regarding the study of the factors that affect the form of the relationship between the muscle force and the EMG [22, 146]. They found that the firing rate strategy has a substantial impact on the form of the sEMG/force relation. They also suggested that this relationship is governed by the relation between electrical and mechanical properties of individual MUs [22]. However, the sEMG approximation model used in this study rely on the HR functions [22, 146] which is not very realistic since it does not take into account MU types, locations or fiber arrangements. It also doesn't consider the effect of the electrode positioning nor the adipose and skin tissue thicknesses [47]. Thus, they made many simplifications to their model as well as hypotheses. Therefore,

their relation models are normalized with respect to sEMG and muscle force values. In our work, we used a more realistic HD-sEMG simulation model [10] that allows us to obtain the sEMG signals in mV. This enabled us to represent the relationship between the sEMG amplitude in mV and the muscle force in N. Thereupon, the 3^{rd} order polynomial equation proposed in this study allowed the computing of the muscle force value in N after estimation of the polynomial coefficients. We also tested the impact of different parameters on the shape of the relationship as well as on the polynomial coefficient values.

The shape analysis of the sEMG/force relationship presented in this work, as mentioned earlier, was based on the BB muscle properties in voluntary, non-fatiguing context and was mainly focused on three groups of parameters. This proposed analysis can be adapted in order to study the sEMG/force relationships for other striated muscles, where both sEMG and force generation models parameters should be adapted in order to simulate the HD-sEMG and force signals appropriate to the considered muscle. Further, this method of data fusion and sensitivity analysis can be employed in a fatiguing context in order to study the effect of additional parameters on the sEMG/force relationship such as the MU synchronization and firing rates [187, 188]. Other additional parameters to consider are the different skin, adipose and muscle tissue conductivities that have an important influence on the RMS amplitude [11, 189]. However, there is a lack of realistic studies in order to determine the values for these conductivities. In our study, we used the values proposed by Farina et al. [7] for their cylindrical model. From the point of view of the force, we can also consider in future work the effect of the different twitch parameters presented in Table 4.10 on the sEMG/force relationship shape. Moreover, a more realistic mechanical model (see chapter 3) of the muscle with personlaized parameters as well as for the electrical model can be used in order to better assess the muscle force generated. This model (chapter 3) describes the muscle mechanical contribution with the corresponding muscle deformation during the isometric contraction. During contraction it is known that the muscle thickness increases and the adipose and skin tissue thicknesses decrease. This issue will be studied in the next section 4.4.

Finally, we hope that the proposed simulation study will help physicians, practitioners, and researchers in biomechanics in a better understanding of the complex mechanisms responsible of the electrical and mechanical manifestations of the muscle contraction. In future work, we intend to employ this model in a multi-muscle experimental context where we will model the individual sEMG/force relationship of the BB from the global moment produced by the elbow flexors (BB, Brachialis and Brachioradialis) during isometric anisotonic non-fatiguing voluntary contractions.

4.4 Quasi-dynamic model of the skeletal muscle during isometric contraction

In this section, we will propose for the first time, an analytical, multiscale and deformable volume model of a skeletal muscle during isometric contraction. During isometric contractions, muscle thickness, the muscle fiber pennation angle, the muscle fascicle length, the adipous tissue thickness as well as the skin tissue thickness change. Because all these architectural parameters modifications, the muscle electrical activity is markedly modified [190]. Thus, sEMG signal generation modeling should consider those changes in the muscle architecture according to the related muscle deformation. The computation scheme is presented in Fig. 4.19.

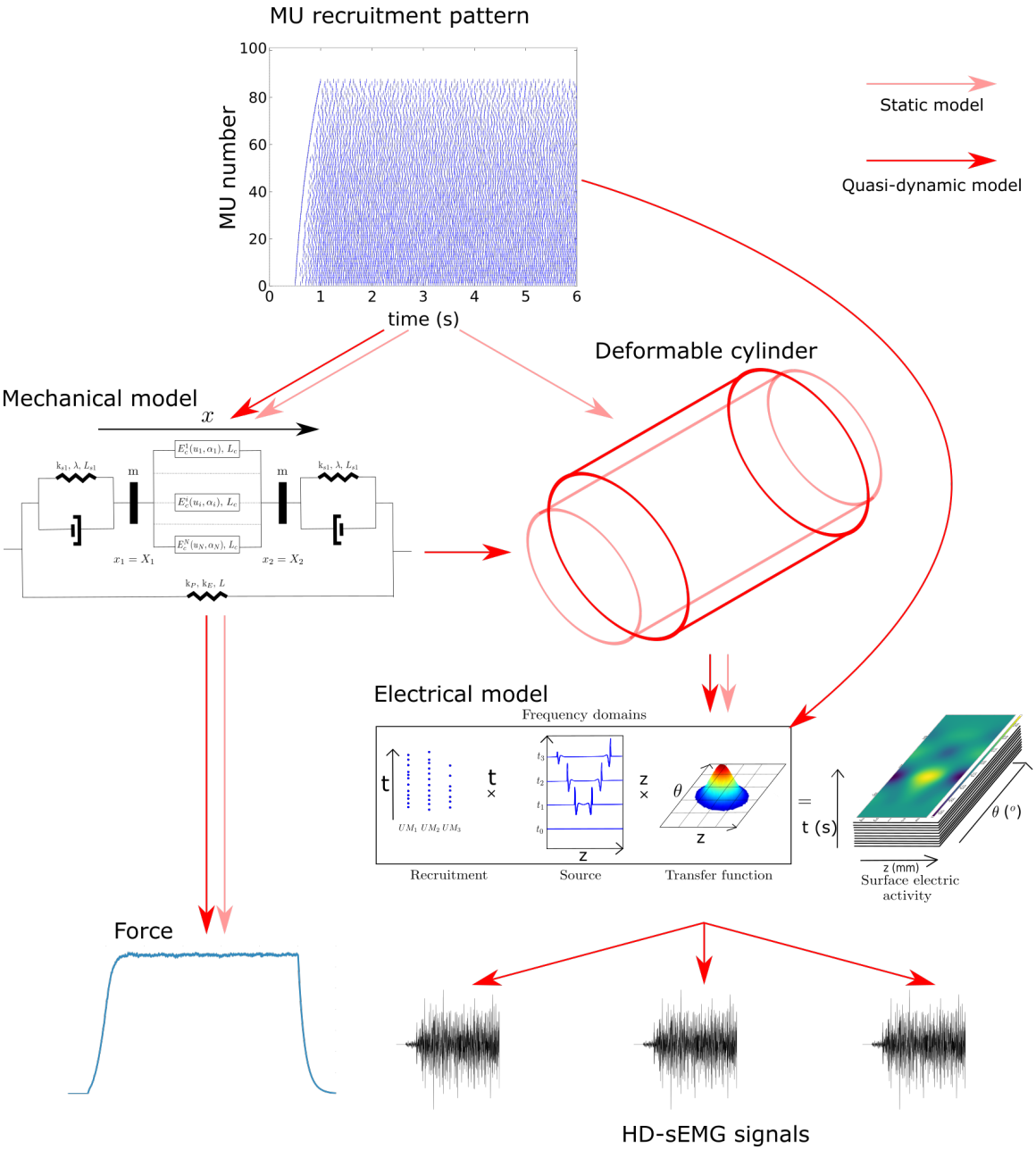

Figure 4.19: Computation scheme of the deformable model. Formerly, both mechanical and electrical models performed the simulations without interacting together (opaque red lines). Currently, the deformable model simulation is performed first and communicate the corresponding muscle deformation according to the MU recruitment pattern. This deformation will be considered to shorten the cylindrical muscle volume under isovolumic assumption (plain red lines).

4.4.1 Deformable muscle model

As introduced, we will define a quasi-dynamic model by using the electrical and the mechanical model of the striated muscle from the same MU recruitment pattern. This quasi-dynamic model will consider the muscle deformation during isometric contractions for the muscle's electrical activity generation.

For this purpose, muscle deformation is obtained from from the mechanical model where the muscle force, stiffness and deformation are computed. Muscle deformation for the isometric contraction is computed as the single scalar from the mean of the deformation during the sustained contraction. From this deformation, we can determine the muscle shortening according to its rest length for the given contraction (see Fig. 4.20).

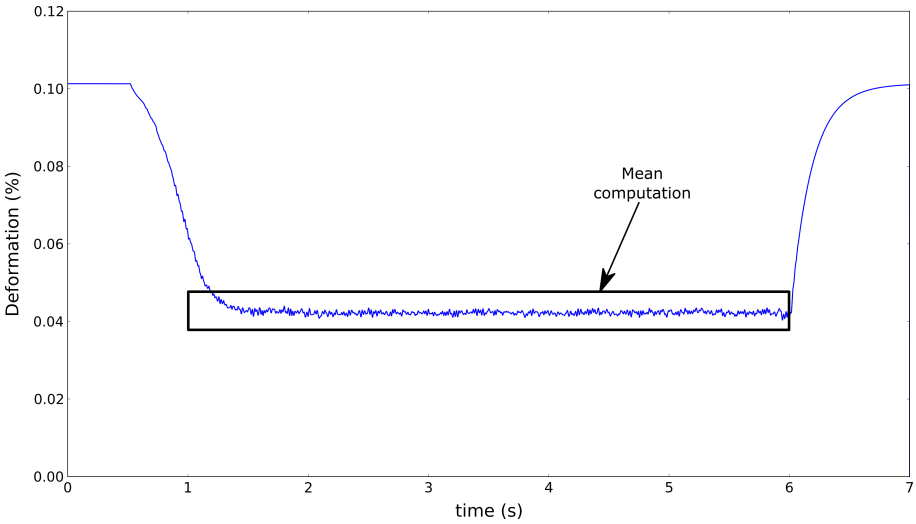

Figure 4.20: Determination of the muscle shortening during the isometric contraction.

Then, assuming isovolumic and isosurfacic hypotheses, the muscle architecture can be updated. Here, the muscle architecture is described as a multilayered cylinder where the muscle, the adipose and the skin tissues are considered. During contraction, the muscle thickness increases whereas the adipose and skin tissues thicknesses decrease. To determine the deformed muscle thickness, we assume the isovolumic hypothesis:

$$V_0 = V_1 \tag{4.12}$$

Where, V_0 is the muscle volume at rest and V_1 is the muscle volume during contraction. Considering the cylinder shape of the muscle, we have:

$$h_1 = h_0 - h_0.\varepsilon \tag{4.13}$$

with, ε is relative deformation according to the mechanical model, h_0 and h_1 are the muscle length at rest and during contraction, respectively. Moreover considering the muscle radius, we have:

$$\begin{aligned} h_0\pi\left(R_m^0\right)^2 &= h_1\pi\left(R_m^1\right)^2 \\ \Rightarrow R_m^1 &= R_m^0\sqrt{\frac{h_0}{h_1}} \end{aligned} \tag{4.14}$$

with, R_m^0 and R_m^1 are the muscle radius at rest and during contraction, respectively. Considering a shortening of the muscle, $h_1 < h_0$ giving a ratio above 1.0 and thus, an increase of the muscle radius. Because the muscle thickness raises during isometric contraction, the fiber diameter also raises. We supposed that the fiber diameter is related to the muscle thickness increase. Also, the MUs and fibers positions have to change

according to the muscle contraction. As well as with the fiber diameter, the MU and fiber radial positions change proportionally to the muscle thickness increase while their angular positions don't change (see Fig. 4.21).

$$d_f^1 = d_f^0 \frac{R_m^1}{R_m^0} \tag{4.15}$$

$$\rho_{MU}^1 = \rho_{MU}^0 \frac{R_m^1}{R_m^0} \tag{4.16}$$

$$\rho_f^1 = \rho_f^0 \frac{R_m^1}{R_m^0} \tag{4.17}$$

Where, d_f^1 and d_f^0 are the fiber's diameter during contraction and at rest, respectively. ρ_X^1 and ρ_X^0 are the radial position of the fiber or the MU during contraction and at rest, respectively.

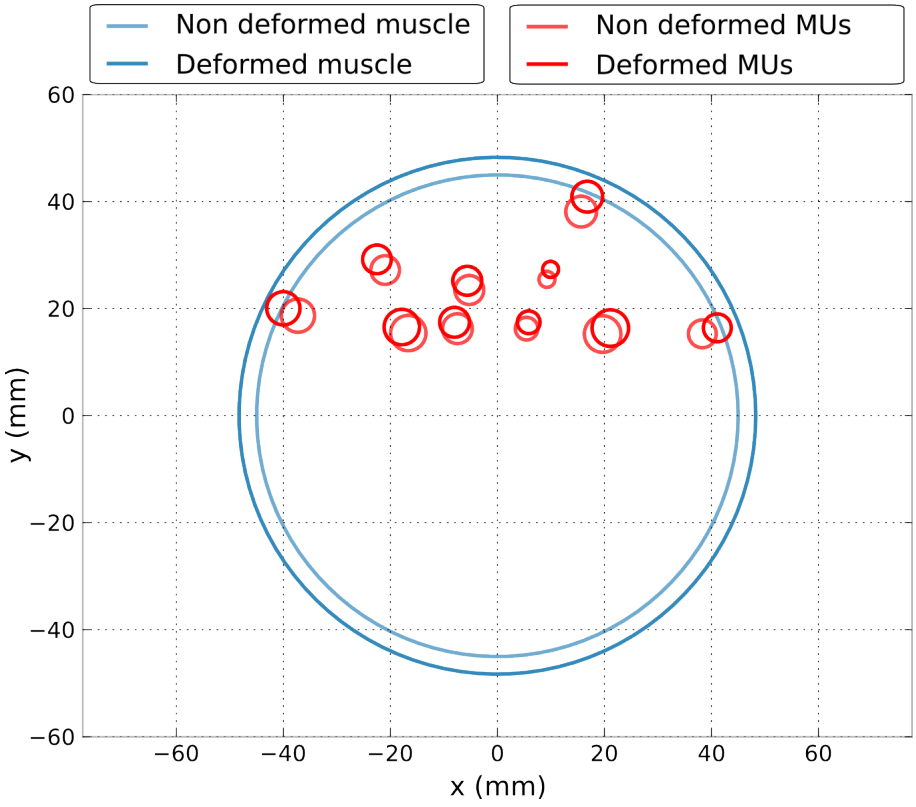

Figure 4.21: Illustration of the anatomical changes in the of the muscle between the non deformed model and the deformed.

Considering the adipose and skin tissues thickness, we use the isosurfacic assumption. Meaning that their area remains stable, if the radius increase then it will induce a decrease of their thickness. Thus, we have for the adipose tissue thickness:

$$\begin{aligned} \pi\left(R_m^0 + t_f^0\right)^2 - \pi\left(R_m^0\right)^2 &= \pi\left(R_m^1 + t_f^1\right)^2 - \pi\left(R_m^1\right)^2 \\ \Rightarrow \left(R_m^1 + t_f^1\right)^2 &= \left(R_m^0 + t_f^0\right)^2 + \left(R_m^1\right)^2 - \left(R_m^0\right)^2 \\ \Rightarrow t_f^1 &= \sqrt{\left(R_m^0 + t_f^0\right)^2 + \left(R_m^1\right)^2 - \left(R_m^0\right)^2} - R_m^1 \end{aligned} \tag{4.18}$$

where, t_f^0 and t_f^1 are the adipous layer thickness at rest and during contraction, respectively. And the skin tissue thickness determines as follow:

$$\begin{aligned}
\pi\left(R_m^0 + t_f^0 + t_s^0\right)^2 - \pi\left(R_m^0 + t_f^0\right)^2 &= \pi\left(R_m^1 + t_f^1 + t_s^1\right)^2 - \pi\left(R_m^1 + t_f^1\right)^2 \\
\Rightarrow \left(R_m^1 + t_f^1 + t_s^1\right)^2 &= \left(R_m^0 + t_f^0 + t_s^0\right)^2 + \left(R_m^1 + t_f^1\right)^2 - \left(R_m^0 + t_f^0\right)^2 \\
\Rightarrow t_s^1 &= \sqrt{\left(R_m^0 + t_f^0 + t_s^0\right)^2 + \left(R_m^1 + t_f^1\right)^2 - \left(R_m^0 + t_f^0\right)^2} - R_m^1 - t_f^1
\end{aligned} \tag{4.19}$$

where, t_s^0 and t_s^1 are the skin thickness at rest and during contraction, respectively.

Following the implementation of the electrical and mechanical models, this model is also implemented in *Python* programming language. Implementation of the deformable muscle model was facilitated thanks to the modular programming of the electrical and mechanical models. Both models were developed using the same approach with the same input, i.e., the MU recruitment pattern. Communication between the mechanical and the electrical models is performed through the update of the muscle anatomy under isovolumic assumtion based on the mechanical deformation. Once the muscle volume updates, the electrical model performs the simulation with the updated parameters.

4.4.2 Results

In this section, we will present a comparison of the same simulation with and without deformation. First of all, we will study the trend of the muscle anatomical deformation according to the contraction level. Finally, a comparison between generated signals and computed statistics will be exhibited at each contraction level from 10 to 100% MVC every 10%. For reliability purpose, we performed the simulations for 5 different anatomies. All the anatomies followed the same parameters, only the MU positions and their firing times are different. The parameters used for the simulations are presented in the Table 4.15.

Where $\mathcal{N}(\mu,\, \sigma^2)$ denotes the Normal distribution with mean μ and variance σ^2, and $\mathcal{U}(a,\, b)$ denotes the Uniform distribution between the interval $[a,\, b]$ with $a < b$.

This table summarizes the personalized parameters values used for the simulations, non exhibited parameter doesn't change compared to their presentation in previous chapter (see Tables 3.1 and 2.8).

Muscle deformation according to contraction level

In this section, we study the effect of the deformation on the anatomical definition of the muscle according to the contraction level. This way, we will be able to assess the reliability of the isovolumic hypothesis. On Fig. 4.22, we can see a geometrical representation of the muscle deformation according to four different contraction levels for one simulated muscle. Since the 5 simulated muscles have the same defined parameters and only the MU positions and the MU recruitment scheme is different, the observed results are the same among the 5 simulated muscles.

As one can see on Fig. 4.22, the muscle length decreases with the increase of the contraction level. This decrease doesn't follow a linear relationship. Moreover, we can also see that the muscle swelling increase with the contraction level. Considering the nature of the muscle contraction that is an isometric contraction we can see on Fig. 4.22 that the structure tendon-muscle remains stable whatever the contraction level.

Table 4.15: Parameters used for the simulations

Parameters	Value (unit)
Number of MUs (n_{MU})	770
MU type distribution (S, FR, FI, FF)	25, 15, 17, 43 (%) [28]
S MU radius (r_S^{MU})	$\mathcal{N}$(2.5, 0.5) (mm)
S MU fibers number (n_S)	$\mathcal{N}$(100, 10)
FR MU radius (r_{FR}^{MU})	$\mathcal{N}$(2.75, 0.5) (mm)
FR MU fibers number (n_{FR})	$\mathcal{N}$(150, 15)
FI MU radius (r_{FI}^{MU})	$\mathcal{N}$(3.0, 0.5) (mm)
FI MU fibers number (n_{FI})	$\mathcal{N}$(200, 20)
FF MU radius (r_{FF}^{MU})	$\mathcal{N}$(3.25, 0.5) (mm)
FF MU fibers number (n_{FF})	$\mathcal{N}$(250, 25)
Muscle length (L)	101.1 (mm) [57]
Muscle radius (ρ_m)	45.0 (mm) [57]
Bone radius (ρ_b)	15.0 (mm) [57]
Recruitment range (RR)	88 (%) [68]
Time sampling (f_t)	4096 (Hz)
Muscle optimal length (L_{c0})	91.8 (mm) [144]
Force/length, force/velocity parameters (a, b)	1.0, 0.54
Maximal force (F_{max})	750 (N)
Maximal stiffness (k_{max})	16 (N.mm^{-1}) [144]
Tendon stiffness (k_s)	30 (N.mm^{-1}) [144]
Tendon viscosity (λ)	19 (kg.s^{-1})
Muscle weight (m)	310 (g) [191]
S fiber diameter (d_f^S)	$\mathcal{N}$(45, 1) (μm)
FR fiber diameter (d_f^{FR})	$\mathcal{N}$(50, 1) (μm)
FI fiber diameter (d_f^{FI})	$\mathcal{N}$(55, 1) (μm)
FF fiber diameter (d_f^{FF})	$\mathcal{N}$(60, 1) (μm)
Conduction velocity (v)	4.0 (m.s^{-1})
Neuromuscular junction center (NMJ_c)	$\mathcal{U}$(-15.0, 15.0)
MU neuromuscular junction dispersion (NMJ_{MU})	10.0 (mm)
Left and right myotendinous length (MTZ_L, MTZ_L)	$\mathcal{N}$(15,2) (mm)
Radial, angular muscle conductivity (σ_m)	0.1 (S.m^{-1})
Longitudinal muscle conductivity (σ_{mz})	0.5 (S.m^{-1})
Adipose tissue conductivity (σ_f)	0.05 (S.m^{-1})
Adipose tissue thickness (t_f^0)	2.0 (mm)
Skin tissue conductivity (σ_s)	1.0 (S.m^{-1})
Skin tissue thickness (t_s^0)	1.0 (m)

In order to better understand the effect contraction level on the muscle deformation, we will present these deformations (shortening and swelling) according to 10 contraction levels from 10 to 100% MVC.

On the Figs. 4.23a and 4.23b, the muscle lengthening and swelling are presented according to the 10 contraction levels. As we can see on Fig. 4.23a, the relationship

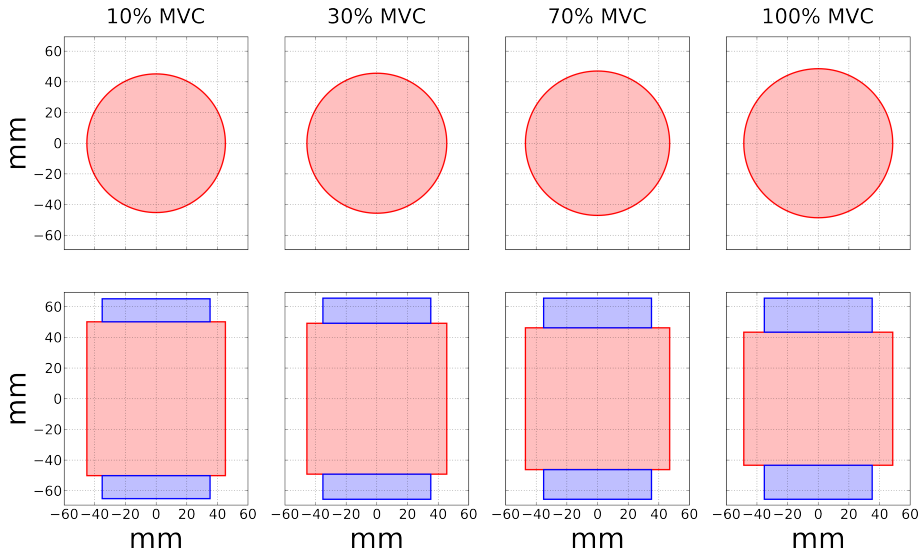

Figure 4.22: Geometrical muscle shortening (bottom) and muscle swelling (top) according to four contraction levels: 10, 30, 70, 100% MVC. In red the muscle and in blue the representative tendons.

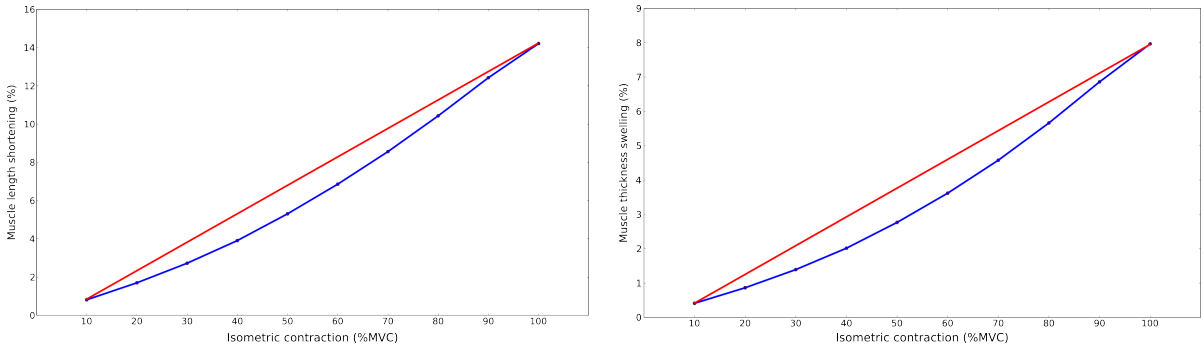

(a) Muscle shortening according to the contraction level

(b) Muscle swelling according to the contraction level

Figure 4.23: Muscle shortening and swelling relationship according to contraction levels. The red dots exhibits the values of the corresponding effect for the given activation. In red the linear relationship.

between muscle activation and muscle shortening is non linear. Comparing to [144], the muscle shortening is measured from the tendon displacement. At 60% MVC the tendon displaces about 9mm leading to a muscle shortening of 8.9%. Moreover, the muscle shortens by 7% that is close to experimental measurement [144]. According to the simulation, this relationship for a muscle like the Biceps Brachii is a convex non linear function. Yet, in [144] the tendon displacement begins to be steady at 40 and 60% MVC supposing a maximal lengthening of the tendon (and thus of the muscle) at this muscle activation level.

Moreover, from observation on Fig. 4.23b, the relationship between the muscle swelling and the muscle activation is also non linear. In contraction, the authors in [144] didn't measure the muscle thickness. As for the shortening this relationship can also be described

by a convex non linear function.

Finally, we studied the elastic modulus of the corresponding muscle. For this purpose, the strain (or proportional deformation) was computed as:

$$\varepsilon = \frac{L - L'}{L} \tag{4.20}$$

Where L is the muscle length during rest and L' is the muscle length during contraction.

Moreover the stress (or force per unit area) value was computed as:

$$\sigma = \frac{F}{A} \tag{4.21}$$

Where, F is the muscle force generated during the contraction and A the area where this force is applied. Considering the cylinder shape of the muscle, this area is a disk giving: $A = \pi R^2$ with R the muscle radius during contraction.

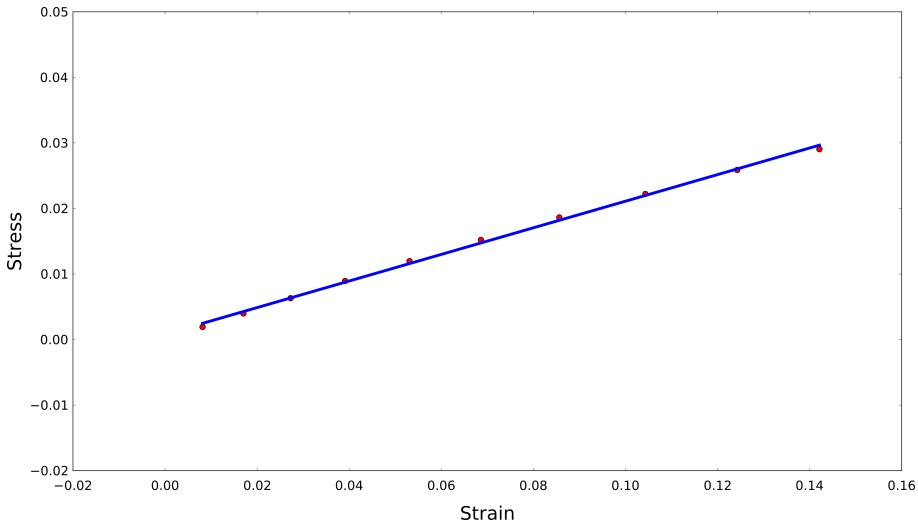

Figure 4.24: Stress-strain curve. Red dots are the values computed for each contraction level. Blue line is the linear regression function computed according the to red dots.

According to Fig. 4.24, one can observe that the stress-strain curve is almost linear. This linearity denotes an elastic response of the muscle to a deformation. This elastic property is well-known for the skeletal muscle [8]. Moreover, from Fig. 4.24, we can extract the Young modulus of the muscle. Thus, for this model of the Biceps Brachii we have a Young Modulus of 0.02 N.mm^{-2} giving 20 kPa for the first point (10% MVC). This value is in agreement with measurements on the Biceps Brachii [192].

Comparison on the signal shape

In this section, we will study the effect of the muscle deformation on a signal at 70% MVC.

As we can see on Fig. 4.25, the deformation of the muscle mainly has an effect of time shift on the signal. This time shift is observed for all the signals of all the simulations. One can observe on Fig. 4.25, that the signal generated with the deformable model is recorded in advance compared to the signal generated with the non deformable model.

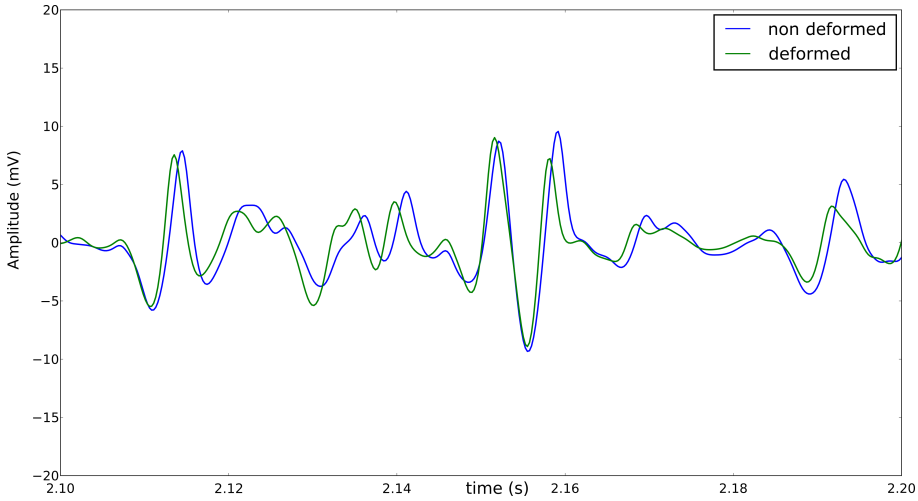

Figure 4.25: sEMG signal on a frame of 100ms recorded from the same electrode from two simulations where the deformation is considered (green) and isn't (blue).

In fact, during the contraction, we assumed that the muscle fiber has a higher diameter than at rest. As supposed in the electrical model [10], the fiber conduction velocity is related to the fiber diameter. Thus, an increase of the fiber diameter will induce an increase of its conduction velocity and then, an electrical signal that propagates faster. Moreover, this time shift effect can be explained from the reduction of the adipose and skin tissues thicknesses. Intermediate layers between the electrical sources and the recording system have a low-pass filtering effect that spreads the signal and thus induce a time shift. Reducing the thickness reduces this filtering effect. Moreover, we can see a slight alteration on the signal amplitude. This amplitude changing can be explained from the layer thicknesses change. In fact, reducing the adipose and skin tissues thickness will also reduce their filtering effect on the signal [57]. On the other hand, there is an increase of the muscle thickness due to the swelling effect. Accumulation of these effect is hard to investigate since they are correlated. Effect of the muscle shortening might also have an effect on the signals since the extinction of the intracellular source along the fiber arises earlier with the muscle shortening.

Global comparison over several contraction levels

In this section, we will study the effect of the muscle deformation on the statistic computed on the sEMG signals. The Normalized Root Mean Square Error (NRMSE) is computed for each simulated muscle between the signals generated with and without deformation as well as the on the statistics computed on them. The NRMSE is computed as follow:

$$NRMSE = \frac{1}{max(S) - min(S)} \sqrt{\frac{\sum_{j=1}^{M} \sum_{i=1}^{N} \left(S_i^j - \hat{S}_i^j\right)^2}{N.M}} \tag{4.22}$$

where S is the signal generated without deformation, $\hat{S}$ is the signal generated considering the deformation, N is the number of time sampling of the signal (in these simulations it is 4096×6) and M is the number of signals (8×8 from a HD-sEMG electrode grid).

The NRMSE computed on the statistics follows the same definition as above but without the sum over the time sampling since the statistics are scalar.

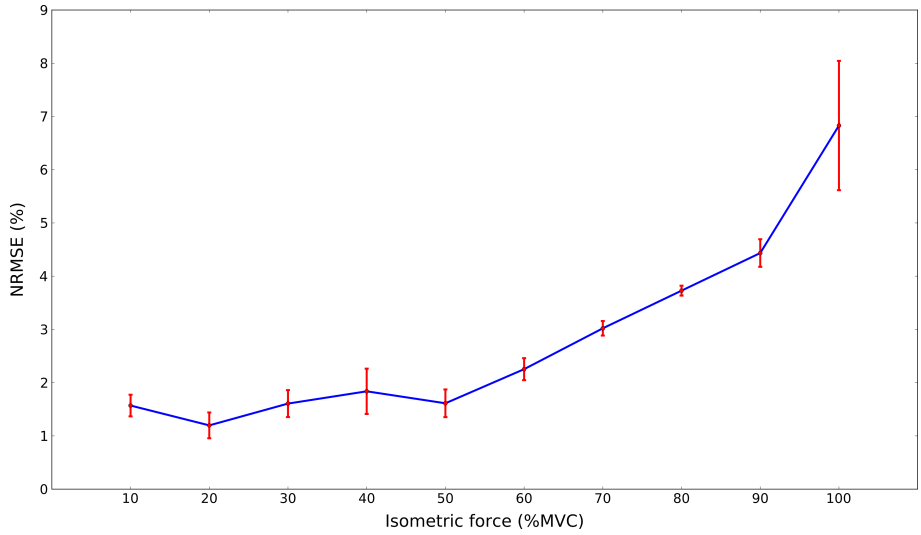

Figure 4.26: Mean ± std (%) NRMSE computed for the 5 anatomies over the 64 signals according to the muscle contraction level.

Firstly, we computed the NRMSE on the HD-sEMG signals from the electrode grid define from Table 4.15 for each anatomy and contraction level. Then, we computed the mean and the std for each contraction level. Computed mean and std NRMSE according to the activation level of the muscle is presented in Fig. 4.26. As one can see, this NRMSE is increasing with the contraction level. The maximum deviation is obtained at 100% MVC with 7% of deviation. Moreover, we can observe a stable std for each contraction level exhibiting a slight sensitivity due to the MU positions. Yet, at 100% a more important std is observed compared to the other contraction level. Thus, at 100% the MU position has more effect and it can explained from the important deformations endured by the muscle. This error can be regarded as small, but as we have seen in chapter 2 about the modeling of the source at the MU scale, a slight deviation on the signals might induce more deviation on the statistics computed on the signals, especially on the computed HOS features.

For this purpose, we computed four classical statistics (RMS, ARV, kurtosis and skewness) over the sEMG signals from the grid in order to see the effect of the muscle contraction for each anatomy. The presented mean ± std NRMSE in Fig. 4.27 is computed as the mean and std of the mean of the NRMSE computed between the statistics computed on each sEMG signal. Results are presented in Fig. 4.27.

On Fig. 4.27a, is depicted the NRMSE computed between the RMS values. The maximum deviation equals to 17.5% and is obtained at 100% MVC, it also increases monotonously according to the contraction level. We can also notice that the deviation computed on the RMS is higher than on the signals. Moreover, non negligible std can be observed for each contraction level, specifically at 20, 50 and 100% MVC. On the RMS values, the MU positions and the muscle deformation have an important effect. This trend should also be observed on the other amplitude statistic, the ARV value. As for the RMS, the NRMSE computed on the ARV is presented in Fig. 4.27b where the maximum deviation equals to 13.5% at 100% MVC. This deviation is continuously increasing according to the contraction level. Compared to the std computes for the NRMSE of the RMS values, the std computed for the NRMSE of the ARV values is more stable for each contraction level. As expected, the maximum std is observed at 100% MVC

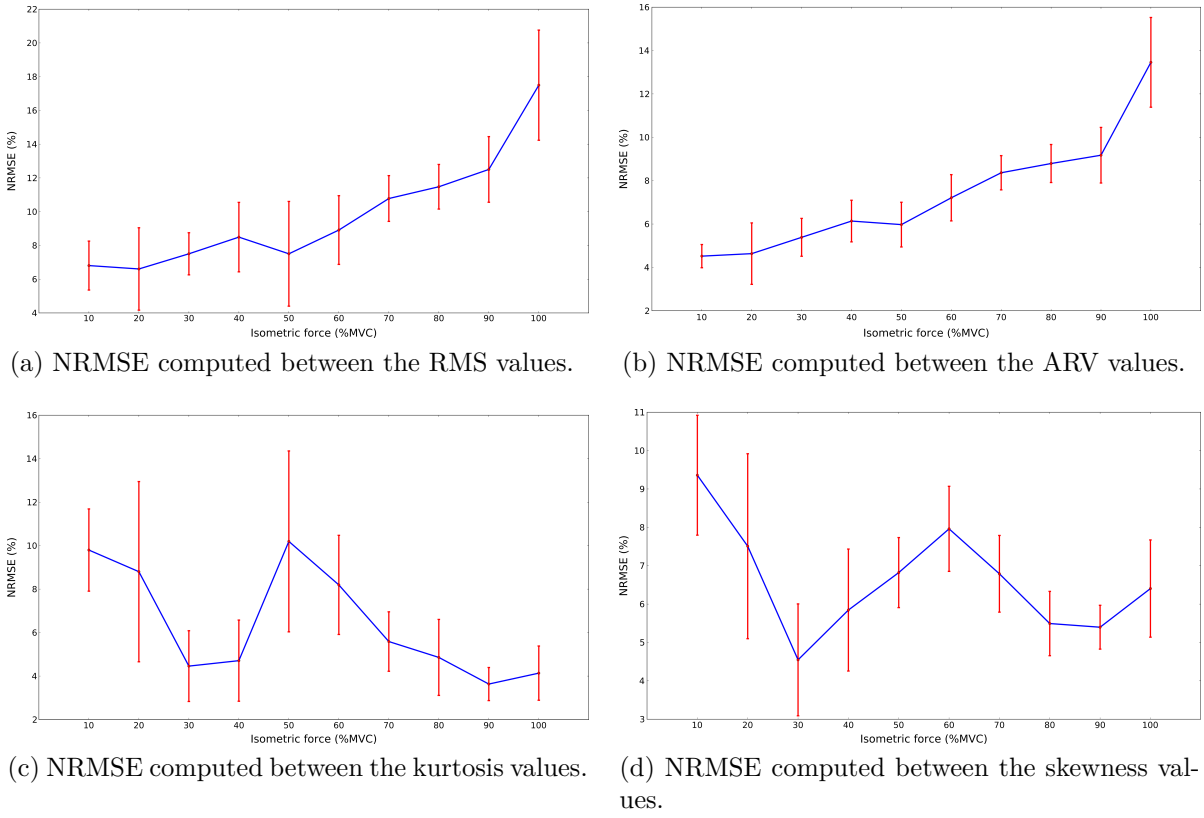

(a) NRMSE computed between the RMS values.

(b) NRMSE computed between the ARV values.

(c) NRMSE computed between the kurtosis values.

(d) NRMSE computed between the skewness values.

Figure 4.27: Mean ± std NRMSE (mean and std) computed between the amplitude statistics from the non deformable model and the deformable according to contraction level for the five anatomies.

since it has the maximum NRMSE over the signals. Beside these amplitude statistics, we also computed Probability Density Function (PDF) shape descriptors, i.e., the flatness (kurtosis) and the asymmetry (skewness) compared to a Gaussian distribution. These parameters seem to be sensitive to neural, instrumental and anatomical parameters of the studied muscle [57].

Concerning the kurtosis deviation (see Fig. 4.27c), the maximum deviation equals to 10.5% at 50% MVC. Important std is observed for the first contraction level (from 10 to 60% MVC), then kurtosis variability becomes more stable. No particular trend of the muscle deformation effect on the kurtosis can be retrieved from Fig. 4.27c. Yet, deeper investigation on the mean kurtosis values for each contraction level exhibits no modification of the kurtosis value profile according to the contraction level. About the skewness (see Fig. 4.27d), the maximum deviation equals to 9.4% at 10% MVC. As for the kurtosis, important std is observed for all contraction levels, particularly between 10 and 60% MVC. Moreover, deeper investigation on the skewness and kurtosis values computed for each contraction level exhibited no modification in the trends of the feature values according to the contraction level [157].

Considering all the results exposed in Fig. 4.27, we can assess that apart from the muscle deformation, the MU positions also have an important effect on the generated signals. The muscle deformation has a monotonous effect on the amplitude statistics (RMS and ARV), yet on the PDF shape descriptors statistics (kurtosis and skewness)

this effect is non monotonous.

4.4.3 Discussion

In this preliminary study, we proposed the first analytical electro-mechanical model of the skeletal muscles that is able to consider the muscle shortening during isometric contraction. In fact, this model can simulate and personalize many electro-mechanical behaviors of the fusiform skeletal muscle in humans as well as animals.

First, we studied the muscle deformation according to contraction level. We saw that both muscle shortening and muscle thickness increase non linearly according to muscle activation. In this study, we also computed the young modulus of the muscle from the given contractions. From these simulations, we were able to determine the stress-strain curve exhibiting the elastic behavior of the skeletal muscle. Moreover, from these relationship we could extract the muscle young modulus and showed an estimated Young modulus in the same range than experimental studies on the Biceps Brachii [144, 192].

Moreover, we studied the effect of the muscle deformation on the recorded HD-sEMG signals. To do so, we computed simulations for 5 anatomies respecting the same parameters presented in Table 4.15 with the static model and the quasi-dynamic. In total 100 simulations were performed 5 anatomies$\times$2 models$\times$10 contraction level. sEMG signals were recorded from a HD-sEMG electrode grid placed at the skin surface and that doesn't move in the plan $(\theta;z)$. Error on the signals (see Fig. 4.26) supposed a slight deviation using the quasi-dynamic model. Yet, NRMSE computed on the amplitude statistics (RMS and ARV values) exhibited non negligible effect from the quasi-dynamic model (see Figs. 4.27a and 4.27b). However, with deeper investigation, the amplitude statistics computed on the signals aren't changed in their trends. RMS and ARV values still increase according to the increase of the contraction level.

We also computed the PDF shape descriptors (kurtosis and skewness) on the generated sEMG signals. We showed that their shape descriptors are also strongly altered from the muscle deformation (see Figs. 4.27c and 4.27d). Even if shape descriptors are changed, their amplitude values remain in the range of the static model according to contraction level. Concerning the kurtosis, it is mainly altered at 50% MVC that is the contraction level when FF MUs start to be recruited. Concerning the skewness, it is importantly altered at 10% MVC that is the contraction level when the fewest number of MU and only S MU are recruited. We can suppose that when the muscle swells, some FF MUs that were detected with the static muscle model currently aren't detected anymore from the electrode or took away the MUs from the electrode and thus, reduce their contribution to the signal. Unfortunately, this is impossible to evaluate this effect in experimental conditions. Moreover, reduction of the adipose and skin tissue thicknesses seem to reduce the filtering on the signals and thus change their shape. Even if the biphasic shape of the S MUAP remains, the amplitude of the non propagating component is altered and thus alters the skewness value (asymmetry of the PDF).

This preliminary study underlines the importance to consider the muscle deformation during contraction on the recorded signals. Considering the muscle deformation adds more realism to the skeletal muscle modeling. Thus, comparison between sEMG signals generated from static electrical model can be more accurate using this quasi-dynamic model. Some studies, such as sEMG/force relationship or MU firing times decomposition efficiency, will be more precise and provide better results and more reliable knowledge.

4.5 Conclusion

In this chapter, we presented three different applications of the model proposed in chapters 2 and 3. Reliability of the developed model is crucial but we also believe reproducibility and repeatability are also important for a model. Representativity of the models correspond to validation of the model and its ability to describe the underlying phenomena arising during isometric contraction. Reliability of the models is presented in their respective chapters (electrical model in chapter 2 and mechanical model in chapter 3).

A first study focused on the sensitivity of sEMG signal descriptors according to variation of the parameters defining the HD electrode grid. These parameters defined the position of the grid (center of the grid position, rotation) over the skin surface and its design (electrode radius, inter-electrode distances). This study pointed out the crucial influence of the grid position and especially the rotation of the grid according to fiber orientation on the recorded sEMG signals. A slight misalignment of the grid will significantly alter the sEMG signals compared to the well aligned grid. This study, hardly feasible in experimental condition, can be performed in silico since all the needed parameters are known and can be fixed between simulations.

The second study proposed a simulation of the sEMG/force relationship in collaboration with another PhD student. This relationship was based on features recorded from the Biceps Brachii muscle [57]. These features were used to supply personalized parameters to the electrical model. A complete study of the different relationship proposed in the literature was performed where we assessed that the 3^{rd} order polynom better describes the sEMG/force relationship for the Biceps Brachii muscle. Moreover, a sensitivity analysis studying the effect of morphological, neural and anatomical parameters on the RMS value of the sEMG performed. For this study, 500 simulations were performed. We used a classical twitch model to describe the force generation. A next study should be performed including the multiscale mechanical model proposed in chapter 3.

Finally, we propose a deformable model of the striated muscle during isometric contraction. This model combines both models presented in chapter 2 and 3. Determining the deformation of the muscle from the mechanical model, the muscle anatomy is updated assuming no change in the muscle volume. Thus shortening of the muscle length will induce a swelling of the muscle thickness. Moreover, we considered the displacement of the MU centers as well as the increase of the muscle fiber diameters. This increase of diameter should induce a faster propagation [111] of the intracellular source along the fiber length, and thus will alter the signals recorded by the electrode compare to the static model. But, this assumption hasn't yet been formally assessed in experiments. Effect of the muscle deformation on the generated signals was assessed computing the NRMSE between the signals generated from the static and the deformable model. This effect was studied from isometric contractions between 10 and 100% of the MVC. It exhibited major influence of the muscle deformation on the generated signals and their statistics. For future simulation studies, muscle deformation should be considered even for isometric contractions. Using the multiscale and multiphysic modeling of the skeletal muscle increase the physiological realism of the studies and thus, provide more accurate results. Moreover, reaching the information at the MU scale has a considerable interest since it is genuinely hard to record these data in experimental conditions.

General conclusion

In this general conclusion, we will run through the essential points that were addressed and developed within this thesis. Then, we will mention some of the limitations of the proposed models and we will finish by elaborating the perspective of future works. As previously explained, this thesis aims at proposing a new multi-physic, multi-scale model describing the skeletal muscle during isometric contractions. For this purpose, we are faced with several steps of applied mathematics, computer science, physiology, biomechanics and signal processing to finally model the electro-mechanical behavior of the skeletal muscle.

The first contribution was the development of an optimized electrical model describing the electrical activity of the muscle at the skin surface. This modeling includes primarily to propose both motor control of the contraction and an anatomical model of the muscle. Considering the high number of Motor Unit simulated, an algorithm insuring fiber density homogeneity in the muscle was developed. In the literature, there exists no model simulating the muscle electrical activity at the skin surface. Current models directly simulate the sEMG signal and thus, induce coupling between the sEMG signal computation and the physical phenomenon. Some new knowledge are available from the modeling the electrical activity instead of the sEMG. Moreover, with an efficiency and optimized programming, computation time of sEMG simulation is significantly reduced. Yet, when reliable and personalized simulation of skeletal muscle was considered, the computation time of a single simulation was too long to perform studies requiring several simulations. This important computation time is due to the important number of fiber source to compute. For this purpose, we also developed a model approximating the fiber electrical sources at the MU scale. Computation time was significantly reduced of 99% compared to the fiber electrical source. Moreover, it was expected that this computation time reduction would induce significant deviation on the reference signal (with the fiber electrical source). But, this alteration was negligible on the generated signals (less than 2% of error) and not significant on the features computed over the signals (less than 10%). It has to be noticed that the error induced on the features is a magnitude error, the original trend of the features are preserved. Thus, the first contribution of the thesis is the development of a fast, optimized and reliable model describing the electrical activity of the skeletal muscle at the skin surface in a high spatial resolution. This model is able to simulate an electrical activity from 770 active MUs in less than 30 minutes.

The second contribution was to propose and develop a new model describing the mechanical behavior of the skeletal muscle during isometric contraction. Currently, in the literature, many skeletal muscle model are proposed. Yet, major issue in these models is their reliability for voluntary contractions or their computation time that is too long. For this reason, it is of great interest to propose a model voluntarily controlled where physiological phenomena, such as the calcium induces by the arriving of a motoneuron firing, are considered. Moreover, description of these mechanical phenomena was defined at the muscle scale where it is known that the smallest functional entities in the muscle

are the motor units. Thus, mechanical description of the muscle was defined at the MU scale instead of the muscle scale like most of the proposed models. This model was validated with force profile recorded from a subject implanted with a neural stimulation device (less than 10% of error on 8 consecutive stimulation). Global trend of the muscle force generation according to the stimulation intensity was preserved and access to the mechanical contribution of each MU during the stimulation was feasible. Moreover, a comparison concerning the optimal stimulation frequency between a classical twitch model describing the force generation and the proposed model was presented. It exhibited some limitations of the twitch model to represent this optimal frequency where the proposed one was able to describe the desire effect. Accordingly, the second contribution of this work is the proposition of a model describing the contractile outcomes of the skeletal muscle at the motor unit scale during voluntary isometric contractions tuned by the neural drive.

After developing the electrical and mechanical models of the skeletal muscle, the next stage of the work was dedicated to the possible applications of these models separately and of their combination. For the possible applications, we performed a global sensitivity analysis of the sEMG statistics while varying the parameters defining the recording system, i.e., the high density surface electrode grid. Thanks to the decoupling of the muscle electrical activity and the recording system, the lone effects of the HD-sEMG grid parameters could be analyzed. This study exhibited and confirmed the major influence of the grid rotation according to the muscle fiber orientation. Experimental studies using HD-sEMG grid should have a particular focus on the good alignement of the grid with the muscle fiber. Afterwards, another contribution in these applications was devoted to the HD-sEMG/force relationship modeling. This study was performed in collaboration with another PhD student working on the sEMG/force relationship [53]. We carried out a focused sensitivity analysis using the cylindrical HD-sEMG generation model for the 64 simulated sEMG signals and a twitch based force model for the simulation. We established the major parameters that affect the HD-sEMG/force relationship and their effect on the estimated relation. Following, we compared between different fitting type equations proposed in the literature and we found the best type that describe the HD-sEMG/force relation. Accordingly, another contribution was to propose and validate, using realistic simulations, a relevant model for the HD-sEMG/force relationship. Subsequently, using this new found equation, we tested the effect of neural, morphological and anatomical parameters on its coefficients in the aim of quantifying this impact for a better force estimation in later work. Finally, the combination of the electrical and mechanical models to provide an electro-mechanical model is developed. Considering the muscle as a multilayered cylinder, we determined the muscle deformation with the mechanical model and use this deformation value to update the cylinder with isovolumic assumption. Then with the updated muscle, the electrical model can simulate the corresponding electrical activity. This, study exhibited the importance of the muscle deformation during contraction and its effect on the recorded sEMG signals. Most of the proposed electrical models simulate the sEMG signals in static condition. When quasi-static condition is considered, the deviation between the static up to 4.5% on the signals and to 90% on certain statistics. Moreover study of the mechanical behavior of the skeletal muscle with in different configurations. Thanks to the cylinder definition of the anatomy, stress-strain relationship can be studied. These applications exhibited the easy use of the developed models and their representativity. In fact, a particular focus was put on the generic definition of the model implementation. This generic definition allows the model to simulate a wide variety of healthy and pathological muscles.

To conclude this work, the approaches presented in this work have applications in many fields; starting by the electrical model that can be applied to clinical studies where pathological muscles are involved. In the short term, global sensitivity analysis of the deformable electro-mechanical model will be performed in order to have an overall view of each parameter influence on the muscle contraction outcomes. This study will provide new knowledge about the parameter significance on the contraction outcomes. Moreover, quantification of this influence will be accessible by simulating thousands of muscle parameter configuration. After performing this study, we will have the opportunity to study the inverse problems of the skeletal muscle contraction. In parallel to the global sensitivity analysis study, more precise analysis of the sEMG/force relationship using the quasi-dynamic electro-mechanical model will be performed. Preliminary investigation of this relationship exhibits the same results presented in [57] , i.e., this relationship can be described as a 3^{rd} order polynom equation. Yet, muscle deformation has an effect on the coefficients leading this polynomial equation.

In the medium term, some extensions of the proposed quasi-dynamic electro-mechanical muscle should be considered such as the including of the muscle fatigue effect or the muscle fiber pinnate angle in order to be able to use the model in different contraction context. In addition to the possible model extensions, the algorithms for identifying the MU firing times during an isometric contraction can be assessed using this model. This study, in complement to the inverse problems study, can provide the possibility to validate the electro-mechanical model. Validation of the electrical activity of the muscle could never have been validated due to the complex estimation of some parameters defining the muscle and of the MUs firing times.

After providing these studies, the quasi-dynamic electro-mechanical model during isometric contraction can be used for patient-specific simulation allowing the access of large amount of complement knowledge about the neuromuscular functioning. In the long term, some studies such as the fatigue evaluation, the detection of neuromuscular disorder or the development of neurorehabilitation can be considered. Moreover, some effects of the muscle physiology arising during specific moment such as the muscle aging could now be investigate. Finally, this model could be used as a benchmark for the development of Finite Element Method (FEM) model described as in the proposed model, i.e., with a cylindrical anatomy. The development of FEM model will give access to the electro-mechanical modeling of the skeletal muscle during anisometric contractions.

Bibliography

[1] E. J. Ciaccio. Honored papers 2016. *Computers in Biology and Medicine*, 86:129–131, 2017.

[2] R. Merletti and P. A. Parker. *Electromyography: Physiology, Engineering, and Non-Invasive Applications*. John Wiley & Sons, 2004.

[3] C.A. Oatis. *Kinesiology: The Mechanics and Pathomechanics of Human Movement*. Lippincott Williams & Wilkins, 2004.

[4] K. Bouillard, A. Nordez, and F. Hug. Estimation of Individual Muscle Force Using Elastography. *PLOS ONE*, 6(12), 2011.

[5] E. F. Hodson-Tole and J. M. Wakeling. Motor unit recruitment for dynamic tasks: current understanding and future directions. *Journal of Comparative Physiology B*, 179(1):57–66, 2009.

[6] T. Heidlauf and O. Rohrle. Modeling the Chemoelectromechanical Behavior of Skeletal Muscle Using the Parallel Open-Source Software Library OpenCMISS. *Computational and Mathematical Methods in Medicine*, 2013, 2013.

[7] D. Farina, L. Mesin, S. Martina, and R. Merletti. A surface EMG generation model with multilayer cylindrical description of the volume conductor. *IEEE Transactions on Biomedical Engineering*, 51(3):415–426, 2004.

[8] A. V. Hill. The Heat of Shortening and the Dynamic Constants of Muscle. *Proceedings of the Royal Society of London B: Biological Sciences*, 126(843):136–195, 1938.

[9] H. El Makssoud, D. Guiraud, P. Poignet, M. Hayashibe, P.-B. Wieber, K. Yoshida, and C. Azevedo-Coste. Multiscale modeling of skeletal muscle properties and experimental validations in isometric conditions. *Biological Cybernetics*, 105(2):121–138, 2011.

[10] V. Carriou, S. Boudaoud, J. Laforet, and F. S. Ayachi. Fast generation model of high density surface EMG signals in a cylindrical conductor volume. *Computers in Biology and Medicine*, 74:54–68, 2016.

[11] M.M. Lowery, N.S. Stoykov, A. Taflove, and T.A. Kuiken. A multiple-layer finite-element model of the surface EMG signal. *IEEE Transactions on Biomedical Engineering*, 49(5):446–454, 2002.

[12] A. F. Huxley. Muscle structure and theories of contraction. *Progress in Biophysics and Biophysical Chemistry*, 7:255–318, 1957.

[13] S. Nandedkar and E. Stålberg. Simulation of macro EMG motor unit potentials. *Electroencephalography and Clinical Neurophysiology*, 56(1):52–62, 1983.

[14] T. H. J. M. Gootzen, D. F. Stegeman, and A. Heringa. On numerical problems in analytical calculations of extracellular fields in bounded cylindrical volume conductors. *Journal of Applied Physics*, 66(9):4504–4508, 1989.

[15] G. J. Tortora and B. H. Dickinson. *Principles of Anatomy and Physiology*. John Wiley & Sons, Hoboken, 12th edition, 2009.

[16] E. P. Widmaier, H. Raff, K. T. Strang, and A. J. Vander. *Vander's Human Physiology: The Mechanisms of Body Function*. McGraw-Hill, New York, 12th edition, 2010.

[17] J. A. Faulkner. Terminology for contractions of muscles during shortening, while isometric, and during lengthening. *Journal of Applied Physiology (Bethesda, Md.: 1985)*, 95(2):455–459, 2003.

[18] E. Henneman, G. Somjen, and D. O. Carpenter. Functional Significance of Cell Size in Spinal Motoneurons. *Journal of Neurophysiology*, 28(3):560–580, 1965.

[19] E. Henneman, G. Somjen, and D. O. Carpenter. Excitability and Inhibitibility of Motoneurons of Different Sizes. *Journal of Neurophysiology*, 28(3):599–620, 1965.

[20] A. J. Fuglevand, D. A. Winter, and A. E. Patla. Models of recruitment and rate coding organization in motor-unit pools. *Journal of Neurophysiology*, 70(6):2470–2488, 1993.

[21] C. J. De Luca and E. C. Hostage. Relationship Between Firing Rate and Recruitment Threshold of Motoneurons in Voluntary Isometric Contractions. *Journal of Neurophysiology*, 104(2):1034–1046, 2010.

[22] P. Zhou and W. Z. Rymer. Factors Governing the Form of the Relation Between Muscle Force and the EMG: A Simulation Study. *Journal of Neurophysiology*, 92(5):2878–2886, 2004.

[23] F. S. Ayachi, S. Boudaoud, and C. Marque. Evaluation of muscle force classification using shape analysis of the sEMG probability density function: a simulation study. *Medical & Biological Engineering & Computing*, 52(8):673–684, 2014.

[24] J. V. Basmajian. Control and Training of Individual Motor Units. In E. Peper, S. Ancoli, and M. Quinn, editors, *Mind/Body Integration*, pages 371–375. Springer US, 1979.

[25] J. A. Hoffer, G. E. Loeb, N. Sugano, W. B. Marks, M. J. O'Donovan, and C. A. Pratt. Cat hindlimb motoneurons during locomotion. III. Functional segregation in sartorius. *Journal of Neurophysiology*, 57(2):554–562, 1987.

[26] V. Von Tscharner and B. Goepfert. Estimation of the interplay between groups of fast and slow muscle fibers of the tibialis anterior and gastrocnemius muscle while running. *Journal of Electromyography and Kinesiology*, 16(2):188–197, 2006.

[27] F. E. Zajac. Muscle and tendon: properties, models, scaling, and application to biomechanics and motor control. *Critical reviews in biomedical engineering*, 17(4):359–411, 1988.

[28] R. Dahmane, S. Djordjevič, B. Šimunič, and V. Valenčič. Spatial fiber type distribution in normal human muscle: Histochemical and tensiomyographical evaluation. *Journal of Biomechanics*, 38(12):2451–2459, 2005.

[29] I. Fuentes, A. R. Cobos, and L. A. G. Segade. Muscle fibre types and their distribution in the biceps and triceps brachii of the rat and rabbit. *Journal of Anatomy*, 192(Pt 2):203–210, 1998.

[30] M. A. Johnson, J. Polgar, D. Weightman, and D. Appleton. Data on the distribution of fibre types in thirty-six human muscles: An autopsy study. *Journal of the Neurological Sciences*, 18(1):111–129, 1973.

[31] P. Rosenfalck. Intra- and extracellular potential fields of active nerve and muscle fibres. A physico-mathematical analysis of different models. *Acta Physiologica Scandinavica. Supplementum*, 321:1–168, 1969.

[32] E. D. Adrian and D. W. Bronk. The discharge of impulses in motor nerve fibres. part ii: The frequency of discharge in reflex and voluntary contractions. *The Journal of Physiology*, 67(2):i3–151, 1929.

[33] I. Martin. Levels of muscle activity in psychiatric patients. *Acta Psychologica*, 12:326–341, 1956.

[34] G. B. Whatmore and R. M. Ellis. Some motor aspects of schizophrenia: an emg study. *American Journal of Psychiatry*, 114(10):882–889, 1958.

[35] R. B. Malmo, C. Shagass, and F. H. Davis. Specificity of bodily reactions under stress; a physiological study of somatic symptom mechanisms in psychiatric patients. *Research Publications - Association for Research in Nervous and Mental Disease*, 29:231–261, 1949.

[36] R. A. Prosek, A. A. Montgomery, B. E. Walden, and D. M. Schwartz. EMG Biofeedback in the Treatment of Hyperfunctional Voice Disorders. *Journal of Speech and Hearing Disorders*, 43(3):282–294, 1978.

[37] H. D. Bouman and E. M. G. Lentzer. The treatment of hyperhidrosis of hands and feet with constant current. *American Journal of Physical Medicine*, 31(3):158–169, 1952.

[38] M. R. Dimitrijevic and A. M. Sherwood. Spasticity Medical and surgical treatment. *Neurology*, 30(7 Part 2):19–27, 1980.

[39] C. D. Hardyck, L. F. Petrinovich, and D. W. Ellsworth. Feedback of Speech Muscle Activity during Silent Reading: Rapid Extinction. *Science*, 154(3755):1467–1468, 1966.

[40] A. J. Fuglevand, D. A. Winter, A. E. Patla, and D. Stashuk. Detection of motor unit action potentials with surface electrodes: influence of electrode size and spacing. *Biological Cybernetics*, 67(2):143–153, 1992.

[41] C. J. De Luca and P. Contessa. Hierarchical control of motor units in voluntary contractions. *Journal of Neurophysiology*, 107(1):178–195, 2012.

[42] T. Masuda, H. Miyano, and T. Sadoyama. The Position of Innervation Zones in the Biceps Brachii Investigated by Surface Electromyography. *IEEE Transactions on Biomedical Engineering*, BME-32(1):36–42, 1985.

[43] J. V. Basmajian. *Muscles alive, their functions revealed by electromyography.* Williams & Wilkins, Baltimore, 1979.

[44] C. A. Sinderby, A. S. Comtois, R. G. Thomson, and A. E. Grassino. Influence of the bipolar electrode transfer function on the electromyogram power spectrum. *Muscle & Nerve*, 19(3):290–301, 1996.

[45] D. Farina, C. Cescon, and R. Merletti. Influence of anatomical, physical, and detection-system parameters on surface EMG. *Biological Cybernetics*, 86(6):445–456, 2002.

[46] M. Nielsen, T. Graven-Nielsen, and D. Farina. Effect of innervation-zone distribution on estimates of average muscle-fiber conduction velocity. *Muscle & Nerve*, 37(1):68–78, 2008.

[47] V. Carriou, J. Laforet, S. Boudaoud, and M. Al Harrach. Sensitivity analysis of HD-sEMG amplitude descriptors relative to grid parameter variations of a cylindrical multilayered muscle model. *Biomedical Physics & Engineering Express*, 2(6), 2016.

[48] D. Staudenmann, K. Roeleveld, D. F. Stegeman, and J. H. van Dieën. Methodological aspects of SEMG recordings for force estimation – A tutorial and review. *Journal of Electromyography and Kinesiology*, 20(3):375–387, 2010.

[49] C. Disselhorst-Klug, T. Schmitz-Rode, and G. Rau. Surface electromyography and muscle force: Limits in sEMG–force relationship and new approaches for applications. *Clinical Biomechanics*, 24(3):225–235, 2009.

[50] H. J. Hermens, B. Freriks, C. Disselhorst-Klug, and G. Rau. Development of recommendations for SEMG sensors and sensor placement procedures. *Journal of Electromyography and Kinesiology*, 10(5):361–374, 2000.

[51] K. G. Keenan, D. Farina, K. S. Maluf, R. Merletti, and R. M. Enoka. Influence of amplitude cancellation on the simulated surface electromyogram. *Journal of Applied Physiology*, 98(1):120–131, 2005.

[52] D. Staudenmann, I. Kingma, A. Daffertshofer, D. F. Stegeman, and J. H. van Dieen. Improving EMG-based muscle force estimation by using a high-density EMG grid and principal component analysis. *IEEE Transactions on Biomedical Engineering*, 53(4):712–719, 2006.

[53] M. Al Harrach. *Modeling of the sEMG/force relationship by data analysis of high resolution sensor network.* PhD thesis, Universite de Technologie de Compiegne, 2016.

[54] Stegeman D. F., Kleine B. U., Lapatki B. G., and Van Dijk J. P. High-density Surface EMG: Techniques and Applications at a Motor Unit Level. *Biocybernetics and Biomedical Engineering*, 32(3):3–27, 2012.

[55] R. Merletti, B. Afsharipour, and G. Piervirgili. High Density Surface EMG Technology. In *Converging Clinical and Engineering Research on Neurorehabilitation*, pages 1205–1209. Springer, Berlin, Heidelberg, 2013.

[56] M. Rojas-Martínez, M. A. Mañanas, and J. F. Alonso. High-density surface EMG maps from upper-arm and forearm muscles. *Journal of NeuroEngineering and Rehabilitation*, 9:85, 2012.

[57] M. Al Harrach, V. Carriou, S. Boudaoud, J. Laforet, and F. Marin. Analysis of the sEMG/Force Relationship using HD-sEMG Technique and Data Fusion: A simulation study. *Computers in Biology and Medicine*, 83:34–47, 2017.

[58] M. Al Harrach, S. Boudaoud, M. Hassan, F. S. Ayachi, D. Gamet, J. F. Grosset, and F. Marin. Denoising of HD-sEMG signals using canonical correlation analysis. *Medical & Biological Engineering & Computing*, 55(3):1–14, 2016.

[59] J. P. van Dijk, J. H. Blok, B. G. Lapatki, I. N. van Schaik, M. J. Zwarts, and D. F. Stegeman. Motor unit number estimation using high-density surface electromyography. *Clinical Neurophysiology*, 119(1):33–42, 2008.

[60] M. J. Zwarts and D. F. Stegeman. Multichannel surface EMG: basic aspects and clinical utility. *Muscle & Nerve*, 28(1):1–17, 2003.

[61] R. Merletti, A. Holobar, and D. Farina. Analysis of motor units with high-density surface electromyography. *Journal of Electromyography and Kinesiology*, 18(6):879–890, 2008.

[62] B. U. Kleine, J. P. van Dijk, B. G. Lapatki, M. J. Zwarts, and D. F. Stegeman. Using two-dimensional spatial information in decomposition of surface EMG signals. *Journal of Electromyography and Kinesiology*, 17(5):535–548, 2007.

[63] G. Drost, D. F. Stegeman, B. G. M. van Engelen, and M. J. Zwarts. Clinical applications of high-density surface EMG: A systematic review. *Journal of Electromyography and Kinesiology*, 16(6):586–602, 2006.

[64] J. C. Coggshall and G. A. Bekey. A stochastic model of skeletal muscle based on motor unit properties. *Mathematical Biosciences*, 7(3–4):405–419, 1970.

[65] C. J. De Luca. A model for a motor unit train recorded during constant force isometric contractions. *Biological Cybernetics*, 19(3):159–167, 1975.

[66] D. Ge, E. Le Carpentier, J. Idier, and D. Farina. Spike Sorting by Stochastic Simulation. *IEEE Transactions on Neural Systems and Rehabilitation Engineering*, 19(3):249–259, 2011.

[67] B. Gustafsson and M. J. Pinter. An investigation of threshold properties among cat spinal alpha-motoneurones. *The Journal of Physiology*, 357(1):453–483, 1984.

[68] C. G. Kukulka and H. P. Clamann. Comparison of the recruitment and discharge properties of motor units in human brachial biceps and adductor pollicis during isometric contractions. *Brain Research*, 219(1):45–55, 1981.

[69] C. J. de Luca, R. S. LeFever, M. P. McCue, and A. P. Xenakis. Behaviour of human motor units in different muscles during linearly varying contractions. *The Journal of Physiology*, 329(1):113–128, 1982.

[70] C. J. De Luca and Z. Erim. Common drive of motor units in regulation of muscle force. *Trends in Neurosciences*, 17(7):299–305, 1994.

[71] C. J. De Luca and E. C. Hostage. Relationship Between Firing Rate and Recruitment Threshold of Motoneurons in Voluntary Isometric Contractions. *Journal of Neurophysiology*, 104(2):1034–1046, 2010.

[72] S. Andreassen and A. Rosenfalck. Regulation of the firing pattern of single motor units. *Journal of Neurology, Neurosurgery, and Psychiatry*, 43(10):897–906, 1980.

[73] D. F. Stegeman, J. H. Blok, H. J. Hermens, and K. Roeleveld. Surface EMG models: properties and applications. *Journal of Electromyography and Kinesiology*, 10(5):313–326, 2000.

[74] D. Farina, M. Fosci, and R. Merletti. Motor unit recruitment strategies investigated by surface EMG variables. *Journal of Applied Physiology*, 92(1):235–247, 2002.

[75] C. T. Moritz, B. K. Barry, M. A. Pascoe, and R. M. Enoka. Discharge Rate Variability Influences the Variation in Force Fluctuations Across the Working Range of a Hand Muscle. *Journal of Neurophysiology*, 93(5):2449–2459, 2005.

[76] B. L. Tracy, K. S. Maluf, J. L. Stephenson, S. K. Hunter, and R. M. Enoka. Variability of motor unit discharge and force fluctuations across a range of muscle forces in older adults. *Muscle & Nerve*, 32(4):533–540, 2005.

[77] P. a. M. Griep, K. L. Boon, and D. F. Stegeman. A study of the motor unit action potential by means of computer simulation. *Biological Cybernetics*, 30(4):221–230, 1978.

[78] N. Ganapathy, J. W. Clark, and O. B. Wilson. Extracellular potentials from skeletal muscle. *Mathematical Biosciences*, 83(1):61–96, 1987.

[79] R. J. Roth, F. L. H. Gielen, and J. P. Wikswo. Spatial and temporal frequency-dependent conductivities in volume-conduction calculations for skeletal muscle. *Mathematical Biosciences*, 88(2):159–189, 1988.

[80] F. L. H. Gielen, H. E. P. Cruts, B. A. Albers, K. L. Boon, W. Wallinga-de Jonge, and H. B. K. Boom. Model of electrical conductivity of skeletal muscle based on tissue structure. *Medical and Biological Engineering and Computing*, 24(1):34–40, 1986.

[81] T. H. J. M. Gootzen, D. F. Stegeman, and A. Van Oosterom. Finite limb dimensions and finite muscle length in a model for the generation of electromyographic signals. *Electroencephalography and Clinical Neurophysiology/Evoked Potentials Section*, 81(2):152–162, 1991.

[82] A. Gydikov and D. Kosarov. Extraterritorial potential field of impulses from separate motor units in human muscles. *Electromyography and Clinical Neurophysiology*, 12(4):283–305, 1972.

[83] A. Gydikov, L. Gerilovsky, N. Radicheva, and N. Trayanova. Influence of the muscle fibre end geometry on the extracellular potentials. *Biological Cybernetics*, 54(1):1–8, 1986.

[84] R. Merletti, L. Lo Conte, E. Avignone, and P. Guglielminotti. Modeling of surface myoelectric signals. I. Model implementation. *IEEE Transactions on Biomedical Engineering*, 46(7):810–820, 1999.

[85] D. Farina and R. Merletti. A novel approach for precise simulation of the EMG signal detected by surface electrodes. *IEEE Transactions on Biomedical Engineering*, 48(6):637–646, 2001.

[86] G. V. Dimitrov and N. A. Dimitrova. Precise and fast calculation of the motor unit potentials detected by a point and rectangular plate electrode. *Medical Engineering & Physics*, 20(5):374–381, 1998.

[87] L. Mesin. Simulation of Surface EMG Signals for a Multilayer Volume Conductor With Triangular Model of the Muscle Tissue. *IEEE Transactions on Biomedical Engineering*, 53(11):2177–2184, 2006.

[88] L. Mesin and D. Farina. Simulation of surface EMG signals generated by muscle tissues with inhomogeneity due to fiber pinnation. *IEEE Transactions on Biomedical Engineering*, 51(9):1521–1529, 2004.

[89] L. Mesin. Simulation of Surface EMG Signals for a Multilayer Volume Conductor With a Superficial Bone or Blood Vessel. *IEEE Transactions on Biomedical Engineering*, 55(6):1647–1657, 2008.

[90] L. Mesin and D. Farina. A model for surface EMG generation in volume conductors with spherical inhomogeneities. *IEEE Transactions on Biomedical Engineering*, 52(12):1984–1993, 2005.

[91] L. Mesin and D. Farina. An analytical model for surface EMG generation in volume conductors with smooth conductivity variations. *IEEE Transactions on Biomedical Engineering*, 53(5):773–779, 2006.

[92] L. Mesin, M. Joubert, T. Hanekom, R. Merletti, and D. Farina. A finite element model for describing the effect of muscle shortening on surface EMG. *IEEE Transactions on Biomedical Engineering*, 53(4):593–600, 2006.

[93] A. M. Gordon, A. F. Huxley, and F. J. Julian. The variation in isometric tension with sarcomere length in vertebrate muscle fibres. *The Journal of Physiology*, 184(1):170–192, 1966.

[94] Y. Nubar. Stress-Strain Relationship in Skeletal Muscle. *Annals of the New York Academy of Sciences*, 93(21):859–876, 1962.

[95] C. P. S. Taylor. Isometric Muscle Contraction and the Active State. *Biophysical Journal*, 9(6):759–780, 1969.

[96] G. I. Zahalak. A distribution-moment approximation for kinetic theories of muscular contraction. *Mathematical Biosciences*, 55(1–2):89–114, 1981.

[97] H. S. Milner-Brown, R. B. Stein, and R. Yemm. Changes in firing rate of human motor units during linearly changing voluntary contractions. *The Journal of Physiology*, 230(2):371–390, 1973.

[98] R. T Raikova and H. T. Aladjov. Hierarchical genetic algorithm versus static optimization—investigation of elbow flexion and extension movements. *Journal of Biomechanics*, 35(8):1123–1135, 2002.

[99] R. Raikova, J. Celichowski, M. Pogrzebna, H. Aladjov, and P. Krutki. Modeling of summation of individual twitches into unfused tetanus for various types of rat motor units. *Journal of Electromyography and Kinesiology*, 17(2):121–130, 2007.

[100] C. Bradley, A. Bowery, R. Britten, V. Budelmann, O. Camara, R. Christie, A. Cookson, A. F. Frangi, T. B. Gamage, T. Heidlauf, S. Krittian, D. Ladd, C. Little, K. Mithraratne, M. Nash, D. Nickerson, P. Nielsen, Ø. Nordbø, S. Omholt, A. Pashaei, D. Paterson, V. Rajagopal, A. Reeve, O. Röhrle, S. Safaei, R. Sebastián, M. Steghöfer, T. Wu, T. Yu, H. Zhang, and P. Hunter. OpenCMISS: A multi-physics & multi-scale computational infrastructure for the VPH/Physiome project. *Progress in Biophysics and Molecular Biology*, 107(1):32–47, 2011.

[101] P. R. Shorten, P. O'Callaghan, J. B. Davidson, and T. K. Soboleva. A mathematical model of fatigue in skeletal muscle force contraction. *Journal of Muscle Research and Cell Motility*, 28(6):293–313, 2007.

[102] A. L. Hodgkin and A. F. Huxley. A quantitative description of membrane current and its application to conduction and excitation in nerve. *The Journal of Physiology*, 117(4):500–544, 1952.

[103] W. Wallinga, S. L. Meijer, M. J. Alberink, M. Vliek, E. D. Wienk, and D. L. Ypey. Modelling action potentials and membrane currents of mammalian skeletal muscle fibres in coherence with potassium concentration changes in the T-tubular system. *European biophysics journal: EBJ*, 28(4):317–329, 1999.

[104] J. Sundnes, B. F. Nielsen, K. A. Mardal, X. Cai, G. T. Lines, and A. Tveito. On the Computational Complexity of the Bidomain and the Monodomain Models of Electrophysiology. *Annals of Biomedical Engineering*, 34(7):1088–1097, 2006.

[105] D. Farina and A. Holobar. Characterization of Human Motor Units From Surface EMG Decomposition. *Proceedings of the IEEE*, 104(2):353–373, 2016.

[106] N. A. Dimitrova, G. V. Dimitrov, and V. N. Chihman. Effect of electrode dimensions on motor unit potentials. *Medical Engineering & Physics*, 21(6–7):479–485, 1999.

[107] J. H. Blok, D. F. Stegeman, and A. van Oosterom. Three-Layer Volume Conductor Model and Software Package for Applications in Surface Electromyography. *Annals of Biomedical Engineering*, 30(4):566–577, 2002.

[108] A. Heringa, D. F. Stegeman, G. J. H. Uijen, and J. P. C. De Weerd. Solution Methods of Electrical Field Problems in Physiology. *IEEE Transactions on Biomedical Engineering*, BME-29(1):34–42, 1982.

[109] J. Clark and R. Plonsey. The Extracellular Potential Field of the Single Active Nerve Fiber in a Volume Conductor. *Biophysical Journal*, 8(7):842–864, 1968.

[110] S. Andreassen and L. Arendt-Nielsen. Muscle fibre conduction velocity in motor units of the human anterior tibial muscle: a new size principle parameter. *The Journal of Physiology*, 391(1):561–571, 1987.

[111] T. I. Arabadzhiev, V. G. Dimitrov, N. A. Dimitrova, and G. V. Dimitrov. Influence of motor unit synchronization on amplitude characteristics of surface and intramuscularly recorded EMG signals. *European Journal of Applied Physiology*, 108(2):227–237, 2009.

[112] D. Farina and C. Cescon. Concentric-ring electrode systems for noninvasive detection of single motor unit activity. *IEEE Transactions on Biomedical Engineering*, 48(11):1326–1334, 2001.

[113] K. Roeleveld, J. H. Blok, D. F. Stegeman, and A. van Oosterom. Volume conduction models for surface EMG; confrontation with measurements. *Journal of Electromyography and Kinesiology*, 7(4):221–232, 1997.

[114] K. C. McGill. Surface electromyogram signal modelling. *Medical and Biological Engineering and Computing*, 42(4):446–454, 2004.

[115] J. A. Nelder and R. Mead. A Simplex Method for Function Minimization. *The Computer Journal*, 7(4):308–313, 1965.

[116] V. Carriou, S. Boudaoud, and J. Laforet. Speedup computation of hd-semg signals using a motor unit specific electrical source model. *Medical & Biological Engineering & Computing*, 2017 (submitted).

[117] M. B. Brown and A. B. Forsythe. Robust tests for the equality of variances. *Journal of the American Statistical Association*, 69(346):364–367, 1960.

[118] C. S. Klein, G. D. Marsh, R. J. Petrella, and C. L. Rice. Muscle fiber number in the biceps brachii muscle of young and old men. *Muscle & nerve*, 28(1):62–68, 2003.

[119] E. Stalberg and P. Dioszeghy. Scanning EMG in normal muscle and in neuromuscular disorders. *Electroencephalography and Clinical Neurophysiology/Evoked Potentials Section*, 81(6):403–416, 1991.

[120] J. Navallas, A. Malanda, L. Gila, J. Rodríguez, and I. Rodríguez. A muscle architecture model offering control over motor unit fiber density distributions. *Medical & Biological Engineering & Computing*, 48(9):875–886, 2010.

[121] J. W. Robertson and J. A. Johnston. Modifying motor unit territory placement in the Fuglevand model. *Medical & Biological Engineering & Computing*, 2017.

[122] D. P. Mitchell. Generating Antialiased Images at Low Sampling Densities. In *Proceedings of the 14th Annual Conference on Computer Graphics and Interactive Techniques*, pages 65–72, New York, NY, USA, 1987.

[123] G. C. Elder, K. Bradbury, and R. Roberts. Variability of fiber type distributions within human muscles. *Journal of Applied Physiology*, 53(6):1473–1480, 1982.

[124] D. Farina, N. Jiang, H. Rehbaum, A. Holobar, B. Graimann, H. Dietl, and O. C. Aszmann. The Extraction of Neural Information from the Surface EMG for the Control of Upper-Limb Prostheses: Emerging Avenues and Challenges. *IEEE Transactions on Neural Systems and Rehabilitation Engineering*, 22(4):797–809, 2014.

[125] S. Boudaoud, S. Allouch, M. Al Harrach, and F. Marin. On the benefits of using HD-sEMG technique for estimating muscle force. *Computer Methods in Biomechanics and Biomedical Engineering*, 18(Suppl 1):1890–1891, 2015.

[126] David Jones, Joan Round, and Arnold de Haan. *Skeletal Muscle from Molecules to Movement*. Churchill Livingstone, Edinburgh, 2004.

[127] P. E. Crago, P. H. Peckham, and G. B. Thrope. Modulation of muscle force by recruitment during intramuscular stimulation. *IEEE transactions on bio-medical engineering*, 27(12):679–684, 1980.

[128] W. K. Durfee and K. E. MacLean. Methods for estimating isometric recruitment curves of electrically stimulated muscle. *IEEE Transactions on Biomedical Engineering*, 36(7):654–667, 1989.

[129] M. Benoussaad, P. Poignet, M. Hayashibe, C. Azevedo-Coste, C. Fattal, and D. Guiraud. Experimental parameter identification of a multi-scale musculoskeletal model controlled by electrical stimulation: application to patients with spinal cord injury. *Medical & Biological Engineering & Computing*, 51(6):617–631, 2013.

[130] R. Riener and J. Quintern. A physiologically based model of muscle activation verified by electrical stimulation. *Bioelectrochemistry and Bioenergetics*, 43(2):257–264, 1997.

[131] L. M. Mendell. The size principle: a rule describing the recruitment of motoneurons. *Journal of Neurophysiology*, 93(6):3024–3026, 2005.

[132] D. R. McNeal. Analysis of a model for excitation of myelinated nerve. *IEEE transactions on bio-medical engineering*, 23(4):329–337, 1976.

[133] S. Gehlert, W. Bloch, and F. Suhr. Ca^{2+} - Dependent Regulations and Signaling in Skeletal Muscle: From Electro-Mechanical Coupling to Adaptation. *International Journal of Molecular Sciences*, 16(1):1066–1095, 2015.

[134] H. Hatze. A general myocybernetic control model of skeletal muscle. *Biological Cybernetics*, 28(3):143–157, 1978.

[135] A. S. Wexler, J. Ding, and S. A. Binder-Macleod. A mathematical model that predicts skeletal muscle force. *IEEE Transactions on Biomedical Engineering*, 44(5):337–348, 1997.

[136] S. M. Baylor and S. Hollingworth. Simulation of ca^{2+} movements within the sarcomere of fast-twitch mouse fibers stimulated by action potentials. *The Journal of General Physiology*, 130(3):283–302, 2007.

[137] B. Dreibati, C. Lavet, A. Pinti, and G. Poumarat. Influence of electrical stimulation frequency on skeletal muscle force and fatigue. *Annals of Physical and Rehabilitation Medicine*, 53(4):266–277, 2010.

[138] S. Watanabe, S. Fukuhara, T. Fujinaga, and H. Oka. Estimating the minimum stimulation frequency necessary to evoke tetanic progression based on muscle twitch parameters. *Physiological Measurement*, 38(3):466, 2017.

[139] D. Guiraud, C. Azevedo Coste, M. Benoussaad, and C. Fattal. Implanted functional electrical stimulation: case report of a paraplegic patient with complete SCI after 9 years. *Journal of NeuroEngineering and Rehabilitation*, 11:15, 2014.

[140] D. Guiraud, T. Stieglitz, K. P. Koch, J.-L. Divoux, and P. Rabischong. An implantable neuroprosthesis for standing and walking in paraplegia: 5-year patient follow-up. *Journal of Neural Engineering*, 3(4):268–275, 2006.

[141] R. Ando, A. Saito, Y. Umemura, and H. Akima. Local architecture of the vastus intermedius is a better predictor of knee extension force than that of the other quadriceps femoris muscle heads. *Clinical Physiology and Functional Imaging*, 35(5):376–382, 2015.

[142] R. M. Erskine, D. A. Jones, C. N. Maganaris, and H. Degens. In vivo specific tension of the human quadriceps femoris muscle. *European Journal of Applied Physiology*, 106(6):827, 2009.

[143] A. J. Blazevich, D. Cannavan, D. R. Coleman, and S. Horne. Influence of concentric and eccentric resistance training on architectural adaptation in human quadriceps muscles. *Journal of Applied Physiology*, 103(5):1565–1575, 2007.

[144] A. Lizu. *Effect of the biceps Brachii tendon on elbow flexor force steadiness in men and women*. PhD thesis, University of British Columbia, 2015.

[145] L. Acosta and R. R. Roy. Fiber-type composition of selected hindlimb muscles of a primate (cynomolgus monkey). *The Anatomical Record*, 218(2):136–141, 1987.

[146] P. Zhou and W. Z Rymer. MUAP number estimates in surface emg: template-matching methods and their performance boundaries. *Annals of biomedical engineering*, 32(7):1007–1015, 2004.

[147] R. Raikova, H. Aladjov, J. Celichowski, and P. Krutki. An Approach for Simulation of the Muscle Force Modeling It by Summation of Motor Unit Contraction Forces. *Computational and Mathematical Methods in Medicine*, 2013, 2013.

[148] M. R. Barnes and R. M. Scully. *Physical therapy*. Lippincott, Philadelphia, 1989.

[149] R. Riener. Model-based development of neuroprosthesis for paraplegic patients. *Philosophical Transactions of the Royal Society B: Biological Sciences*, 354(1385):877–894, 1999.

[150] R. M. Enoka and J. Duchateau. Muscle fatigue: what, why and how it influences muscle function. *The Journal of Physiology*, 586(1):11–23, 2008.

[151] T. Siatras, G. Poumarat, J. P. Boucher, and J. C. Le Flohic. Normal and paralyzed muscle force and fatigability induced by electrical stimulation. *Journal of Manipulative and Physiological Therapeutics*, 17(5):321–328, 1994.

[152] E. A. Clancy and N. Hogan. Probability density of the surface electromyogram and its relation to amplitude detectors. *IEEE transactions on bio-medical engineering*, 46(6):730–739, 1999.

[153] F. Ayachi, S. Boudaoud, J. F. Grosset, and C.Marque. Study of the Muscular Force/HOS Parameters Relationship from the Surface Electromyogram. In Ratko Magjarevic, Kim Dremstrup, Steve Rees, and Morten Ølgaard Jensen, editors, *15th Nordic-Baltic Conference on Biomedical Engineering and Medical Physics (NBC 2011)*, volume 34, pages 187–190. Springer Berlin Heidelberg, Berlin, Heidelberg, 2011.

[154] M. D. Morris. Factorial Sampling Plans for Preliminary Computational Experiments. *Technometrics*, 33(2):161–174, 1991.

[155] A. Saltelli and F. Campolongo. Screening important inputs in models with strong interaction properties. *Reliability Engineering & System Safety*, 94(7):1149–1155, 2009.

[156] A. Saltelli, editor. *Global sensitivity analysis: the primer*. John Wiley, Chichester, England ; Hoboken, NJ, 2008.

[157] M. Al Harrach, S. Boudaoud, D. Gamet, J. F. Grosset, and F. Marin. Evaluation of HD-sEMG Probability Density Function deformations in ramp exercise. *Annual International Conference of the IEEE Engineering in Medicine and Biology Society. IEEE Engineering in Medicine and Biology Society. Annual Conference*, 2014:2209–2212, 2014.

[158] E. M. Maathuis, J. Drenthen, J. P. van Dijk, G. H. Visser, and J. H. Blok. Motor unit tracking with high-density surface EMG. *Journal of Electromyography and Kinesiology*, 18(6):920–930, 2008.

[159] A. Phinyomark, S. Thongpanja, H. Hu, P. Phukpattaranont, and C. Limsakul. The Usefulness of Mean and Median Frequencies in Electromyography Analysis. In G. R. Naik, editor, *Computational Intelligence in Electromyography Analysis - A Perspective on Current Applications and Future Challenges*. InTech, 2012.

[160] A. Zaylaa, A. Diad, M. Al Harrach, and S. Boudaoud. Evaluation of HD-sEMG grid misalignment with muscle fibers using nonlinear correlation. In *IEEE International Conference on Advances in Biomedical Engineering*, pages 289–292, 2015.

[161] B. Bigland-Ritchie. EMG/force relations and fatigue of human voluntary contractions. *Exercise and Sport Sciences Reviews*, 9:75–117, 1981.

[162] Y. Yoshitake and M. Shinohara. Low-frequency component of rectified emg is temporally correlated with force and instantaneous rate of force fluctuations during steady contractions. *Muscle & nerve*, 47(4):577–584, 2013.

[163] G. R. Naik and D. K. Kumar. Evaluation of higher order statistics parameters for multi channel semg using different force levels. In *2011 Annual International Conference of the IEEE Engineering in Medicine and Biology Society*, pages 3869–3872, 2011.

[164] E. N. Kamavuako, J. C. Rosenvang, M. F. Bøg, A. Smidstrup, E. Erkocevic, M. J. Niemeier, W. Jensen, and D. Farina. Influence of the feature space on the estimation of hand grasping force from intramuscular emg. *Biomedical Signal Processing and Control*, 8(1):1–5, 2013.

[165] S. P. Arjunan, D. K. Kumar, and G. Naik. Computation and evaluation of features of surface electromyogram to identify the force of muscle contraction and muscle fatigue. *BioMed research international*, 2014, 2014.

[166] R. Merletti and L. R. Lo Conte. Surface emg signal processing during isometric contractions. *Journal of Electromyography and Kinesiology*, 7(4):241–250, 1997.

[167] D. K. Kumar, S. P. Arjunan, and G. R. Naik. Measuring increase in synchronization to identify muscle endurance limit. *IEEE transactions on neural systems and rehabilitation engineering*, 19(5):578–587, 2011.

[168] H. S. Milner-Brown and R. B. Stein. The relation between the surface electromyogram and muscular force. *The Journal of Physiology*, 246(3):549–569, 1975.

[169] J. V. Basmajian. *Muscles alive, their functions revealed by electromyography.* Baltimore: Williams & Wilkins, 1979.

[170] M. Hayashibe and D. Guiraud. Voluntary emg-to-force estimation with a multi-scale physiological muscle model. *Biomedical engineering online*, 12(1):1, 2013.

[171] J. Lobo-Prat, P. Kooren, M. Janssen, A. Keemink, P. Veltink, A. Stienen, and B. Koopman. Implementation of EMG and force-based control interfaces in active elbow supports for men with duchenne muscular dystrophy: a feasibility study. *IEEE Transactions on Neural Systems and Rehabilitation Engineering*, 24(11), 2016.

[172] Y. Fan and Y. Yin. Active and progressive exoskeleton rehabilitation using multisource information fusion from emg and force-position epp. *IEEE Transactions on Biomedical Engineering*, 60(12):3314–3321, 2013.

[173] T. Moritani and H. A. DeVries. Reexamination of the relationship between the surface integrated electromyogram (iemg) and force of isometric contraction. *American Journal of Physical Medicine & Rehabilitation*, 57(6):263–277, 1978.

[174] J. H. Lawrence and C. J. De Luca. Myoelectric signal versus force relationship in different human muscles. *Journal of Applied Physiology: Respiratory, Environmental and Exercise Physiology*, 54(6):1653–1659, 1983.

[175] A. Botter, H. R. Marateb, B. Afsharipour, and R. Merletti. Solving EMG-force relationship using Particle Swarm Optimization. In *2011 Annual International Conference of the IEEE Engineering in Medicine and Biology Society*, pages 3861–3864, 2011.

[176] V. Carriou, J. Laforêt, S. Boudaoud, and M. A. Harrach. Realistic motor unit placement in a cylindrical HD-sEMG generation model. In *2016 38th Annual International Conference of the IEEE Engineering in Medicine and Biology Society (EMBC)*, pages 1704–1707, 2016.

[177] M. Gobbo, P. Gaffurini, L. Bissolotti, F. Esposito, and C. Orizio. Transcutaneous neuromuscular electrical stimulation: influence of electrode positioning and stimulus amplitude settings on muscle response. *European Journal of Applied Physiology*, 111(10):2451–2459, 2011.

[178] T. M. Vieira, R. Merletti, and L. Mesin. Automatic segmentation of surface EMG images: Improving the estimation of neuromuscular activity. *Journal of Biomechanics*, 43(11):2149–2158, 2010.

[179] P. K. Sahoo, S. Soltani, and A. K. C. Wong. A survey of thresholding techniques. *Computer Vision, Graphics, and Image Processing*, 41:233–260, 1988.

[180] N. Otsu. A Threshold Selection Method from Gray-Level Histograms. *IEEE Transactions on Systems, Man and Cybernetics*, 9(1):62–66, 1979.

[181] B. Afsharipour, U. Khalil, and R. Merletti. Amplitude indicators and spatial aliasing in high density surface electromyography recordings. *Biomedical Signal Processing and Control*, 22:170–179, 2015.

[182] M. Solomonow, R. V. Baratta, and R. D'Ambrosia. EMG-force relations of a single skeletal muscle acting across a joint: Dependence on joint angle. *Journal of Electromyography and Kinesiology*, 1(1):58–67, 1991.

[183] E. A. Clancy and N. Hogan. Relating agonist-antagonist electromyograms to joint torque during isometric, quasi-isotonic, nonfatiguing contractions. *IEEE Transactions on BioMedical Engineering*, 44(10):1024–1028, 1997.

[184] X. Chen, H. Wen, Q. Li, T. Wang, S. Chen, Y.-P. Zheng, and Z. Zhang. Identifying transient patterns of in vivo muscle behaviors during isometric contraction by local polynomial regression. *Biomedical Signal Processing and Control*, 24:93–102, 2016.

[185] J. Vredenbregt and G. Rau. Surface electromyography in relation to force, muscle length and endurance. *New Developments in Electromyography and Clinical Neurophysiology*, 1:607–622, 1973.

[186] C. Nordander, J. Willner, G. A. Hansson, B. Larsson, J. Unge, L. Granquist, and S. Skerfving. Influence of the subcutaneous fat layer, as measured by ultrasound, skinfold calipers and bmi, on the emg amplitude. *European journal of applied physiology*, 89(6):514–519, 2003.

[187] P. Contessa, A. Adam, and C. J. De Luca. Motor unit control and force fluctuation during fatigue. *Journal of applied physiology*, 107(1):235–243, 2009.

[188] B. Bigland-Ritchie and J. J. Woods. Changes in muscle contractile properties and neural control during human muscular fatigue. *Muscle & nerve*, 7(9):691–699, 1984.

[189] C. Gabriel, S. Gabriel, and E. Corthout. The dielectric properties of biological tissues: I. Literature survey. *Physics in Medicine and Biology*, 41(11):2231, 1996.

[190] P. W. Hodges, L. H. M. Pengel, R. D. Herbert, and S. C. Gandevia. Measurement of muscle contraction with ultrasound imaging. *Muscle & Nerve*, 27(6):682–692, 2003.

[191] M. Miyatani, H. Kanehisa, M. Ito, Y. Kawakami, and T. Fukunaga. The accuracy of volume estimates using ultrasound muscle thickness measurements in different muscle groups. *European Journal of Applied Physiology*, 91(2-3):264–272, 2004.

[192] A. Nordez and F. Hug. Muscle shear elastic modulus measured using supersonic shear imaging is highly related to muscle activity level. *Journal of Applied Physiology*, 108(5):1389–1394, 2010.